A Study of Absorption and Scattering of Microwaves by Dielectric Scatterers such as Insects

-

With Application to MIMO Radar for Imaging Termites and UAV Imaging MIMO Radar

-

And

-

An Investigation of Modes without Cutoff, Open Waveguides and Artificial Dielectrics

Gerard Anthony Rankin

Bachelor of Electrical Engineering, Chisholm Institute of Technology

Master of Science and Technology Commercialisation, University of Adelaide

Thesis submitted for the degree of

Doctor of Philosophy

School of Electrical and Electronic Engineering

The University of Adelaide, Australia

August 2015

To Kymberly and Paris

Table of Contents

Abstract

The application of radar to the detection of termites and the imaging of their activity in-situ poses many challenges. Insects such as termites and ants are dielectric scatterers with large values of refractive index and absorption at microwave and millimeter wave frequencies, and radar sensing in-situ is performed through building materials which have widely varying losses and anisotropies.

The research presented in this thesis seeks to understand the phenomena of absorption and scattering from dielectric scatterers such as termites, and to design a Multiple Input Multiple Output (MIMO) imaging radar for detecting and imaging termite activity based on that understanding. The investigation undertaken here comprises theoretical, numerical and experimental studies, and demonstrates the possibility of not only the detection and imaging of termite activity, but also the possibility of the provocation and control of termites using suitable millimeter and sub-millimeter waves wave emissions.

This thesis also presents the design and experimental testing of a novel wave guiding structure consisting of an open waveguide with an artificial dielectric coating supporting the HE_{11} mode, a mode which is inherently broadband, and which could be used to provide a millimeter wave stimulus directly to a termite. This guiding structure has the potential to deliver millimeter waves through the skin more efficiently than other techniques, and has possible applications to millimeter wave therapeutic treatments including acupuncture.

Finally, this thesis presents research on the design of an imaging MIMO radar for Unmanned Aerial Vehicles (UAVs), where target and platform velocities are very much greater than those observed in detecting and imaging termite activity. This investigation shows that small Kasami, Kamaletdinov construction 2 and Moreno-Tirkel Family B sequence families have

properties which make them suitable candidates for the sequences for high resolution imaging MIMO radar, though the Kamaletdinov construction 2 and Moreno-Tirkel Family B sequence families are the superior of the three. These results have application to a wide range of problems in imaging radar such as through-the-wall radar, medical imaging, security screening and non-destructive testing.

Declaration of Originality

This work contains no material which has been accepted for the award of any other degree or diploma in any university or other tertiary institution and, to the best of my knowledge and belief, contains no material previously published or written by another person, except where due reference has been made in the text.

I give consent to this copy of my thesis when deposited in the University Library, being made available for loan and photocopying, subject to the provisions of the Copyright Act 1968.

The author acknowledges that copyright of published works contained within this thesis resides with the copyright holder(s) of those works.

I also give permission for the digital version of my thesis to be made available on the web, via the University's digital research repository, the Library catalogue, the Australasian Digital Theses Program (ADTP) and also through web search engines, unless permission has been granted by the University to restrict access for a period of time.

Signed _____ Dated _____

Acknowledgements

To my supervisors Dr Andrew Tirkel and Adjunct Professor Bevan Bates. Thank you for your inspiration, encouragement and advice.

To Associate Professor Cheng Chew Lim, Head of the School of Electrical and Electronic Engineering, The University of Adelaide. Thank you for hosting my studies in the School, for the use of the School's facilities, and for the Departmental Scholarship, which supported the early phase of these studies.

To the IEEE South Australian Section. Thank you for the financial assistance which assisted with conference and travel expenses to the Progress in Electromagnetics Research Symposium, Marrakesh, Morocco.

To the late Associate Professor Charles Osborne. Thank you for your motivation, mentoring and friendship.

To friends and colleagues. Thank you for your support and for being there.

To my family. Mum and Dad, my sister Carmel, Tim, James, Sarah and Matthew, my brother Donald, Angus and Tara, my sister Gabrielle and Isabella. Thank you for your love and support.

Finally, to Kymberly and Paris. Thank you for your love and support and for helping to see it through to the end. I dedicate this thesis to you.

Publications of Author's original research contributions arising from this Thesis

The following is a list of peer reviewed conference publications and a granted patent of the Author's original research contributions which arose from the research conducted in this Thesis.

G. A. Rankin, and A. Z. Tirkel, "Sequences for MIMO Imaging Radar", submitted to the Australian Microwave Symposium 2016, Adelaide, Australia, 2016.

G. A. Rankin, and A. Z. Tirkel, "Sequence Families for MIMO Imaging Radar", presented at the Progress in Radar Research Workshop, Adelaide, Australia, 2015.

G. A. Rankin, A. Z. Tirkel, and A. N. Leukhin, "Millimeter Wave Array for UAV Imaging MIMO Radar," presented at the International Radar Symposium 2015, Dresden, Germany, 2015.

G. A. Rankin, and A. Z. Tirkel, "Excitation of Low Loss HE_{11} Modes on an Acupuncture-Like Needle," presented at the 39th International Conference on Infrared, Millimeter, and Terahertz Waves, Tucson, AZ, U.S.A., 2014.

G. A. Rankin, A. Z. Tirkel, L. Q. Bui, and N. W. D. Le Marshall, "Radar Imaging: Conventional and MIMO", presented at the Fourth International Conference on Communications and Electronics, Hue, Vietnam, pp. 171-176, 2012.

G. A. Rankin, N. W. D. Le Marshall, and A. Z. Tirkel, "MIMO Array for Radar Imaging Applications," presented at the Progress in Radar Research Workshop, Adelaide, Australia, 2012.

A. Z. Tirkel, J. C. S. Lai, T. A. Evans, and G. A. Rankin, "Effects of Millimeter Wave Exposure on Termite Behavior," presented at the Progress in Electromagnetics Research Symposium, Marrakesh, Morocco, pp. 1581-1585, 2011.

A. Z. Tirkel, J. C. S. Lai, T. A. Evans, and G. A. Rankin, "Heating and Provocation of Termites Using Millimeter Waves," presented at the Progress in Electromagnetics Research Symposium, Marrakesh, Morocco, pp. 1586-1589, 2011.

G. A. Rankin, and A. Z. Tirkel, "Hybrid Modes on a Single Conductor Waveguide," presented at the Progress in Radar Research Workshop, Adelaide, Australia, 2011.

N. W. D. Le Marshall, G. A. Rankin, and A. Z. Tirkel, "High Resolution, Wide Coverage Termite Imager," presented at the Progress in Electromagnetics Research Symposium, Xi'an, China, pp. 663-667, 2010.

N. W. D. Le Marshall, G. A. Rankin, and A. Z. Tirkel, "Hybrid Array for the Detection and Imaging of Termites," presented at the IEEE Radio and Wireless Symposium, Orlando, FL, U.S.A., pp. 288-291, 2010.

Patent: A. Z. Tirkel, N. W. D. Le Marshall, and G. A. Rankin, "Wide Area Detection of Insects Using Reflected Microwaves," WO 2011047426, 2009.

List of Figures

List of Tables

This page has intentionally been left blank.

1 Introduction

1.1 Research Aim

The aim of the research presented in this thesis is to study the application of radar to the detection of termites and the imaging of their activity in-situ, and to develop a design for a Multiple Input Multiple Output (MIMO) imaging radar for detecting and imaging termite activity.

The application of radar to detect and image termite activity in-situ poses many challenges. Generally, radar designers consider target scattering only in terms of the radar cross section of a target with a conductive surface, and have no need to consider the physics of absorption or scattering of a scatterer composed of a dielectric material. However, insects such as termites and ants are composed mainly of water, a substance which is characterized as a dielectric material with large values of both refractive index and absorption at microwave and millimeter wave frequencies, and therefore the characteristics of absorption and scattering of a dielectric object are important in designing a radar for detection and imaging of termite activity. In addition, radar sensing of termites in-situ is performed through building materials which have widely varying losses and anisotropies, and sensing is performed at short ranges in the near-field of the radar's antenna or array. Radar returns from termites are comparatively small, yet the building materials produce enormous backscatter returns which make detecting returns from termites in-situ extremely difficult. These and other challenges complicate the design of an imaging radar for detecting and imaging termite activity.

The investigation undertaken in this thesis will consider aspects of absorption and scattering from dielectric scatterers from theoretical, numerical and experimental viewpoints, with the

objective of understanding and absorption and scattering from termites and ants and to apply in the design of a radar to detect and image termite activity in-situ.

The thesis sets out to answer the important questions of:

- What are the important aspects of absorption and scattering from dielectric scatters?
- Which of these is important in the case of insects such a termites and ants?
- How does this understanding influence the design of a radar to detect and image termite activity in-situ?
- What other design considerations are important in the design a Multiple Input Multiple Output (MIMO) imaging radar for detecting and imaging termite?
- Is it possible to provoke or control termites using microwaves or millimeter waves?

This thesis also explores whether it might be possible to excite the HE_{11} mode on an open waveguide such as a conductor, a mode, which on an open guide, is theoretically inherently broadband having no cut-off, and whether an artificial dielectric coating could be incorporated to the guiding structure to propagate the mode, with little loss. Such a guide, if practicable, could be used to provide a millimeter wave stimulus directly to a termite. It could also have the potential to deliver millimeter waves through the skin efficiently and therefore have possible applications to millimeter wave therapeutic treatments including acupuncture.

This thesis will also consider the question of what sequences are suitable choices as candidates for the sequences for high resolution imaging MIMO radar. Although it has been assumed that the sequences exist and are suitable for MIMO radar, many of the proposed sequences have unsuitable properties. This thesis then seeks to answer the question as to whether there are sequences which have preferred properties for imaging MIMO radar.

1.2 Thesis Outline

The research presented in this thesis may be broadly separated into the following areas:

- the absorption and scattering of microwaves by dielectric scatterers such as insects,
- the design of a MIMO radar for imaging termites,
- an investigation of the HE_{11} mode, open waveguides and artificial dielectrics, and
- the design of a millimeter wave MIMO array for UAV imaging.

The bringing together of this research is linked by underlying ideas in seeking to understand absorption and scattering from dielectric scatterers, which may be used, as is done in this thesis, to model scattering from termites in-situ and to develop and assess imaging radar techniques for their detection. This research develops relevant theoretical knowledge and understanding and applies it to the practical problems of detecting and imaging termite activity. It also seeks a deeper understanding of biological and thermal effects of microwaves and millimeter waves upon termites and more deeply questions previous assumptions about propagation of modes on open guides which could have application in sensing and stimulating biological entities to stimulate and catalyze changes in behaviors at cellular and higher levels effects. The research presented in this thesis ranges across several disciplines including entomology, biology, engineering and physics.

The research in this thesis is presented in five chapters and one appendix:

- Chapter 1 is this introduction which sets out the broad scope of the research presented in this thesis and briefly recounts the original research of the author as denoted by the list of publications of the author's original research contributions provided in the front matter of this thesis.
- Chapter 2 examines absorption and scattering of microwaves by dielectrics and in particular insects such as termites and ants. Consideration is then given to some

biological aspects of the interaction between insects and millimeter and sub-millimeter waves which offer the possibility of termite provocation or control using suitable millimeter wave emissions.

- Chapter 3 incorporates the knowledge and understanding developed in Chapter 2 and applies this to the development and feasibility of the design of an MIMO imaging radar for termites. The chapter then extends the concepts so developed to exploring the feasibility of developing a millimeter wave array for UAV imaging MIMO radar.
- Chapter 4 rediscovers and reexamines the HE_{11} mode on a bare conductor, hitherto overlooked and forgotten, and investigates the possibilities using an artificial dielectric to support the Fano mode on an acupuncture-like needle to overcome losses in the conductor structure.
- Chapter 5 summarizes the conclusions of Chapters 2, 3 and 4 and avenues for future research.
- An Appendix surveys some background concepts and analysis underlying Chapters 2, 3 and 4.

1.3 Original Research Contributions of the Author

The section summarizes the author's original research contributions to knowledge in the field of absorption and scattering of microwaves by insects such as termites and ants:

- An analytical study of the mechanisms and effects of absorption and scattering from a dielectric sphere incorporating geometrical optics, diffraction optics and polarization effects and the analysis of a dielectric prolate spheroid to establish a model of absorption and scattering from an insect.
- A numerical study of absorption and scattering from insects over the microwave and millimeter wave frequencies using computer software.

- The investigation of some thermal and behavioral effects when termites are exposed to microwave and millimeter waves which have the potential to eradicate termites, or to alter their social behavior.
- The introduction of a hybrid array antenna array concept and its extension to incorporate MIMO processing concepts as an alternative to manual or mechanical scanning to detect termite activity over a large part of a wall and to image the activity using the hybrid array, which comprises a receiver sub-array to detect termite activity over a wide area at long range, and a second receiver sub-array to image termites in a small area with high resolution.
- The introduction of a new prototype array design which uses MIMO array synthesis techniques and the introduction of particular transmit sequences which make this practical. To the author's knowledge this is the first time that the techniques developed in this thesis have been used for a two-dimensional imaging radar, for imaging termite activity and for UAV imaging radar.
- A detailed discussion on the geometric pairing that occurs between each transmitter element and every receiver element in a MIMO array, which causes the phase centre of a virtual array element pairing to form at the mid-point (or mean in Cartesian co-ordinates) of a transmitter and receiver element, and consideration of the impact and design tradeoffs of transmitter and receiver spacing.
- The first instance of the use of the Moreno-Tirkel sequence Family B for high resolution imaging radar, and the first of the analysis of the Kamaletdinov construction 2 and Moreno-Tirkel Family B sequence families for imaging MIMO radar.
- Experimental observation of millimeter wave higher level biological interactions.
- A study into the problem of the existence, the excitation and the propagation with low loss of the HE_{11} mode on a conductor.

- An alternative interpretation of waveguide modes based on the current distribution on the guiding structure, rather than the field distribution.
- That for a dielectric with negative permittivity, there is a displacement D in the opposite direction to the E field in free space that can be used to close the E field loop and thus permit the propagation of electromagnetic waves without loss.
- The design of an acupuncture-like needle for the efficient delivery of millimeter waves through the skin. The study investigated the excitation of the HE_{11} mode on a conductor-like needle and demonstrated the potential for propagation of the TM_{01} mode and the HE_{11} mode on the needle with low loss using the Fano mode.

2 Absorption and Scattering of Microwaves by Insects

2.1 Introduction

The problem for investigation in this chapter is the absorption and scattering of microwaves from a scatterer such as an insect. This chapter will examine absorption and scattering and the relationship between them in general terms. It will introduce a model for scattering from an individual insect, notably a termite or an ant, in order to study the absorption and scattering from insects. It will also note that insects are composed mainly of water of a particular form, which has large values of refractive index and absorption at microwave and millimeter wave frequencies.

The starting point for this study will be Mie's well-known solution of scattering from a conductive sphere at resonance, and the contributions which led to a thorough analysis of the shadow zones which arise from scattering from a conductive sphere. The study will then apply this methodology to a dielectric sphere, and consider the contributions from geometric and diffraction optics to the particular case of the object geometry and composition of the insect model, a prolate spheroid, presented here, which introduces an additional dependence on the polarization of the incident wave due to the non-spherical nature of the prolate spheroid.

Having developed a suitable body of theoretical understanding of the absorption and scattering of microwaves from a scatterer such as an insect, consideration is then given to some biological aspects of the interaction between insects and millimeter and sub-millimeter waves which offer the possibility of termite provocation or control using suitable millimeter wave emissions.

With a knowledge of the theory of absorption and scattering of microwaves from an insect and an appreciation of some of the possible interactions between insects and microwaves, a numerical study will be undertaken, using computer software, of absorption and scattering from insects over microwave and millimeter wave frequencies.

Following this, some experiments at microwave and millimeter wave frequencies, where measurements of the absorption and scattering from termites will be made, and an investigation of some thermal and behavioral effects when termites are exposed to microwave and millimeter waves will be observed.

2.2 Absorption and Scattering

Absorption of, and scattering from, a scatterer depends on the frequency and polarization of the electromagnetic radiation falling on a scatterer, and the aspect angle, shape, size and composition of the scatterer. Resonances in absorption and scattering arise due to the geometry and the dielectric properties of the scatterer and are functions of wavelength. In the short and long wavelength regions, simple models of optical and Rayleigh scattering quite accurately describe absorption and scattering in these regions [1]. However, in the resonance scattering region, simple models cannot accurately describe absorption and scattering due to the complexities of the scattering processes which arise in this region.

2.2.1 Scattering

Some of the most important aspects of microwave scattering by insects are the dependence of the scattering on wavelength, polarization and aspect angle, and the effect of insect size, shape and composition on the return signal.

The most important component of scattering from insects such as termites and ants is backscatter [2]. However, scattering from other angles may experience reflections and absorption from surrounding building materials and structures, and can contribute significant

scattering also. Backscatter can also be enhanced or reduced by multiple scattering (multipath).

2.2.2 Relationship between Scattering and Absorption

All causal materials are dispersive. That is, in general, the dielectric permittivity and the magnetic permeability of causal materials are complex functions of frequency. This is because the alignment of the polarizations [3] of the dipole moments of the molecules and atoms in these materials [4] do not change instantaneously in response to the changes in electromagnetic fields applied to these materials. This becomes particularly evident when the applied fields have frequencies close to a resonant frequency of the material's natural ionic and atomic polarization oscillations. In fact, the real parts and the imaginary parts of the material parameters, $\varepsilon(\omega)$ and $\mu(\omega)$, are related to each other by the Kramers–Kronig relations. The imaginary parts of ε and μ relate directly to the absorption of electromagnetic radiation in the material, and dispersion and dissipation in thermodynamic media always accompany each other. As with any resonance, the response follows the applied field at frequencies below the resonance, and above the resonance the response is anti-phased with respect to the applied field. If the resonance can be made sharp enough, it will be possible to drive the real parts of the effective ε or μ negative. This under-damped, over-screened response is responsible for the negative material parameters. In dispersive media, it is assumed that the resonance is responsible for the negative real parts. Thus, media with real parts of ε and μ negative are causal, and necessarily both dispersive and dissipative.

There is no fundamental objection to the real parts of ε and μ being negative [5]. In media at thermodynamic equilibrium, there is, however, a restriction that the imaginary parts of the corresponding ε and μ are not to be negative. This is so that the total absorbed energy in a volume V of the medium,

$$\int_V d^3r \int_{-\infty}^{\infty} \omega \left[Im\big(\varepsilon(\omega)\big)|\boldsymbol{E}(\boldsymbol{r},\omega)|^2 + Im\left(\big(\mu(\omega)\big)|\boldsymbol{H}(\boldsymbol{r},\omega)|^2\right)\right] \frac{d\omega}{2\pi} \tag{2.1}$$

is positive definite [5]. Thus, negative permittivity or permeability of a medium is localized in frequency or space as the integral in Equation (2.1) must be positive definite over the frequency-space integrand.

2.2.3 Absorption

Absorption is a key physical process for the extermination of insects by microwaves. Termites have no inherent thermal regulation, and can only tolerate a small amount of localized heating.

Conventional extermination of insects by microwaves relies on indirect heating of termites. The surrounding structure is heated by microwave absorption. Termites are exterminated through being in contact with heated building materials.

Microwave scattering experiments conducted in this study will show that absorption is important because it may influence termite behavior by intentional or incidental provocation. Although provocation may be of a thermal or non-thermal nature, only thermal effects are considered here. As inferred by the optical theorem, absorption is affected by the same factors as scattering. Thermal effects, leading to provocation, may be dependent upon the location of elevated temperature regions in the insect body, the position of thermal sensors in the insect body, heat flow and a lack of thermal regulation in termites. These aspects pertain to provocation and will be considered separately.

2.2.4 Insect Model

In this study, a termite is considered to be a prolate spheroid [6] composed of water with a thin coating of chitin. Chitin is a glucose derivative and is the material that forms the

exoskeleton of many insects and crustaceans. Other insects such as ants have waists, and are therefore indented objects, which may be modeled as single or multiple Chebyshev particles. Our rationale for studying Chebyshev particles is derived from the motivation of Mugani and Wiscombe [7]:

"Since our motivation was not to examine the scattering features of individual particles but rather to unearth general nonspherical scattering properties, we have selected a two-parameter family of hitherto unstudied nonspherical particles (which we call Chebyshev particles) that can be obtained by continuously deforming a sphere by means of a Chebyshev polynomial of degree n*".*

2.2.5 Resonant Scattering and Absorption

Scattering and absorption have the most variation at a resonance or Mie region [8], where the wavelength is the same order as the insect size. For insects 4 to 12 mm in length, this is wavelengths 3 to 30 mm i.e. 100 through 10 GHz. In this region, it is difficult to model both scattering and absorption. This contrasts with the optical (short wave) region, where the Radar Cross Section (RCS) is relatively constant, or the Rayleigh (long wave) region where the RCS increases monotonically with frequency, and where simple models are quite accurate. Termites in this size range are estimated to have a mass of 15 mg, which is representative of the range of interest suggested by CSIRO of 3 to 35 mg [9, 10].

Additionally, termites are 75% water. In the frequency range 22 to 26 GHz, free water [11], has a molecular resonance which is both broad, and temperature and altitude dependent [12], and hence the dielectric properties of free water are highly frequency dependent. Due to differences in composition and molecular bonding, bound water [13] and biological water

[14], have different resonances. The large magnitudes of the refractive index, the real part varies between 3.5 and 8, and absorption, the imaginary part varies between 2 and 3, make modeling difficult. This is discussed in Section 2.6.1 below.

2.3 Analysis of Resonant Scattering and Absorption

Scattering in a resonance or Mie region has been analyzed using:

a) Analytical methods developed early in the 20th century culminating in the seminal work of Watson [15].
b) The T-matrix method proposed by Waterman [16] in 1971 and employed in numerous numerical programs.

The analytical method uses expansions involving spherical and related functions, and is quite general. As such, there are great technical problems to be overcome to obtain numerical results for arbitrary objects. The analytic method gives great insight into the processes involved in scattering and absorption.

In contrast, the T-matrix gives numerical results for any scatterer shape, but offers little insight into the mechanisms responsible for the scattered wave. The convergence of the solution depends on the shape of the object, and post-hoc analytic methods are required when unusual results are obtained.

The above considerations have led to the investigation of scattering and absorption from termite and ant like objects numerically, using “Mieschka” [17], a program developed by the German Aerospace Centre's Virtual Laboratory, and to analyze these results following the analytical method described by Inada and Plonus [18, 19], based on the pioneering work of Watson [15].

2.4 Analytical Treatment

Closed form scattering equations for a dielectric sphere can be found in Stratton [20], and those for other simple shapes in numerous standard radar scattering reference works, e.g. [2], and optics text books, e.g. [6]. They are a result of the expansion of the electromagnetic fields inside and outside the sphere using the appropriate spherical harmonics (Bessel-like functions on the inside of the sphere and Hankel-like functions on the outside of the sphere), followed by the application of boundary conditions at the origin, the surface and infinity [21]. The backscattered fields are:

$$E_\theta = \frac{e^{-ikr}}{ikr} S(\pi) \cos\varphi \tag{2.2}$$

$$E_\varphi = \frac{e^{-ikr}}{ikr} S(\pi) \sin\varphi \tag{2.3}$$

where

$$S(\pi) = \sum_{n=1}^{\infty} (-1)^n \left(n + \tfrac{1}{2}\right)(a_n - b_n) \tag{2.4}$$

and the scattering coefficients a_n and b_n are

$$a_n = \frac{j_n(x)[y j_n(y)]' - j_n(y)[x j_n(x)]'}{h_n{}^{(2)}(x)[y j_n(y)]' - j_n(y)\left[x h_n{}^{(2)}(x)\right]'} \tag{2.5}$$

$$b_n = \frac{m^2 j_n(y)[x j_n(x)]' - j_n(x)[y j_n(y)]'}{m^2 j_n(y)\left[x h_n{}^{(2)}(x)\right]' - h_n{}^{(2)}(x)[y j_n(y)]'} \tag{2.6}$$

where the primes denote differentiation with respect to the argument, $x = ka = 2\pi a/\lambda$, a is the radius of the sphere, k is the propagation constant in free space, $m = \varepsilon_r{}^{1/2} = k_1/k$ is the relative refractive index, ε_r is the relative dielectric constant of the sphere material, and $y = mx$.

The introduction of Mie's series in Equations (2.2) and (2.3), arose originally in Gustav Mie's study of light scattering from colloidal metal solutions [8]. Mie developed a solution to Maxwell's equations for the diffraction around a conducting sphere. He assumed that the electromagnetic field would establish itself in the shadow zone (see Figure 2.1), and be a super-position of spherical harmonic functions or modes. However, the solution did not take into account the transient field. The series was difficult to evaluate, due to its slow convergence [22]. It also lacked a physical interpretation because it didn't explain or provide any insight into how these harmonic modes were excited in the shadow zone. This was not resolved until Fock gave an explanation based on the diffusion of edge currents in the lit zone diffusing out and establishing currents in the shadow zone [23].

Von Lommel [24] was the first to realize that Bessel functions of real order exist and can form an orthogonal basis for the Fourier-Bessel expansion of any function [25]. Fourier had restricted himself to integer order. Von Lommel modified Fresnel diffraction [1] to apply to the transition zone, the region between the far point of the Fresnel diffraction region and the near point of the Fraunhoffer region [1]. His analysis works best on axis but has validity in the axial region. For a survey on the history of Bessel functions, refer to Gray [26] and Watson [25]. Nicholson and Poincaré came up with the idea for the crucial transform to make the Mie series converge, and Watson completed the task, presumably because he knew more about Bessel functions than anyone else [25], having the benefit of Von Lommel's insight [24]. The Watson-Sommerfeld transform [27] used to convert the scattering amplitude and obtain its asymptotic behavior was first discussed in the mathematical literature by Nicholson [28] in 1907 and by Poincaré [29] in 1910. It was re-discovered in 1918 by Watson [15], and used later by Sommerfeld [30] to treat the problem of propagation of radio waves on the surface of the earth.

The division of shadow zones for a conductive sphere is illustrated in Figure 2.1. The range dimension is partitioned into three zones:

1. the Fresnel,
2. the von Lommel or Fresnel-von Lommel or transition zone, and
3. the Fraunhoffer zone [31].

The off-axis regions can also be partitioned into three regions:

1. the lit region,
2. the axial region, and
3. the transition or Fock region.

Fock dealt with the interference between the waves in the lit region and the axial region [23].

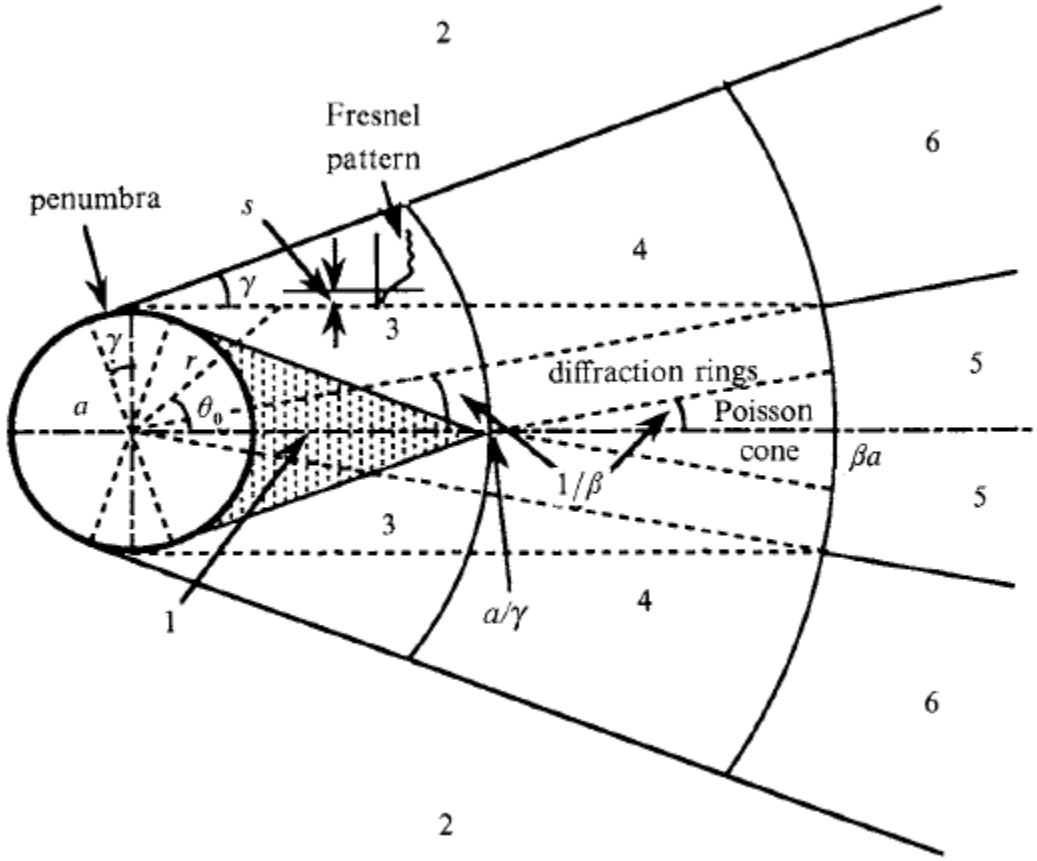

Figure 2.1 – Shadow zones for a conductive sphere. From [31].

(1) Deep shadow. (2) Deep illumination. (3) Fresnel region: a Fresnel patterns show the shift s of the shadow boundary. (4) Fresnel-von Lommel region, showing the genesis of the Poisson cone surrounded by diffraction rings. (5) Forward diffraction peak. (6) Fock transition region. (The angles are greatly exaggerated).

In Figure 2.1, three special regions are noted:

1. The penumbral region on the sphere, where there is interference between the current induced directly by the incident radiation and the surface waves excited in the shadow zone. The Physical Theory of Diffraction, as described by Ufimtsev [32], consists of geometrical optics and the induced edge current, that is the current induced directly by the incident radiation and the surface waves excited in the shadow zone.

2. The deep shadow zone, where surface and creeping wave modes dominate. Creeping wave modes are excited by edges currents[1].
3. The region of the "Poisson bright spot" which is strictly a cone of reinforcement, which starts in the Fresnel region and merges into the diffraction pattern in the Fraunhoffer region. Nussenzveig [31] appears to be the first to have analyzed the cone.

The "Poisson bright spot" has a fascinating history. Fresnel submitted his explanation of near-field diffraction to a committee judging the French Academy of Sciences competition to resolve the nature of light as either a particle or a wave [33]. The judges included Poisson, Laplace and some of their supporters, who all favored Newton's particle theory of light. Poisson thought he had Fresnel on the ropes when he concluded that if light were a wave, there should be a bright spot in the middle of the shadow, where positive reinforcement from the penumbral region should take place. Arago, another judge, who was more open minded, did the experiment, and found the bright spot. It was named Poisson's spot to mock Poisson's ability to dig a hole and to fall into it. Others have called it the Arago spot. Actually, the spot had been observed more than a century earlier by Delisle (1715) and Maraldi (1723), so this is yet another example where the history of an idea has been misrepresented.

In the case of Rayleigh scattering, the shadow zone of the sphere is a small fraction of a wavelength, and so it cannot support even the first order spherical harmonic. In the case of Mie scattering, a termite, 5 mm in length, may support two harmonics (Mie resonances) at 60 GHz –the first and second harmonic, see Figure 2.17 and Figure 2.18. For larger termites,

[1] The reason that the shadow zone is more pronounced on the sphere than on a disc is that all the surface waves on a conducting sphere are creeping waves, because of the curvature of the sphere, and hence shed radiation and are "creeping". In contrast, the shadow zone on a disc is sharper because the waves are classic Zenneck waves, and do not shed radiation due to curvature.

more harmonics can be supported. They are analogous to standing open waveguide spherical modes. This description does not include attenuation. When the mode number is low, the attenuation of the mode is low. Attenuation is measured in dB/wavelength, so the greater the number of wavelengths, the greater the attenuation. Attenuation is due to ohmic losses and wave shedding as radiation due to the curvature of the scatter [34, 35]. Edge currents excite guided waves as well as radiating of electromagnetic waves into space. This results in a sag in the standing wave modes in the centre of the shadow zone. Eventually the sag is extreme, as in the optical scattering regime. Then the shadow zone has only highly attenuated modes just past the shadow line and the shadow zone is in darkness i.e. edge currents decay quickly.

Mie's series resurfaced in connection with the theory of the diffraction of electric (radio) waves around a partially conducting sphere, and the excitation of an infinitesimal dipole at a small height above a partially conducting earth in the study of radio propagation around the earth. Macdonald's attempt to approximate Mie's series [36], then replace the series by an integral which was evaluated by the calculus of residues [37], was discredited by Poincaré and Lord Rayleigh. Both Poincaré and Rayleigh suggested some modifications, and subsequently Macdonald offered a better approximation [38]. March proposed a method of replacing the series by a definite integral [39], but this was discredited by Love [40]. Ultimately, the problem was solved by Watson [15], at the instigation of van der Pol, who was critical of all previous approaches [41]. Watson developed a solution based on the Laplace-Bessel using Bessel functions of complex order, and then integrated over a deformed contour where the sum of residues due to the enclosed poles converged [15], refer Figure 2.2 below. In considering propagation around the earth, ionospheric reflection and refraction need to be considered, so propagation occurs within a spherical shell, which is what Watson then solved.

2.4.1 Dielectric Sphere

The methods of correcting the geometrical optics scattering for the perfectly conducting sphere are not applicable in the case of dielectric or penetrable spheres because of edge currents exciting waves outside and inside the sphere which can contribute significantly to scattering.

The Watson method was followed for a dielectric sphere by Inada and Plonus [18], who identified the contributions of geometrical optics: front and back surface reflections, multiple reflections, and glory and rainbow rays. Rays in this context are the normals to wavefronts and are thus related to reflection waves. In [19], Inada and Plonus make the connection with contributions of diffracted waves, creeping waves and whispering gallery modes. All of these contributions correspond to poles in the Watson contour integral and represent the significant terms in the Mie series of Equation (2.2) and (2.3) above. These connections are shown explicitly in Figure 2.2 below.

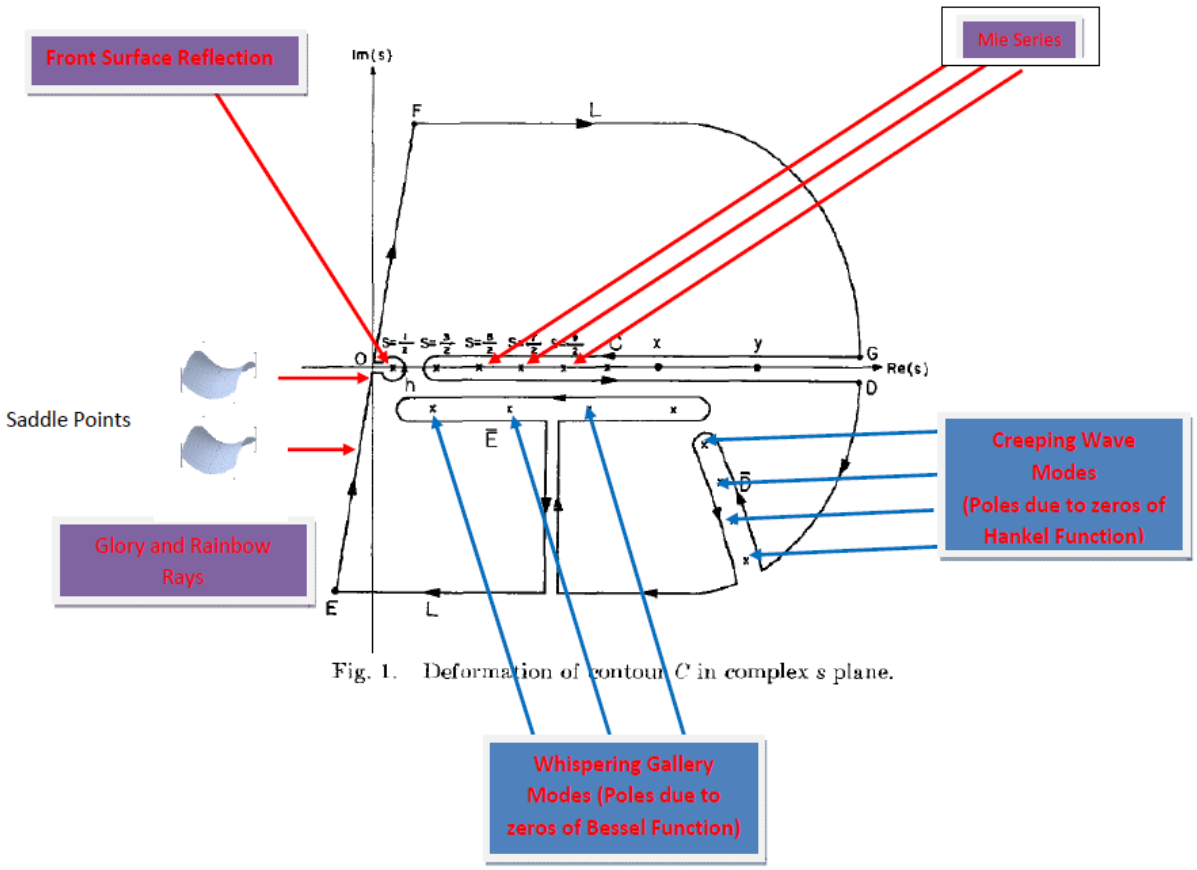

Figure 2.2 – Deformation of contour C in complex s plane. Adapted from [18].

It can be shown that the only contributions to Mie scattering occur from:

1. The isolated pole at $s = 1/2$, which is identified with the phasor sum of the front surface reflection and odd order multiple reflections within the sphere.
2. Saddle point contributions to the line integral (stationary phase approximation) in the 3rd quadrant. There is a saddle point at $s = 0$ and this adds to the axial return. Other saddle points are identified with glory rays (see Figure 2.3) and rainbow rays (see Figure 2.4).
3. A finite series of poles (Type E) just below the real axis, bounded by the argument ka. These are identified with whispering gallery modes (waveguide modes) inside the sphere. In a nonabsorbing sphere, these are lightly damped. The number of poles corresponds to the number of whispering gallery modes.

4. An infinite series of poles (Type D) with high damping (regardless of the absorption properties of the sphere). These are identified with creeping wave modes, which circumnavigate the sphere. These were the waves that allowed Watson to explain the propagation of radio waves around the earth. For dielectric spheres, these waves are more complicated, since they can take short cuts through the sphere, subject to Snell's law of refraction, as explained by van de Hulst, which may give rise to glory or rainbow rays [42]. Rays tangential to or which are internally reflected by a dielectric sphere, may emerge from the sphere as surface waves and skip a short distance before reentering the sphere. Under appropriate conditions of material parameters and geometry these glories can exist.

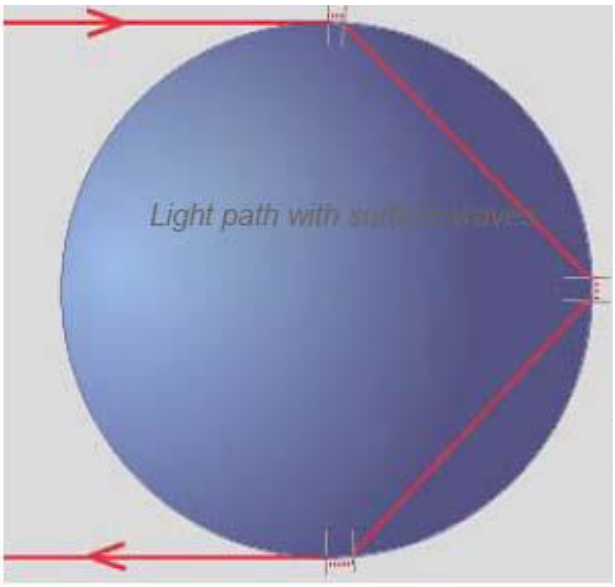

Figure 2.3 – Ray path of glory ray. From [43].

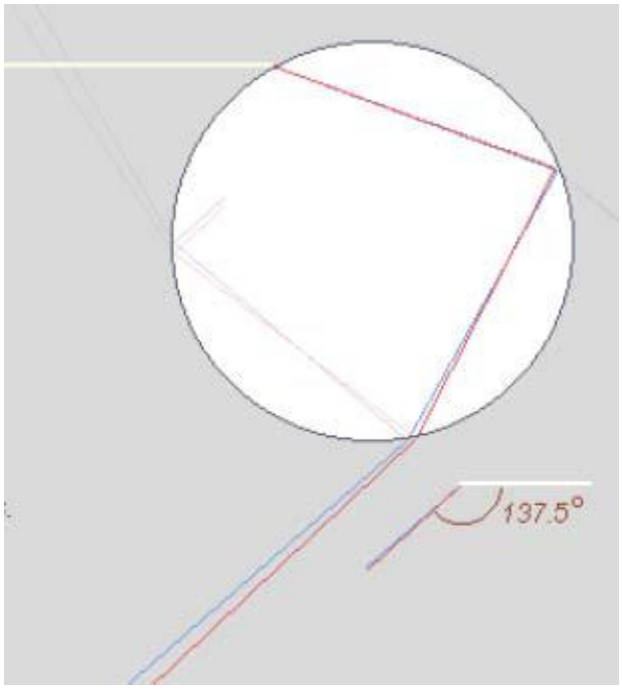

Figure 2.4 – Ray path of rainbow ray. From [42].

The backscatter (and scattering at all other angles), including the absorption properties of the sphere can be understood by summing the significant contributions from the above four sources, provided that they are treated as complex quantities with magnitude and phase.

Inside the sphere, only Bessel Functions (of the first kind) can be used in the expansion of the electromagnetic field, since the Neumann Function (Bessel Function of the second kind) is singular at the object's centre. Outside the sphere, Hankel functions provide a complete basis since they vanish at infinity, which is a necessary condition [21].

Analysis of the poles of a and b coefficients in Equations (2.5) and (2.6) requires an examination of the zeroes of Bessel functions and Hankel functions for a real argument (ka) as a function of their order. Both the order and the argument may be complex numbers. For Bessel functions, and their derivatives, the zeroes occur on or near the real axis, bounded by 0 and ka, the argument. For Hankel Functions of the second kind, the zeroes occur on a contour in the fourth quadrant, with the real component exceeding the argument (ka) and a

substantial (negative) imaginary component. The argument of the zeros lies in the range $\left[\frac{\pi}{3}, \frac{\pi}{2}\right)$.

For a complex exponential the imaginary part can be negative, zero or positive. If the imaginary part is negative, the exponential is damped and decays. If the imaginary part is zero, the exponential is neither damped nor undamped, and the exponential has a constant amplitude. If the imaginary part is positive, the exponential is undamped, and the exponential tends to infinity. For Bessel function of complex order, it is speculated that these functions may exhibit a similar behavior if the complex order is imaginary negative, zero or positive. However, to the author's knowledge this question has not been resolved.

The following result is due to Magnus and Kotin [44] (extract below), which demonstrates the important result that solutions of the Mie series are decoupled from each other inside and outside of the dielectric sphere.

This shows that the distance between two consecutive zeroes of $H_v^1(x)$ tends to zero, and that the argument of the zeros tends towards $\pi/2$, although their real part tends towards infinity. Therefore the behavior of the zeroes as derived from the formulas of van der Pol and Bremmer [25, 45] is not the final one. According to these, for large x (i.e. for $x \gg 1$), the approximate expression

$$v_n \sim x + x^{1/2}\tau_n \tag{2.7}$$

for the n^{th} zero v_n of $H_v^1(x)$, where for large n

$$\tau_n = \frac{1}{2}\left[3\pi\left(n + \frac{3}{4}\right)\right]^{2/3} e^{i\pi/3} \tag{2.8}$$

and where

$$\tau_0 = 1.856e^{i\pi/3} \tag{2.9}$$

$$\tau_1 = 3.245e^{i\pi/3} \tag{2.10}$$

and so on.

The conditions for the existence of poles in the a and b coefficients reduce to:

$$\frac{[y^{1/2}\boldsymbol{J}_s(y)]}{m[y^{1/2}\boldsymbol{J}_s(y)]'} = \frac{[x^{1/2}\boldsymbol{H}_s{}^{(2)}(x)]}{[x^{1/2}\boldsymbol{H}_s{}^{(2)}(x)]'} \tag{2.11}$$

and

$$\frac{[y^{1/2}\boldsymbol{J}_s(y)]'}{m[y^{1/2}\boldsymbol{J}_s(y)]} = \frac{[x^{1/2}\boldsymbol{H}_s{}^{(2)}(x)]'}{[x^{1/2}\boldsymbol{H}_s{}^{(2)}(x)]} \tag{2.12}$$

Therefore, the only regions where any of these functions have significant variations as a function of the (complex) argument s, is near their zeros in the complex plane. Since the zeros of the Bessel and Hankel functions, $\boldsymbol{J}_s(y)$ and $\boldsymbol{H}_s{}^{(2)}(x)$ respectively, occur in disjoint regions of the complex plane, they are largely decoupled, and the poles occur near the zeros of either the Bessel or the Hankel functions, or their respective derivatives. Thus the solutions of the Mie series are decoupled from each other inside and outside of the dielectric sphere. Bessel functions are the solutions inside the dielectric sphere and Hankel functions are the solutions outside the dielectric sphere [21].

2.4.2 Geometrical Optics Contributions

The previous discussion was on the shadow zone. The section will now consider the behavior in the lit zone and the contribution of geometrical optics.

2.4.2.1 Front and Back Surface Reflections

Material loss for a lossy dielectric is characterized by the skin depth= $\frac{c}{\pi f\sqrt{2\varepsilon'\left(\sqrt{1+tan^2\delta}-1\right)}}$ [46].

Figure 2.5 below shows the skin depth in millimeters in water versus frequency in GHz, for the E field parallel to the long axis of the scatterer (the most favorable for a back surface reflection ray), refer Section 2.4.4. Here the back surface of the termite is 1.2 mm away from the front surface for the paraxial ray. The round trip length is 2.4 mm. The smallest material loss for a paraxial ray occurs at 20 GHz, where it is 24 dB. Therefore the back surface reflection is at best 0.01 of the incident amplitude (40 dB down) and can be considered negligible, regardless of its phasing.

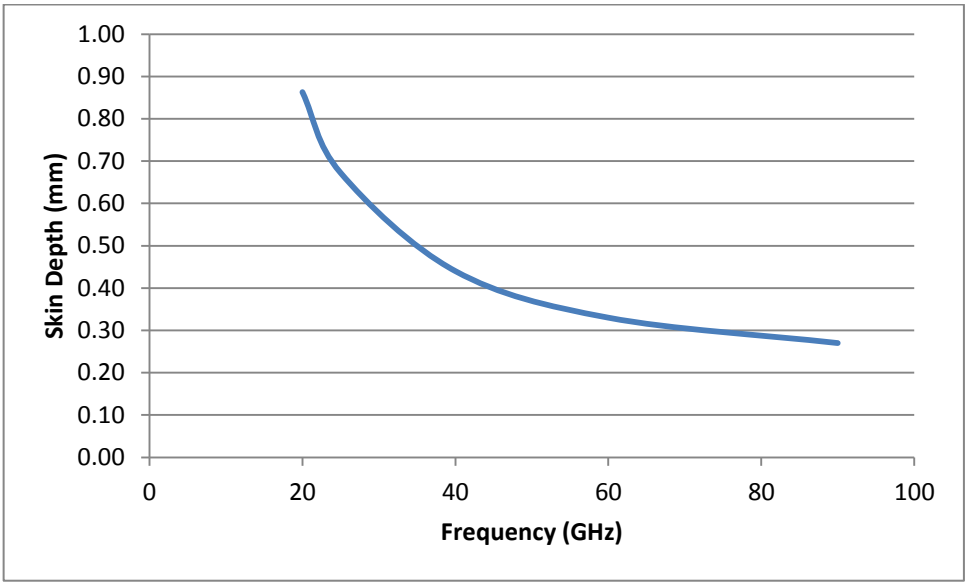

Figure 2.5 – Skin depth (mm) in water at 20°C as a function of frequency (GHz).

2.4.2.2 Rainbow and Glory Waves

The necessary conditions for the existence of rainbow and glory rays have been studied over a range of modes, refractive indices etc. However, these results do not necessarily include the geometry of the scattering particle, nor the high dielectric loss. Inada and Plonus [18] applied Snell's Law for absorbing materials incorrectly, limiting the usefulness of their results. The correct interpretation of Snell's law for absorbing materials is given in [46]. This matter was

investigated in this study using Lekner's interpretation [46] by simulation using Light Tools (a ray tracing package) [43]. No rainbow or glory rays were found for representative refractive index range and typical termite geometry, as shown in a typical result in Figure 2.6 below. It was found that rainbow and glory rays were absent in this simulation.

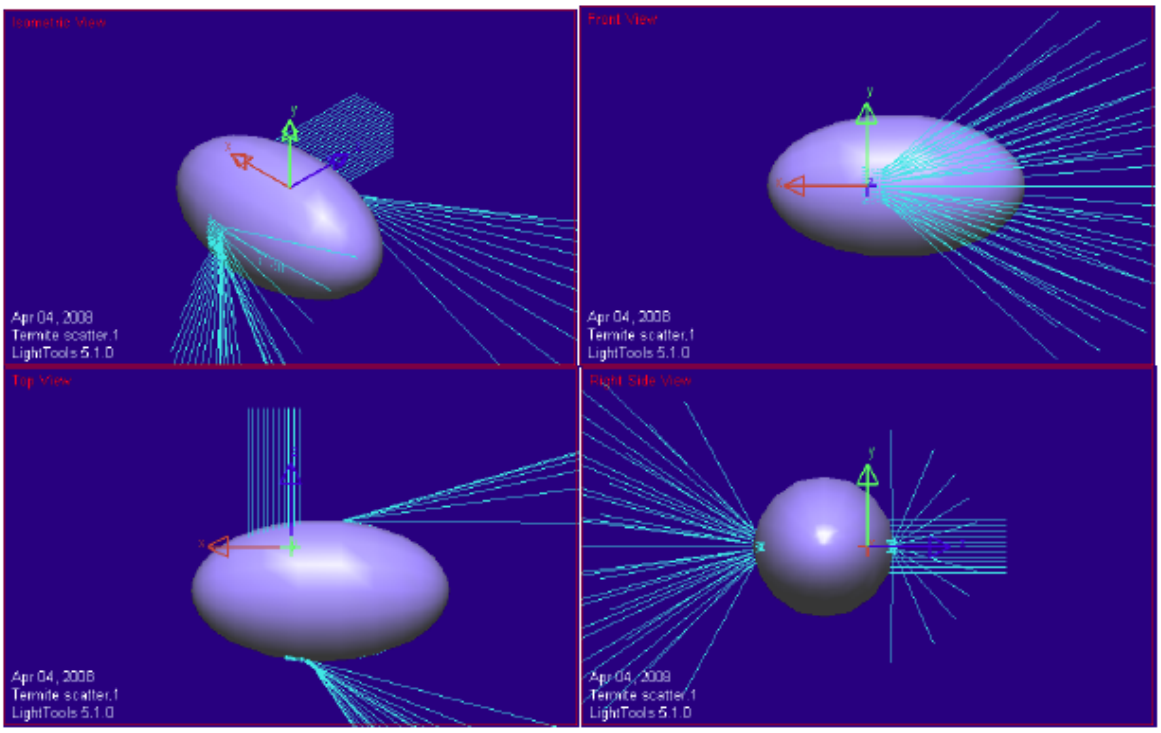

Figure 2.6 – Ray tracing demonstrating performed with LightTools [43], showing absence of rainbow and glory rays.

2.4.3 Diffraction Optics Contributions

The previous discussion was on the behavior in the lit zone and the contribution of geometrical optics. Now the dialogue will return to a discussion on the shadow zone, the Inada-Plonus and Watson analysis and the contribution of diffraction optics.

2.4.3.1 Whispering Gallery Modes

A major factor in assessing this contribution arises from the refractive index of water. The real and imaginary components of the refractive index of water at 20°C are shown in Figure 2.7

and Figure 2.8. This shows a high refractive power, high dielectric loss and high dispersion. Such dielectrics are avoided in the literature. The only case this author has found of a dispersive dielectric is treated by Jiao [47].

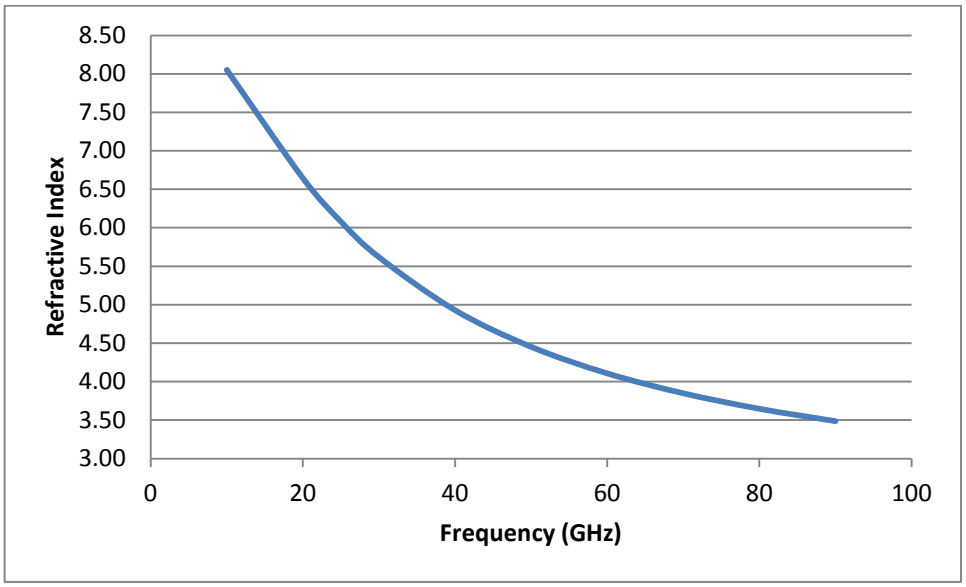

Figure 2.7 – Refractive index of pure liquid (aqueous) water at 20°C – real component.

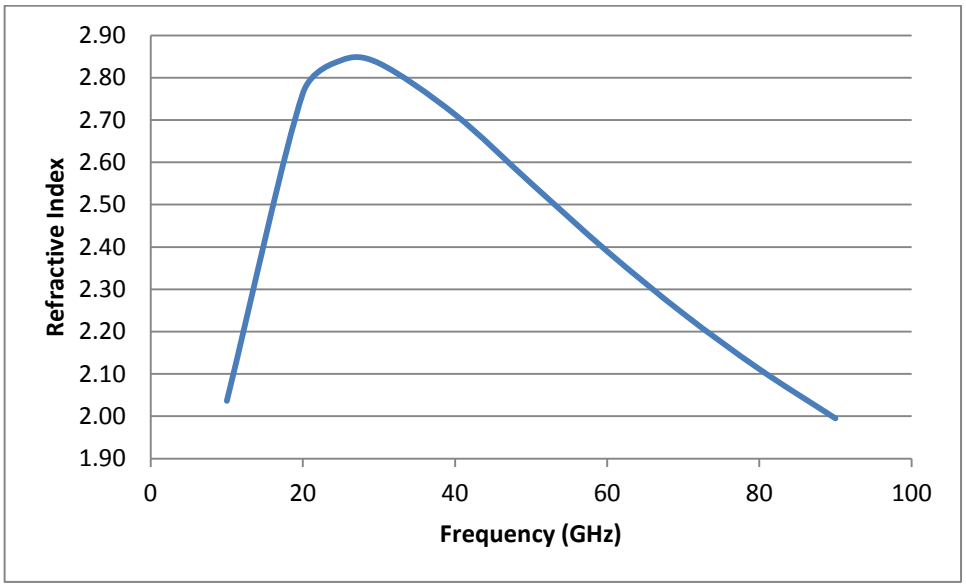

Figure 2.8 – Refractive index of pure liquid (aqueous) water at 20°C – imaginary component.

A general conclusion can be drawn regarding whispering gallery modes. These modes are excited by rays refracted into the object. Snell's law for an absorbing dielectric yields

$\tan^2\theta_c = \frac{2}{(\varepsilon_R-1)+\sqrt{(\varepsilon_R-1)^2+\varepsilon_I{}^2}}$ [46]. For water, this means that all refracted rays are confined to a cone with a half angle of 14° around the normal to the surface; i.e. the rays penetrate steeply and deep into the dielectric. In order to excite whispering gallery modes, they have to bounce around inside the object (total internal reflection) and reinforce constructively (in phase) to form the modes. This means the modes would be of a high radial index and severely attenuated due to the very small skin depth. Therefore, they should contribute significantly to the absorption and negligibly to backscatter.

2.4.3.2 Creeping Waves

For a dielectric object, the creeping waves will be present, except that, unlike for a conducting object, the waves can take short cuts through the sphere [42]. This has been verified experimentally at optical and microwave frequencies, including some remarkable pulsed experiments for metallic spheres by Rheinstein [48], and for dielectric spheres by Inada [49], who catalogued the time delays for waves which did and did not use short cuts. The geometry of a short cut ray is shown in Figure 2.9 below [48].

Van de Hulst [42] has suggested that surface waves can take a number of shortcuts through the sphere. Let us consider his scattering model for surface waves as shown in Figure 2.9. Surface waves are excited by rays of a grazing incidence and propagate along the surface. The surface waves may enter the sphere at point A, taking a shortcut through the sphere, and reemerge as surface waves at point B at the critical angle ac. The critical angle of total internal reflection is defined by $\sin ac = 1/m$, where m is the real part of a complex refractive index. Such a shortcut may take place any number of times around the entire path of surface waves.

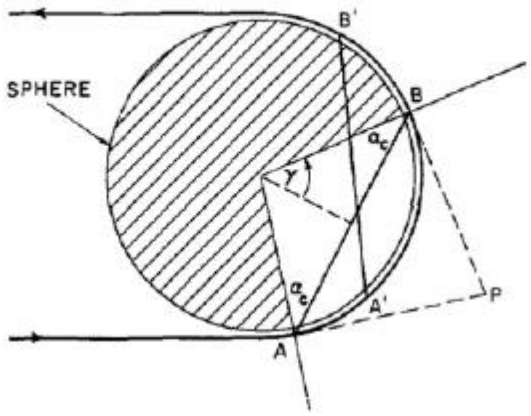

Figure 2.9 – Creeping wave short cut through a dielectric sphere. From [48].

Using the surfaces of constant phase, Snell's Law for an absorbing dielectric at critical incidence or exit becomes: $\tan^2\theta_c = \frac{2}{(\varepsilon_R-1)+\sqrt{(\varepsilon_R-1)^2+\varepsilon_I{}^2}}$ [46]. Using this result, it is possible to ray-trace the short cut for various frequencies for an object resembling a termite, as shown in Figure 2.10 below.

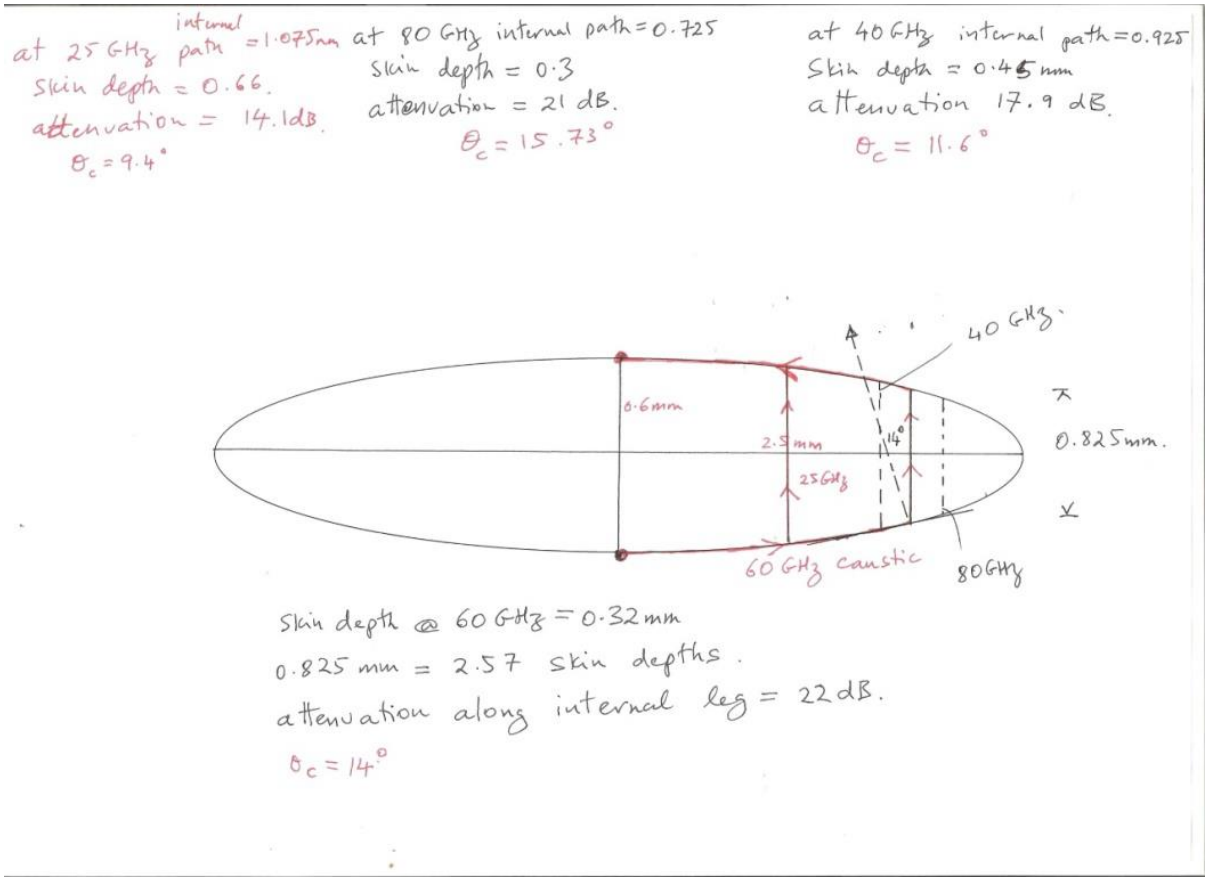

Figure 2.10 – Ray trace of short-cuts through a dispersive prolate spheroid.

Ray tracing programs, including Light Tools [43], do not include creeping waves, so this analysis was performed by hand. The frequency variation of the real and imaginary components of the refractive index was included. The trajectory, and hence the magnitude and delay of the creeping ray, is a function of frequency. The magnitude varies by at least 8 dB. The phase is difficult to calculate, involving a complex index of refraction inside the dielectric, and a calculation of an elliptical integral for the path along target. The calculations are in 3D. An order of magnitude estimate indicates the path varies from 16 mm at 25 GHz to 6 mm at 80 GHz (i.e. 8.3 radians to 10 radians). This is a relatively small phase variation: approximately ±45° (i.e. 1.7 radians or 97°). This is insufficient to result in maxima and minima in backscatter as a result of interference of the short cut ray with the specular reflection. It is as if the wave finds a phase equalizer by doing its short cut. Whether this generalizes to more sophisticated models is an open question. In [47], the authors deal with a dispersive sphere,

and report a similar result, without explaining the difference in behavior. Their model (PMCHWT: Poggio, Miller, Chang, Harrington, Wu and Tsai [50]) is a merge of Waterman's T-matrix [16] and Harrrington's surface current analysis, as modified by Wu [51]. The work reported here could be modified to include Wu's modifications. As a future investigation, it should be possible to include Ikuno's work on ray paths in various objects [52], including some that resemble ants and include asymmetries like those in his treatment (all non-dispersive).

2.4.4 Polarization

The case more of interest in nature is that of a prolate spheroid as very few organisms have spherical symmetry. Absorption in the case of a prolate spheroid scatter depends on the polarization of the electric and magnetic fields and has been examined by Barber [53]. Coupling of the electric field is greatest when the field is tangential to the scatterer, and coupling of the magnetic field is greatest when the cross-sectional area is perpendicular to the field.

When the electric field is parallel to the long axis of the scatterer, both the electric and magnetic fields couple well. The magnetic field is perpendicular, and drives a current around the insect inducing currents everywhere. The electric and magnetic fields induce linear and circulating currents into the scatterer.

When the electric field is perpendicular to the long axis of the scatterer, the magnetic field couples well as the scatterer cross-section is perpendicular to the field much the same as when the electric field is parallel to the long axis of the insect. However, the electric field couples poorly as the scatterer has curvature away from the field and very quickly, coupling falls away. Only on the ends of the scatterer is the electric field absorbed strongly.

When the electric field is along the short axis of the scatterer, the electric field couples poorly like when the field is perpendicular to the long axis of the scatterer. However, now also the

magnetic field also couples poorly because the field now only sees a small cross-section of the scatterer.

2.4.5 Conclusion

From the above analysis of both a conducting sphere and dielectric prolate spheroid, the principal component of the backscatter should be a coherent superposition of the front surface reflection and a first order creeping wave component, as shown in Figure 2.11 below, except that the creeping wave may make one or more short cuts through the object, depending on its geometry and refractive index.

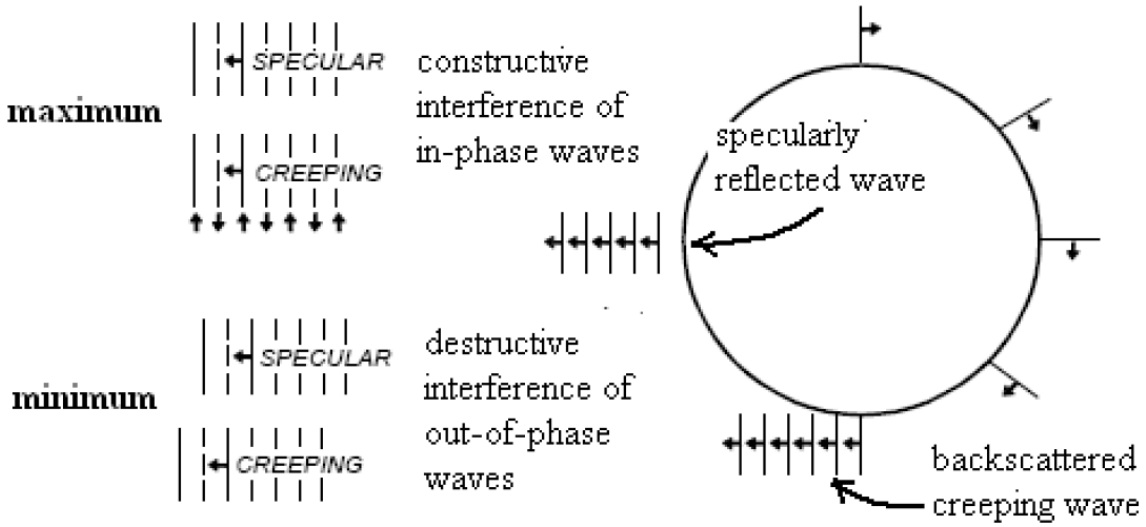

Figure 2.11 – Illustration of the specular reflection, and the creeping wave, whose mutual interference causes oscillations in the backscatter. From [54].

Therefore, the RCS is due to the superposition of two waves: the specular reflection and the creeping wave, as shown in Figure 2.11 above. In that classical case, for a conducting sphere, the creeping wave suffers a delay of $\pi R + 2R$ relative to the specular reflection, and this is responsible for the interference pattern. It is assumed that multiple revolutions around the object are too weak to be considered.

This argument does not hold for a dielectric object. In a dielectric, it is possible for the creeping wave to make a short-cut (or multiple short-cuts through the object, subject to Snell's law refraction at a critical angle (incidence or refraction at 90°), refer Section 2.4.3.2. Therefore, the above path difference may not be the same as for the conducting sphere, but must include the effect of the short cuts. The sphere can sustain such short-cuts anywhere on its circumference, but a spheroid can only sustain a single short cut perpendicular to the axis. However, a dielectric object should exhibit a similar oscillatory interference pattern as a conducting one, with maxima and minima in different places. Since absorption is largely influenced by coupling to whispering gallery modes inside the target, where they get dissipated, it is likely that this absorption is concentrated just below the surface of the target. This will require a more thorough analysis. There may be exaggerated absorption peaks due to the coincidence of the water absorption resonance at 22 GHz with whispering gallery mode resonances for a termite sized object. This is borne out in the simulations reported in the Section 2.6. Coupling to whispering gallery modes is polarization and shape dependent.

2.5 Biological Aspects

Apart from thermal effects, little is known about the effects of millimeter wave exposure on termite senses. However, theoretical and experimental investigation of the interactions of millimeter and sub-millimeter waves with living things has a rich and varied history. This offers the intriguing possibility of termite provocation or control, using suitable emissions.

An understanding of the non-thermal effects of microwaves and millimeter waves on biological systems has far reaching consequences, whose impact cannot be underestimated. It is relevant to the hazards of microwave exposure [55], its therapeutic use [56], biological control, sensing and weapons. It is also a complex problem, which has occupied many researchers, and perhaps that is why the debate has been clouded by emotion. Two types of interactions are pertinent to termites:

1. Cellular Interactions.
2. Higher level interactions.

These interactions are discussed in the following sections.

2.5.1 Cellular Effects

A model of microwave-cell interactions was studied theoretically by Fröhlich [57] in the 1960's and 1970's, who concentrated on the cell membrane. He calculated that the natural resonance of dipole charges on a typical cell membrane would be in the 50 GHz region, which was difficult to study experimentally at the time. "How typical," Fröhlich must have thought, "for Nature to take advantage of our experimental incapabilities!" (see [58], page 151). Fröhlich's enthusiasm proved contagious, and a search for confirmation of the theory resembled the search for El Dorado or the fountain of youth. The quest persists today.

Fröhlich's evidence for resonances of dipole charges on a cell membrane was indirect. There was biological evidence that cell colonies synchronize their growth spurts, and this coincides with the appearance of sharp Raman absorption lines in the far infra-red. Sharp lines below 6 THz are found in active (metabolizing) synchronized cells, whereas broad bands only are exhibited by both resting cells and nutrient solutions. The intensities of the Stokes and anti-Stokes Lines were almost equal, so the process could not be attributed to a thermal effect. A thermal effect results in an unequal intensity ratio and this has been used to measure temperature [59]. Fröhlich concluded that living cells exhibited sharp energy states, which were pumped by a new metabolic process. The smallest separation of the levels which could be resolved at the time was 150 GHz [60], but Fröhlich speculated that smaller separations must exist [60], and that these should be commensurate with the natural frequencies of the oscillating dipoles of his model of the cell membrane. Fröhlich speculated further that stimulation of such life altering metabolic processes should be possible by excitation of the

relevant frequencies [61]. However, millimeter wave sources were unreliable at the time, so Fröhlich's hypothesis could not be tested properly by measurement or excitation.

Today, the precision of Raman spectroscopy has improved to the point where 1.5 cm^{-1} = 45 GHz resolution is possible [62]. Likewise, millimeter wave sources have improved dramatically, and although the literature abounds with reports of such excitation, the Raman line measurements have never been repeated to the best of the author's knowledge, so the theory remains unproven.

An explanation of the narrowband nature of the absorption lines was needed. Fröhlich postulated that this effect was due to a Bose condensation of the dipole oscillators, causing them to synchronize their frequencies, and therefore excite extremely narrow lines. Davydov [63] considered that the effect was due to soliton resonance. This led to the conclusion that metabolic energy may be used by biological systems to excite coherent vibrations in the millimeter and sub-millimeter region. Therefore, conversely, it should also be possible to use radiation at these frequencies to intervene in biological processes.

At a similar time, reports from the former Soviet Union indicated that narrowband absorption in many biological systems was observed, particularly around the 43 GHz, 51 GHz and 60 GHz regions, with some variation on that theme. This led to a frenzy of publications; experiments demonstrating the effects of narrowband absorption on cell growth and behavior, and modifications to the above theory justifying these results and vice versa. This has led to spin-offs, such as therapeutic use of specific millimeter wave frequencies as acupuncture treatment, specific cancer [64], and other pathology treatment, mimicking the Rife Machine [65], which purports to achieve such effects at lower frequencies. Millimeter wave therapy equipment and facilities are currently quite popular in the U.S.A., Russia and Eastern Europe.

A persistent issue is that of a threshold in the power density required for the effects to become apparent, i.e. a threshold. Belyaev et al. [66] claim to have demonstrated that exposure at the exact resonance frequency at power densities exceeding 10^{-19} W/cm^2 was sufficient to induce the "synchronization" effect in cell growth, therefore claiming that the threshold is practically zero. Osepchuk et al. [67] questioned the measurements as potentially flawed, a claim which was not addressed adequately in Belyaev's subsequent rebuttal [68].

Numerous experimental papers give scant regard to the exact details of the equipment and measurement techniques, and thus, many results have not been successfully replicated, and must be called into question. This also applies to the theoretical papers justifying these results.

This does not mean however, that the effects do not exist, or that all experimental papers are flawed. A counter example, pertinent to insects is found in [69], where it was found that exposure of insects receiving ^{32}P orthophosphate to low-intensity (power density 0.5 μW/cm^2) millimeter waves (42.2 GHz) changes the rate of label incorporation into their antennae. The magnitude of the effect is no less than 100-200%. The maximum response is reached 1.5 to 2 minutes after the onset of exposure. This evidence suggests that there is the possibility of cellular and biological effects and that these can be observed by an independent objective measure.

2.5.2 Higher Level Effects

The previous discussion focused on cellular effects. This section will now discuss higher level effects.

It has long been hypothesized that insects may use electromagnetic waves for sensing, navigation and communication. Pioneering work by Callahan, such as [70] demonstrates that various moths are capable of modulating resonant infra-red emissions and presumably detecting such emissions. Callahan analyzed the performance of various anatomical parts of

moths as dielectric waveguides and antennas, and constructed and characterized scale models at X-band (8 to 12 GHz), demonstrating excellent agreement [71]. Gavan [72, 73] has extended this analogy to antenna arrays formed by spiked elements on the hornet's cuticle. He speculated that hornets may use these arrays for navigation, deploying frequencies between 140 GHz and 600 GHz. His attempts to detect such emissions at 140 GHz were unsuccessful, but this was attributed to instrument limitations. An aspect of such investigations which appears to have been overlooked is the polarization of the transmissions, and the sensitivity of the detection to that polarization. Insects with the ability of vision actively use polarization of skylight and reflected light for navigation [74], so it is also possible that any millimeter/sub-millimeter wave communication/navigation system might do so.

If it is true that insects employ millimeter and sub-millimeter wavelength emissions for communications, sensing and navigation, it offers the intriguing possibility of jamming their emissions or substituting false signals, in order to control them. A mechanical analogue of this method has already been applied successfully by Evans et al. [75], who established that termites tap their food, and analyze its vibrational response, to assess its suitability as a food source. By recording various responses, and broadcasting them to termites, Evans et al. [75] managed to deceive termites, and induce them to sample wood that they would not normally eat, and conversely shun their favorite wood species.

A difficulty in assessing insect response to a given stimulus is that insects have multiple senses, and their social interaction compounds the problem. Becker [76] has studied the effects of low-frequency magnetic fields on termites. Recently, Esquivel et al. [77] have demonstrated, using X-band (8 to 12 GHz) ferromagnetic resonance, that sufficient amounts of magnetite can accumulate in a termite body to act as a magnetic sensor.

Another aspect of the issue of insects employ millimeter and sub-millimeter wavelength emissions for communications, sensing and navigation arises because there exist commercial

and exploratory termite sensors employing millimeter waves. The commercial sensor Termatrac®, operates in the Industrial Scientific and Medical (ISM) band at 24.125 GHz [78]. An experimental sensor by Fuji [79] operates at 100 GHz. As the millimeter wave spectrum becomes more congested, there are pressures to redistribute the ISM bands upwards in frequency. Concurrently, more devices are becoming available in these higher bands. Many of them involve components which generate harmonics, which are not easy to measure or control.

Therefore, it is important to establish whether exposure to these sensing frequencies, or any other critical millimeter wave frequencies can incidentally excite any of the non-thermal effects.

In view of this, it was decided to investigate termite response when exposed to 24 GHz, 43.2 GHz and 60.2 GHz [80]. No unusual effects were observed, although many more tests, as explained above, are required to confirm this.

2.6 Numerical Treatment

In this section will investigate the absorption and scattering of electromagnetic waves from termite and ant like objects numerically using “Mieschka” [17], and analyze these results following the analytical method described by Inada and Plonus [18, 19].

The radar cross section of insects has been modelled numerically by treating them as droplets of water of equivalent mass [81]. However, until now, very few scattering and absorption measurements of insects have been performed beyond 13 GHz. Liquid water exhibits dielectric relaxation at around 22 GHz causing significant dispersion and loss. Also, termites possess an exoskeleton, whose thickness is an increasing fraction of a wavelength as the frequency increases. Both these effects are considered in order to develop an appropriate physical model for frequencies between 13 GHz and 110 GHz.

2.6.1 Simulation Tool and Scatterer Parameters

Termites are composed of approximately 77% water [82]. The water component in living organisms is further divided into free water [11], and bound water. When bound water molecules are attached to proteins, lipids etc., the combination is known as biological water. The dielectric properties of biological water have been studied extensively from low frequencies through to the infra-red. This has led to a model for the dielectric constant based on a frequency-dependent dielectric function, $\epsilon(z)$, (where $z = j\omega$) which includes n Debye relaxation processes and m vibrational modes [14]. Thus:

$$\epsilon(z) = \epsilon_0 + \sum_{i=1}^{n} \frac{\Delta\epsilon_i}{1 + z\tau_i} + \sum_{j=1}^{m} \Delta w_j \left[1 - \Phi_j(z)\right] \tag{2.13}$$

where $\Delta\epsilon_i$ is the weight of the ith Debye relaxation with relaxation time constant τ_i, and Δw_j is the weight of the jth vibrational mode with vibrational moment correlation function Φ_j.

The major component of the relaxation spectrum due to water is between 8 and 10 ps with a weight of about 60 [83]. Other relaxation processes are far removed from this. There are two Debye absorption peaks around 100 MHz and 20 GHz for most biological materials. The low-frequency absorption is due to bound water, while the high-frequency absorption is due to free water and corresponds to the 8-10 ps relaxation time [84]. The bound water contribution at frequencies above 10 GHz is assumed to be negligible. Pure water and biological water have another much higher relaxation frequency around 850 GHz, and resonant absorption peaks between 2 and 20 THz. Therefore, the Debye absorption peak around 20 GHz is the only factor falling within the range of microwave frequencies that of interest to us, as all the other peaks are too far removed.

Insect bodies are covered by an exoskeleton composed of a thin layer of chitin which can be modelled. So, the other factor which also needs to be considered in modelling a termite, is the influence of the exoskeleton because it may affect either the absorption or scattering

behavior. An image of a part of the leg of a typical termite is shown in Figure 2.12. It indicates a chitin layer thickness of 5 µm. The dielectric properties of chitin have been studied extensively [85]. Insect exoskeleton is claimed to have a dielectric constant between 2.5 and 3 [86].

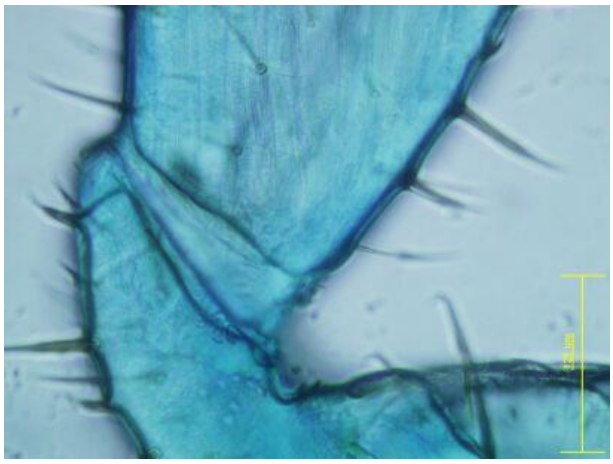

Figure 2.12 – Leg of a Coptotermes acinaciformis. (Courtesy of Ra Ata Inta, CSIRO Entomology.)

To evaluate the effect of the chitin layer on scattering, reflection and transmission was computed for pure water and for water coated with a 5 µm layer of chitin at normal incidence using Luxpop [87], assuming planar geometry. The real and imaginary components of the dielectric constant of water are shown in Figure 2.13 and Figure 2.14. These were derived from [12, 88], for the frequency range 10 GHz to 110 GHz.

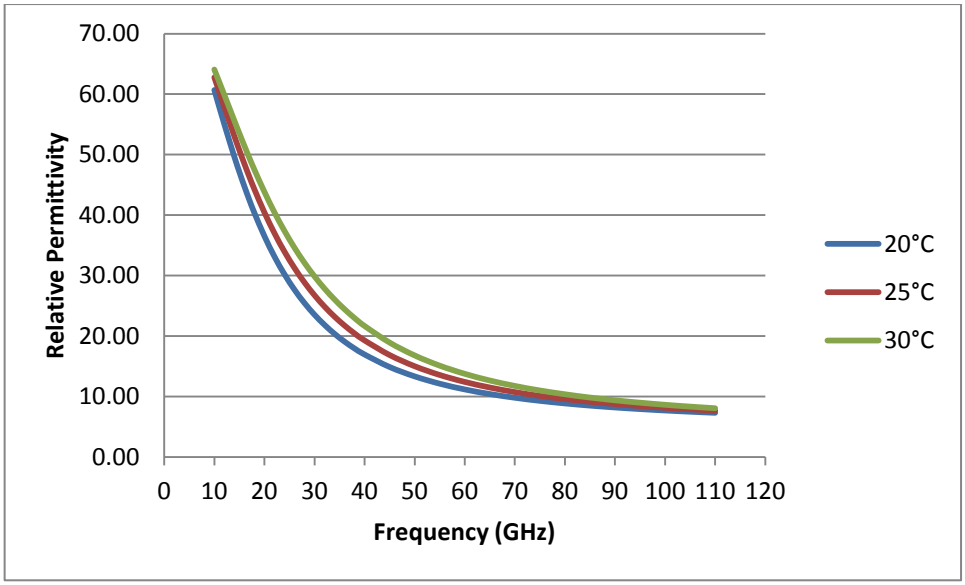

Figure 2.13 – Dielectric constant of pure liquid (aqueous) water – real component.

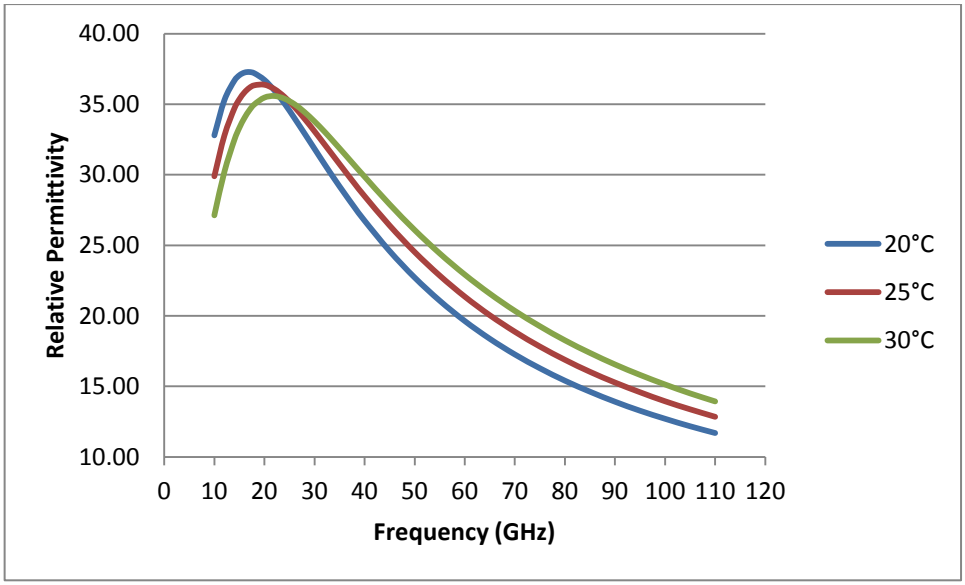

Figure 2.14 – Dielectric constant of pure liquid (aqueous) water – imaginary component.

It is clear from the computed reflection and transmission in Table 2.1 that at normal incidence the chitin layer reduces the transmission into water slightly. The effect appears to be independent of frequency from 10 GHz to 100 GHz. This is due to the small thickness of the layer compared to the wavelength. The errors due to the omission of the chitin layer from the scattering and absorption simulations at normal incidence is less than 10% and is therefore

considered negligible. For other angles of incidence, the effect of the chitin layer may not be negligible.

Model		Reflection	Transmission
Layer 1	**Layer 2**		
Chitin [85]	Water	0.58	0.44
Chitin [86]	Water	0.58	0.44
None	Water	0.58	0.49

Table 2.1 – Effect of chitin layer on scattering, computed reflection and transmission.

The scattering and absorption of termites was investigated in a series of simulations using the program Mieschka [6], for a spheroid where the dielectric is liquid water. A dielectric spheroid is a representative object which can approximate the overall size, aspect ratio and composition of an actual termite. Mieschka computes the total scattering of an incident plane wave from an object using Waterman's T-matrix method [16] which relates the incident field and the object geometry to the scattered field, and the absorption of an object based on the difference between the incident field and the scattered field. Mieschka's uniqueness lies in its ability to compute scattering estimates from objects in the resonant region where approximations cannot be applied due to diffraction and induced current effects. Mieschka was extensively validated against well-known results for resonant metallic and non-dispersive dielectric spheres [17].

The smallest termites are of the order of 4 mm in length and a typical termite may be 6 mm in length, although an upper limit is 12 mm. These simulations examine a spheroid with semi-major axis 2 mm, 2.5 mm and 3 mm corresponding to a termite of length 4 mm, 5 mm and 6 mm, which is an average size.

The results for a 4mm, 5 mm and 6 mm long termite at 20°C follow. The plots of cross sections against particle size and frequency are no longer isomorphic, requiring a doubling of the calculations. In an initial set of exploratory calculations, Gandhi's results [89], for rats were extrapolated. Since Gandhi used the frequency range of 0.9 GHz to 1.2 GHz where the dielectric constant of water is very well behaved (almost constant, and relatively low loss) the extrapolation is invalid. Therefore, here the matter will be investigated via simulation using Mieschka [6].

2.6.2 Absorption Results

Absorption sweeps computed using Mieschka [6] for the three principal cases, E Parallel broadside, H Parallel broadside and End-on are shown in Figure 2.17, Figure 2.18, Figure 2.19 and Figure 2.20 below.

Absorption results for the broadside aspect ($\theta = 0°,\ \phi = 90°$) for the electric field parallel and perpendicular and end-on to the major axis of a 4 mm prolate spheroid at 20°C with aspect ratio of 3 and 4 respectively are presented in Figure 2.15 and Figure 2.16 below. Note the reduction in *E* Parallel absorption as the aspect ratio changes from 3 to 4.

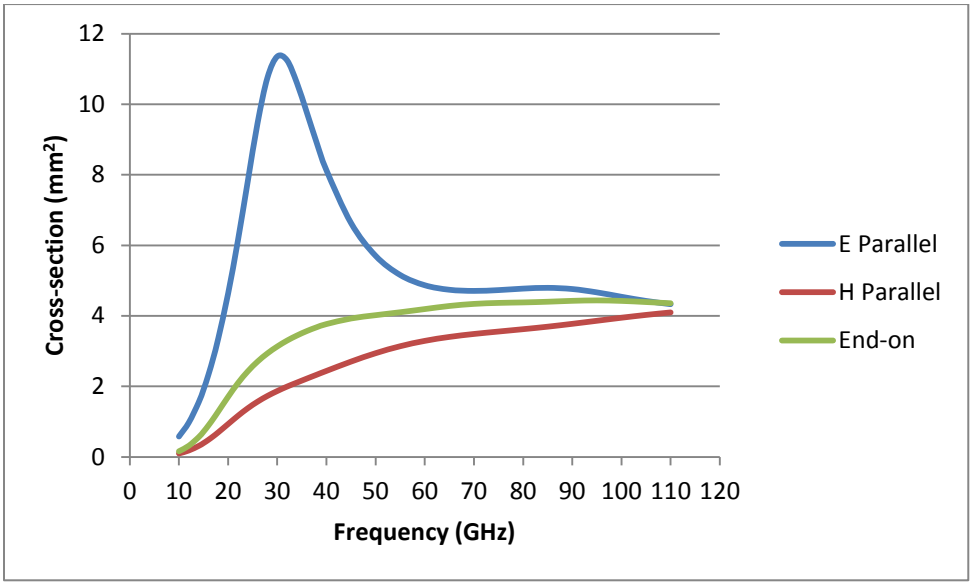

Figure 2.15 – Absorption cross-sections in mm^2 for a 4 mm long termite, aspect ratio 3, at 20°C as a function of frequency in GHz.

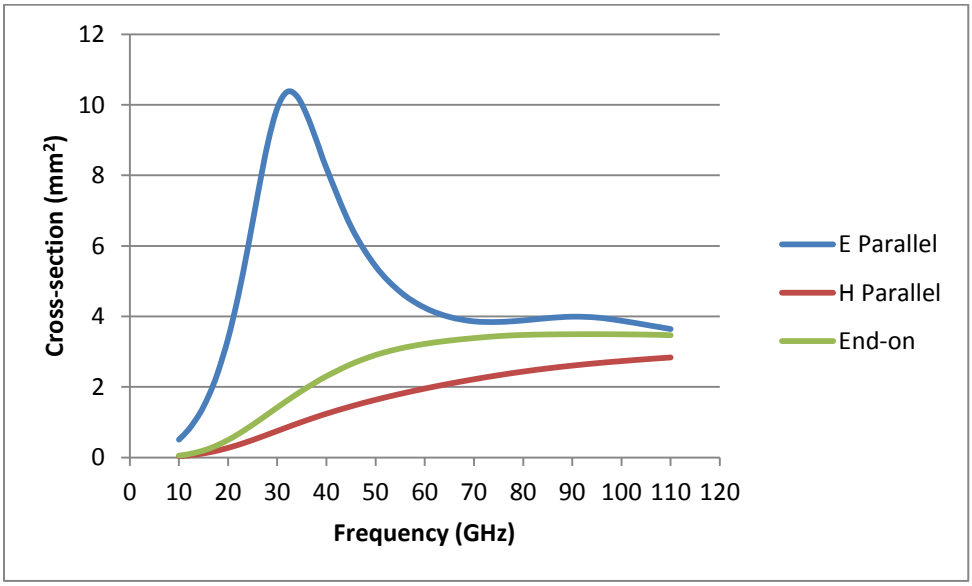

Figure 2.16 – Absorption cross-sections in mm^2 for a 4 mm long termite, aspect ratio 4, at 20°C as a function of frequency in GHz.

Absorption results for the broadside aspect ($\theta = 0°,\ \phi = 90°$) for the electric field parallel and perpendicular and end-on to the major axis of a 5 mm prolate spheroid at 20°C with aspect ratio of 3 and 4 respectively are presented in Figure 2.17 and Figure 2.18 below. Note

the reduction in *E* Parallel absorption as the aspect ratio changes from 3 to 4 as before, and the increase in absorption as the prolate spheroid is made larger in size.

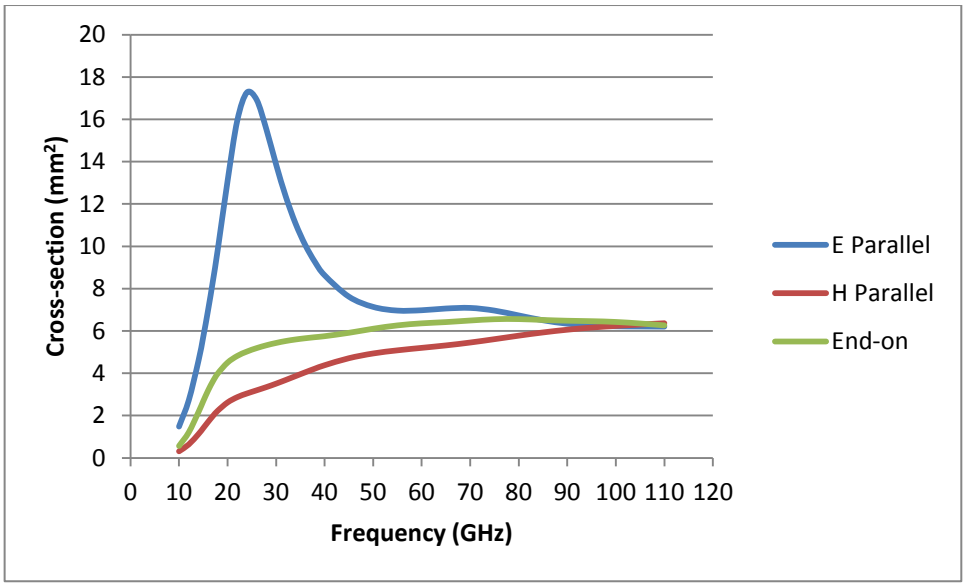

Figure 2.17 – Absorption cross-sections in mm^2 for a 5 mm long termite, aspect ratio 3, at 20°C as a function of frequency in GHz.

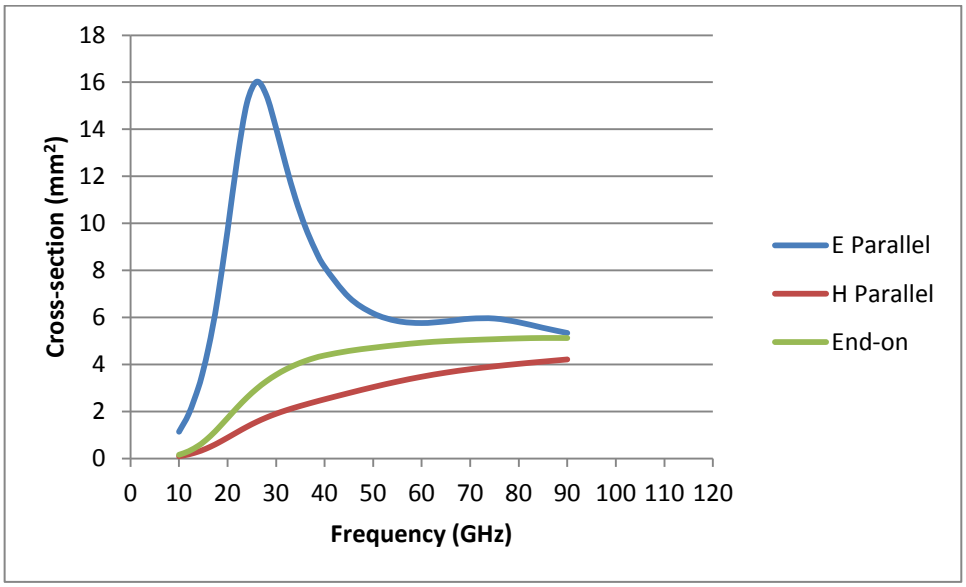

Figure 2.18– Absorption cross-sections in mm^2 for a 5 mm long termite, aspect ratio 4, at 20°C as a function of frequency in GHz.

Absorption results for the broadside aspect ($\theta = 0°$, $\phi = 90°$) for the electric field parallel and perpendicular and end-on to the major axis of a 6 mm prolate spheroid at 20°C with

aspect ratio of 3 and 4 respectively are presented in Figure 2.19 and Figure 2.20 below. Note the reduction in *E* Parallel absorption as the aspect ratio changes from 3 to 4, and the further increase in absorption as the prolate spheroid is made larger in size again. The results in Figure 2.20 are valid below 65 GHz, however above this frequency the convergence criteria were marginal and there was doubt about their validity, when negative absorption cross-sections were indicated.

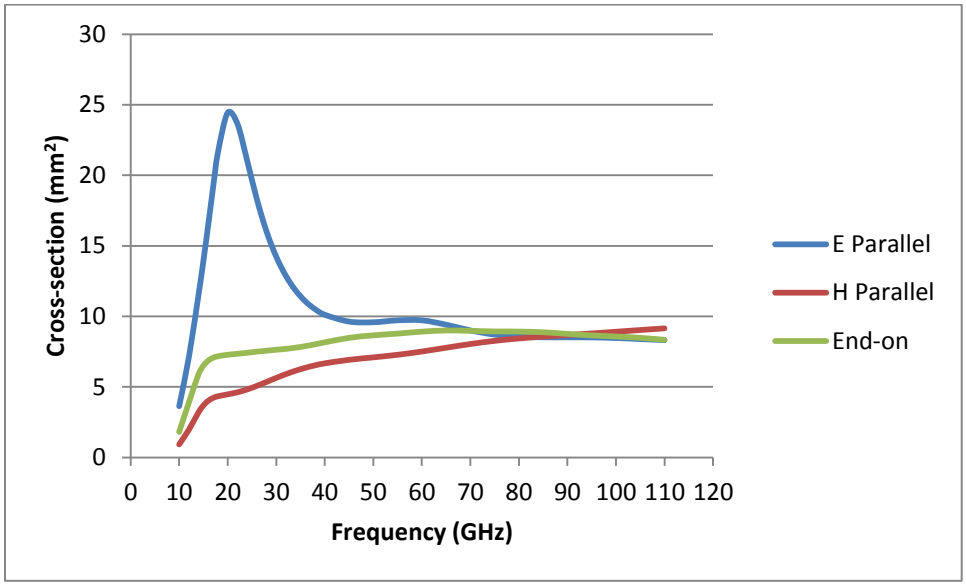

Figure 2.19 – Absorption cross-sections in mm^2 for a 6 mm long termite, aspect ratio 3, at 20°C as a function of frequency in GHz.

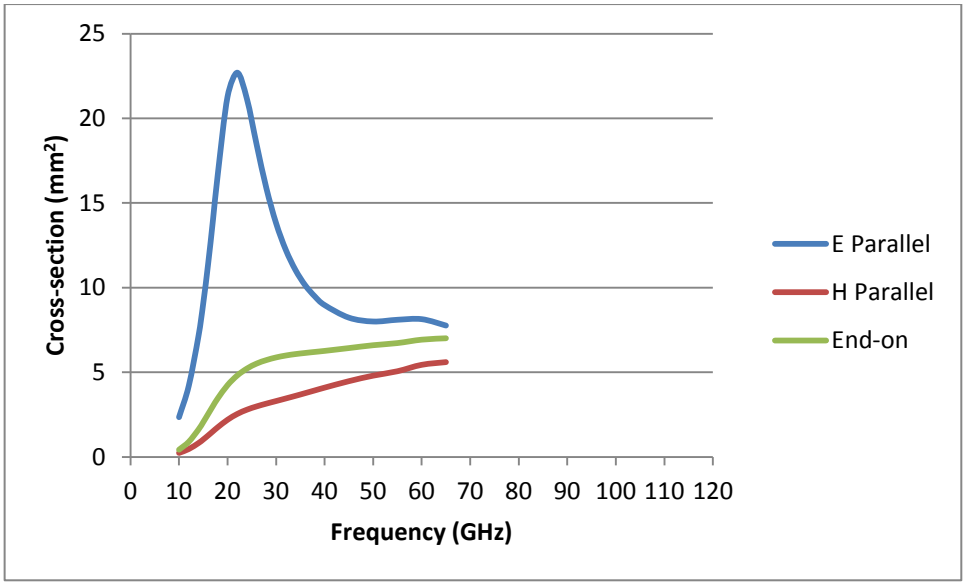

Figure 2.20 – Absorption cross-sections in mm^2 for a 6 mm long termite, aspect ratio 4, at 20°C as a function of frequency in GHz.

As compared to Gandhi's generic plot, Figure 2.21, there is qualitative agreement in ranking and general shape. There is quantitative agreement also with Barber's predications in the ranking of coupling of the E field with the E field along the long axis, and E along the short axis. Two subtle differences in the plots are: (a) Mieschka plots straddle a water resonance, whilst Gandhi's have fixed dielectric constant, (b) Gandhi's ordinate scale is logarithmic and ours is linear.

A direct method of computing and simulating absorption is also possible. This is the method used by Barber [53], Ghandi [89] and others. The method used by Mieschka is indirect: it computes scattering at all angles and then uses the optical theorem to deduce the absorption from the computed scattering. By conservation of energy, an absorption maxima should correspond with a scattering minima and vice versa.

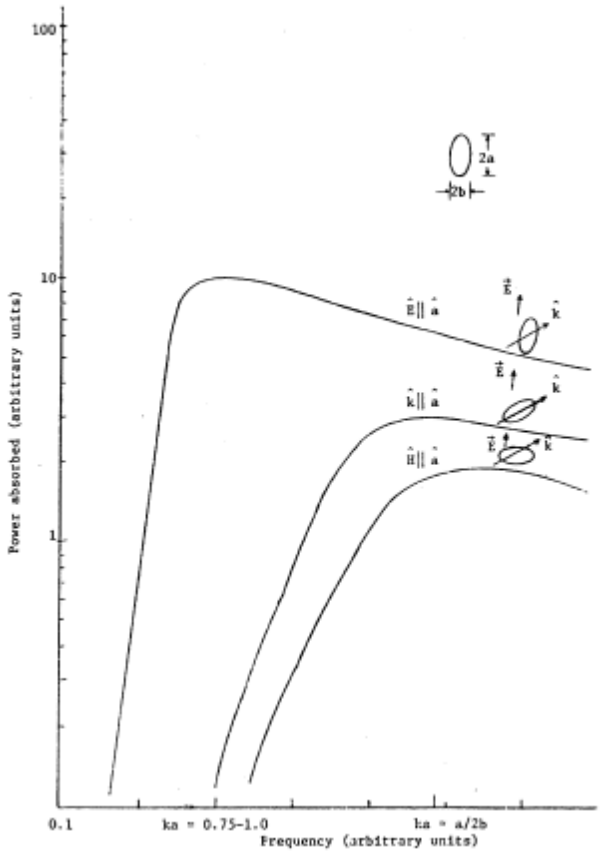

Figure 2.21 – Generic absorption plot for rats. From [89].

The absorption curve dependence on polarization can be obtained by the direct method, by modelling the termite as a receiving antenna of finite resistance. The resistance is the so-called "radiation resistance" [90]. For a long, thin antenna driven parallel to its long direction, the radiation resistance as a function of length in wavelengths is shown in Figure 2.22 below. This is also the radiation resistance as a function of frequency. The curves presented are approximations to the complicated exact results. However, it is clear that a resonance occurs at a frequency where the object is close to $\lambda/2$ long for E parallel. By the principle of reciprocity [91], a highly absorbing material of that shape would show a similar absorption characteristic for an E field parallel to the long axis. This is applicable to termites. The major difference is that termites have a much lower height to width ratio and are spheroidal.

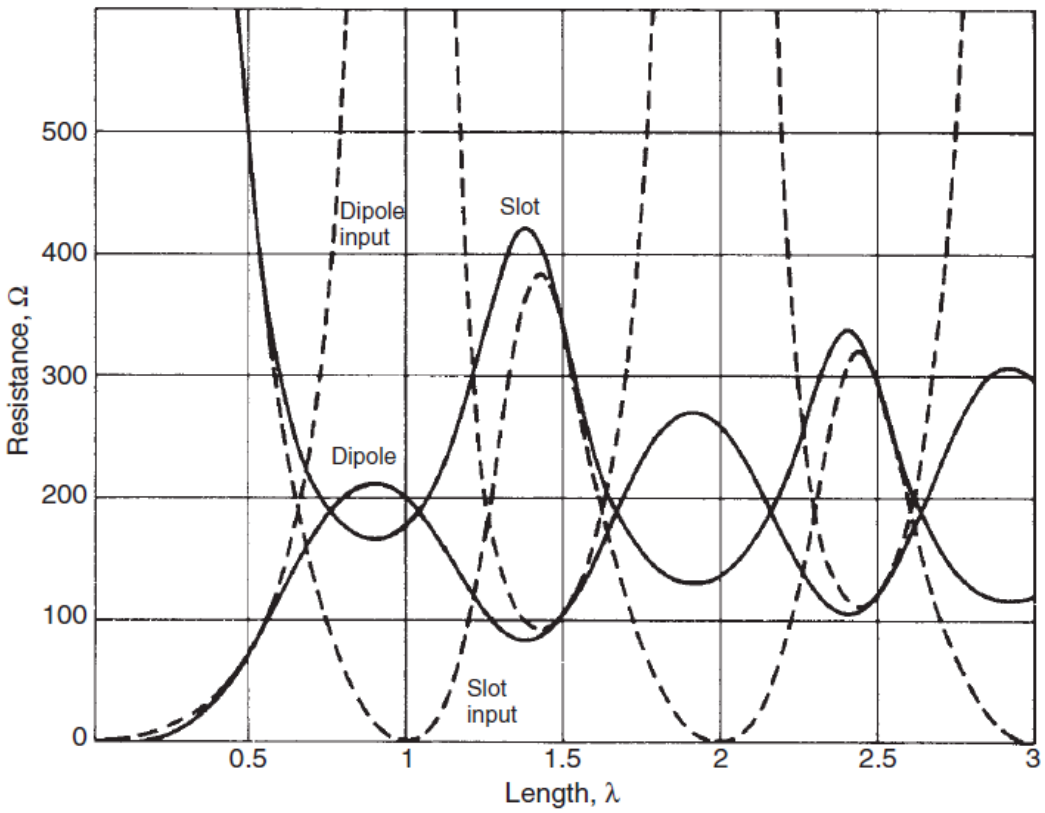

Figure 2.22 – Radiation resistance of a dipole as a function of length, in wavelengths. From[92].

Nevertheless, this dipole antenna model explains why the absorption for termites and rats peaks close to a frequency where the object is about $\lambda/2$ long for E parallel. The absorption peak for termites may be exaggerated because it coincides with water resonance absorption at 22 GHz. For the orthogonal polarization (H parallel) the absorption reaches a plateau at about 3 times the resonance peak for E parallel, which agrees with the aspect ratio of the termite. Similar comments apply to Gandhi's rats [89].

These simulations show that near resonance the amount of absorption and scattering is much larger than the geometric cross-section. They also show that the absorption cross section decreases with an increase in aspect ratio and that correspondingly then, the scattering cross-section decreases with the increase in aspect ratio, and that the absorption resonances are constant with the change in the aspect ratio.

2.6.2.1 Variation with Temperature

Absorption results for the broadside aspect ($\theta = 0°$, $\phi = 90°$) for the electric field parallel and perpendicular and end-on to the major axis of a 4 mm, 5 mm and 6 mm prolate spheroid at 30°C with aspect ratio of 3 respectively are presented in Figure 2.23, Figure 2.24 and Figure 2.25 below.

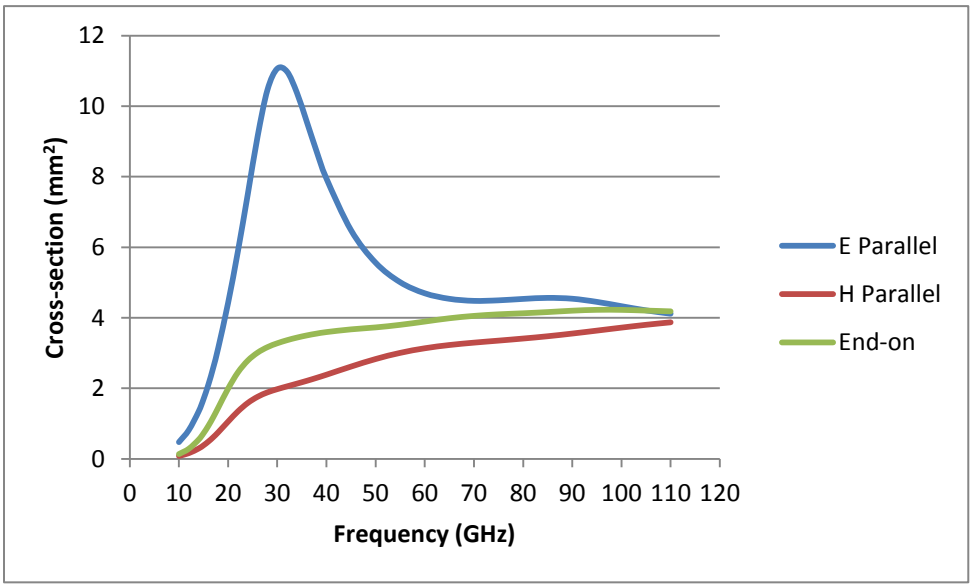

Figure 2.23 – Absorption cross-sections in mm^2 for a 4 mm long termite, aspect ratio 3, at 30°C as a function of frequency in GHz.

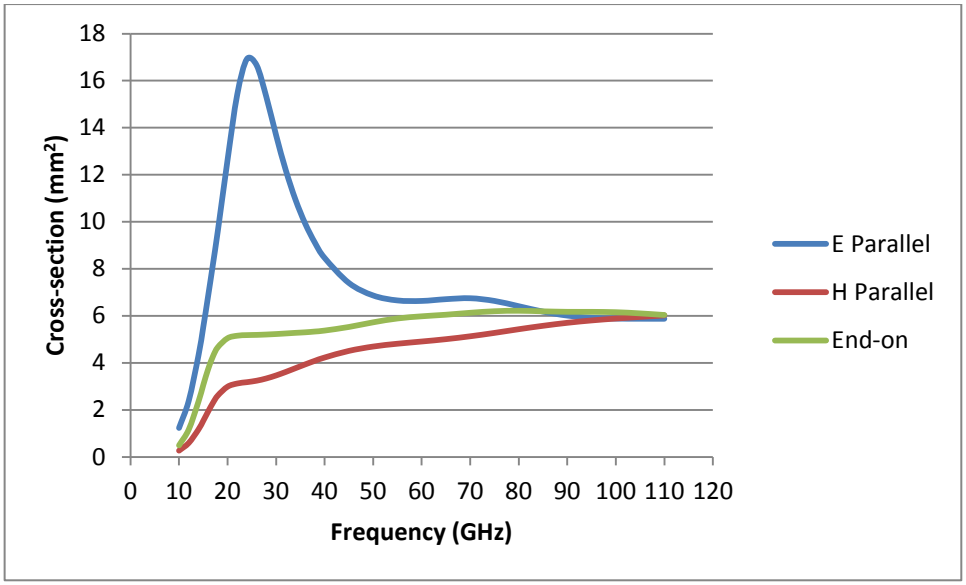

Figure 2.24 – Absorption cross-sections in mm^2 for a 5 mm long termite, aspect ratio 3, at 30°C as a function of frequency in GHz.

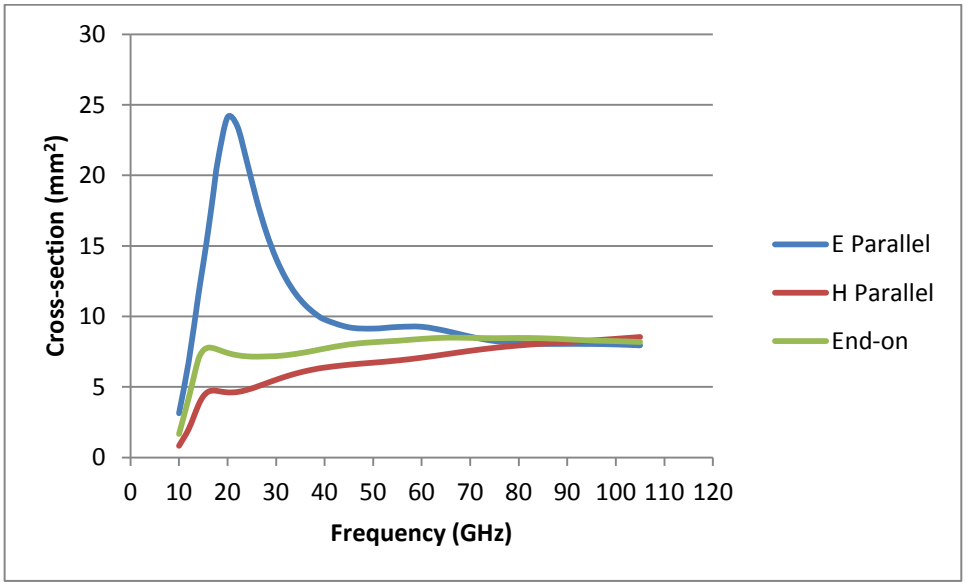

Figure 2.25 – Absorption cross-sections in mm^2 for a 6 mm long termite, aspect ratio 3, at 30°C as a function of frequency in GHz.

These simulations show only minor variations in the amounts of scattering and absorption with a 10°C change in temperature. This suggests that the water resonance due to molecular water relaxation at 22 GHz and the object self-resonance are well separated for the *E* Parallel case, ($\theta = 0°,\ \phi = 90°$), whereas for the *H* Parallel case, ($\theta = 0°,\ \phi = 90°$), and the End-on

case, ($\theta = 0°,\ \phi = 0°$), the water resonance and object resonance are much closer together giving rise to a shift in resonances in the range 15 to 20 GHz. In Figure 2.25 above, a single anti-resonance occurs for the *H* Parallel case, ($\theta = 0°,\ \phi = 90°$), and the End-on case, ($\theta = 0°,\ \phi = 0°$), in the range 25 to 30 GHz. This can be accounted for by the shift and broadening in the resonance in the imaginary part of the permittivity of liquid water, see Figure 2.14.

2.6.3 Backscatter Results

Backscatter sweeps computed using Mieschka [6] for the two principal cases, *E* Parallel broadside and *H* Parallel broadside are shown in Figure 2.26, Figure 2.27 and Figure 2.28 below.

Consider the backscatter plot for the broadside incidence, shown in Figure 2.26 below. The H parallel is easy to explain. The short circumference is 4.21 mm, which corresponds to 71.3 GHz wavelength and is the first Mie resonance for that orientation and in the frequency agrees with the naive theory. Simulation data at or above 110 GHz were determined to be questionable due to failure of the simulation to converge or computation of negative absorption values. The E parallel backscatter first Mie resonance should be at 8.92 mm (elliptical circumference) or 33.6 GHz and indeed, there is such a resonance. The suppression of creeping wave resonances is most likely due to the high absorption of water at 33.6 GHz where $\varepsilon_{water}@33.6\,GHz = 20.64 + j29.9$. This seems to be followed by harmonic resonances at 71.3 GHz and 91 GHz where $\varepsilon_{water}@71.3\,GHz = 9.64 + j17$ and $\varepsilon_{water}@91\,GHz = 8.11 + j13.78$. The "optical" cross-section varies approximately as the reciprocal of the real part of ε. Hence, if the optical cross section at 32 GHz is 1, it would be expected to be 2 at 63 GHz and 3 at 95 GHz and that is what the graphs seem to indicate with the backscatter following the real part of ε. The inverse rule was also tested using spheres and was found to be supported. A similar analysis performed for Figure 2.27 and Figure 2.28,

where the short circumference is 5.22 mm and 6.28 mm, corresponding to 57.4 GHz and 47.7 GHz, and the elliptical circumference is 11.13 mm and 13.36 mm, corresponding to 26.5 GHz and 22.5 GHz confirmed this analysis. As a further indication of the instability of the program above 110 GHz, Mieschka does not converge, using default integration parameters. By adjusting these parameters to produce convergence, the absorption cross-section becomes negative above 110 GHz, indicating a serious integration problem. Therefore, results above 90 GHz may be suspect and should be treated with a degree of caution. Unfortunately, this is the region that could explain a lot of phenomena.

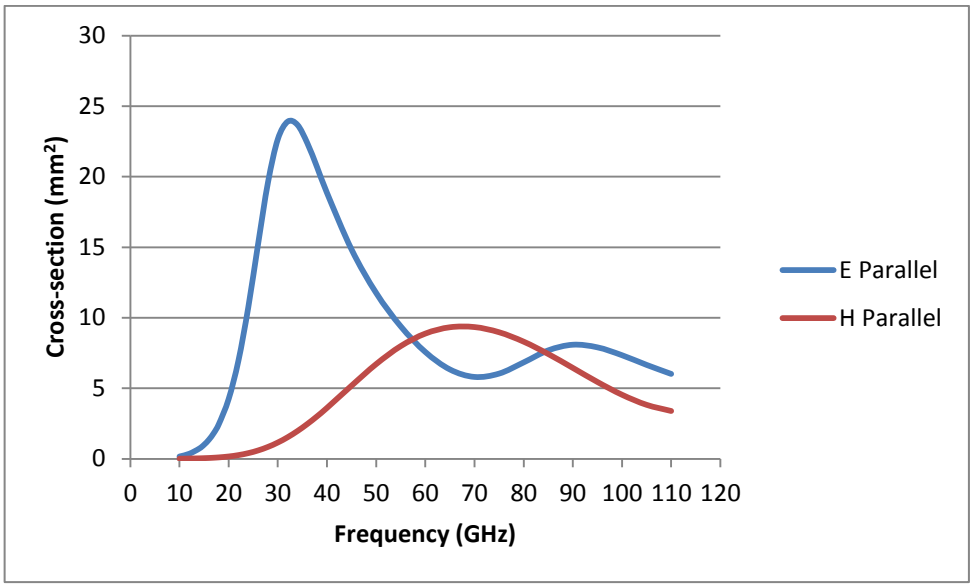

Figure 2.26 – Broadside incidence backscatter cross-sections in mm^2 for a 4 mm long termite, aspect ratio 3, at 20°C as a function of frequency in GHz.

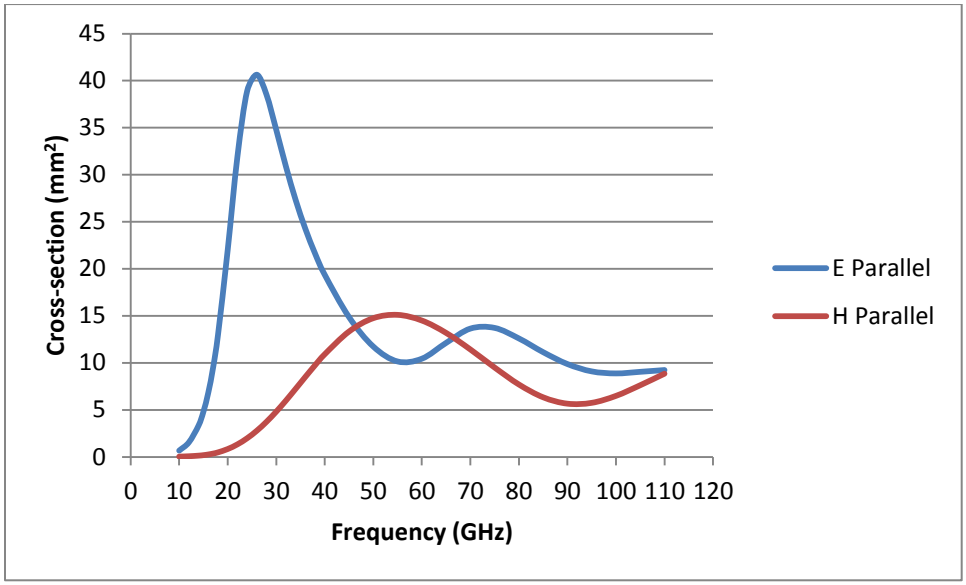

Figure 2.27 – Broadside incidence backscatter cross-sections in mm^2 for a 5 mm long termite, aspect ratio 3, at 20°C as a function of frequency in GHz.

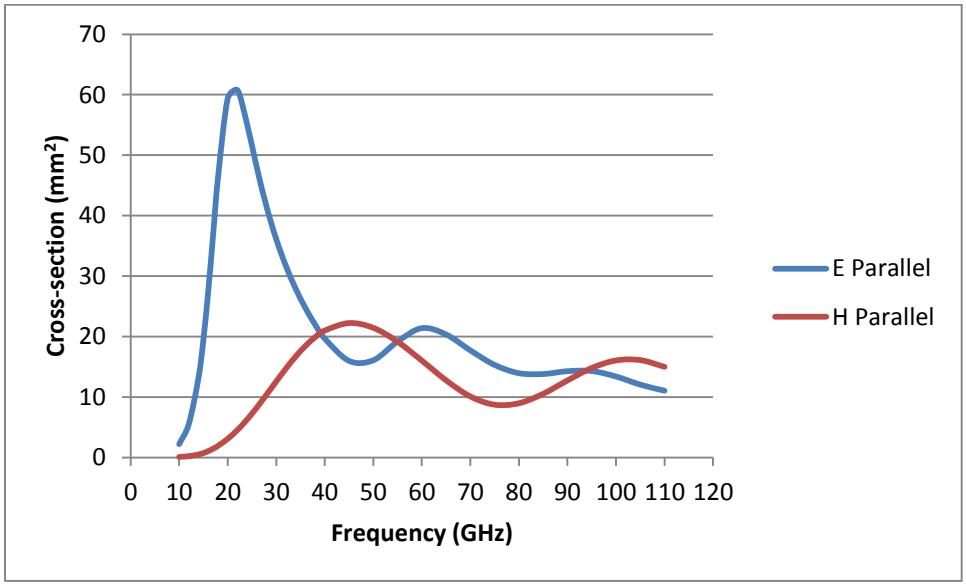

Figure 2.28 – Broadside incidence backscatter cross-sections in mm^2 for a 6 mm long termite, aspect ratio 3, at 20°C as a function of frequency in GHz.

Backscatter sweeps computed using Mieschka [6] for the principal case End-on is shown in Figure 2.29, Figure 2.30 and Figure 2.31 below.

Now consider the backscatter plot for the end-on incidence, shown in Figure 2.29, Figure 2.30 and Figure 2.31 below. The cross-section is tiny and exhibits resonances at the same frequencies as the *E* parallel case above.

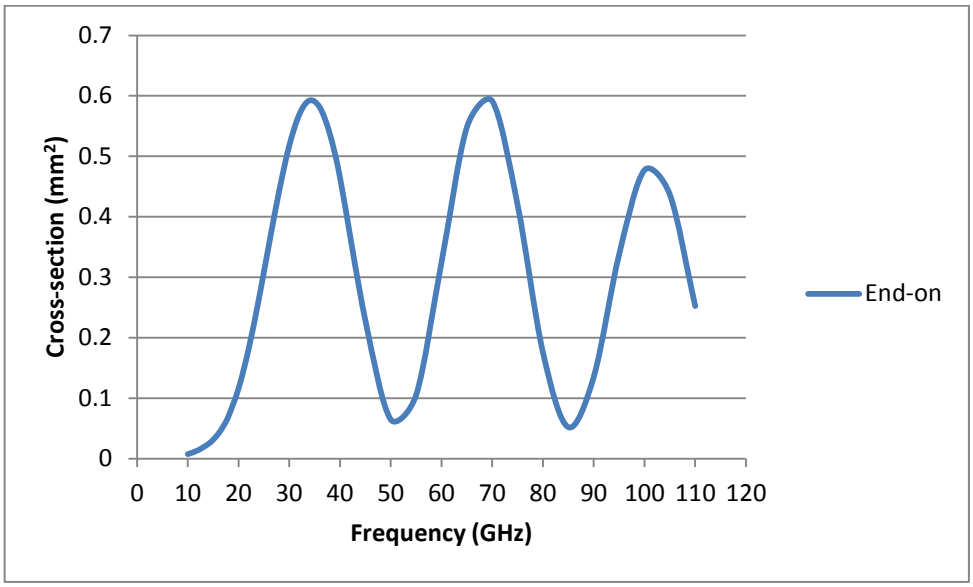

Figure 2.29 – End-on incidence backscatter cross-section in mm^2 for a 4 mm long termite, aspect ratio 3, at 20°C as a function of frequency in GHz.

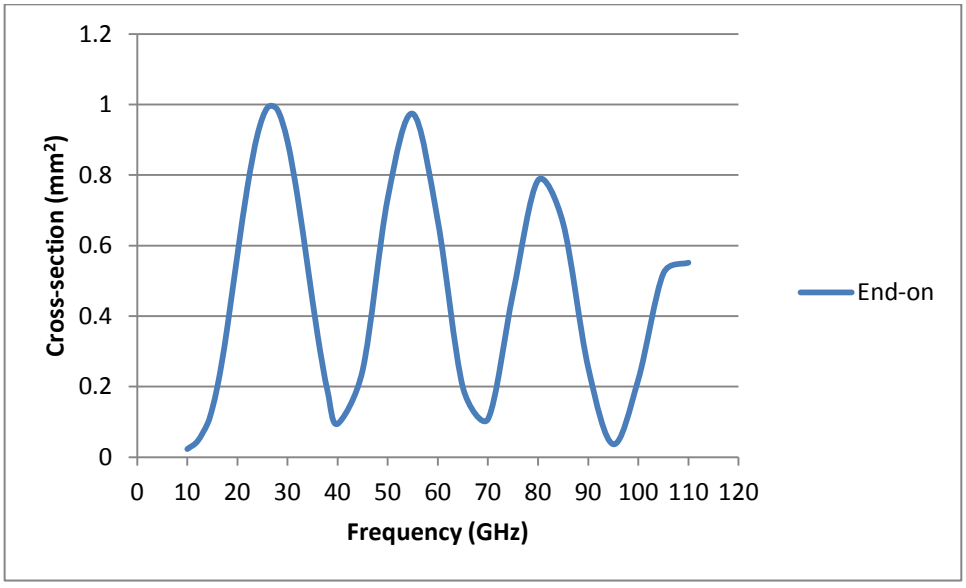

Figure 2.30 – End-on incidence backscatter cross-section in mm^2 for a 5 mm long termite, aspect ratio 3, at 20°C as a function of frequency in GHz.

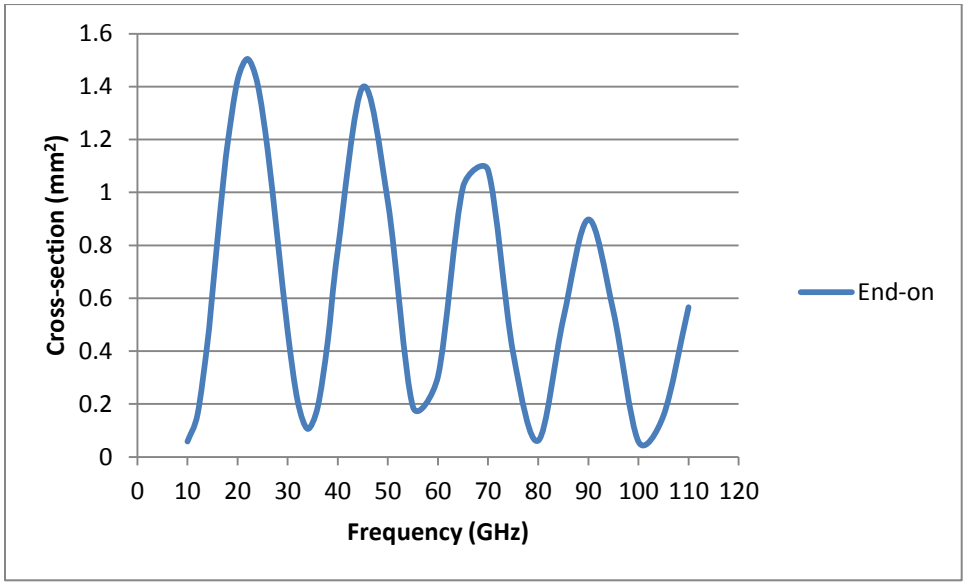

Figure 2.31 – End-on incidence backscatter cross-section in mm^2 for a 6 mm long termite, aspect ratio 3, at 20°C as a function of frequency in GHz.

2.6.3.1 *Forwardscatter Results*

Forwardscatter sweeps computed using Mieschka [6] for the two principal cases, *E* Parallel broadside and *H* Parallel broadside are shown in Figure 2.32, Figure 2.33 and Figure 2.34 below. Also, forwardscatter sweeps computed using Mieschka [6] for the principal case End-on is shown in Figure 2.35, Figure 2.36 and Figure 2.37 below.

These results are included for completeness and for further insights as to what is happening. Forward scattering is larger than backscatter, as expected. It seems to show few resonance effects. It is expected that, since absorption is so severe in the region 15 to 60 GHz, any resonances would be damped out.

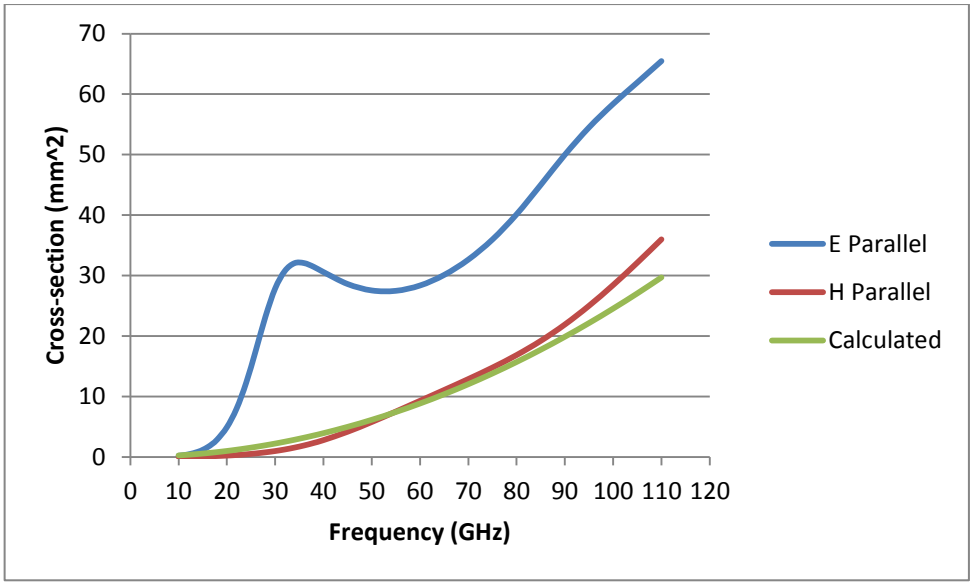

Figure 2.32 – Broadside incidence forwardscatter cross-sections in mm^2 for a 4 mm long termite, aspect ratio 3, at 20°C as a function of frequency in GHz.

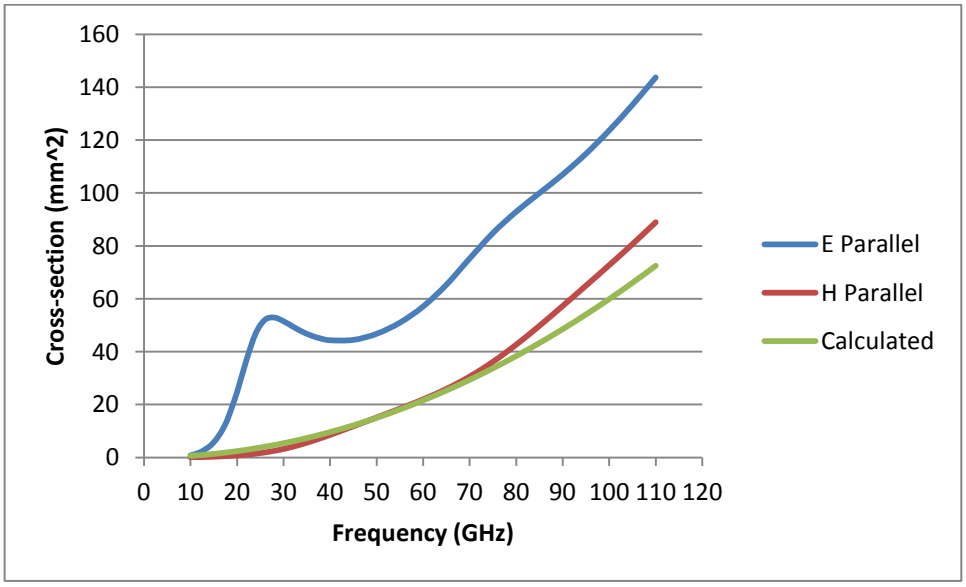

Figure 2.33 – Broadside incidence forwardscatter cross-sections in mm^2 for a 5 mm long termite, aspect ratio 3, at 20°C as a function of frequency in GHz.

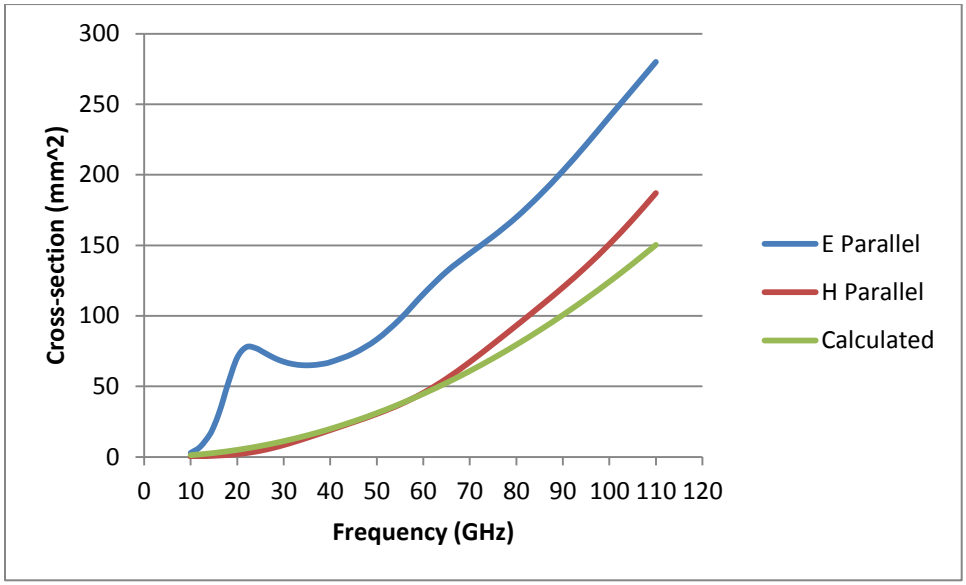

Figure 2.34 – Broadside incidence forwardscatter cross-sections in mm^2 for a 6 mm long termite, aspect ratio 3, at 20°C as a function of frequency in GHz.

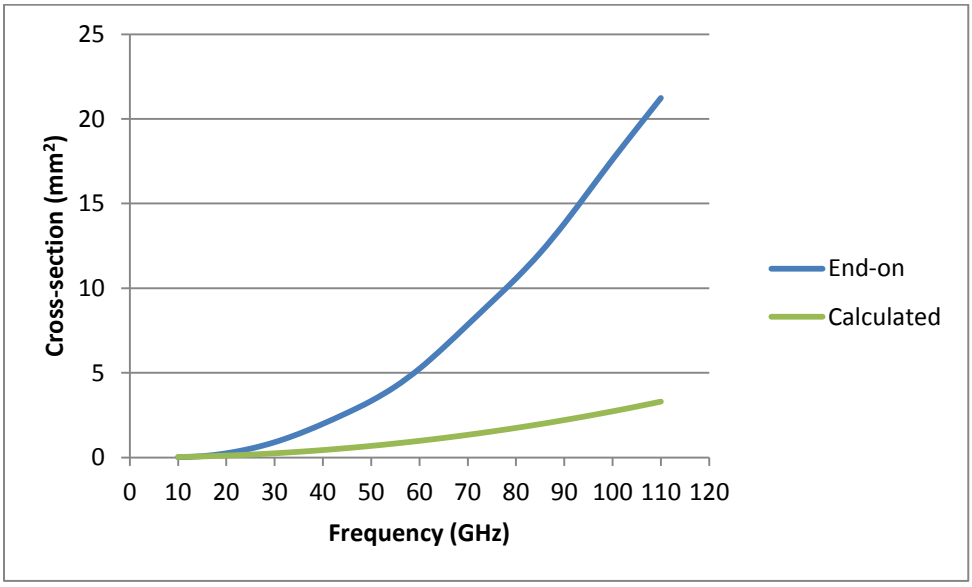

Figure 2.35 – End-on incidence forwardscatter cross-section in mm^2 for a 4 mm long termite, aspect ratio 3, at 20°C as a function of frequency in GHz.

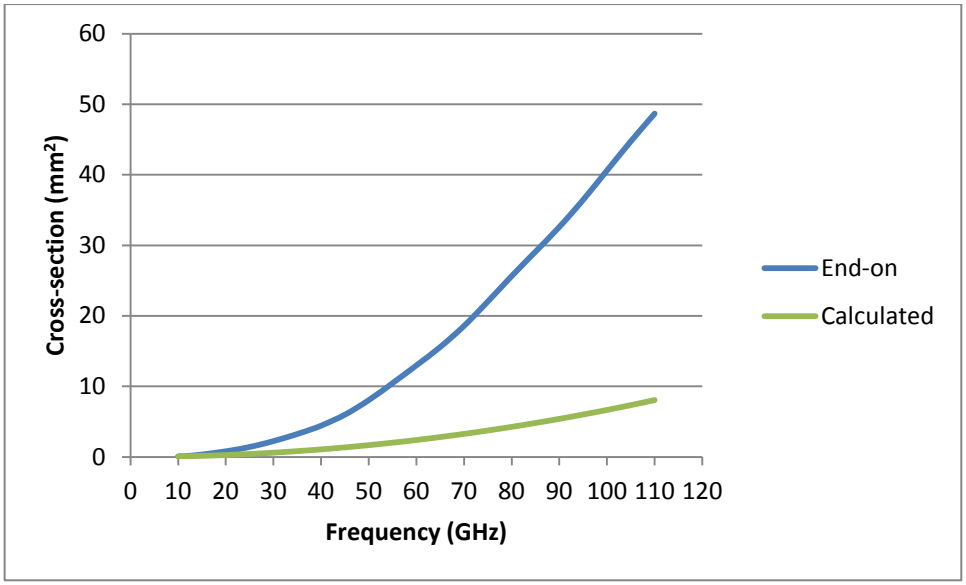

Figure 2.36 – End-on incidence forwardscatter cross-section in mm^2 for a 5 mm long termite, aspect ratio 3, at 20°C as a function of frequency in GHz.

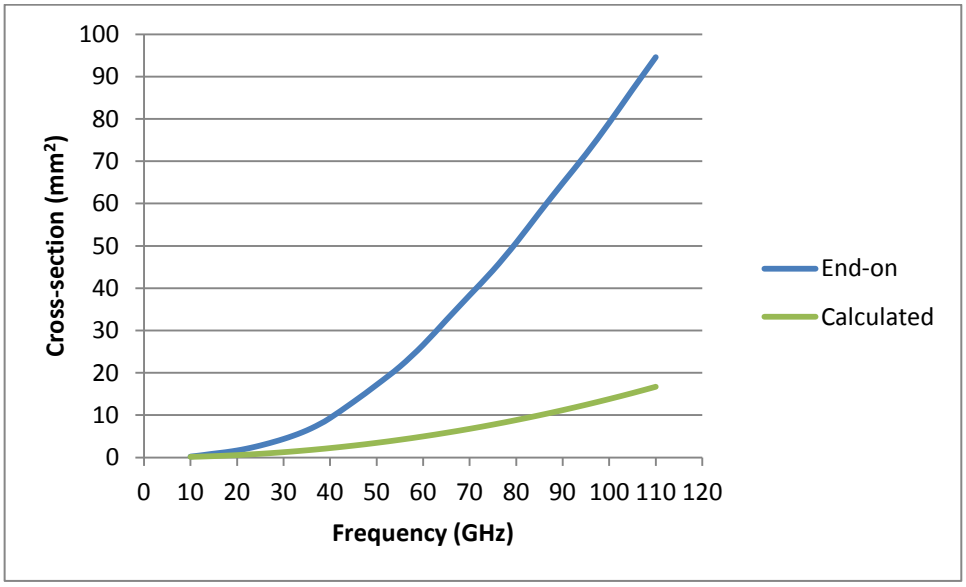

Figure 2.37 – End-on incidence forwardscatter cross-section in mm^2 for a 6 mm long termite, aspect ratio 3, at 20°C as a function of frequency in GHz.

2.6.4 Comparative Results – Non-dispersive Prolate Spheroid

To compare the absorption and scattering effects for the dispersive prolate spheroid objects in Section 2.6.2 above, with those for a non-dispersive prolate spheroid object, similar simulations using Mieschka [6] for a non-dispersive prolate spheroid were performed. These

results are shown in Figure 2.38, Figure 2.39, Figure 2.40, Figure 2.41 and Figure 2.42 below. Note that the Mieschka results are valid below 45 GHz, however above this frequency the program's convergence criteria were not met.

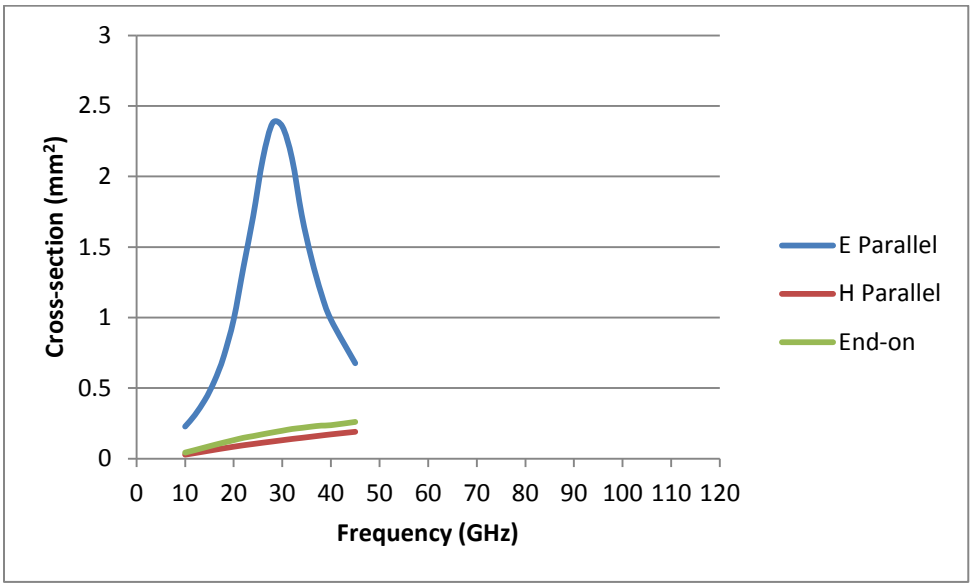

Figure 2.38 – Absorption cross-sections in mm^2 for a non-dispersive prolate spheroid, major axis 4 mm, aspect ratio 3, at 20°C as a function of frequency in GHz.

Comparing Figure 2.38 to Figure 2.23 shows that as expected, the resonance is reduced and narrower (32 GHz to 28 GHz), and that the absorption is markedly reduced by approximately five times (11 mm^2 down to 2.4 mm^2 for *E* Parallel).

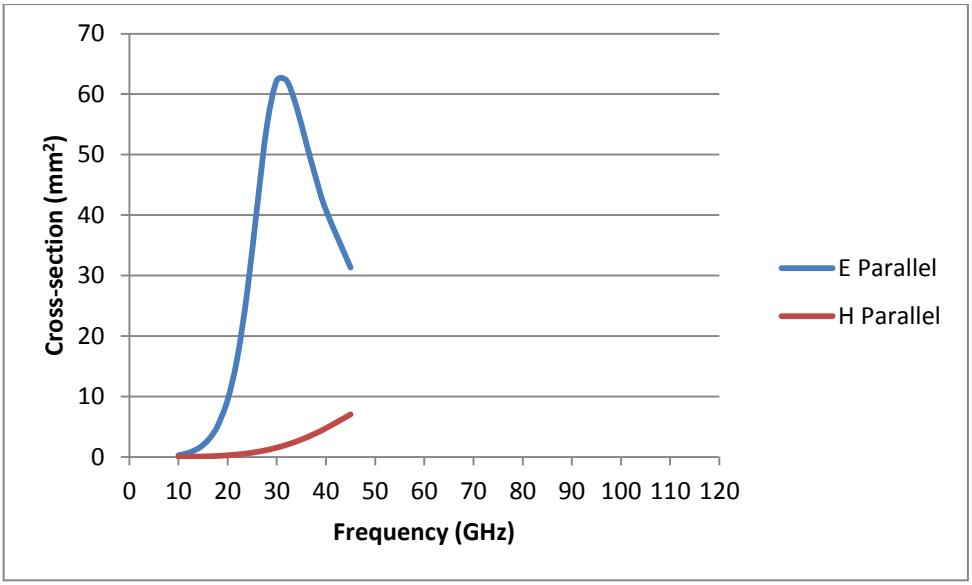

Figure 2.39 – Broadside incidence backscatter cross-sections in mm^2 for a non-dispersive prolate spheroid, major axis 4 mm, aspect ratio 3, at 20°C as a function of frequency in GHz.

Comparing Figure 2.39 to Figure 2.26 shows that as expected, the resonance is reduced and narrower (32 GHz to 28 GHz), and that the broadside backscatter is markedly increased by approximately three times (24 mm^2 up to 62 mm^2 for *E* Parallel).

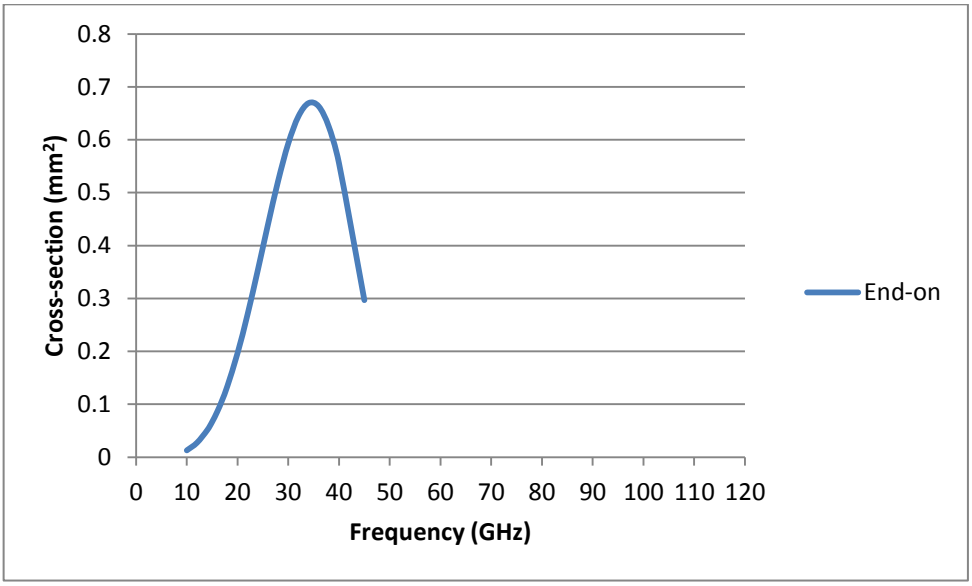

Figure 2.40 – End-on incidence backscatter cross-section in mm^2 for a non-dispersive prolate spheroid, major axis 4 mm, aspect ratio 3, at 20°C as a function of frequency in GHz.

Comparing Figure 2.40 to Figure 2.29 shows that the resonance is similar, and that the end-on backscatter is also similar (0.6 mm^2 to 0.65 mm^2).

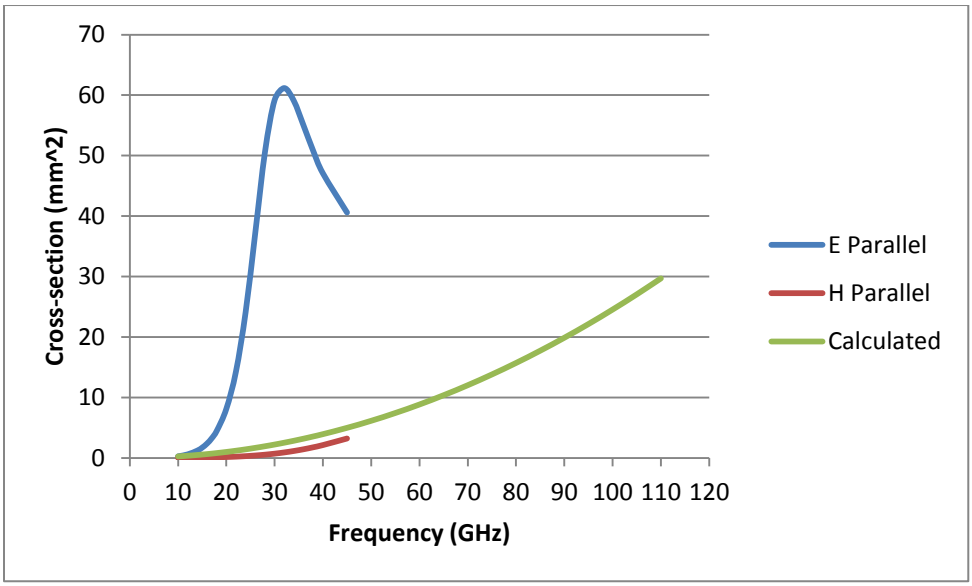

Figure 2.41 – Broadside incidence forwardscatter cross-sections in mm^2 for a non-dispersive prolate spheroid, major axis 4 mm, aspect ratio 3, at 20°C as a function of frequency in GHz.

Comparing Figure 2.41 and Figure 2.32 shows that as expected, the resonance is reduced and narrower (32 GHz to 28 GHz), and that the broadside forwardscatter is markedly increased by approximately two times (32 mm^2 up to 61 mm^2 for *E* Parallel).

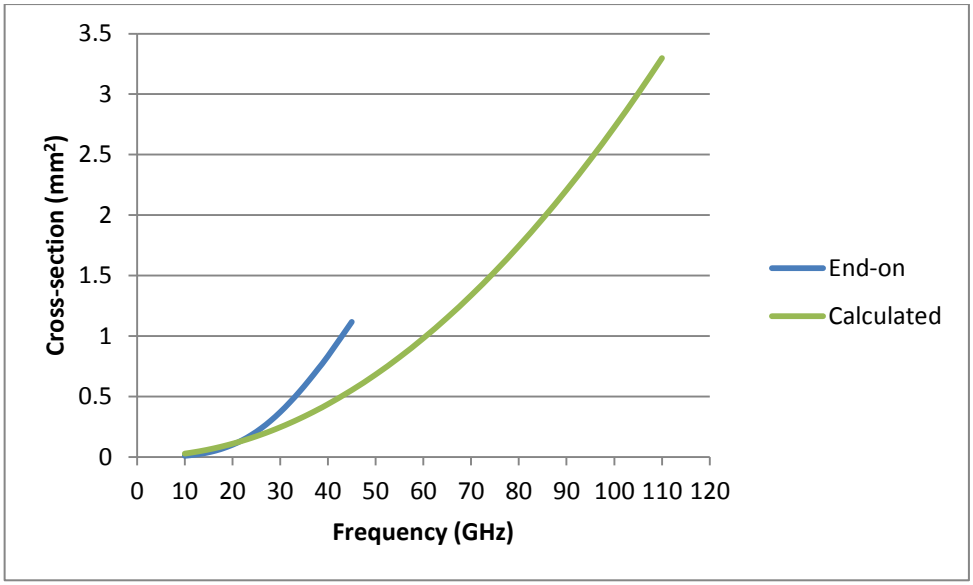

Figure 2.42 – End-on incidence forwardscatter cross-sections in mm^2 for a non-dispersive prolate spheroid, major axis 4 mm, aspect ratio 3, at 20°C as a function of frequency in GHz.

Comparing Figure 2.42 and Figure 2.35 shows that the end-on forwardscatter is reduced by approximately two times (2 mm^2 down to 1 mm^2 at 40 GHz).

In general then, compared to a non-dispersive scatterer, the effect on scattering of a dispersive scatter is greatest for broadside incidence where a (small) reduction in resonance will be observed as well as an increase in absorption and a decrease in backscatter. For end-on, the effect is small. For observing insects, broadside incidence however is preferred, as this aspect presents the greatest scattering cross-section.

2.6.5 Comparative Results – Spheroid

To compare the absorption and scattering effects for the dispersive prolate spheroid objects in Section 2.6.2 above, with those for a dispersive spherical object, similar simulations using Mieschka [6] for a dispersive spheroid of radius 2 mm were performed. These results are shown in Figure 2.43, Figure 2.44, Figure 2.45, Figure 2.46 and Figure 2.47 below. The theoretical resonance is at 22 GHz, in agreement with Figure 2.43, Figure 2.44, Figure 2.45,

Figure 2.46 and Figure 2.47 below. Note also that due to symmetry of a sphere, scattering is independent of polarization or aspect angle.

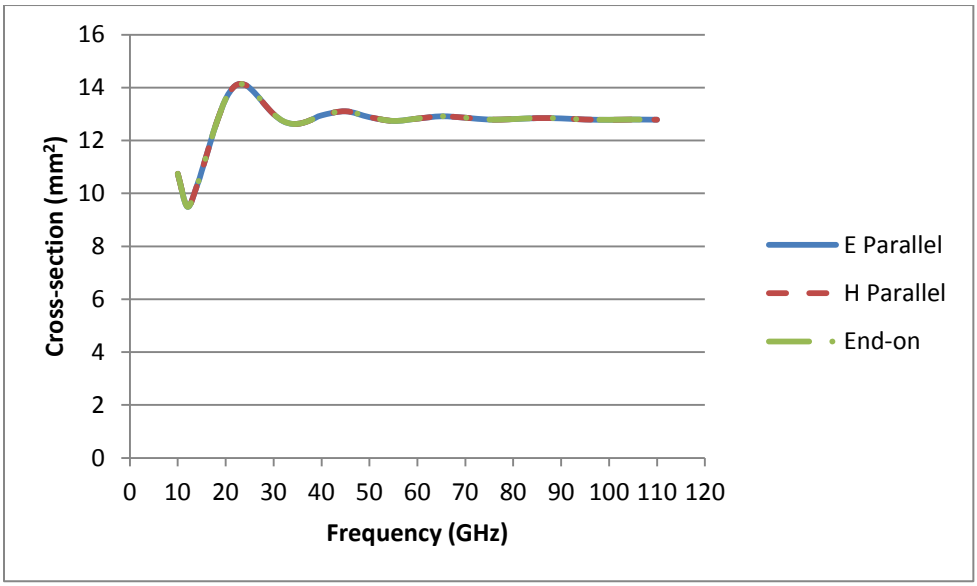

Figure 2.43 – Absorption cross-sections in mm^2 for a sphere, radius 2 mm, at 20°C as a function of frequency in GHz.

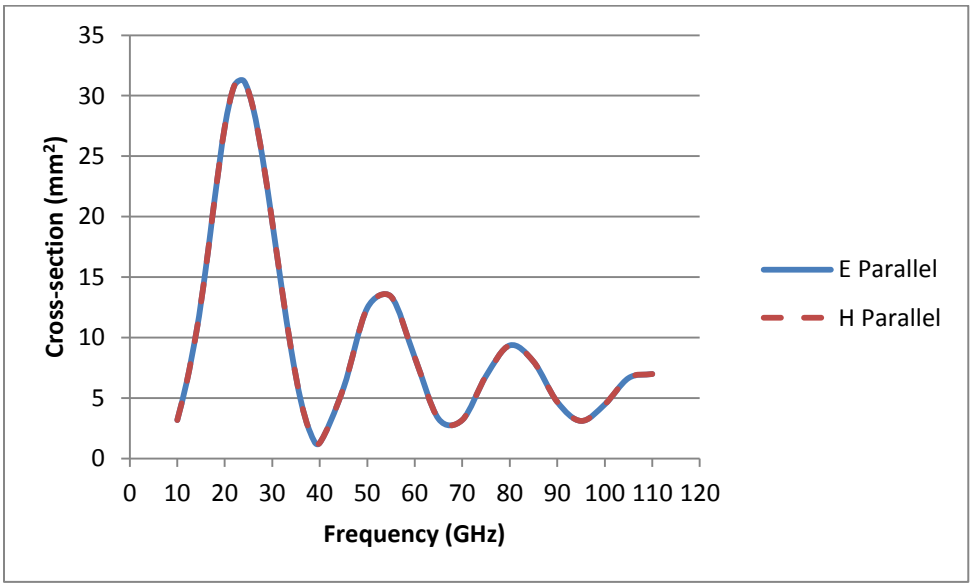

Figure 2.44 – Broadside incidence backscatter cross-sections in mm^2 for a sphere, radius 2 mm, at 20°C as a function of frequency in GHz.

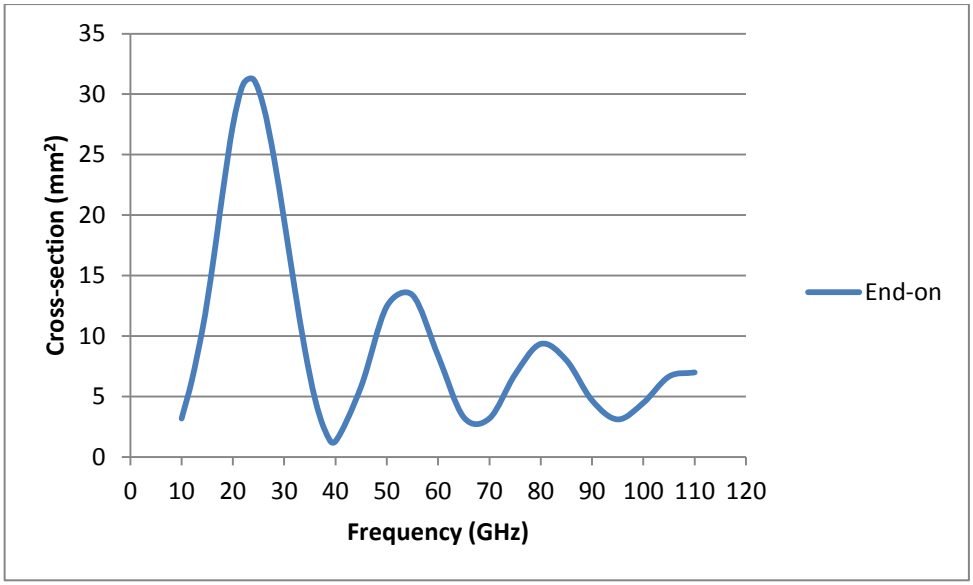

Figure 2.45 – End-on incidence backscatter cross-section in mm^2 for a sphere, radius 2 mm, at 20°C as a function of frequency in GHz.

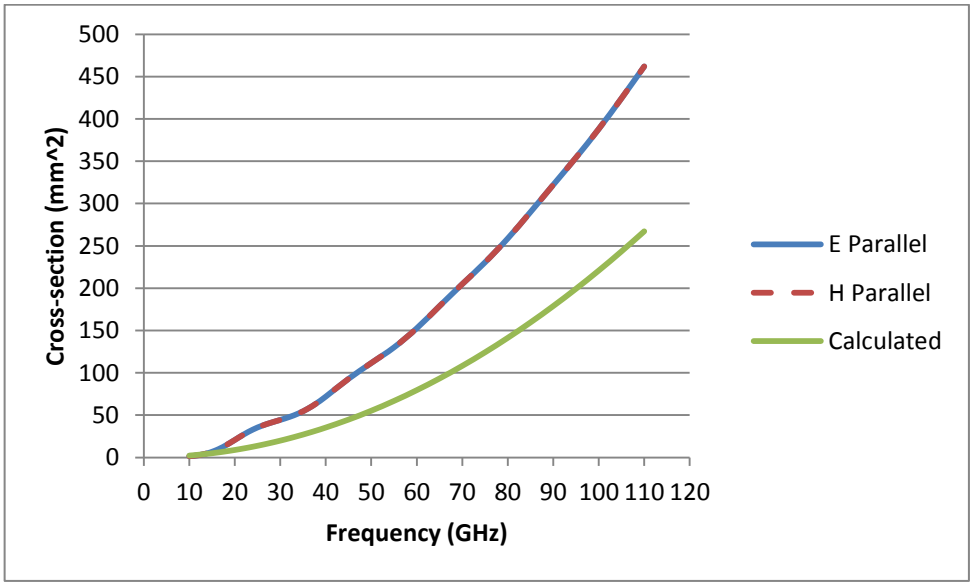

Figure 2.46 – Broadside incidence forwardscatter cross-sections in mm^2 for a sphere, radius 2 mm, at 20°C as a function of frequency in GHz.

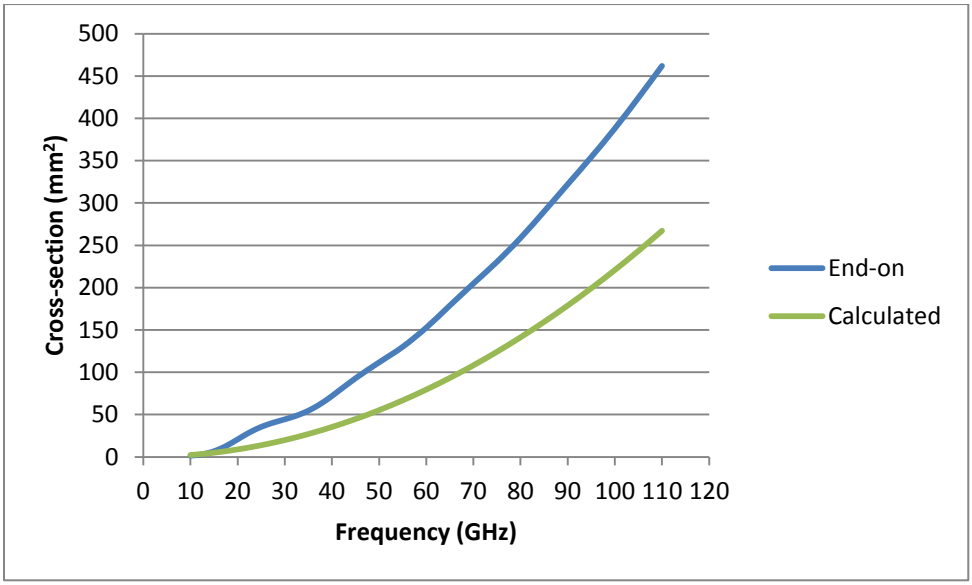

Figure 2.47 – End-on incidence forwardscatter cross-section in mm^2 for a sphere, radius 2 mm, at 20°C as a function of frequency in GHz.

2.6.6 Comparative Results – Non-dispersive Spheroid

To compare the absorption and scattering effects for the dispersive prolate spheroid objects in Section 2.6.2 and Section 2.6.3 above, with those for a non-dispersive spherical object, similar simulations using Mieschka [6] for a non-dispersive spheroid of radius 2 mm with a fixed dielectric constant of $-99 + j20$ were performed. These results are shown in Figure 2.48, Figure 2.49, Figure 2.50, Figure 2.51 and Figure 2.52 below. The theoretical resonance is at 22 GHz, in agreement with Figure 2.48, Figure 2.49, Figure 2.50, Figure 2.51 and Figure 2.52 below. Note also that due to symmetry of a sphere, scattering is independent of polarization or aspect angle.

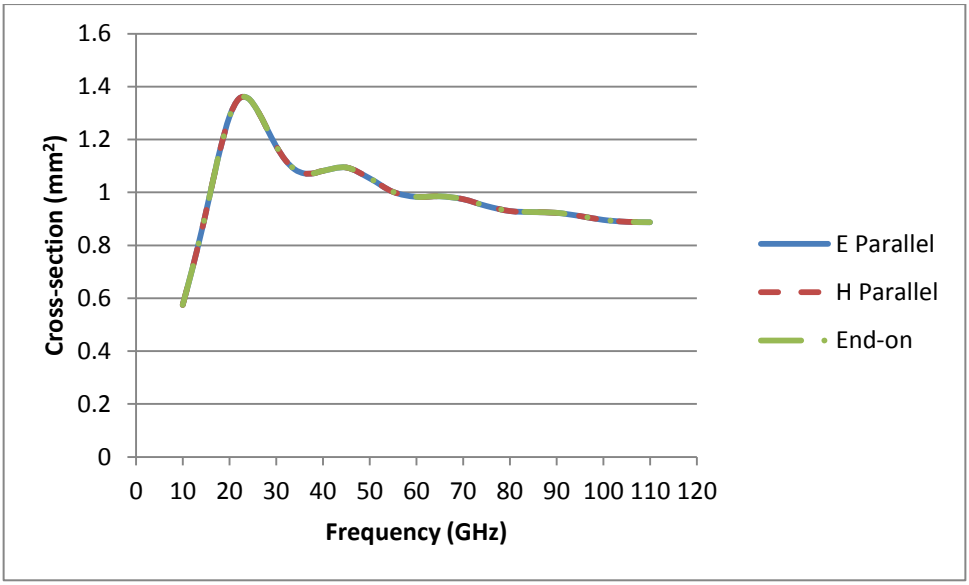

Figure 2.48 – Absorption cross-sections in mm^2 for a non-dispersive sphere, radius 2 mm, at 20°C as a function of frequency in GHz.

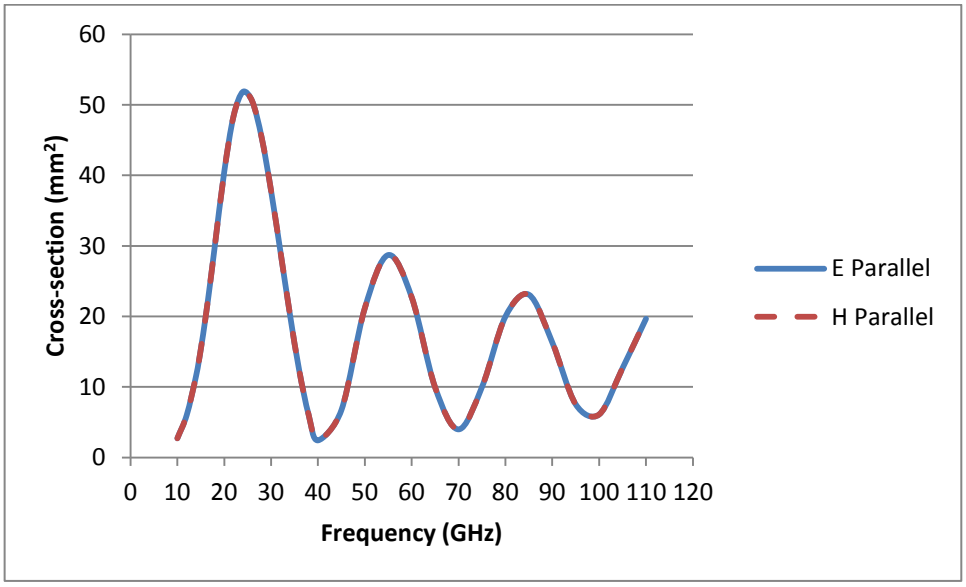

Figure 2.49 – Broadside incidence backscatter cross-sections in mm^2 for a non-dispersive sphere, radius 2 mm, at 20°C as a function of frequency in GHz.

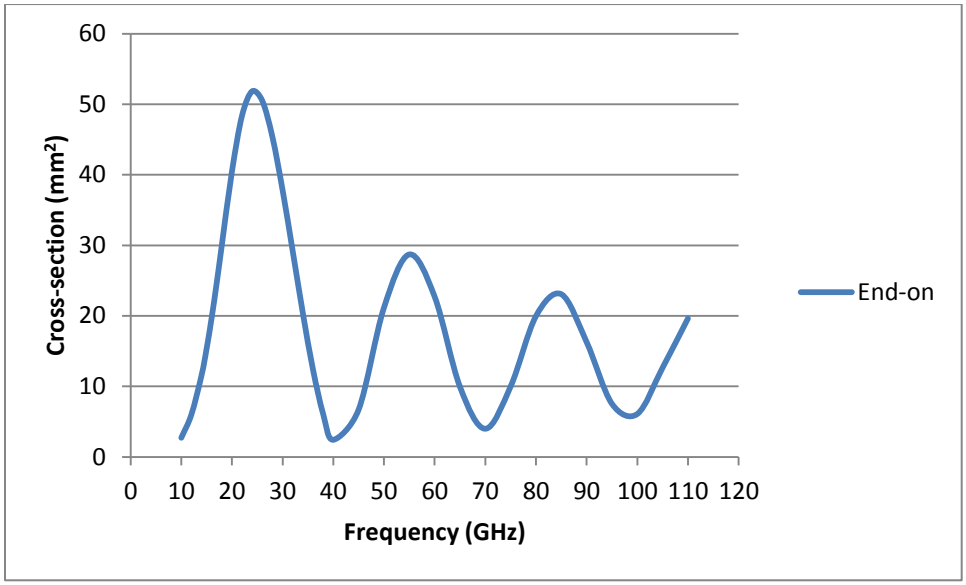

Figure 2.50 – End-on incidence backscatter cross-section in mm^2 for a non-dispersive sphere, radius 2 mm, at 20°C as a function of frequency in GHz.

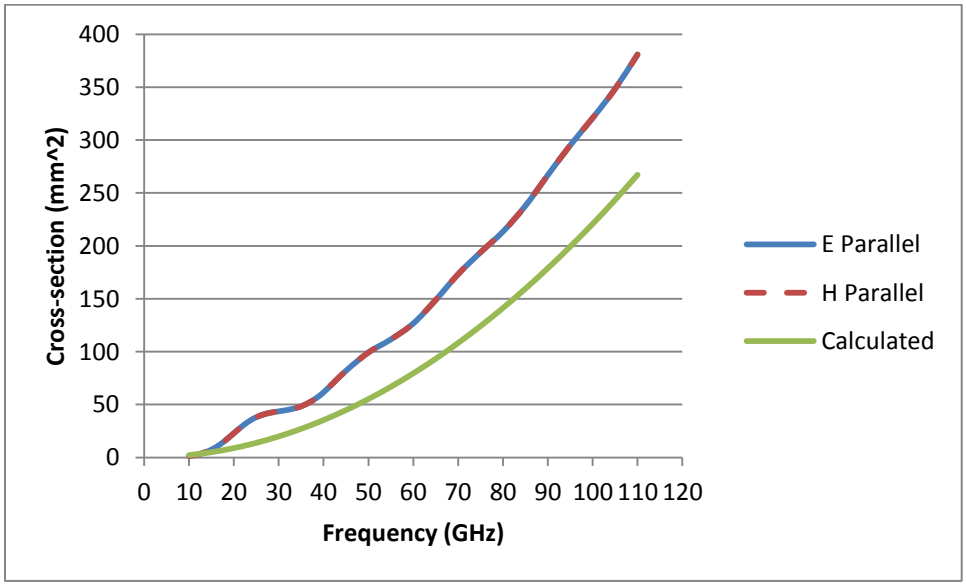

Figure 2.51 – Broadside incidence forwardscatter cross-sections in mm^2 for a non-dispersive sphere, radius 2 mm, at 20°C as a function of frequency in GHz.

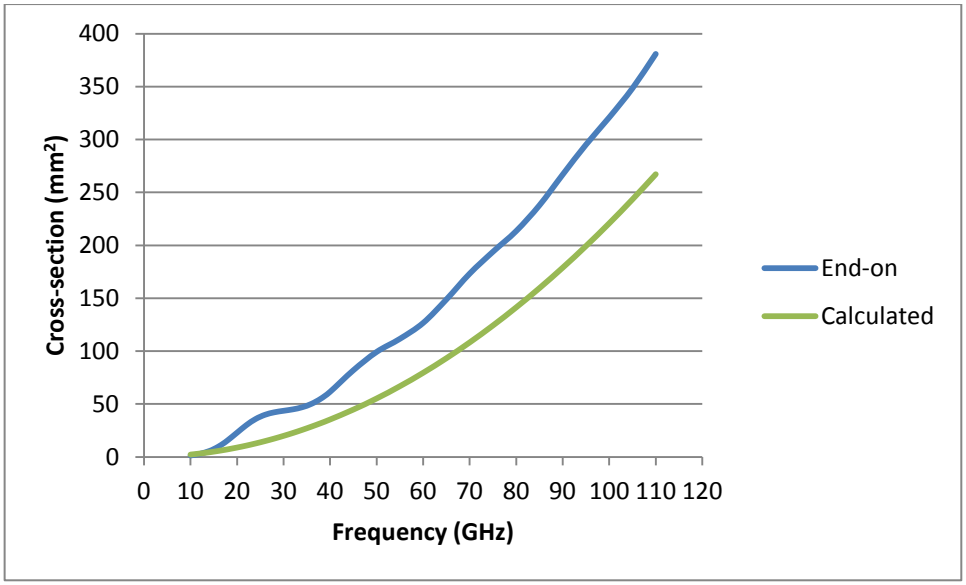

Figure 2.52 – End-on incidence forwardscatter cross-section in mm^2 for a non-dispersive sphere, radius 2 mm, at 20°C as a function of frequency in GHz.

2.6.7 Summary

In summary:

- For the broadside aspect, these results show that there is significant scattering and absorption, with minimal variation with temperature. Scattering and absorption exhibit a resonance dependent upon size and frequency. Scattering and absorption resonance also are dependent upon orientation and polarisation.
- For the end-on aspect, these results show that the results are consistent with Barber's modelling [93].

From these results then, the coupling of the electric field is greatest when the field is tangential to the scatterer, and coupling of the magnetic field is greatest when the cross-sectional area is perpendicular to the field. The rationale for this deduction has been discussed in Section 2.4.4 above.

In conclusion, scattering is greatest for broadside E field parallel, followed by End-on, with the scattering for E field perpendicular being the least for the three orientations. For both cases, these results agree qualitatively with Barber's model.

2.7 Experimental Results

2.7.1 Absorption and Scattering Results

Termites in-vivo in a Petri dish were exposed to microwaves at 24 GHz by a pyramidal horn antenna (55 × 45 mm aperture) directly above the dish. Figure 2.53 shows thermal signatures of various termites in-vitro exposed to 24 GHz. The outlines of the Petri dish and pyramidal horn are visible in the thermal images taken by a NEC Thermo Tracer TH7102WV thermal camera. These are labeled in Figure 2.54 and can also be seen in Figure 2.53 and Figure 2.55. The distinct circular outline of the Petri dish and pyramidal outline of the horn antenna can also be seen in Figure 2.56. The transmitter power into the antenna was 1.5 W.

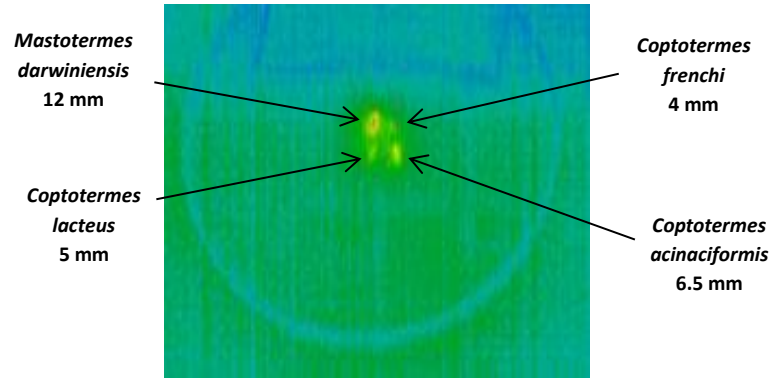

Figure 2.53 – Dependence of temperature rise on size.

Figure 2.54 shows the polarization dependence of the temperature rise, once again in-vitro. The termite oriented with its long axis parallel to the electric field shows much greater heating, indicating that absorption is greater. Thermal signatures of various termites exposed to 43.2 GHz (transmitter power into the antenna was +24 dBm, the antenna aperture was 35 mm x 26 mm) and 60.2 GHz (transmitter power into the antenna was +18 dBm, the antenna

aperture was 19 mm x 14.5 mm) showed high back scatter, consistent with the second and third Mie resonance peaks, and negligible heating due to absorption.

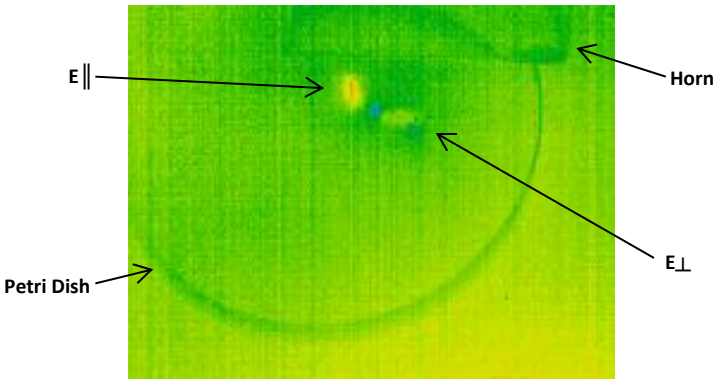

Figure 2.54 – Dependence of temperature rise on polarization.

2.7.2 Thermal and Behavioural Results

It has been known that termites are affected by thermal and light gradients [94]. This section demonstrates that individual and collective behavior of termites can be influenced by thermal effects induced by millimeter wave exposure. This offers the possibility of termite control. Three types of experiments were performed. First, termites in vivo in a Petri dish were exposed to 1.0 W of power at 24 GHz out of a pyramidal horn antenna (55 × 45 mm aperture) directly above the dish. The outlines of the dish and horn are visible in the thermal images taken by a NEC Thermo Tracer TH7102WV thermal camera, as shown in Figure 2.55. The test worker termites (Mastotermes darwiniensis, approximately 12 mm long, and used in all three experiments) moved freely into and out of the beam and took turns in “basking” under the horn, achieving a maximum temperature of 31°C, which is within their thermal comfort zone, and preferable to the ambient temperature of 22°C.

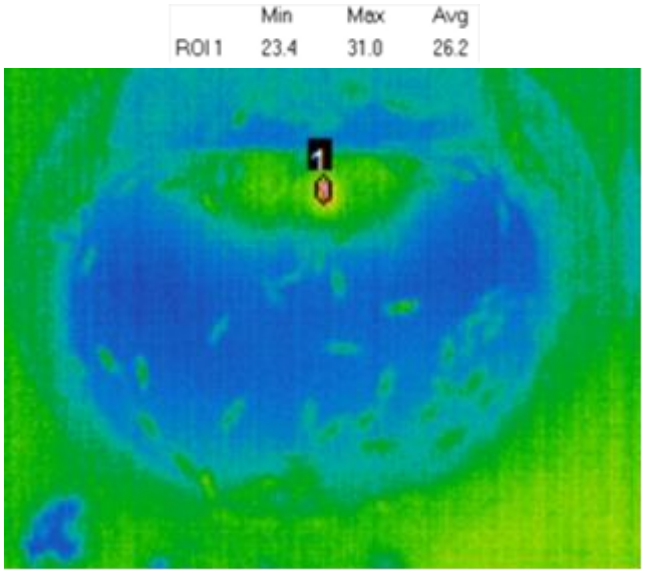

Figure 2.55 – Termites "basking" under a horn antenna.

The second in vivo experiment was also carried out in a Petri dish. Termites were exposed to 1.3W at 28.24 GHz from a 30 × 30 mm pyramidal horn. It has recently been shown that 12 mm long termites exhibit resonant absorption near 25 GHz [80, 95]. Individual termites exposed to the increased power density heated to 42°C. This was clearly uncomfortable for them, as evidenced by their avoidance of the beam, and evasive behavior, such as reorienting their body to reduce the heating. In order to entice termites into the beam, a dead termite was placed in the centre. This resulted in some termites venturing into the beam to investigate. These termites became distressed, and presumably sent distress signals to others, who followed, resulting in a huddle. This huddle proved suicidal, as shown in Figure 2.56, where the peak temperature exceeded 55°C. Termites lack internal thermal regulation, and under the conditions in Figure 2.56, lose most of their heat by radiation. The latter is proportional to ST^4, in accordance with the Stefan-Boltzmann law, where S is the surface area and T is temperature in °K [1]. By huddling, termites reduce their effective radiating surface area and increase the heat exchange between neighbors by radiation. This accounts for the extra 13°C rise in the huddle. Suicidal huddling behavior was also observed in termites "trying" to cross a water barrier, and it was also speculated that such huddles were also due

to individuals in distress (who fell into the water) attracting a crowd of other victims. Such social behavior for termites under distress has implications for termite control.

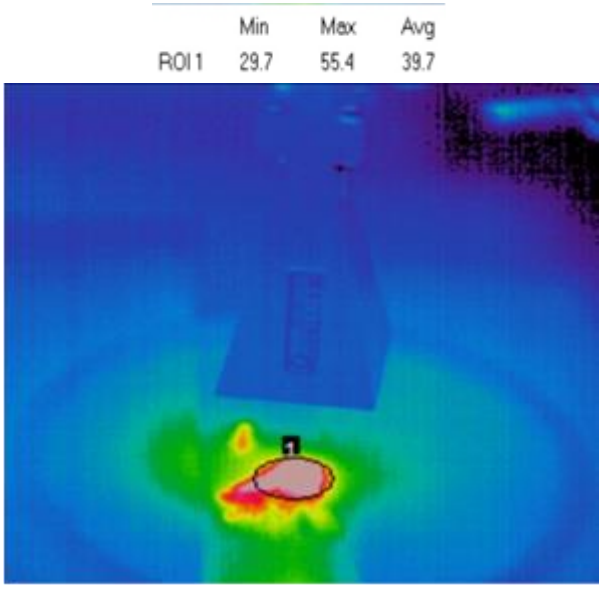

Figure 2.56 – Termite "death huddle".

The setup involved in the third experiment is shown in Figure 2.57. This simulates termites travelling to and from their nest via mud tubes. The "nest" with or without vermiculite is on the left, whilst the food (timber block) is on the right. In this case, no huddling was observed. However, after exposure, three soldier termites were observed in the beam, close to death, and unable to move. The soldiers did not attract the other caste termites, unlike what happened in the second experiment, Figure 2.56. It is still not known why the soldiers did not save themselves. One possible reason is perhaps to stop workers from entering a danger zone as the job of the soldiers is to protect workers [96].

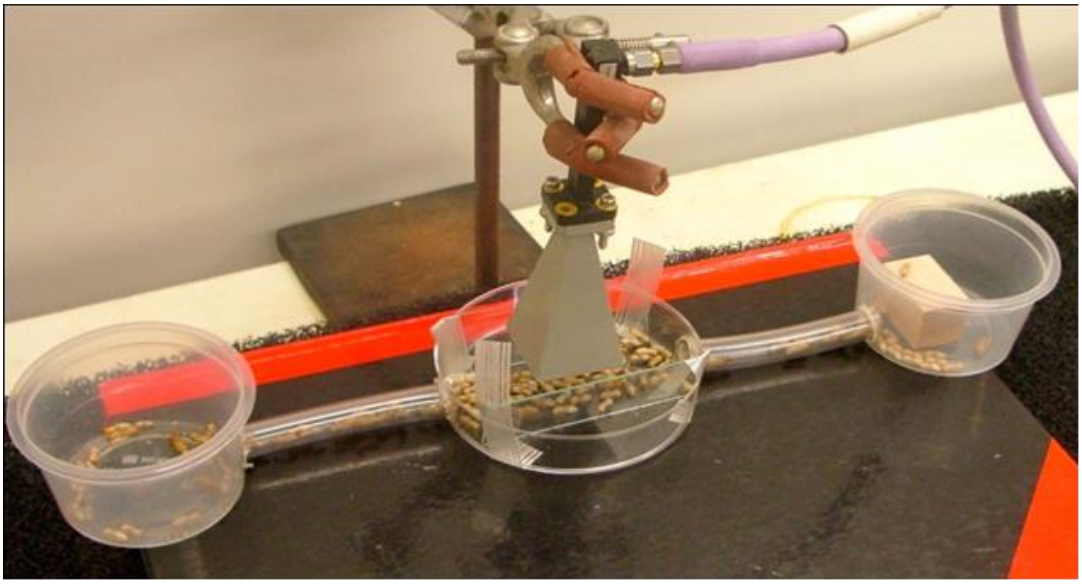

Figure 2.57 – Experiment setup for termites travelling to and from their nest along a simulated mud tube.

2.8 Conclusion

The problem studied in this chapter has been the absorption of scattering of microwaves from a scatterer such as an insect in general terms. It has introduced a model for scattering from an individual insect, notably a termite or an ant, in order to study the absorption and scattering from insects. It has also noted that insects are composed mainly of biological water which has large values of refractive index and absorption at microwave and millimeter wave frequencies.

The starting point for this study has been Mie's well-known solution of scattering from a conductive sphere at resonance, and the contributions which led to a thorough analysis of the shadow zones which arise from scattering from a conductive sphere. The study then applied this methodology to a dielectric sphere, and considered the contributions from geometric and diffraction optics to the particular case of the object geometry and composition of the insect model, a prolate spheroid, which introduced an additional dependence on the polarization of the incident wave due to the non-spherical nature of the prolate spheroid.

It has developed a sufficient body of theoretical understanding of the absorption and scattering of microwaves from a scatterer based on the work of Mie [8] and Richtmyer [21], the pioneering insight of Nicholson [28], von Lommel [24] and Watson [15], Fock [23], Ufimtsev [32] and others, and followed the analytical method described by Inada and Plonus [18, 19], for a dielectric sphere and applied these ideas to the analysis of the prolate spheroid.

Having developed a suitable body of theoretical understanding of the absorption and scattering of microwaves from a scatterer such as an insect, consideration was then given to some biological aspects of the interaction between insects and millimeter and sub-millimeter waves which offered the possibility of termite provocation or control using suitable emissions.

With a knowledge of the theory of absorption and scattering of microwaves from an insect and an appreciation of some of the possible interactions between insects and microwaves, a numerical study was undertaken, using computer software “Mieschka” [17], of absorption and scattering from insects over the microwave and millimeter wave frequencies. From these simulations it was concluded that scattering is greatest for broadside *E* field parallel, followed by End-on, with the scattering for *E* field perpendicular being the least for the three orientations.

Following this, some experiments at microwave and millimeter wave frequencies, where measurements of the absorption and scattering from termites were undertaken, and an investigation of some thermal and behavioral effects when termites are exposed to microwave and millimeter waves were observed. From these experiments it was concluded that that resonant absorption of millimeter wave radiation follows the theory developed in this chapter and has the potential to terminate termites, or to alter their social behavior.

This page has intentionally been left blank.

3 Radar Imaging of Termites

3.1 Introduction

In Chapter 2 the problem of the absorption and scattering of microwaves from a scatterer such as an insect was investigated. With the knowledge of the theory of absorption and scattering of microwaves from an insect, and an appreciation of some of the possible interactions between insects and microwaves, thus developed, a numerical study of absorption and scattering from insects over the microwave and millimeter wave frequencies using computer software was undertaken. Following this, some experiments at microwave and millimeter wave frequencies where conducted, and measurements of the absorption and scattering from termites were made, and some thermal and behavioral effects were observed, when termites were exposed to microwave and millimeter waves.

Building upon the foundational work and original research contributions of the Chapter 2, the problem studied in this chapter is the design of a radar suitable for the imaging of termites. The study will commence by briefly reviewing the earlier research in developing a radar for detecting termites [97] which led to the commercialization of the termite detection product Termatrac®. It will then, also briefly, discuss applying phased array techniques to detect termite activity over a large part of a wall and to image the activity using a hybrid array consisting of a receiver sub-array to image termite activity over a wide area at long range, and a second receiver sub-array to image termites in a small area with high resolution [95, 98].

To overcome the impractical need for a large number of elements of the hybrid array, this chapter introduces a new array design which uses Multiple Input Multiple Output (MIMO) array synthesis techniques. To the author's knowledge this is the first time that these techniques have been used for a two-dimensional imaging radar, and for imaging termite activity.

Although the term MIMO has become a fashionable nomenclature, and has been used to describe many different techniques, the designs to be presented here consider code division MIMO exclusively [99]. In this study, it is assumed that the the path length from a transmit element to the target and from the target to a receive element differ by a small fraction of a wavelength, so that each transmit and receive pair can be considered a transmit-receive element at the geometric centre of the pair. Also, the term "element" in this study means an individual antenna in an array.

The study will then discuss in detail the geometric pairing that occurs between each transmitter element and every receiver element and considers the impact and design tradeoffs of transmitter and receiver spacing. A design aim will be to maximize intra-element spacing so-far as is possible, with a view to minimizing mutual coupling between elements, while not introducing gaps in the coverage. In this the design will demonstrate the advantages of maximizing the receiver element spacing over the transmit element spacing. The study will discuss at some length various aspects of mutual coupling and provide a floor plan for the design of the array which embodies the principles investigated in this chapter.

In Section 3.7, new designs to address the problem of imaging radar for Unmanned Aerial Vehicles, which embody many of the principles examined in this chapter will also be presented. In these designs the position of the transmit and receive elements are transposed to minimize mutual coupling between receiver elements. These designs are also the first instance of the use of the Moreno-Tirkel sequence Family B [100] for high resolution imaging radar.

3.2 Background to Radar Imaging of Termites

Annually, termites cause billions of dollars of damage to buildings [9]. The imaging of termite activity in buildings is a challenging area of radar research. Termites are difficult to detect because they are small and obscured by building structures. Building materials cause

significant distortion to signals due to dielectric and near-field effects, and signals scattered by termites are very small. The goal of this chapter is investigate the design of an imaging radar to image termite activity by sensing the movement of termites in a single snapshot over a large area, such as wall, and provide high resolution imaging. As with Steinberg's goal of the radio camera [101], the aim in this chapter is to obtain images of sufficient fidelity that insect activity may be localized to a small region within a larger area, that potential targets may be counted, their relative positions observed, and their species deduced. To do this, it is desirable to measure the relative size of targets, their shape and their orientation.

Currently, the only instrument which reliability detects termite activity through most common building materials without damage to the structure under investigation is a hand-held 24 GHz radar developed by the author's supervisor and successfully commercialized as the product Termatrac® [78, 97], see Figure 3.1 and Figure 3.2. Other techniques of non-invasive termite detection, such as vibration sensing and gas detection or sniffer dogs, have in practice proven less effective than sensing termite movement by means of radar [78].

Figure 3.1 – Radar for detecting termite activity I – Termatrac®. From [78, 97].

Figure 3.2 – Radar for detecting termite activity II – Termatrac®. From [78, 97].

Termatrac® incorporates a single fixed antenna sensor to detect movement of termites and other in situ insects such as ants inside building structures at short range. The sensor consists of an IQ mixer and a fixed dual array (one for transmit and one for receive). The array is covered by a radome. The radome converts linear to circular polarization and partially overcomes polarization effects due to anisotropies in building materials such as plasterboard, timber noggins, ceramic tiles, electrical wiring and insulation, and random termite orientation. Termatrac® also incorporates a fixed temperature sensor and a fixed moisture sensor. Termites regulate the temperature and moisture of the galleries they occupy so there is almost always a differential between a region infested by termites and surrounding areas. Through field testing, fusion of data from all three sensors has been demonstrated to ensure a high probability of detection and a low false alarm rate [78]. Detection of insect movement and extraction of targets is difficult as returns from insects are very small and have very low signal to noise ratio (SNR). Clutter returns are more than 60 dB greater than insect returns, and signals are significantly distorted by building structures and materials due to dielectric and near-field effects. Termite and insect targets are differentiated from stationary background clutter by target Doppler and amplitude fluctuations as targets cross near-field equi-amplitude and equi-phase contours [102] due to termite and insect movement. The measured near-field equi-amplitude contours of a pyramidal horn antenna at 10 GHz are plotted in Figure 3.3, and the measured near-field equi-phase contours of the same antenna are plotted in Figure 3.4.

These plots show the equi-amplitude and equi-phase contours in the antenna pattern. Any other antenna or antenna array will have similar contours in its near-field antenna pattern. A moving target crossing these contours will induce modulations in the amplitude and phase of the wavefronts radiating from the antenna and in the waves scattered by the target. These modulations are the basis for differentiating between stationary clutter and moving targets. Stationary background clutter is separated and suppressed from targets by Doppler bandpass filtering. The filter pass band is 0.1 to 10 Hz and has proven over years of field experience to effectively suppress stationary clutter signals.

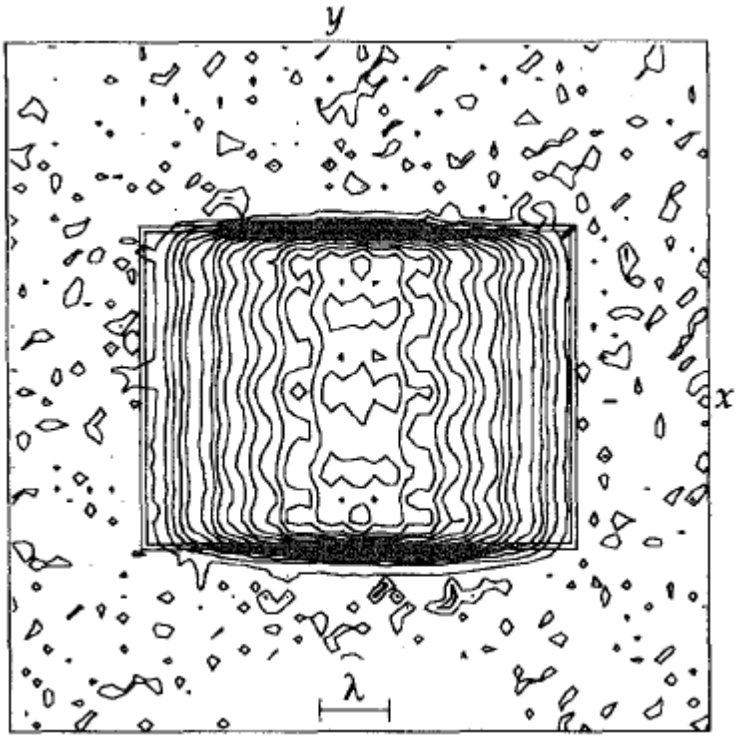

Figure 3.3 – Measured equi-amplitude contours of E_y in the plane z = 20 mm. From [102].

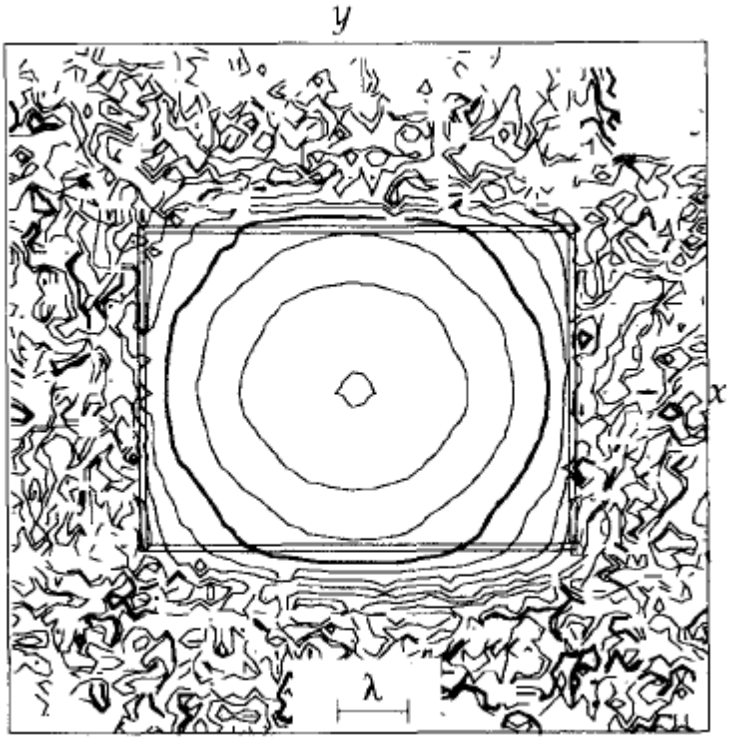

Figure 3.4 – Measured equi-phase contours of E_y in the plane z = 20 mm. Full lines are at intervals of 2π. Contour spacing is π/4. From [102].

Incidental movement of the sensor causes relative motion of the background clutter. This reduces the effectiveness of the Doppler bandpass filtering in rejecting stationary clutter signals, and results in extra noise being added to target signals due to leakage of non-stationary clutter into the filter pass band. Termatrac® incorporates a 3 axis accelerometer to detect such movement to alert the operator that sensor movement has occurred or to display the accelerometer outputs. In order to capture termite movement, the minimum sampling rate to satisfy the Nyquist criteria is 20 Hz. Field testing has shown that the minimum dwell time is between 1 s and 10 s. Although the current instrument reliably detects termite activity through most common building materials, it has no imaging capability. A device which could image termite activity by sensing the movement of termites in a single snapshot over a large area such as wall and provide high resolution imaging would be a major improvement.

Radar imaging may be achieved by physical scanning an antenna over an area. As any relative motion is difficult to suppress and can generate false targets, scanning across a large area by hand or by mechanical means is not feasible as any incidental motion will induce false targets. Therefore, only electronic scanning holds the possibility of imaging termites over a wide area. Among the advantages of an electronic scanned phased array is the absence of mechanical elements, scope to apply advances in signal processing techniques for improving performance and scope to beamform and steer multiple beams simultaneously and/or to incorporate Direction Of Arrival (DOA) processing to provide multi-target tracking and/or the raising of alarms in response to the detection of targets.

3.3 Hybrid Array

The next generation of design of a radar for detecting termite activity considered the possibility of applying phased array techniques to detect termite activity over a large part of a wall and to image the activity. This design [95, 98] is a hybrid array consisting of a receiver sub-array to image termite activity over a wide area at long range, a second receiver sub-array to detect termites in a small area with high resolution, and a transmitter sub-array to provide illumination for both receiver arrays, see Figure 3.5.

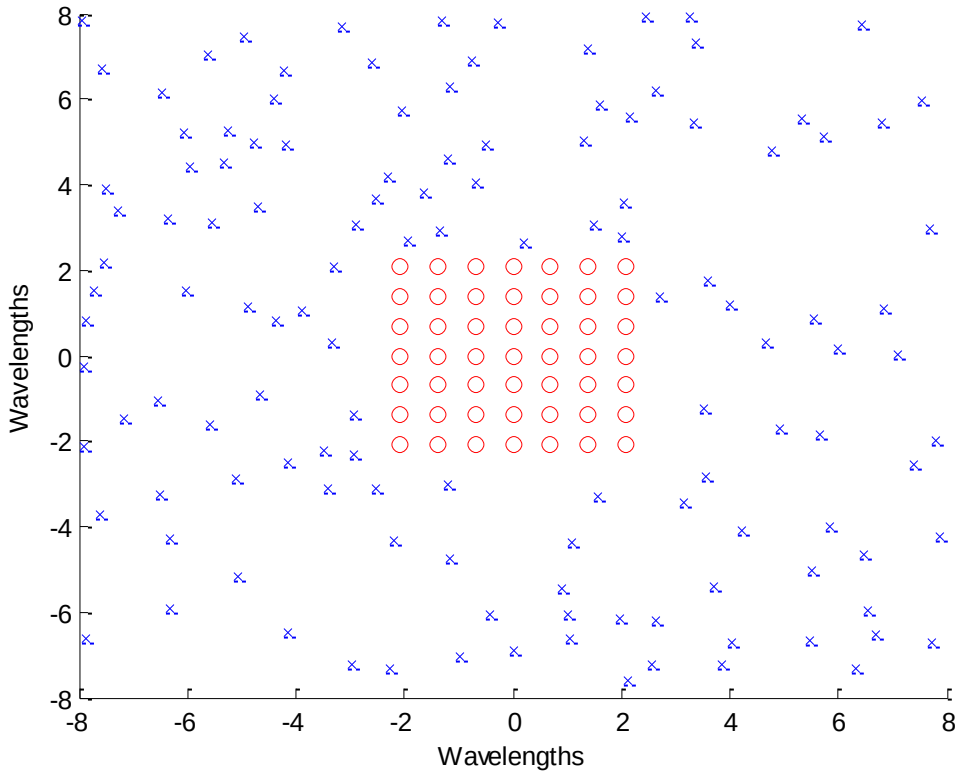

Figure 3.5 – Hybrid array for imaging termite activity.

The hybrid array has a large number of elements. In the construction of a planar substrate for the array, placement of components, routing of signals lines, and managing mutual coupling between array elements are very challenging and reduce the attractiveness of the array as a solution. A development by BAe Systems [103], proposes a 10,000 element array incorporating a phased array MMIC. Even this approach may not be practical given the challenges of MMIC design, component placement and packing, heat dissipation, power consumption, mutual coupling and cost. Component placement in particular is a challenge because signal and power lines need to be routed between components and to and from transmit and receive elements. Spacing between components becomes a premium in order to provide sufficient isolation between signals for distributing oscillator signals and routing receiver lines. If the number of elements can be reduced to a bare minimum, without sacrificing too much in performance , then the issues of handling the routing on a planar substrate can be made manageable. In the following sections it is proposed to use MIMO

array synthesis to minimize the number of transmit and receive elements and to consider some of the important design considerations in creating such a design.

3.4 MIMO Array Synthesis

As an array for detecting termite activity, the hybrid array would need a large number of elements to provide the necessary resolution. However, such a large number of elements is impractical [104]. To overcome the requirement for a large number of elements, MIMO array synthesis techniques offer a possible solution.

Sequential MIMO array synthesis techniques [105] multiplex the signals in time and have the effect of reducing the dwell time on targets and this has the effect of lowering the SNR. For detecting termites, this is an issue because the returns are very weak and any reduction in target SNR cannot be tolerated as this may cause termite activity to go undetected. Code division MIMO overcomes this limitation by permitting 100% dwell on targets. This chapter will consider code division MIMO exclusively.

A one-dimensional MIMO array synthesis technique has been verified for calibration targets [106]. However, to the author's knowledge this is the first time that code division MIMO array synthesis techniques have been considered and applied to the problem of imaging of termite activity [99, 104]

In conventional phased array synthesis, the antenna pattern is determined by the number and spacing of the elements. The relative phase displacement of each element introduces a progressive phase shift, so that the signals from the array elements sum constructively or destructively to form and steer the array pattern.

With MIMO array synthesis investigated here, the paired transmit and receive element forms a transmit/receive element at the geometric centre of the two physical elements causing the phase centre of a virtual array element pairing to form at the mid-point (or mean in Cartesian

co-ordinates) of a transmitter and receiver element. Referring to Figure 3.6, orthogonal coding of each transmitter element enables the synthesis of all combinations of transmitter (blue elements) and receiver (red elements) element pairings i.e. a virtual array (black elements) from the geometry of each pairing of the elements of the physical array. This synthesis is performed in digital hardware in the back-end of the array receiver or in software after digitization.

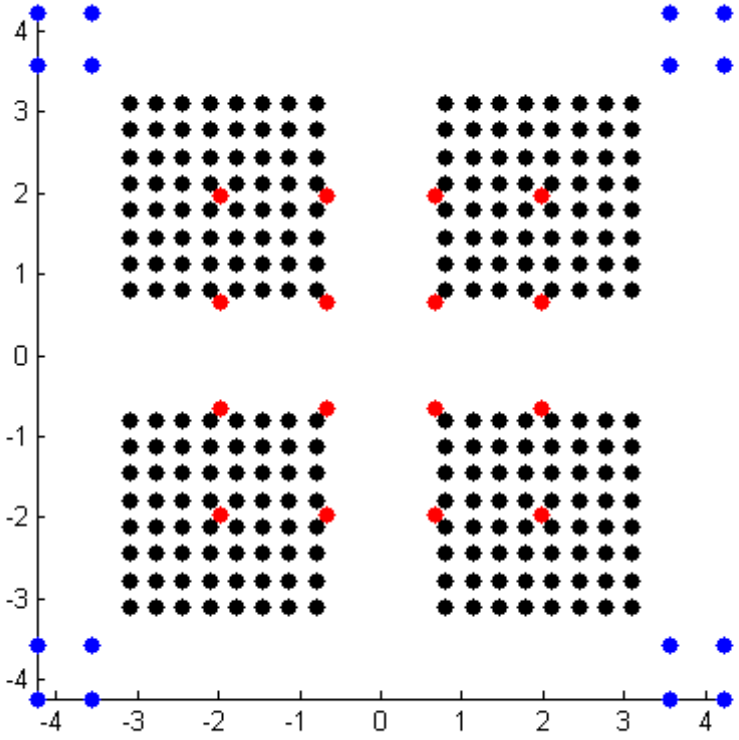

Figure 3.6 – Synthesis of Virtual MIMO array (black elements) from the geometry of the transmitter (blue) and receiver (red) elements. Horizontal and vertical scales are in wavelengths.

An advantage of this approach is that the number of elements in the synthesized array is the product of the physical number of transmitter and receiver elements. In contrast, for example, the BAe array requires 10,000 physical transceiver elements. This could be synthesized by a MIMO array having 100 transmitter elements and 100 receiver elements and an appropriate orthogonal coding scheme.

Another advantage of this approach is that the synthesized array does not require sequential scanning as all synthesized elements are formed simultaneously. Therefore small targets such as termites are illuminated with the maximum power available and termite motion can readily be captured and multiple targets can be tracked if required.

Bi-phase codes are superior to all other forms of modulation for this application because the modulation amplitude is uniform and the signal constellation has the greatest distance, making it less susceptible to noise and interference. Also, the energy efficiency of biphase codes is 100%.

In conventional beamforming, transmitter and receiver elements have to be equalized in delay. A further advantage of a MIMO array is that transmitter element delays do not need to be equalized in the transmitter chain as orthogonal coding of each element effectively isolates each element, and delays can be equalized in back-end processing. This frees the array design allowing elements to be placed without the need to consider the physical restrictions imposed by the design of equalized delay lines.

Anything that reduces waveform orthogonality is undesirable. Once such effect is mutual coupling between antenna elements. This is discussed in Section 3.5 below.

3.5 MIMO Array for Radar Imaging of Termite Activity

The physical realization of the MIMO array for radar imaging of termite activity [99] comprises four 2x2 element transmitter sub-arrays located in the corners of the array and a single 4x4 element receiver sub-array located in the centre of the array. The array is shown in Figure 3.7.

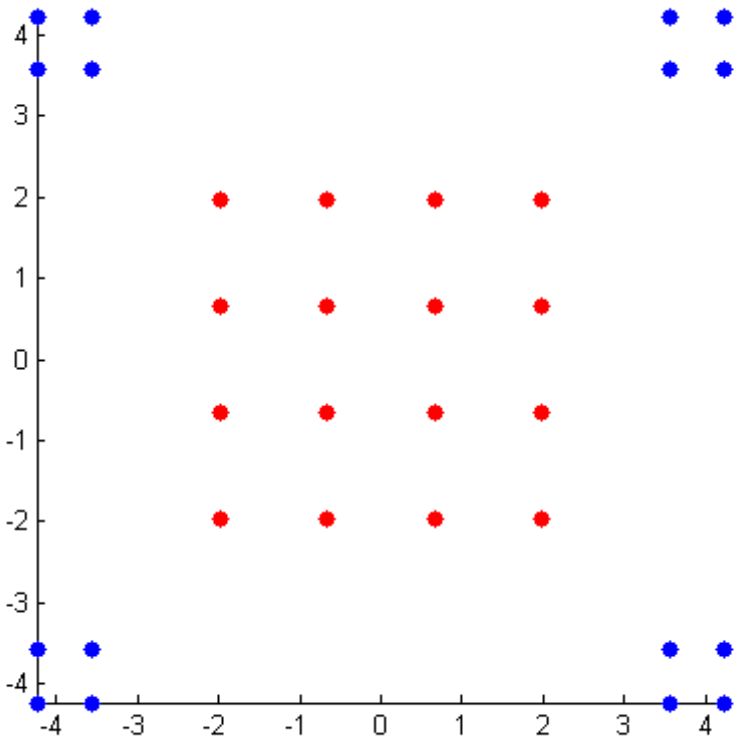

Figure 3.7 – MIMO array. Horizontal and vertical scales are in wavelengths.

The array has a total of 16 transmitter elements and 16 receiver elements. The geometric action of MIMO array synthesizes a virtual array having 256 transmitter-receiver elements. The transmitter elements are arranged in four groups of 2×2 elements, and the receiver elements are arranged in a single 4x4 element grouping. The four transmitter groupings are placed at the extremities of the physical array to minimize the mutual coupling between the groupings. The physical spacing between the receive elements in the centre of the array is a full wavelength which minimizes the mutual coupling between receiver elements. The increased spacing between the receiver elements significantly eases the routing of signals to the receive elements and their electronics such as active devices including MMICs on the reverse side of the array of the radar [99].

In comparison with the hybrid array , which uses a receiver sub-array to image termite activity over a wide area at long range, and a second receiver sub-array to detect termites in a small

area with high resolution, the MIMO synthesized array uses all transmitter and receiver elements for both activity detection at long range and high resolution tracking at short range.

In this design vectorial differences between the virtual array elements in the style of a random or sparse array [101], or of a Gilbert-Costas array [107] in which all the vectors form a uniformly redundant array [108] or co-array [109] are not used. However it is noted that if other codes [100] are chosen, redundancy in the co-array could be minimized. The decomposition of these other codes into a geometry which can synthesize the co-array array is a new avenue of ongoing research [110-112], which the author has applied in Section 3.7 to the problem of UAV imaging radar.

3.5.1 Orthogonal Coding

The orthogonal coding for MIMO array synthesis depends on the path delays. This is possible, since the round trip delay to the targets is negligible and so is its variation, so that the codes need to be orthogonal for zero delay only, therefore only synchronous codes are required. The simplest of these are codes formed by a Hadamard matrix [113]. Walsh-Sylvester codes are formed from the matrix $\begin{bmatrix} +1 & +1 \\ +1 & -1 \end{bmatrix}$ with powers of 2, and thus only codes of length 2^n are formed [113]. The Paley-Hadamard construction of $(p+1)(p+1)$ can be formed from cyclic shifts of Legendre sequences or m-sequences [113]. The transmitter element signals are coded using sequences obtained from rows or columns of a Hadamard matrix of suitable size [104].

3.5.2 Element Response

A typical wall can be covered using a 40˚ field of view in azimuth and elevation at a range of 1.5m. Response beyond these angular limits is undesirable because it only adds to clutter. Therefore, it is desirable to restrict the array response towards end-fire. The end-fire response was simulated in CST [114], see Figure 3.8.

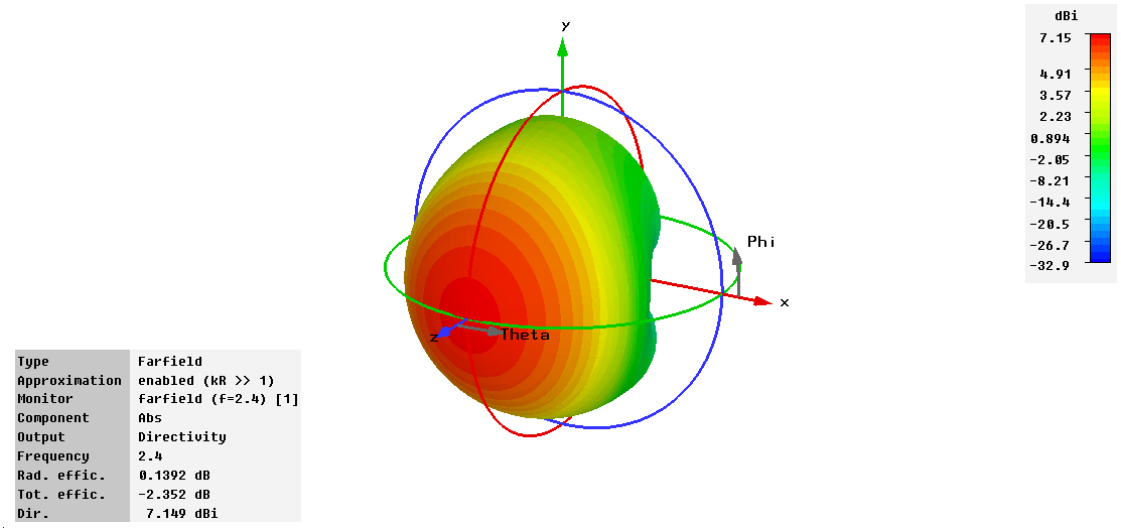

Figure 3.8 – End-fire response.

This can be achieved by using a radome as a superstrate. It has the added benefit of permitting the array elements to be spaced further apart than required by the Nyquist criterion and increasing the element gain in the directions of interest.

The element spacing of the array is 1.3λ for the receiver elements, and 0.65λ for the transmitter elements. The increased physical element spacing reduces mutual coupling, see Section 3.6 below. It also provides increased space for components and interconnects, so dual-polarized elements are feasible. Normally the spacing for the transmitter elements is λ and for the receiver is $\lambda/2$ but for this array using a superstrate, it is possible to increase the physical spacing to 1.3λ for the receiver elements, and 0.65λ for the transmitter element and still avoid grating lobes while still satisfying the Nyquist criterion. Thus the receiver element spacing has been increased by almost 3 to 1 (from $\lambda/2$ to 1.3λ). All the array elements are dual-polarized circular patches, shown in red, in the preliminary circuit board floor plan of the array in Figure 3.9. HMC571LC5 IQ downconverters are shown connected to the 4x4 group circular receiver patches in the centre of Figure 3.9. HMC815LC5 IQ upconverters are shown connected to each 2×2 group of circular transmitter patches in the four corners of Figure 3.9. Refer to [99] for further details of the transmitter and receiver block diagrams and the other

devices incorporated into the design. The floor plan provides a level of confidence that it is possible to fit all the important components of the array on a single planar printed circuit board within the constraints imposed by the required transmitter and receiver element spacing.

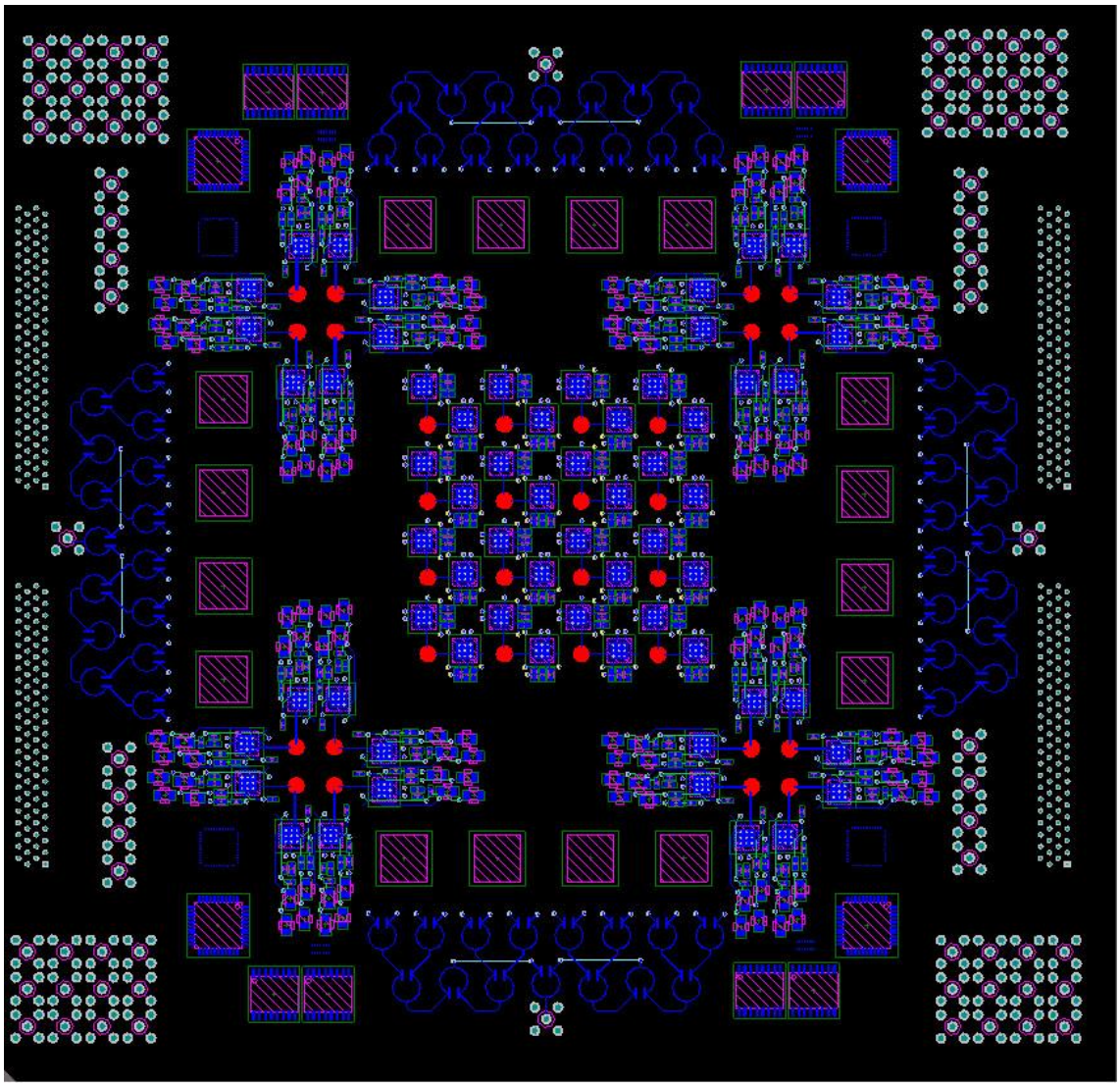

Figure 3.9 – MIMO array floor plan.

3.5.3 Superstrate

A dielectric with two dielectric surfaces functions as a Fabry-Perot resonator. A superstrate (Fabry-Perot resonator) is used to suppress the array response at end-fire [115, 116] and thereby avoid grating lobes within the scan limits of z. The radome superstrate is a low

permittivity dielectric material, spaced $\lambda/2$ from the ground plane of the array, with an electrical thickness of $\lambda/4$. The array was simulated in CST [114]. A single array element with the superstrate is shown in Figure 3.10. The radiation pattern of the element is shown in Figure 3.11.

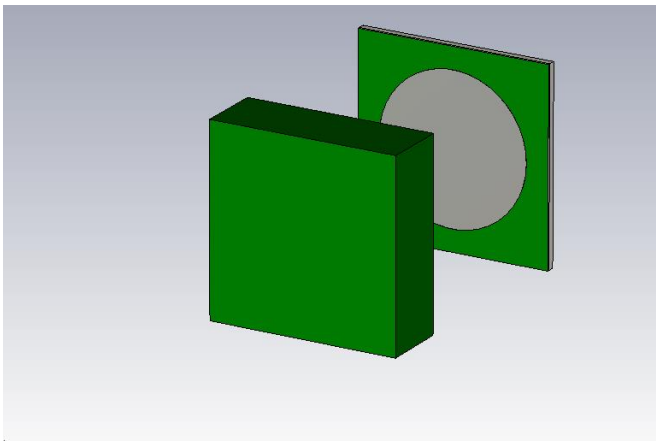

Figure 3.10 – Single array element with superstrate.

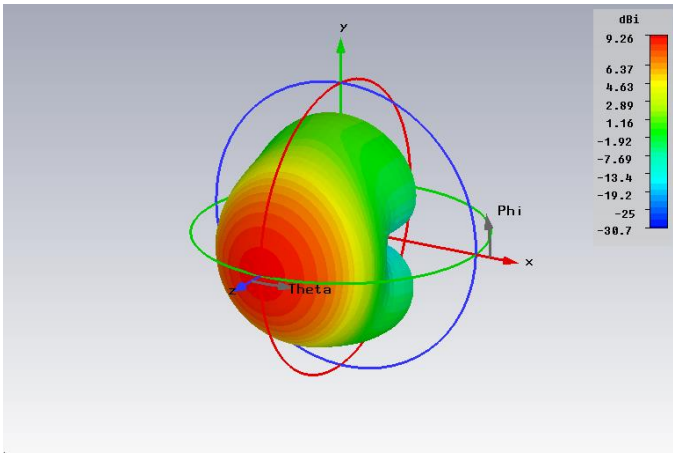

Figure 3.11 – Radiation pattern of single element with superstrate.

The element spacing of the fully synthesized virtual array's transmitter/receiver elements is 0.325λ. The pattern of the virtual array steered to boresight is shown in Figure 3.12. The beamwidth of the pattern is 9.4˚ in both elevation and azimuth.

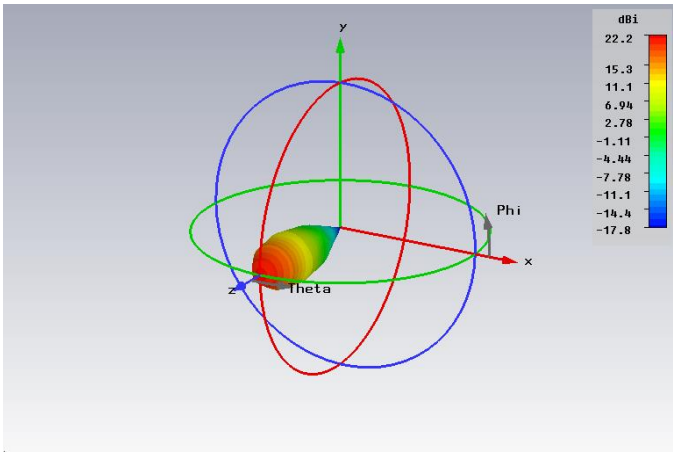

Figure 3.12 –Virtual array radiation pattern steered to boresight (element spacing 0.325λ).

3.5.4 Direction Of Arrival

A key objective is sensing the movement of termites in a single snapshot over a large area such as wall and providing high resolution imaging. These objectives are achieved in two steps. The first objective is achieved by DOA. The second is achieved by subsequent beamfoming. DOA is performed using the Matrix Enhanced Matrix Pencil [117, 118] to localize targets. Several DOA methods were considered, however only the Matrix Pencil performs well with coherent signals with low SNR [104]. Then, imaging is achieved by beamforming the virtual array. Cancellation signals are synthesized for the strongest targets and applied before beam patterns are formed over the virtual array. The effectiveness of the target cancellation is better than 30 dB, so the beamforming processing only has to deal with a target contrast of up to 30 dB [104]. Beams are formed simultaneously with Chebyshev weighting.

3.6 Mutual Coupling

The physical realisation of the MIMO array for radar imaging of termite activity has five sub-arrays. There are four transmitter sub-arrays and one receiver sub-array. All five sub-arrays are affected by inter and intra-array mutual coupling. This affects the transmitter signals, the received signals and the local oscillator (LO) signals. The LO signals in the design are at half

the operating frequency and are harmonically up and down converted to the operating frequency. An advantage of distributing the LO at half the operating frequency is improved isolation and reduced interference with the operating frequency [99].

Since inter-array coupling is mainly determined by the proximity of one array to another, it is relatively easy to control because of the relatively large spacing between each of the transmitter sub-arrays and between them and receiver sub-array. The large, i.e. several wavelengths, spacing between each of the sub-arrays permits the insertion of conducting (metal) guards and vias as required to suppress guided waves through the substrate.

Since the four transmitter arrays are identical, and share the same symmetry with the receiver array, then it is only necessary to consider a single transmitter array and the receiver array.

3.6.1 Transmitter Element Mutual Coupling

Inter-element coupling in the transmitter array causes the transmitter pattern to squint i.e. tilt the main beam centre off boresight. This is shown in the Figure 3.13 through Figure 3.16 below which were generated using the software tool Fazar [119].

With no mutual coupling between the transmitter elements, the absence of transmitter pattern squint is illustrated in Figure 3.13.

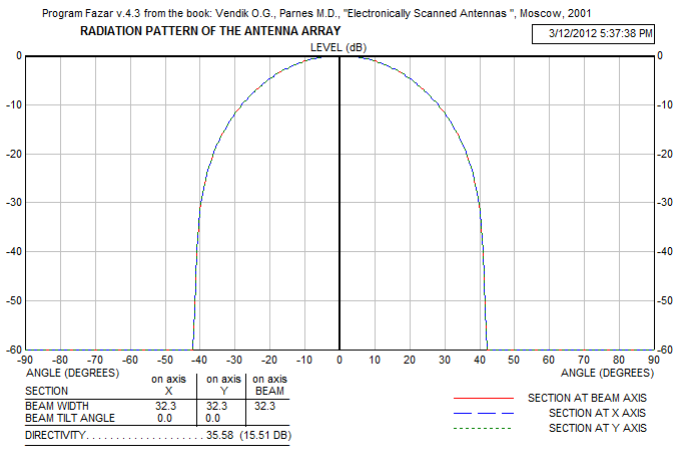

Figure 3.13 – Transmitter pattern squint: No mutual coupling.

With -20 dB of mutual coupling between the transmitter elements, the transmitter pattern squint is illustrated in Figure 3.14. The transmitter pattern has squinted 1.7° in the x axis and 1.8° in the y axis.

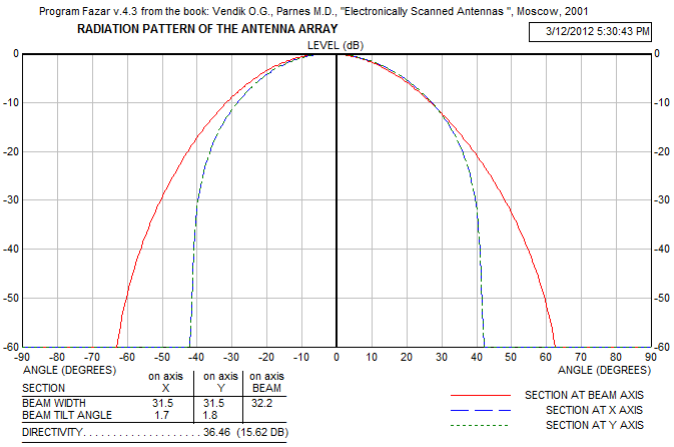

Figure 3.14 – Transmitter pattern squint: -20 dB mutual coupling.

With -30 dB of mutual coupling between the transmitter elements, the transmitter pattern squint is illustrated in Figure 3.15. The transmitter pattern has squinted -0.8° in the x axis and -0.6° in the y axis.

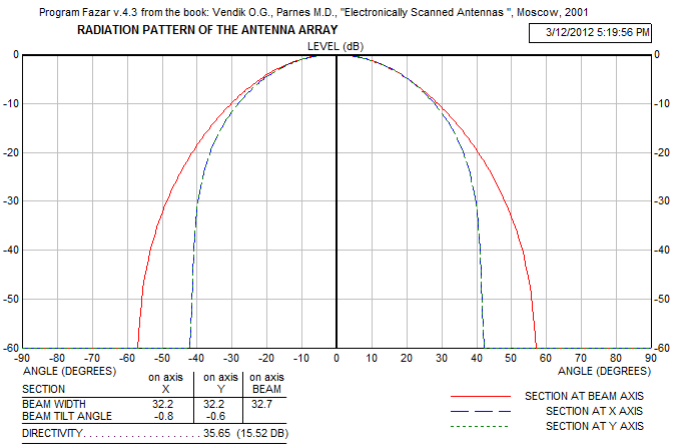

Figure 3.15 – Transmitter pattern squint: -30 dB mutual coupling.

With -40 dB of mutual coupling between the transmitter elements, the transmitter pattern squint is illustrated in Figure 3.16. The transmitter pattern shows negligible squint in either

the x axis or the y axis as the mutual coupling between the elements is very small, and mimics the case of no mutual coupling between the elements.

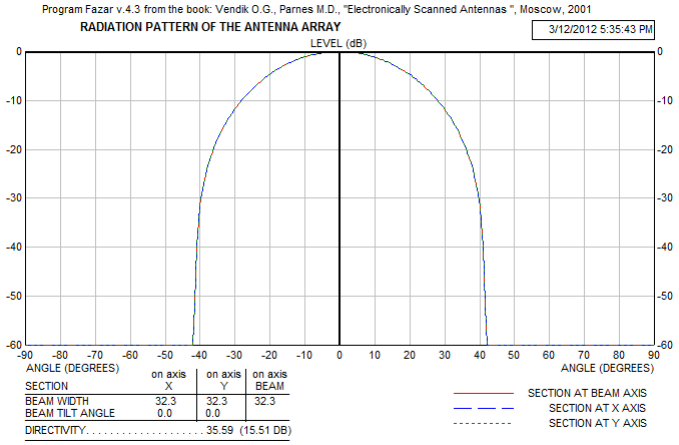

Figure 3.16 – Transmitter pattern squint: -40 dB mutual coupling.

Squint in the transmitter beam pattern cannot be controlled by the insertion of metal guards or vias as for inter-array coupling because of the close physical spacing between the elements. However, it is possible to measure the effects of this coupling by calibration. This can be done by applying an orthogonal code modulation to each transmitter element and beamforming on a receiver element in the far field. The mutual coupling can then be calibrated and deliberate signals of same magnitude but opposite phase introduced artificially to cancel the effects of mutual coupling. This can be applied to the cross-polarization as well, since it is just a special case of mutual coupling, and the design is using modulating orthogonal polarizations with orthogonal codes. Cross-polarization is most significant for adjacent apertures under the same patch, see [120] and [121].

With no mutual coupling between the transmitters and receivers, the received signal, S_i, at receiver element i scattered from a target t in the far field of both the transmitter and receiver, is a result of a summation of signals from N transmitter elements. For a MIMO design, the transmitted signals are all modulated by orthogonal codes c_n. The phase of the microwave carrier signal, as well as the code modulation envelope are both delayed by the

round trip passage to and from the target. If, R_{nt} is the distance from the transmitter n to the target t, and R_{ti} is the distance from the target t to the receiver i, then the delay is given by $\frac{R_{nt}+R_{ti}}{c}$, where c is the speed of light in a vaccum. The elevation pattern of a single transmitter element is $g(\theta)$. It is assumed that the element is a circular patch. Therefore the antenna pattern is independent of azimuth and has only variation only in θ. T is proportional to transmitter power, and L to path loss [122]. Thus:

$$S_i = \sum_{n=0}^{N-1} TLc_n\left(t - \frac{R_{nt}+R_{ti}}{c}\right) g(\theta) TL e^{j\omega(t-\frac{R_{nt}+R_{ti}}{c})} \tag{3.1}$$

The first processing step in the receiver is to down-convert the microwave signal to a convenient baseband such as 20 kHz, and to form a dot product (correlate) of the resultant baseband signal with the local reference of the orthogonal code. The code chip rate is 5 kHz, corresponding to a chip period of 0.2 ms, whilst the time delay $\frac{R_{nt}+R_{ti}}{c}$ never exceeds 10ns. Hence, the received and reference codes are almost synchronous, and the dot product of the code family is a set of delta functions, to within an error of 5×10^{-5}. Hence:

$$c_n\left(t - \frac{R_{nt}+R_{ti}}{c}\right) c_m(t) \approx \delta_{mn} \tag{3.2}$$

The role of transmitter beamforming is to equalize all the baseband carrier phase factors $e^{j\omega(t-\frac{R_{nt}+R_{ti}}{c})}$, to remove the variation with n, by adding a deliberate correction phase ψ_n so that $\frac{R_{nt}}{c} + \psi_n = \alpha$.

Therefore, under these ideal conditions, after correlation with the orthogonal codes, c_n, appropriate phase shifting to achieve transmitter beamforming, and final down-conversion to baseband, the received signal, S_i, from receiver element i is:

$$S_i = TLg(\theta) \sum_{n=0}^{N-1} \sum_{m=0}^{M-1} \delta_{mn} e^{j\beta} \tag{3.3}$$

$$= nTL\delta_{mn} g(\theta) e^{j\beta} \tag{3.4}$$

Mutual coupling introduces multipath components

$$S_i = TLg(\theta) \sum_{k=0}^{K-1} \sum_{n=0}^{N-1} \|\gamma_{kn}\| c_n \left(t - \frac{R_{nt} + R_{ti} + (1-\delta_{kn}) R_{kn}}{c} \right) e^{j\omega \left(\frac{R_{nt} + R_{ti} + (1-\delta_{kn}) R_{kn}}{c} \right)} \tag{3.5}$$

where $\|\gamma_{kn}\|$ are the magnitudes of the mutual coupling coefficients, with $\|\gamma_{nn}\| = 1$. R_{kn} is the propagation delay between element k and n. Thus:

$$S_i \approx TLg(\theta) \sum_{k=0}^{K-1} \sum_{n=0}^{N-1} \|\gamma_{kn}\| c_n(t) e^{j\omega \left(\frac{R_{nt} + R_{ti} + (1-\delta_{kn}) R_{kn}}{c} \right)} \tag{3.6}$$

After correlation beamforming, the received signal, S_i, becomes:

$$S_i \approx nTLg(\theta) e^{j\omega t + \beta} + \Delta \tag{3.7}$$

where

$$\Delta = \sum_{k=0}^{K-1} \sum_{n=0}^{N-1} \|\gamma_{kn}\| (1 - \delta_{mn}) e^{j\omega \left(\frac{(1-\delta_{kn}) R_{kn}}{c} \right)} \tag{3.8}$$

The Gaussian sum, Δ, becomes a beamforming error, which can be significant. The next section will discuss compensation for the beamforming error for the transmitter array.

3.6.2 Compensation for Mutual Coupling

3.6.2.1 Transmitter Array

For the transmitter array beamforming, the beamforming error, Δ, from Equation (3.7) can be cancelled by adding appropriate complex weighting terms to each modulating signal carrying orthogonal codes. This can be done if $\|\gamma_{kn}\|$ and R_{kn} are both known. Alternatively, these

values can be found adaptively, by adding the compensating terms with variable magnitudes e_{kn} and phases, φ_{kn}, until the value of S_i is maximized. Thus:

$$S_i \approx nTLg(\theta)e^{j\omega t+\beta} + \Delta + \sum_{k=0}^{K-1}\sum_{n=0}^{N-1} e_{kn}(1-\delta_{mn})e^{j\omega t-\varphi_{kn}} \qquad (3.9)$$

However, this may not be the best solution as it does not address the issue of the level of the sidelobes, and therefore other optimization criteria may be desirable such as minimization of sidelobes which attempts to reduce clutter seen through the sidelobes.

3.6.2.2 Receiver Array

The receiver array suffers from similar (or worse) mutual coupling problems, because signals from the transmitter elements are summed whereas signals at the receiver elements are 'scrambled' by the target, and therefore it is not possible to compensate the receiver signals for the effects of scattering from the target. Thus it is not possible to apply the method of compensation described above for the transmitter array to the receiver array because the receiver signals are affected by the target.

The standard method of compensation [123], is to multiply the array manifold matrix by an array transformation matrix, where the coefficients of the transformation matrix are the complex values of the mutual coupling between the respective elements. This works well, if these coupling values are known. However, measuring these values requires the receiving array to be able to function in transmit mode so that elements can be driven, and their effect determined at other elements, which act as receivers. This is impractical, or impossible, as in this case. Therefore, the mutual coupling coefficients have to be obtained by other means.

Standard methods are:

1. Start with undetermined magnitudes and phases for the coupling coefficients, and adjust them for maximum received signal. This is the method adopted by

Friedlander et al. [124]. There is no control over the received magnitude and phase of signals at each receiver element due to the unknown scattering from the target. This is quite different from the transmitter case, where there is total control over both and without the complication of scattering from a target.

2. Treat the array as a multi-port network, and determine S parameters or mutual impedances between ports. This suffers from two major drawbacks: it requires all ports which are not driven, or used as measurement ports, to be matched. This is impractical, so using this method assumes that the elements do not exist and alters the scenario in a major way. For example, Sarkar [118] deals with an array composed of dipole antennas suspended in space, coupled only by the radiation field. This is correct for this example, but not relevant to the physical array.
3. Simulate the mutual coupling by using a full Method Of Moments (MOM) analysis. These computed coupling coefficients can then be used to construct a compensation matrix. This is the preferred method, because it enables us to recreate all the geometry of the array and predict the coupling as realistically as possible.

There are some methods which deal well with infinite arrays with mutual coupling. Also, the problem is simpler in one dimension. Some people have tried to solve the mutual coupling problem for infinite arrays, and then use Floquet analysis [125] (a generalization of Fourier) to convolve the solution for that infinite case with a finite aperture, to deduce a likely result for a finite array. However, this works poorly for the edge elements. In the array, there are many edge elements, so this is a serious issue.

For a 2×2 transmitter array design mutual coupling between transmitter elements is symmetrical. For the 4×4 version of the receiver array, there are three classes of elements in terms of E, H and D (Diagonal) by symmetries, elements e.g. corner elements, side elements,

central elements, and it is difficult to see how convolution techniques could treat these elements equally. The element classes are:

1. Four elements at the corners of a 2×2 square.
2. Eight elements at the edges of a 3×2 square.
3. Four elements at the centre of a 3×3 square.

Another issue is mutual coupling between transmitter and receiver elements as illustrated in Figure 3.17. In the design presented, this is minimized because the design has maximized the spacing between the transmitter elements (group of four elements in the lower left of the figure) and the receiver elements (group of 3x2 elements of the 4x4 receiver array, in the upper right of the figure) and is thus over a large spacing. In this case, mutual coupling is dominated by surface waves . These can be reduced by making the substrate as thin as possible so most of them are cut off.

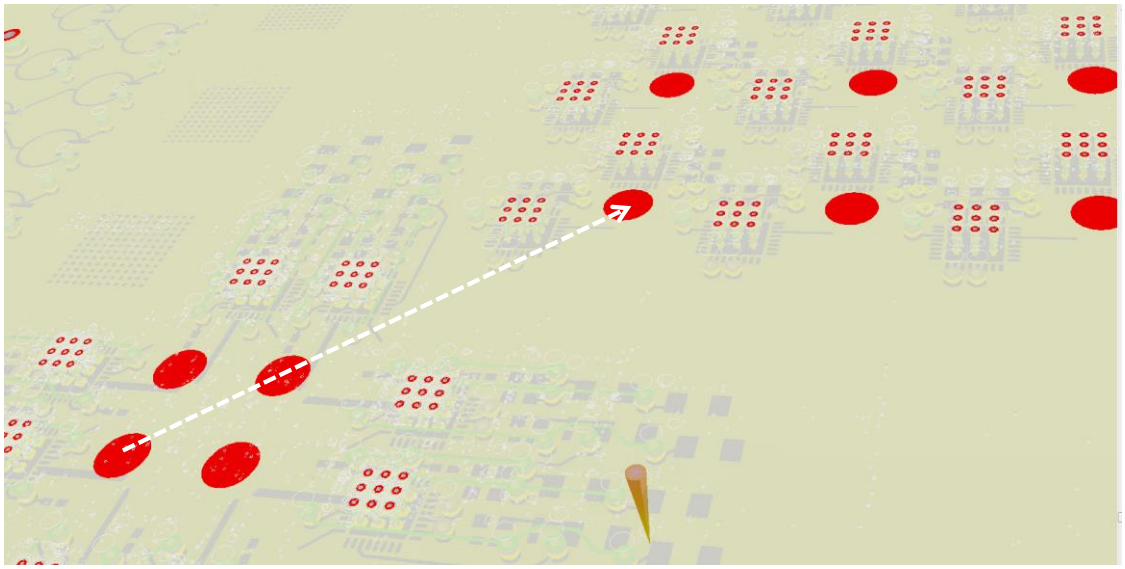

Figure 3.17 – Minimized mutual coupling between transmitter and receiver elements.

Mutual coupling between receiver elements, which is illustrated in Figure 3.18, is reduced because the design has increased the spacing between receiver elements.

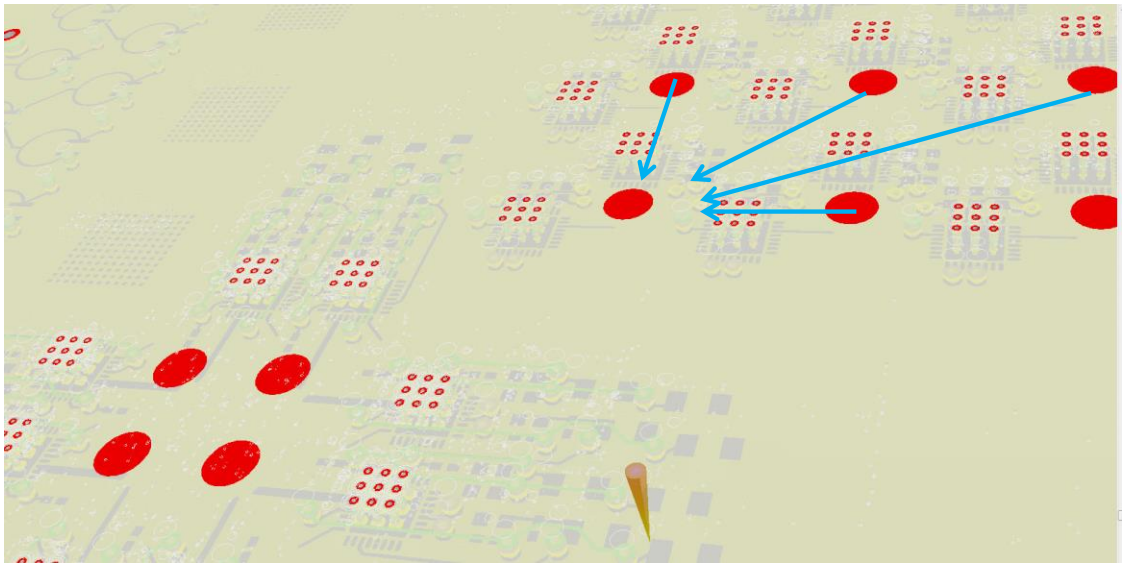

Figure 3.18 – Reduced mutual coupling between receiver elements.

Mutual coupling between transmitter elements, which is illustrated in Figure 3.19, causes a single transmitter element to become an array of four, causing the beam to squint and causes asymmetries in the beam pattern in the E and H planes. This has been discussed previously in Section 3.5.1.

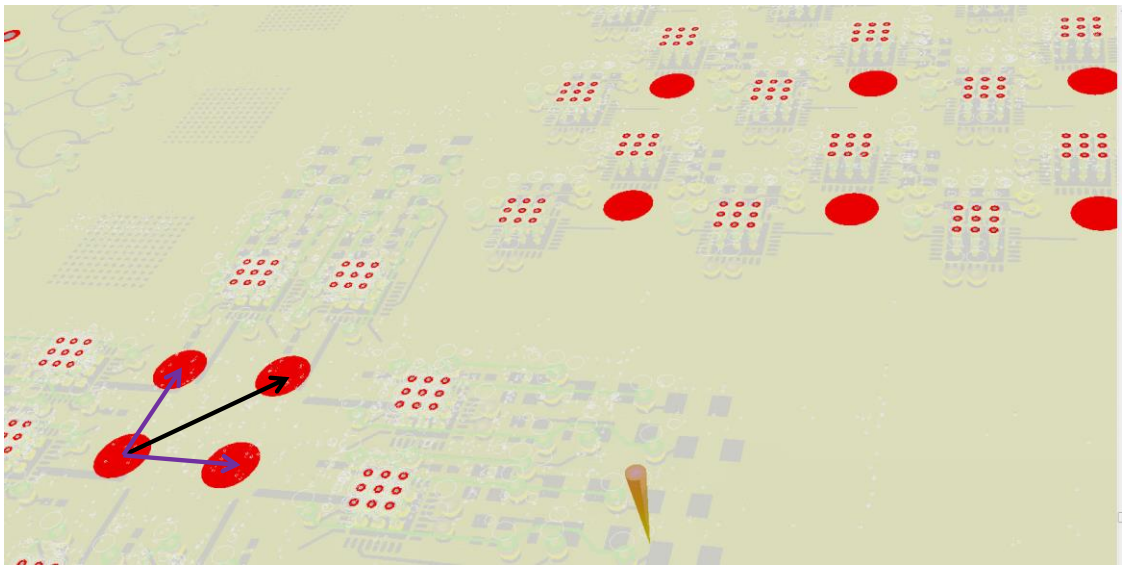

Figure 3.19 – Mutual coupling between transmitter elements.

Therefore, the method using an infinite array model is questionable for the relatively small physical array.

Modelling or measuring of and compensating for mutual coupling in the array is thus difficult and therefore suppression of mutual coupling is a preferred option.

3.6.3 Suppression

In order to determine what means can be used to suppress mutual coupling an understanding of the coupling mechanism is required.

3.6.3.1 Nature of the mutual coupling mechanism

There are several different paths that the mutual coupled signals travel between the array elements. Since the signals are almost pure sine wave at 24 GHz, and the sum of the four coupled sine waves from the four transmitter elements is still a sine wave, with its own phase, which corresponds to an effective delay of R_{kn}. The coupling paths are:

Far Field Wavefront Coupling

This is the effect of periodical loading of a received wavefront by the receiver sub-array. The coupled E field decreases as $1/r$ and since the wavefront is in air, the electrical delay depends only on the geometric separation of the sub-array elements. The amount of wavefront disturbance is greatest for elements aligned along the E field direction [126].

Near Field Coupling

This is due to sub-array elements being within the induction field of each other. It varies as $1/r^2$ for magnetic coupling and $1/r^3$ for electrostatic coupling. Since part of the coupling is through air and part through the substrate material, the delays are influenced by the geometric separation, as well as the dielectric permittivity and magnetic permeability of the substrate [127].

Surface Wave Coupling

This is a mode excited in the radiating layer of the substrate material of the circuit board of the array, which travels partly in air above the top surface, and partly within the dielectric material of the substrate. It is as if the wave were incident at a critical refraction angle for that dielectric. (See Section 3 a further explanation of surface waves and Figure 3.28 for an illustration.) Unfortunately, this means that the wave inside the dielectric reflects from the bottom surface, and depending on the dielectric and its thickness and the frequency, it is possible for it to interfere with itself, resulting in different waveguide mode patterns. The wave spreads in two dimensions out as a cylindrical wave from the centre of each transmitter element, and hence the electric field varies as $1/r^{1/2}$ i.e. $r^{-0.5}$. However, the delay is a function of many variables, including geometric separation, dielectric, and mode number. The surface wave decays more slowly than the others (its decay is equal (similar) to that of the parallel plate mode). This means that surface waves can bounce around a complex circuit board and become focused into hot spots by reflections [128].

Parallel Plate Mode Coupling

Parallel plate mode coupling occurs because circuit board layers below the active patch form a closed or semi-closed waveguide-like structure. The layer just below the radiating layer carrying the array patches, is a dielectric layer surrounded by predominantly ground-plane metallization. The top metallization of that layer has the apertures required for polarization analysis, whilst the bottom metallization has coplanar waveguide feeds. This layer is prone to parallel plate modes, which are simple waveguide modes, propagating cylindrical waves with E field nulls at the metallizations. These modes can be suppressed by suitable vias placed throughout the offending layer. However, if the active elements are close together, these vias may be impossible to implement, or may affect the performance of the active elements, so

these parallel plate modes cannot always be ignored. Their electric field varies as $r^{-0.5}$, just as for surface waves, whilst the delay depends on the dielectric and the mode.

A formal expression for the most significant coupling mechanisms is summarized in the following equation:

$$Z_{ab} = \eta_0 \frac{e^{jk_0 r}}{4\pi} \sum_{n=-1/2,0,1,2} \left\{ \left[\frac{1}{(k_0 r)^{n+1}} \right] \times \left[c_{n,0} + c_{n,2} \cos(2\varphi) + c_{n,4} \cos(4\varphi) \right] \right\} \qquad (3.10)$$

where $n = -1/2$ for surface waves, $n = 0$ for radiation coupling, $n = 1$ for magnetic coupling, $n = 2$ for electric coupling, and $c_{i,j}$ are complex coefficients. Measured plots, see for example Figure 3.21 and the tabulation in Table 3.1 for an actual array which is similar to the one proposed, show perturbations in mutual coupling variation with separation r. These are likely to be caused by the interference between the various coupling mechanisms and their relative phasing and by the excitation patterns of the coupling mechanism. Here the first three spatial (azimuthal) excitation patterns are considered: point source, dipole and quadrupole. It is likely that the patches have very little quadrupole type interaction.

3.6.4 Aperture Orientation

A factor which affects the coupling between array elements is that of orientation. This is identified by the presence of a dependence on φ in Equation (3.10). A reference for φ is the E field orientation. Since the array has dual polarization, each element therefore has a reference E_v and E_h orientation. The concept of orientation for arbitrary polarization is shown in Figure 3.20.

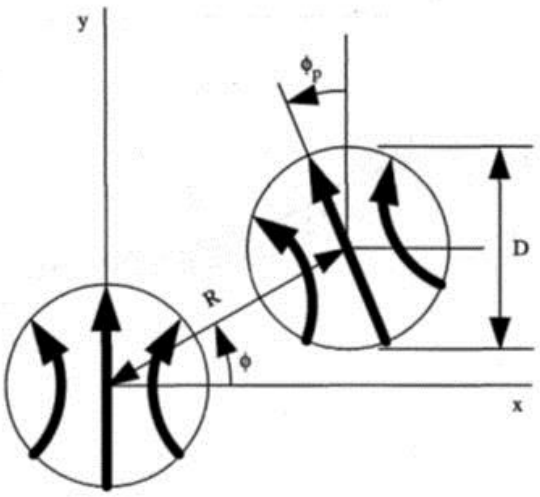

Figure 3.20 – Orientation of circular patches operating in the dominant TE_{11} mode. From [129].

Plots for the measured coupling in the E plane and H plane are shown in Figure 3.21 and calculated and measured values are tabulated in Table 3.1. These are in general agreement with Equation (3.10). The actual exponents of range are -2.75 for H plane coupling and about -1.5 for E plane coupling. For a spacing of $\lambda/2$ the two curves intersect, which means that the interference between nearest neighbours in a rectangular array is the same, regardless of whether the separation is horizontal or vertical. However, this is not true for further elements. Also, this is for a particular substrate thickness. The E plane coupling plot shows interference perturbations, so the suspicion is that there is significant surface wave and/or radiation coupling.

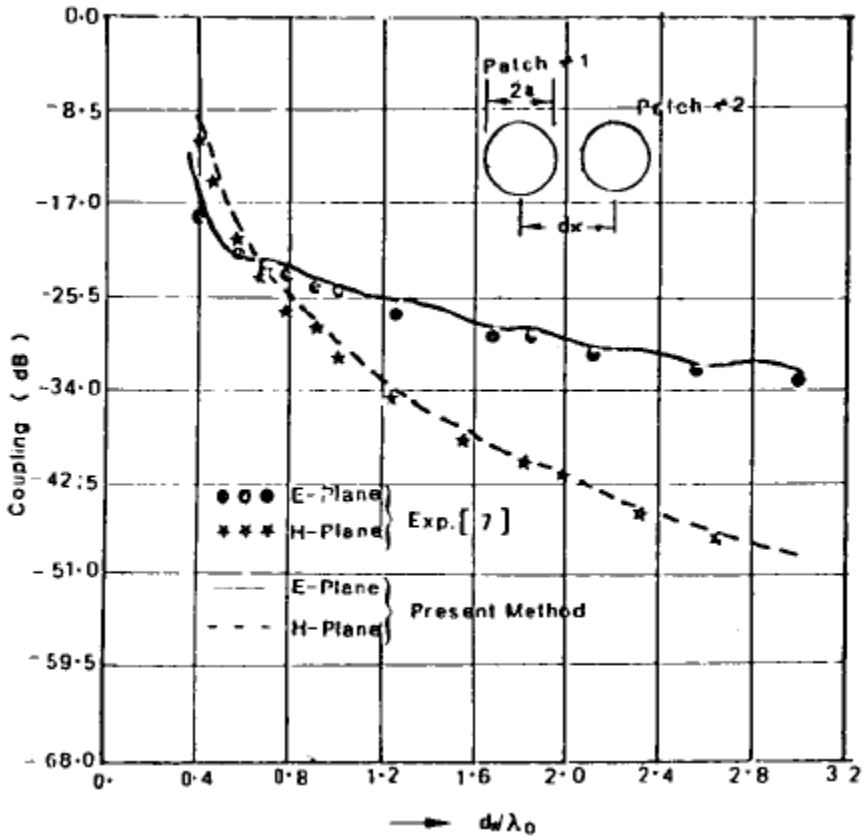

Figure 3.21 – Calculated mutual coupling between two circular microstrip disk antennas as a function of separation with dimensions as given in Table 3.1. From [130].

Element No.	E-plane coupling (in dB)		H-plane coupling (in dB)	
	Calculated	Expt.	Calculated	Expt.
2	-17.0	-16.5	-10.1	-
3	-19.6	-20.0	-18.3	-
4	-21.6	-22.2	-21.6	-
5	-23.9	-24.2	-27.1	-
6	-26.8	-25.8	-30.7	-
7	-29.4	-27.0	-34.3	-
8	-31.4	-30.5	-36.9	-

$2a = 1.86$ cm, $d = z' = 0.16$ cm, $\epsilon_r = 2.5$, $\tan(\delta) = 0.002$, $f_0 = 5.6375$ GHz, element spacing, $d_x = 2.24$ cm.

Table 3.1 – Measured coupling between elements of an eight element linear microstrip disk array with leftmost element excited. From [130].

The mechanism of radiation coupling through wavefront loading is illustrated in Figure 3.22. Other plots show the intersection occurring for other separations, which tends to support the view that other coupling mechanisms may contribute, depending on substrate thickness and material properties.

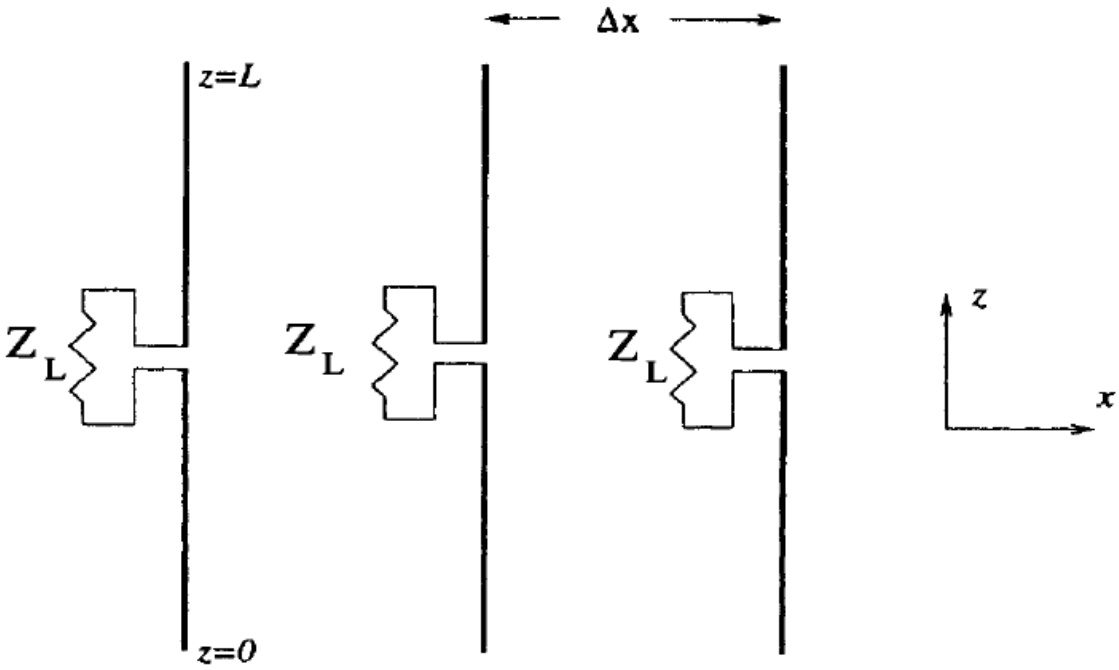

Figure 3.22 – Radiation loading of elements on a wavefront. From [126] p. 104.

Figure 3.23, Figure 3.24 and Figure 3.25 from [131] shows that the coupling at a skew angle of 53˚ is about 8 dB lower than that for E plane coupling and about 2 dB lower than H plane coupling. Unfortunately the plots do not extend down to a spacing of $\lambda/2$, but it is unlikely that the improvement disappears.

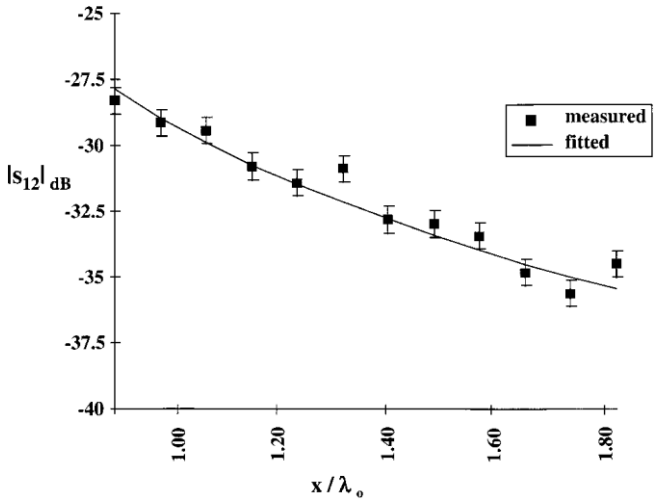

Figure 3.23 – E plane mutual coupling. From [131].

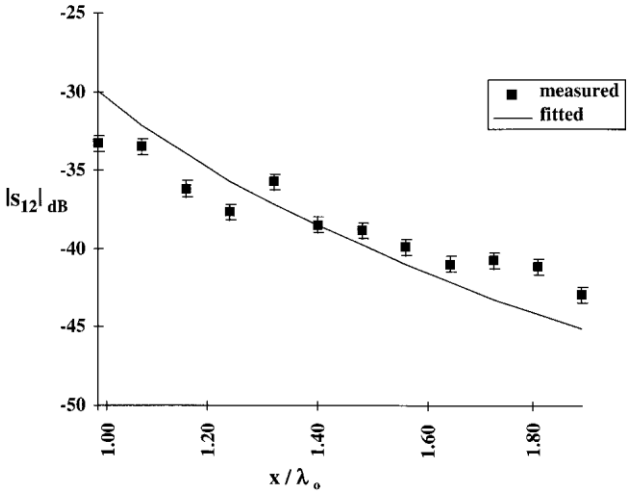

Figure 3.24 – H plane mutual coupling. From [131].

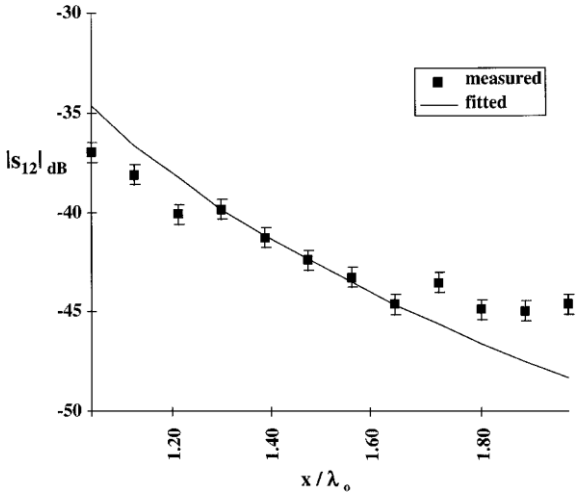

Figure 3.25 – Mutual coupling at θ = 53˚. From [131].

Therefore, by angling the coupling apertures at 45˚ from the principal axes of the array lattice, significant reduction of mutual coupling can be expected, at no cost. Both radiating apertures which feed each element benefit from this reduction. It is likely that the reduction in mutual coupling occurs because in this arrangement, the dipoles are further apart, never end to end, and displaced laterally, so that the near field coupling occurs at a greater range. For the end to end arrangement for the patches (diameter = 3.7 mm) and spacing of 6.2 mm the spacing between the closest poles belonging to adjacent dipoles is 2.5 mm. For the skewed arrangement at 45˚ this spacing is larger, 4.4 mm, with a predominant H plane coupling. From

the inverse square law, one would expect a reduction of the coupling electric field by a factor of 3.18 or 10 dB, which is in approximate agreement with the experimental data for larger separations [131]. It is likely that the skewed arrangement reduces the radiation coupling for similar reasons. For the end to end dipole arrangement, the wavefront is loaded along an electric field line for the length of the array.

In a skewed arrangement, the loading is distributed better. This suggests that the apertures in the receiver sub-array should be tilted at 45˚, and for consistency, so should the transmitter sub-arrays. It should be noted that once an array is constructed, this skewed arrangement does not avoid end to end (E plane) coupling. This occurs between diagonal neighbours. However, the electrical spacing between these is $\lambda/\sqrt{2}$ instead of $\lambda/2$. Hence, according to the inverse square law, the coupling should be suppressed by $20\log 2$ i.e. 6 dB.

3.6.5 Surface Waves

For close transmitter element spacing of $\lambda/2$, surface wave coupling is weaker than the other coupling mechanisms in most circuit boards. However, it is the slowest to decay with distance along the interface, varying as $r^{-0.5}$and may be significant. This may be exacerbated by reflections at the edges of the board. Therefore, some attention is required to minimize the effect. They can be excited in dielectric slabs and in slabs with a groundplane, such as the top layer. They can also exist in open waveguides which will be explored in detail in the Chapter 4. Note also that surface waves are solutions to the inhomogeneous wave equation, and present field components which attenuate exponentially with distance from the dielectric interface, see Figure 3.26.

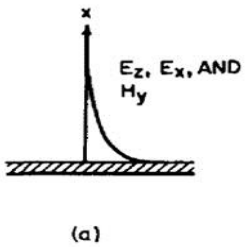

Figure 3.26 – Variation of electromagnetic fields with height above the dielectric surface. From [132].

The isoclines for a surface wave mode on a circuit board are shown in Figure 3.27. This figure correctly shows the significant bending of the isoclines at the interface between the circuit board and air.

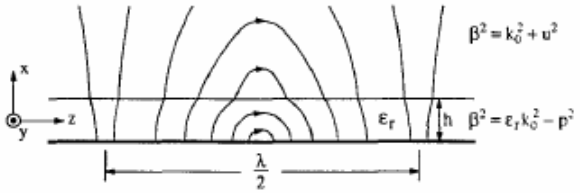

Figure 3.27 – *E* field patterns along the direction of propagation for the lowest order mode, TM_0, where the magnetic field inside the dielectric is transverse (into the page) and constant. From [132].

Fooks and Zakarevicius [132] suggest that the surface wave is a result of the superposition of two totally internally reflecting waves in the dielectric, incident at or near the critical refraction angle, see Figure 3.28. This may be misleading, because regular waveguide modes, including the parallel plate modes can also be represented this way, and they have totally different boundary conditions.

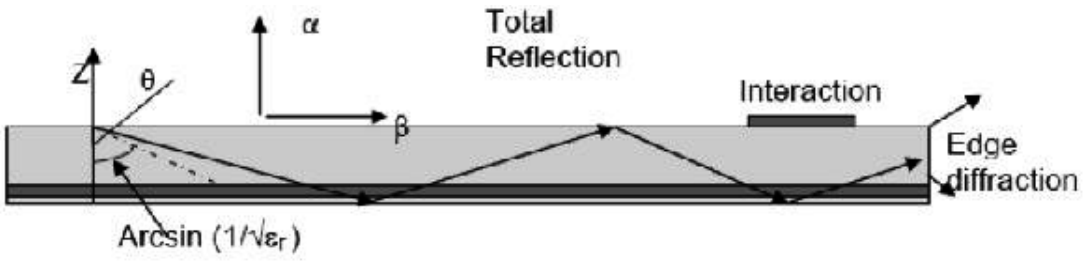

Figure 3.28 – Physical interpretation of surface waves. From [128].

The *TE* surface wave mode has an electric field null at the ground plane and a maximum at the dielectric-air surface, whilst waveguide modes have nulls at both surfaces [132]. Both modes can coexist in the dielectric, if the thickness and dielectric constant permit these boundary conditions to be satisfied.

These boundary conditions require that the electric and magnetic thickness of the substrate be larger than an integer multiple of $\lambda/2$ for waveguide modes, an odd multiple of $\lambda/4$ for *TE* surface wave modes, and an even multiple of $\lambda/4$ for *TM* surface wave modes. The radiation loss for a particular resonance, and that the loss decreases with decreasing thickness and with decreasing dielectric constant, is shown in Figure 3.29.

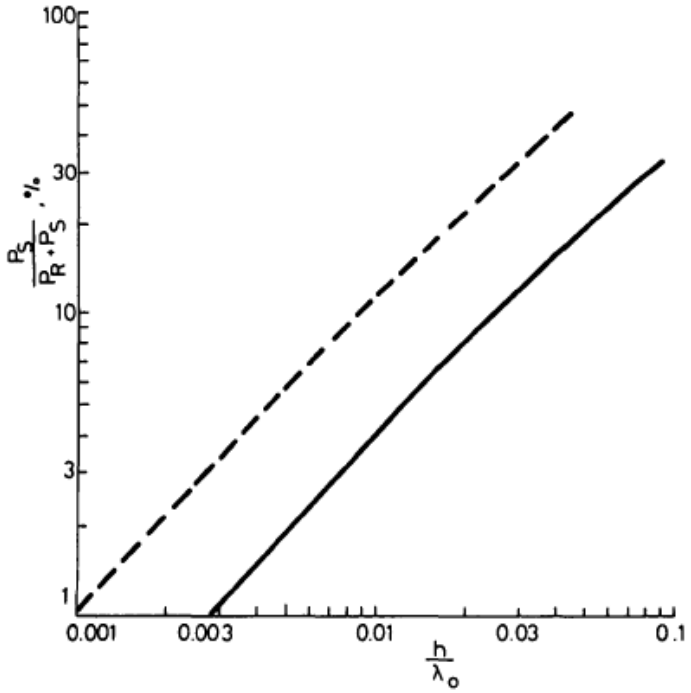

Figure 3.29 – Surface wave coupling versus substrate thickness. From [133].

However, this still leaves the suppression of the dominant TM_0 surface wave, which has no cut-off [132]. Three methods have been devised to achieve this.

1. Place some metallization on the top face, and remove some from the groundplane. Special patterns are involved here. These are designed to mimic

photonic or electromagnetic bandgap materials, so that the propagation wave-vector for the dominant TM_0 surface wave mode is in the forbidden region and hence the mode cannot propagate, see [134].

2. The TM_0 surface wave mode can also be suppressed by placing vias between the two metallizations. This is a widely applied technique in microwave layouts [135].
3. A similar effect can be achieved by introducing artificial defects in the groundplane alone. The technique is called defected groundplane, see [136].

Methods 1 and 2 are not attractive for this application, principally because the most vulnerable array, the receiver array, even with the increased spacing described here, still doesn't have enough space between elements to introduce such structures. In addition, it is not known what field disturbances will be produced by extra metal in the top layer and extra apertures in the groundplane, in such close proximity to the active elements. Also, it is not known how holes in the groundplane will affect the layer beneath it, which carries the coplanar waveguide feeds, and an extra groundplane layer would be required.

A factor which has been overlooked in this analysis is the presence of the superstrate layer, or a radome layer which may also be required for protection. These may support their own surface wave modes, or may modify the propagation of existing surface waves. Some theory for multilayer surface waves is available, but this has not been pursued.

3.7 Millimeter Wave Array for UAV Imaging MIMO Radar

3.7.1 Introduction

High resolution imaging radars at millimeter-wave frequencies for obstacle avoidance for UAV utilize a large antenna aperture and sequential mechanical scanning of the aperture to form images with high fidelity [99]. Planar arrays are an attractive alternative. They do not require mechanical scanning, and images are formed digitally using beamforming techniques [123].

To achieve image quality comparable to mechanically scanned radars, fully populated arrays require inordinate numbers of elements. These are costly, a challenge to design, and difficult to produce. Thinned or sparse arrays are a potential solution to this problem. MIMO techniques are an efficient method of thinning an array using spreading sequences to create an overlay of paired transmitter and receiver elements, without sacrificing image quality. The use of MIMO techniques to thin an array is a relatively recent development [106]. To be of practical use at millimeter-wave frequencies, MIMO techniques require the development of novel array geometries and architecture. This research presents designs for the implementation of millimeter-wave planar arrays which have been thinned using MIMO techniques and considerers the limitations on the length of spreading sequences due to the increasingly pronounced effect of Doppler at higher frequencies. These considerations have led to the first instance of the use of the Moreno-Tirkel sequence Family B [100] for high resolution imaging radar.

In-flight, the returns a UAV radar receives consist mainly of aerial targets with some ground returns. As the UAV's velocity relative to the ground is known, stationary ground clutter can be rejected by range gating and Doppler processing. During take-offs and landings though, the UAV radar receives mostly ground returns which cannot be readily discriminated from targets. Nonetheless, 94 GHz mechanically scanned UAV radar has been shown to provide high quality images in real-time suitable for avoiding fixed and moving obstacles in fog, dust, or sand, and for detecting and locating hazards with small cross-sections such as overhead power lines. For UAV obstacle avoidance [99], it is desirable to have an array with resolution as shown in Figure 3.30, and sidelobe suppression as shown Figure 3.31. These figures were created using the Fazar program [119].

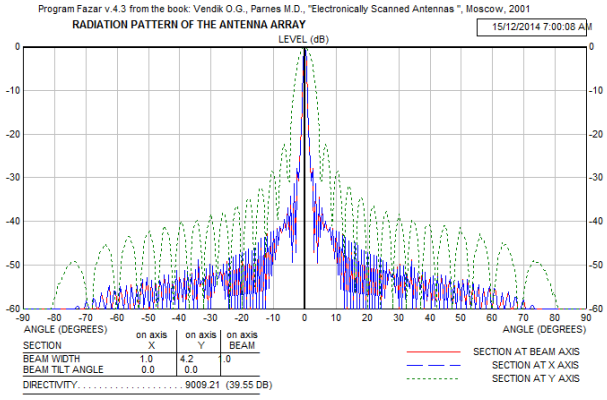

Figure 3.30 – Pattern Optimized for Resolution.

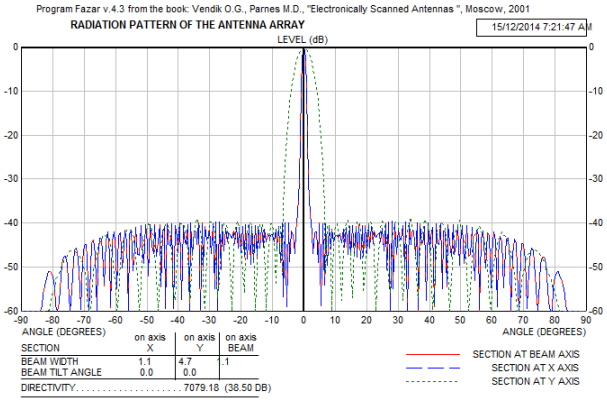

Figure 3.31 – Pattern Optimized for Sidelobe Suppression.

3.7.2 Rationale for MIMO Techniques for Array Thinning

MIMO techniques are an efficient method of thinning phased arrays using spreading sequences to create an overlay of paired transmit-receive elements, without sacrificing image quality. The principal advantage of a MIMO overlay or virtual array is the effect that the overlay has on the gain and the reduction in physical elements in the array. The processing gain due to the use of a spreading sequence under ideal conditions with no interference from any other spreading sequence is $10 \log L$ dB, where L is the sequence length, and the gain due to beamforming of a fully populated array is $10 \log N$ dB, where N is the number of transceivers in the array. However, the introduction of a MIMO overlay transforms N transmitter and N receiver physical elements into a virtual array of N^2 virtual transmit-receive

elements. Therefore, introducing a MIMO overlay transforms $2N$ physical elements of a fully populated array into N^2 elements of a virtual array. The effect on the gain of the array is illustrated with the following example. The signal-to-noise (SNR) improvement of an N element array over a single array element is $10\log N$ dB. With the MIMO overlay, the SNR improvement over a single array element is $10\log N^2 + 10\log L$ dB. Hence, squaring of N, now the number of virtual array elements, is a doubling, in dB, of the gain ($20\log N$ dB), and is in addition to the coding gain of the spreading sequence used ($10\log L$ dB). This analysis assumes ideal conditions – perfect element radiation efficiency, no mutual coupling and no effects from aperture tapers. Also, a filled transmitter array produces higher power density on target, whilst in a MIMO array the physical power density is much lower. These implementation issues and a tradeoff between a MIMO and a filled array will studied in the following sections.

A further advantage of the MIMO overlay is that target motion can be captured, as all transmit-receive element pairings are formed simultaneously, and all beamforming and Direction of Arrival (DOA) processing can be performed digitally at the back-end of the array [104]. This investigation does not consider DOA processing further.

3.7.3 Practical MIMO Arrays for Imaging Radar

The feasibility of constructing MIMO transmitter and receiver arrays at strategically important millimeter-wave frequencies for high resolution imaging radar is examined. At the lowest frequencies, it is possible to consider constructing the arrays out of unit cells, but this is problematic as the physical spacing between antenna elements decreases at higher frequencies, and it becomes difficult to fit the transmitter and receiver components and layout tracking into such small unit cells. In fact, passive components required for local oscillator distribution have to be embedded in internal layers. Some relevant parameters and details are summarized in Table 3.2 below.

Allocation GHz [137, 138]	ISM	RAIN ATT'N 5mm/hr [139]	UNIT CELL	LTCC	MAX PERIOD @200km/hr	MMIC SUPPLIERS
24.00-24.25	Y	0.6	Y	N	2698	HITTITE/ AVAGO
35.50-36.00	N	1.2	Y	Y	1821	HITTITE/ AVAGO
61.00-61.50	Y	2.6	N	Y	1062	GOTMIC
77.50-78.00	N	3.2	N	Y	840	GOTMIC/ NORTHROP
92.00-94.00	N	3.7	N	Y	700	GOTMIC/ NORTHROP

Table 3.2 – Millimeter-wave bands and some relevant parameters and details.

The schematic for a four element (2×2) transmitter unit cell for 24 GHz is shown in Figure 3.32. Each transmitter consists of two SPDT switches which select either a signal path with a minimum delay, or a path with a delay of $\lambda/2$. This permits differential-BPSK modulation of the carrier frequency.

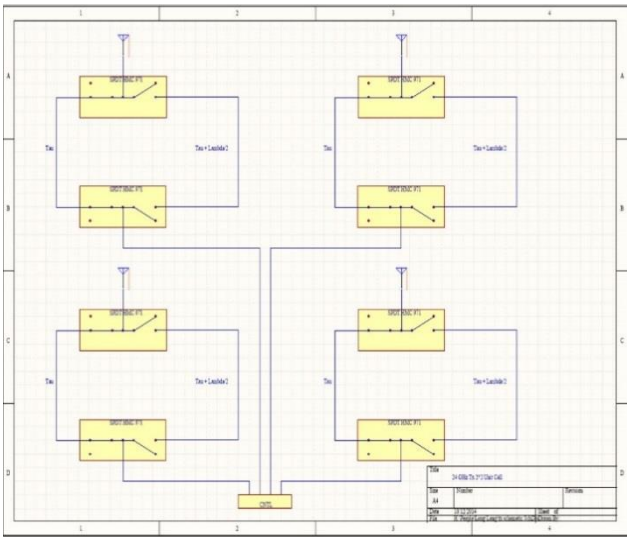

Figure 3.32 – 2×2 Transmitter Unit Cell Schematic.

The schematic for a four element (2×2) receiver unit cell for 24 GHz is shown in Figure 3.33. Each receiver consists of an LNA, IQ mixer, IF amplifier and a high-speed ADC. The multi-channel ADC in Figure 3.33 is followed by a FFT-based parallel correlator, which is being designed for FPGA implementation, and not shown here.

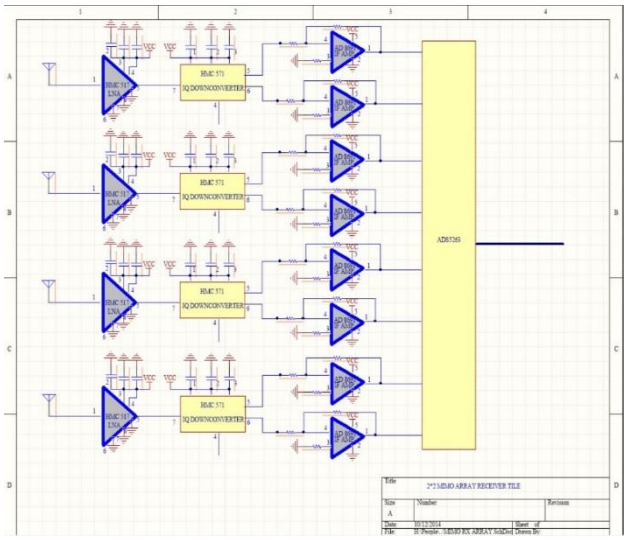

Figure 3.33 – 2×2 Receiver Unit Cell Schematic.

The layout for a four element (2×2) transmitter unit cell for 24 GHz is shown in Figure 3.34. The substrate material is alumina. The red rectangles are the rectangular transmitter element patches and the blue rectangles are the HMC971 switches for the bi-phase modulation as shown in the transmitter unit cell schematic in Figure 3.32.

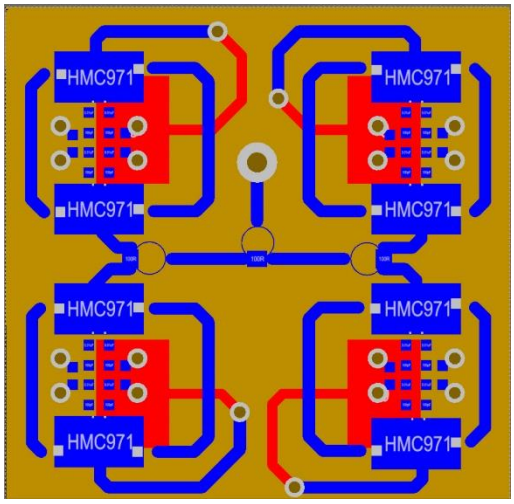

Figure 3.34 – 2×2 Transmitter Unit Cell Layout.

The layout for a four element (2×2) receiver unit cell for 24 GHz is shown in Figure 3.35. The substrate material is alumina. The red rectangles are the rectangular receiver element patches and the blue rectangles are HMC517 LNA's and HMC571 IQ downconverters as shown in the receiver unit cell schematic in Figure 3.33

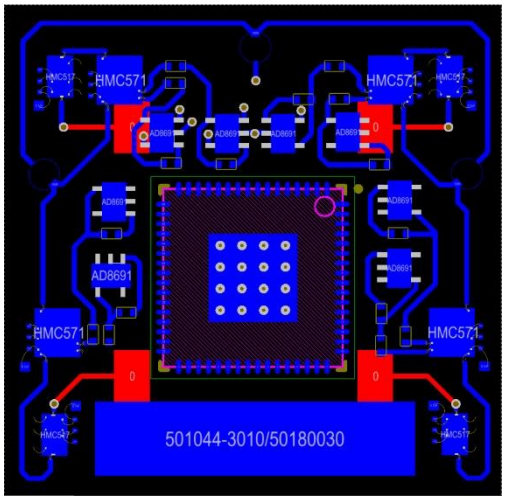

Figure 3.35 – 2×2 Receiver Unit Cell Layout.

A preliminary floor plan for a complete array for a 94 GHz imaging radar showing all transmitter elements, all receiver elements, all SPDT switches, all LNA's, IQ mixers, IF amplifiers and all multi-channel ADC's for an array with 8×8 transmitter elements, and four

8×2 receiver elements, shown in red, to yield an array of 4096 virtual elements is shown in Figure 3.36.

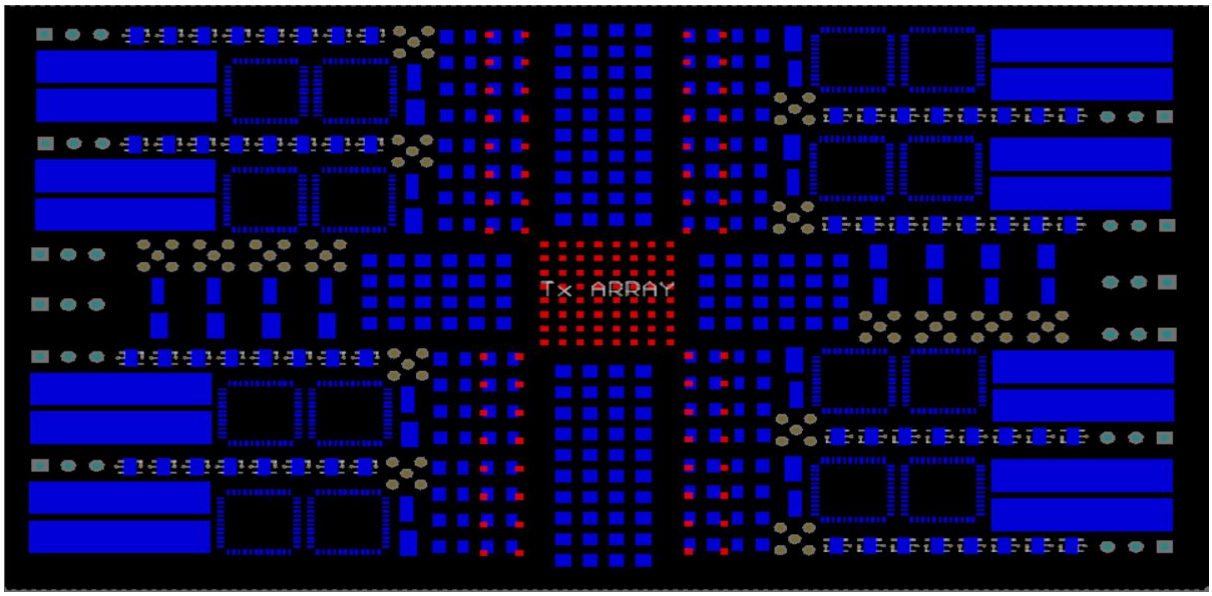

Figure 3.36 – 94 GHz MIMO Array preliminary floor plan. The virtual array has 4096 elements.

3.7.4 Selection of Spreading Sequences for UAV Imaging MIMO Radar

In a MIMO overlay or virtual array, the purpose of the spreading sequences is to provide adequate signal isolation between all the transmitting elements, and to provide range discrimination. An effect which becomes more pronounced at higher frequencies is the Doppler effect. This limits the period of the spreading sequences and makes it more difficult to construct a sufficiently large family of sequences for UAV imaging MIMO radar for obstacle avoidance.

The selection of receiver hardware and MIMO spreading sequences is challenging in this case, because the relative motion between a UAV and targets may be very high. For a UAV speed of 200 km/h ≈ 60 m/s, the carrier phase drifts beyond 90^0 after 7 µs at 94 GHz, so the code correlation calculation must be performed more quickly than this, unless dedicated Doppler processing is included. Time-frequency processing for rapid acquisition of GPS signals has recently been described in [140]. If implemented, it would permit the use of longer spreading

sequences, or accommodate higher UAV speeds. Doppler processing will be considered in future research.

If the ADC sample rate is 160 MHz, the fastest square wave that can be sampled without aliasing is around 50 MHz, which corresponds to a chip duration of 10 ns. Consequently, the longest possible sequence length is around 700 chips. In order to generate a virtual array of size 4096, the number of sequences required is the square root of the size of the array i.e. 64.

There are four potential sequences which could be used in this application. Complete Complementary Codes (CCC), Zero Correlation Zone (ZCZ) sequences or Low Correlation Zone (LCZ) sequences, small or large Kasami sequences, or the Moreno-Tirkel sequences. CCC requires multiple code periods to accumulate enough correlations which add to zero. Target Doppler causes imperfect cancellation. ZCZ and LCZ sequences have poor correlation outside the zero or low correlation zone, restricting the unambiguous range. The number of codes and the length of the correlation zone determines the code period. For a ZCZ or LCZ sequence of 500 chips, corresponding to 500 range gates, the period of the sequences is excessive because the carrier phase would become decorrelated for a chip rate of 10 ns. ZCZ and LCZ sequences are also inefficient in time. Kasami sequences are available for lengths 2^{2k-1} which are too sparse, and the small set has insufficient family size, while the large set has inferior auto and cross-correlation.

In [100], a binary sequence construction quadratic shift polynomial called Family B is presented. These sequences are of length $L = p(p+1)$ where p is a prime of the type $4k-1$. For a quadratic shift polynomial, the Moreno-Tirkel sequence Family B contains $p-1$ sequences with off-peak autocorrelation and all pairwise cross-correlation taking on the values $-(p+1), 0, (p+1)$. The post-correlation SNR for a single sequence is approximately p. In order to satisfy the Doppler criterion, set $p = 23$. One such sequence is shown in Figure 3.37.

1,-1,1,-1,1,1,1,1,1,-1,-1,1,-1,1,1,-1,-1,-1,-1,-1,1,-1,1,-1,1,1,-1,1,-1,-1,-1,1,-1,-1,-1,1,-1,1,1,1,1,1,-1,-1,-1,1,1,-1,1,1,-1,-1,1,-1,-1,1,1,1,1,-1,1,-1,
-1,1,-1,1,-1,-1,1,-1,1,-1,1,-1,-1,1,-1,1,1,-1,-1,1,1,-1,-1,1,-1,1,1,-1,1,-1,1,-1,1,-1,1,-1,-1,1,1,-1,1,1,-1,1,-1,1,1,-1,1,1,-1,-1,1,1,-1,-1,-1,-1,-1,1,1,
-1,1,1,-1,-1,-1,1,-1,-1,-1,1,1,1,-1,1,1,1,-1,-1,1,-1,1,1,1,-1,-1,-1,-1,1,-1,1,1,1,-1,1,-1,-1,-1,-1,1,1,1,1,-1,-1,-1,-1,1,1,-1,-1,1,1,1,-1,-1,-1,-1,-1,-1,1,
-1,1,1,1,1,1,1,-1,1,-1,1,1,1,-1,-1,-1,1,1,1,-1,-1,-1,1,-1,1,-1,-1,1,-1,1,1,-1,1,1,1,-1,1,-1,1,-1,1,-1,-1,-1,1,1,-1,1,1,-1,1,-1,-1,1,-1,-1,-1,-1,-1,-1,-1,1,
-1,1,1,1,-1,-1,1,1,1,1,1,-1,-1,1,1,1,-1,-1,-1,1,1,1,-1,1,-1,1,1,1,-1,1,1,-1,-1,-1,1,-1,1,-1,-1,-1,1,-1,1,-1,-1,-1,1,1,-1,-1,-1,-1,-1,1,1,-1,-1,
-1,1,1,1,1,1,1,1,-1,1,-1,1,1,-1,1,-1,-1,1,-1,1,1,1,1,-1,1,-1,1,-1,1,-1,-1,-1,-1,-1,-1,1,-1,1,1,1,1,-1,1,1,1,-1,-1,-1,1,1,1,-1,-1,-1,1,-1,-1,-1,-1,-1,-1,-1,
-1,1,-1,1,1,1,1,1,1,1,-1,-1,1,1,-1,-1,1,1,-1,1,1,-1,-1,-1,1,1,1,1,-1,1,-1,-1,-1,1,-1,1,1,1,1,-1,-1,-1,-1,-1,1,1,-1,-1,-1,1,-1,-1,-1,1,1,1,-1,1,1,1,-1,-1,1,1,
-1,1,-1,1,1,1,1,-1,1,1,-1,-1,1,-1,-1,1,-1,1,-1,-1,1,-1,-1,1,1,-1,-1,-1,1,-1,1,1,1,-1,-1,1,-1,1,1,-1,-1,1,1,-1,-1,1,-1,1,1,-1,-1,-1,1,-1,1,1,-1,1,-1,1,1,-1,1,
-1,1,-1,-1,1,1,-1,1,1,-1,-1,-1,-1,-1,1,1,1,-1,-1,1,-1,-1,1,-1,1,1,1,-1,1,1,1,-1,1,-1,-1,-1,-1,1,-1,1,1,1,1,1,-1,-1,1,-1,1,1,-1,-1,-1,-1,-1,1,-1,1,1,-1.

Figure 3.37 – Binary Sequence Family B Quadratic Shift Polynomial of length 552 *(p=23)*.

The periodic autocorrelation for the sequence, plotted as an array, is shown in Figure 3.38.

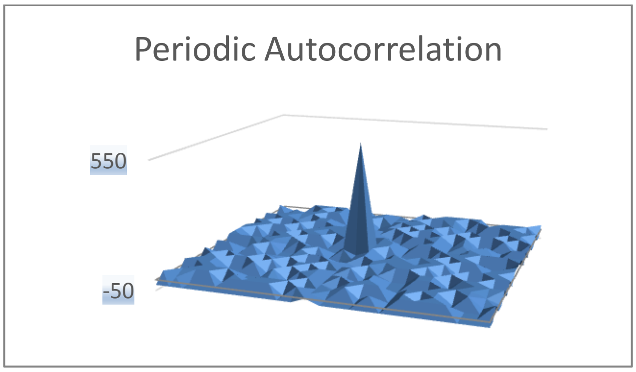

Figure 3.38 – Periodic autocorrelation: Binary Sequence Family B Quadratic Shift Polynomial of length 552 *(p=23)*.

This family provides 22 sequences of the 64 required for the 8×8 transmitter array. To provide the remaining 42 sequences, cubic shift polynomials need to be used. These have an additional auto and cross-correlation value of $2(p+1)$. With all 64 transmitter elements modulated by this combination of sequences, the expected SNR after correlation is +3.4 dB. The beamforming gain of a 4096 element virtual array is 36.12 dB. Under ideal conditions, the expected SNR due to self-interference of the spreading sequences is almost 40 dB.

3.7.5 Summary

This research presents a rationale for using MIMO techniques to thin an array without sacrificing image quality, and the concepts behind the MIMO overlay or virtual array. Designs of practical MIMO arrays for imaging radars at millimeter-wave frequencies and an analysis of spreading sequences suitable for UAV imaging radar have been presented. The considerations here have led to the first application of the Moreno-Tirkel sequence Family B for high-

resolution imaging MIMO radar for UAV obstacle avoidance. The geometry and architecture presented in here can be extended to higher frequencies in the future.

3.8 Conclusion

The problem investigated in this chapter has been the design of a radar suitable for the imaging of termites. The study commenced by briefly reviewing the earlier work in developing a radar for detecting termites [97] which lead to the commercialization of a product, Termatrac®. It then, also briefly, discuss applying phased array techniques to detecting termite activity over a large part of a wall and to imaging the activity using a hybrid array consisting of a receiver sub-array to image termite activity over a wide area at long range, and a second receiver sub-array to detect termites in a small area with high resolution [95, 98].

To overcome the impractical need for a large number of elements of the hybrid array, the chapter introduced the design for a new imaging array which uses MIMO array synthesis techniques. To the author's knowledge this is the first time these techniques have been used for a two dimensional imaging radar, and for imaging termite activity.

The study discussed in detail the geometric pairing that occurs between each transmitter element and every receiver element and considered the impact and design tradeoffs of transmitter and receiver spacing. A design aim has been to maximize intra-element spacing so far as is possible, with a view to minimizing mutual coupling between elements, while not introducing gaps in the coverage. In this, the design demonstrated the advantages of maximizing the receiver element spacing over the transmit element spacing. The study has discussed at some length various aspects of mutual coupling and provided a floor plan for the design of the array which embodies the principles that have been investigated in this chapter.

The proposed MIMO array provides the capability to image termite activity so that a complete wall can be inspected rapidly. This image will enable an operator to quickly determine an area

of activity and change over to high resolution mode and track termites back to the nest, where eradication treatment can to be delivered. The MIMO overlay is essential in reducing the number of physical elements, spacing the elements further apart, forming beams in parallel, suppressing mutual coupling by cancellation, and permitting the image to be formed in real time.

Variations of such the array presented here can be applied to through the wall radar, medical imaging, security screening and non-destructive testing.

In Section 3.7, new designs to address the problem of imaging radar for Unmanned Aerial Vehicles, which embody many of the principles examined in this chapter have been presented. In these designs the position of the transmit and receive elements are transposed to minimize mutual coupling between receiver elements. These designs are the first instance of the use of the Moreno-Tirkel sequence Family B [100] for high resolution imaging radar.

This page has intentionally been left blank.

4 Artificial Dielectric Open Waveguide

4.1 Introduction

Motivated by the intriguing possibilities of millimeter wave cellular and higher level biological interactions, as discussed in Section 2.5, and the potential to terminate termites, or to alter their social behavior, as reported in experiments in Section 2.7, a design of an acupuncture-like needle for the efficient delivery of millimeter waves through the skin will be studied in this chapter. Two of the facets that will make this study unique are the investigation of the excitation of the HE_{11} mode on the conductor-like needle and the study of the potential for propagation of the TM_{01} mode and the HE_{11} mode on the needle with low loss.

In this chapter, the problem of the existence, the excitation and the propagation with low loss of the HE_{11} mode on a conductor will be studied. Contrary to prevailing understanding, it will be shown that a bare conductor can sustain two dominant modes: the well-known symmetric TM_{01} mode, and the asymmetrical HE_{11} mode, which hitherto has been overlooked and forgotten due to early analysis [141, 142] which concluded that higher order modes are highly damped by eddy currents and do not propagate [143, 144] or that hybrid modes cannot exist at all on a bare conductor [145, 146]. The HE_{11} mode has two main lobes separated by nulls, i.e. is asymmetrical in the azimuthal plane. This enables the selective delivery of power to tissue in preferred directions by appropriate positioning of the two lobes, whilst avoiding others by the positioning of the nulls. Unlike the TM_{01} mode, it will be shown that the HE_{11} mode can propagate on a bare conductor as a pair of orthogonally polarized modes, enabling polarization sensing and control. However, as both modes are dominant, exciting the HE_{11} mode is a challenge. It will be shown that the HE_{11} mode can be made to propagate on a conductor with low loss. However, loss in the conductor to support the propagation of the mode is essential, and unavoidable.

This study will describe the nature of the electric and magnetic fields at an interface between to media and the conditions for establishing fields on a conductor. If the conductor has finite conductivity then the finite conductivity of the conductor results in the current producing an ohmic potential drop and hence a small tangential field within the conductor. This closes the E field loop, which by Ampere's Law, induces an orthogonal magnetic field in or out of the page, if it is assumed that the E field loop is planar with the page, and thereby permits the continuation of the propagating mode.

This study will then examine the TM_{01} field mode and show how it has zero cutoff because there is no azimuthal dependence of the current and hence no frequency dependence. It will also be shown how the HE_{11} field mode has zero cutoff because the azimuthal dependence can be induced by interposing a perfectly conducting sheet down the middle of the waveguide. This study will also explained why higher order modes have a cutoff frequency.

Numerical studies will demonstrate the design of a structure to launch the HE_{11} mode onto an acupuncture-like needle. Experiments at microwave frequencies will be made which measure the HE_{11} mode propagating on the conductor. In these experiments the measured nulls in the HE_{11} mode are shown to be more than 20 dB deep.

This study will then investigate the possibility of removing the requirement for losses in the conductor to support either the TM_{01} mode or the HE_{11} mode, by coating a bare conductor with an artificial dielectric having negative permittivity, which can support the lossless Fano mode [147], and propagating both TM_{01} and HE_{11} modes with no ohmic conductor losses.

Contrary to that which has been known or demonstrated previously [143-146], this study will demonstrate that an acupuncture-like needle can sustain the propagation of the two dominant modes, and that an artificial dielectric coating can lower or avoid losses. This

phenomenon is frequency independent and does not depend on the circumference of the conductor.

4.2 TM_{01} Mode

The focus of this section will be on a discussion of the TM_{01} mode [148].

The E and H field patterns at an interface are shown for the TM_{01} mode in Figure 4.1.

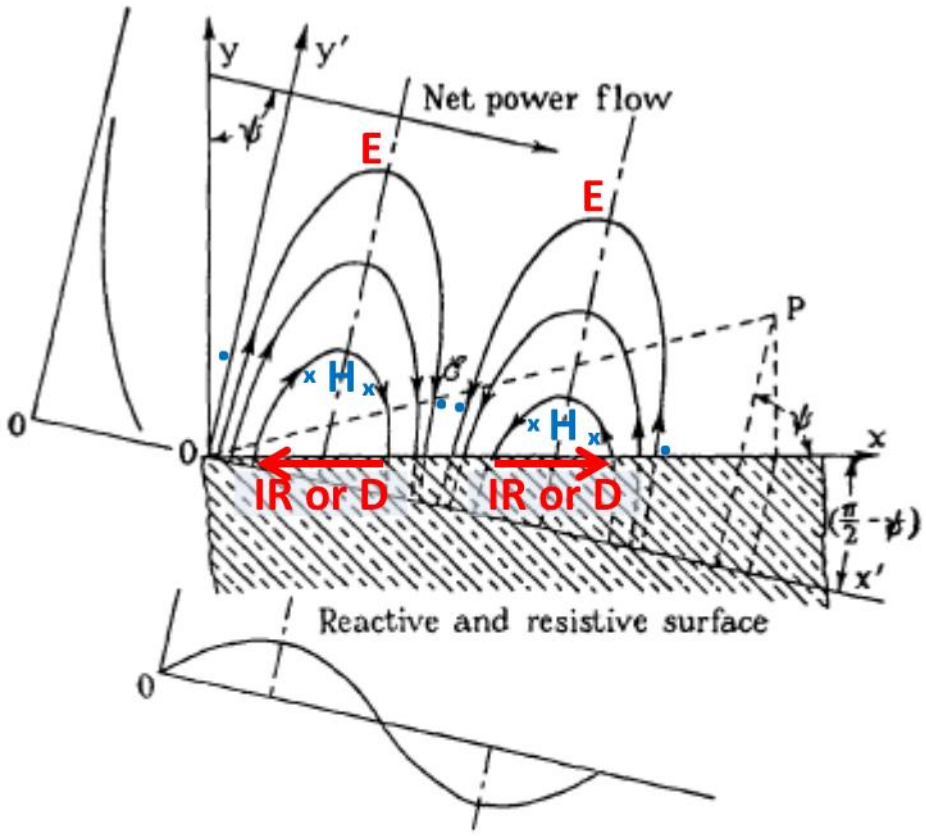

Figure 4.1 – TM_{01} mode sinking into a lossy surface. Adapted from [149].

Each solitary E field loop is tilted slightly forwards in the direction of propagation, so that there is a tangential component at the interface of the surface causing a power loss. The power loss is required to support propagation of the wave.

This is the field pattern for all TM01 modes:

1. Cartesian plane i.e. Zenneck wave [148, 149].

2. Radial plane. Only the spherical variant is plausible e.g. a dipole above a sphere such as the Earth. Mie and Watson studied this problem as discussed in Chapter 2. This wave will not be considered further.
3. Cylindrical e.g. Sommerfeld and Sommerfeld-Goubau waves [148, 149].

All mode field patterns are conformal transformations of each other.

For the sake of simplicity and without loss of generality, consider the circular geometry such as a smooth conductor, see Figure 4.2.

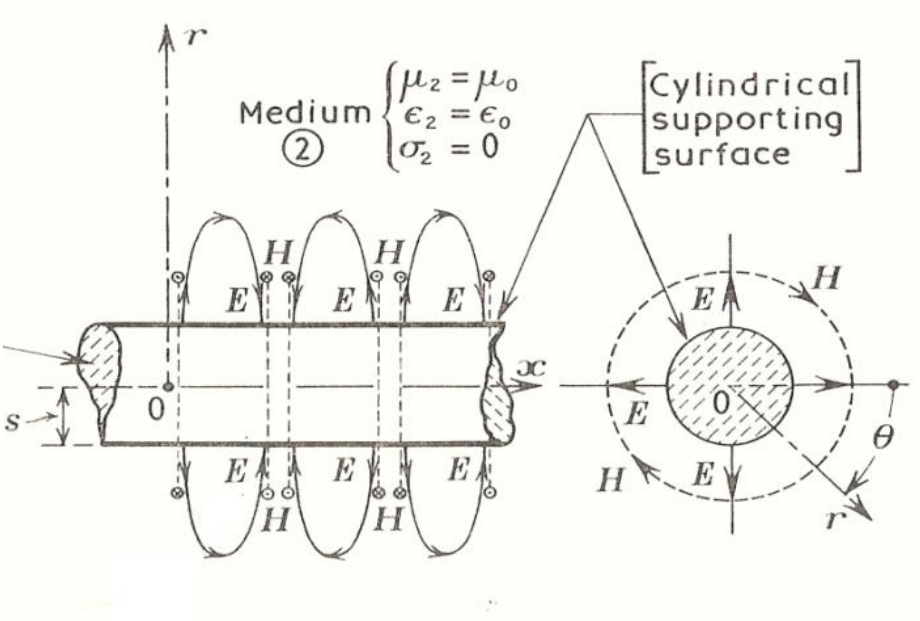

Figure 4.2 – TM_{01} mode isoclines for cylindrical geometry (Sommerfeld-Goubau mode). From [149].

A changing magnetic flux induces an E field loop according to with Faraday's Law. For a smooth conductor, if the E field loop exists, the loop is closed by a real current within the skin depth of the conductor.

If the conductor is of finite conductivity, then the real current in the surface of the conductor gives rise to an ohmic potential drop along the conductor's surface, and hence a small tangential field within the conductor. This closes the E field loop, which by Ampere's Law, induces an orthogonal magnetic field in or out of the page, if it is assumed that the E field

loop is planar with the page, and thereby permits the continuation of the propagating mode. For a conductor, the ohmic loss produces attenuation along the direction of propagation, since the energy to sustain the propagation of the wave is taken directly from the wave. Theoretically a bare conductor of finite conductivity [141], or a dielectric, or a magnetic coated conductor of infinite conductivity can support the propagation of TM_{01} mode electromagnetic waves with low loss.

If the conductor has infinite conductivity, the TM_{01} mode cannot exist as a voltage drop must exist in the conductor in order to close the E field loop and induce a H field. However, Harms [150] showed that a dielectric or magnetic coated conductor of infinite conductivity can support the propagation of electromagnetic waves with low loss [146]. This surface wave propagation was shown to take place for infinite conductivity of the conductor, as speculated by Harms, provided that the surface of the conductor is coated with a dielectric layer [146].

For a conductor with a corrugated surface sufficient to produce a significant reactance (typically inductive) the loss is negligible, but the tangential E field component can be maintained to sustain the mode [149]. In this case, the problem could be considered as a two interface problem: a smooth conductor core, a set of waveguide channels, and free space. This provides two sets of boundary conditions, and hence the situation resembles a dielectric-clad conductor, or a clad optic fiber. The matching of fields at two boundaries produces totally different solutions.

4.3 Modes in Closed Waveguides

This section will next discuss modes in closed waveguides for background and explore an alternative analysis in terms of currents (as opposed to fields) in order to understand hybrid modes which will be examined in particular detail in Section 4.4.

Closed waveguides, such as those with thick highly-conductive outer walls can support electromagnetic fields with either the electric field, E, or the magnetic field, H, being transverse. In a special case, both can be transverse i.e. a *TEM* mode can exist in coaxial waveguide. Since at least one of the fields is transverse, it is easy to describe the propagating mode by its Cartesian or circular periodicity in two dimensions.

Consider circular geometry. The electric and magnetic fields for significant modes in cylindrical guide are shown in Figure 4.3. The H_{01} mode is equivalent to the TE_{10} mode in modern terminology. Likewise the E_{01} mode is equivalent to the TM_{01} mode, and the H_{11} mode is equivalent to the TE_{11} mode. Note that the transverse field is described by simple symmetries, and that this is true for all modes.

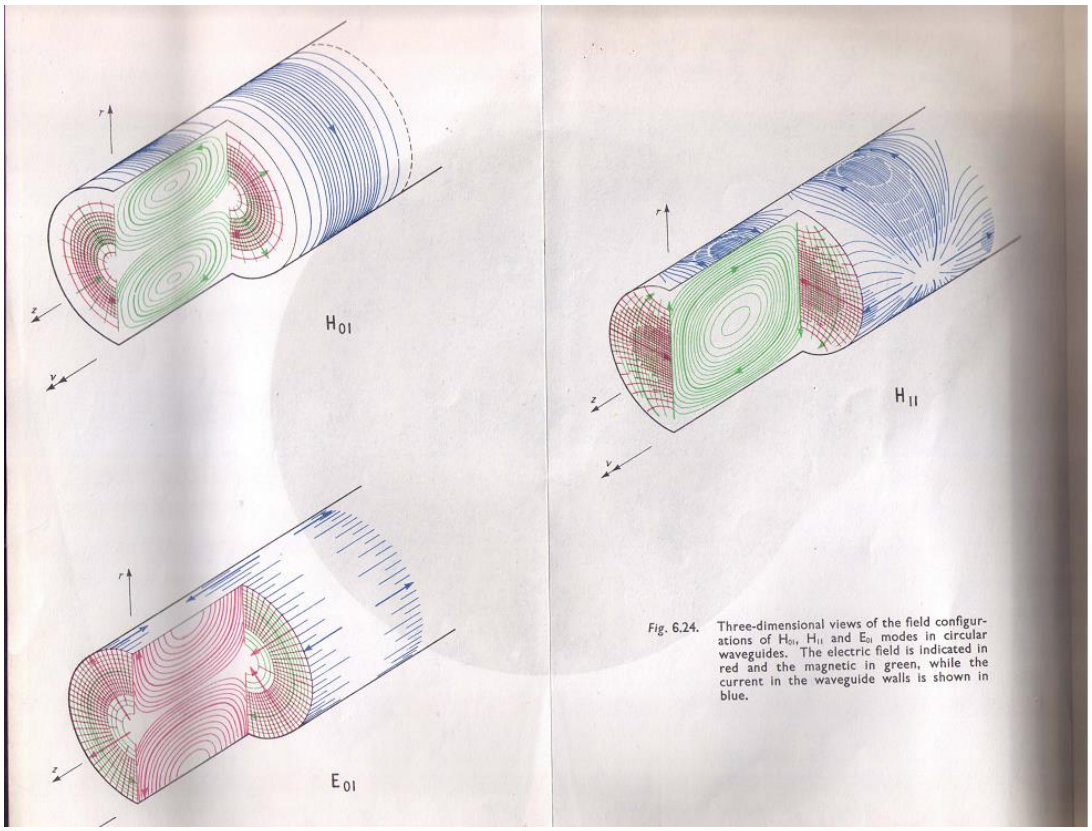

Figure 4.3 – Three-dimensional views (isoclines) of the field configurations of the H_{01} (TE_{10}), E_{01} (TM_{01}) and H_{11} (TE_{11}) modes in circular waveguides. From [151].

Higher order modes just have more nodes (and antinodes) in the azimuthal and/or radial coordinate.

Apart from the TE_{10} and TM_{01} modes, the currents induced on the inside of the outer walls are complicated, for example, the current patterns (blue) for the TE_{11} mode in Figure 4.3. This situation becomes increasingly more complicated for higher order modes with more fields loops and for hybrid modes in which neither the electric or magnetic fields are transverse to the direction to wave propagation.

The concept of standing waves in the waveguide is analogous to two plane waves propagating along a waveguide. The paths for the three important cases followed by waves travelling back and forth between the sides of a waveguide for values of free space wavelengths differing from the cutoff wavelength for λ much less than cutoff is illustrated in Figure 4.4, for λ moderately less than cutoff is illustrated in Figure 4.5, and for λ close to cutoff is illustrated in Figure 4.6.

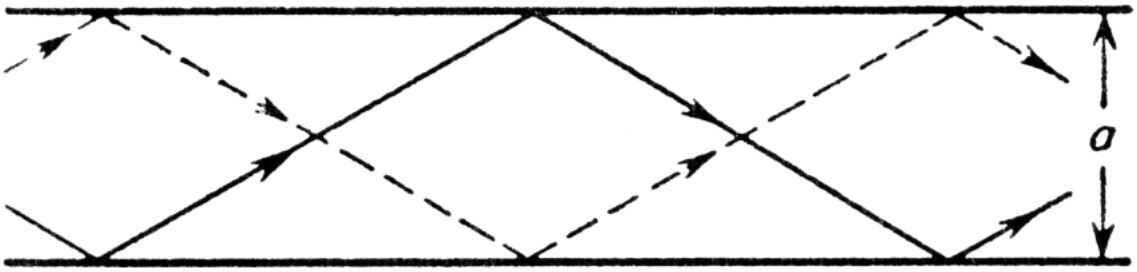

Figure 4.4 – The paths followed by waves travelling back and forth between the sides of a waveguide, λ much less than cutoff. From [152].

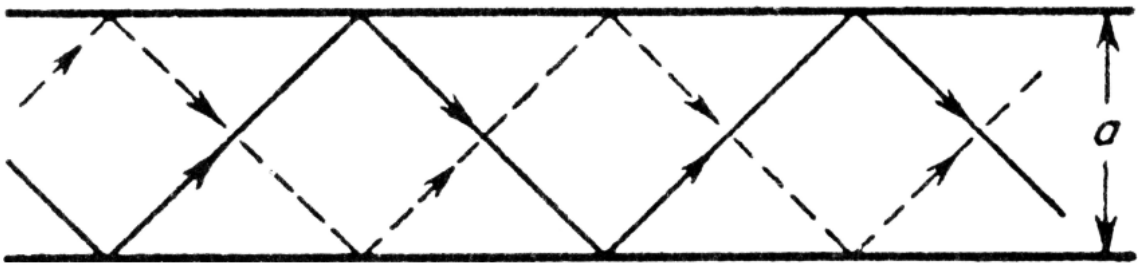

Figure 4.5 – The paths followed by waves travelling back and forth between the sides of a waveguide, λ moderately less than cutoff. From [152].

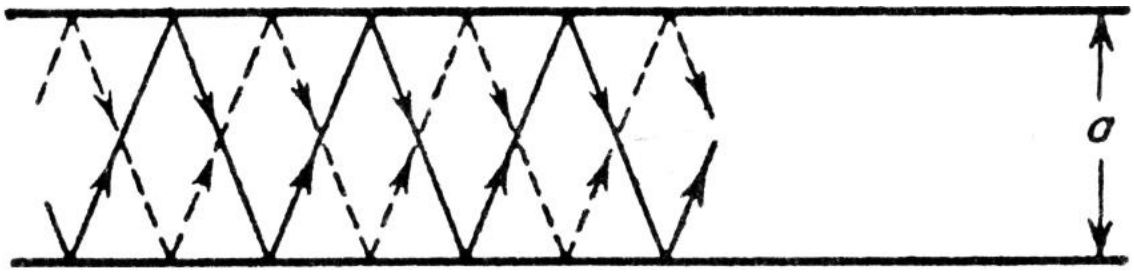

Figure 4.6 – The paths followed by waves travelling back and forth between the sides of a waveguide, λ close to cutoff. From [152].

4.4 Asymmetric and Hybrid Modes and Open Waveguides

This section will now examine three modes with no cut off, the TM_{01} mode on a conductor which has circular symmetry and the HE_{11} mode on a conductor which has dipole symmetry. The HE_{11} mode has two main lobes separated by nulls, i.e. is asymmetrical in the azimuthal plane. This enables the selective delivery of power to tissue in preferred directions by appropriate positioning of the two lobes, whilst avoiding others by the positioning of the nulls [153]. Unlike the TM_{01} mode, the HE_{11} mode can propagate on a bare conductor as a pair of orthogonally polarized modes, enabling polarization sensing and control.

Asymmetric modes were first discussed by Hondros though it was unclear whether these modes were a mathematical curiosity or whether they could be made to propagate on a wave guiding structure [144]. Sommerfeld [142] mentions the phenomena of asymmetrical modes but refers the reader to Hondros for details [143]. Perhaps the earliest reference to hybrid modes is by Schelkunoff [154]. The classification of modes into *HE* and *EH* varieties is likely due to Snitzer in the context of optical fibers [155].

The E and H field patterns for the HE_{11} mode on a bare conductor are shown in Figure 4.7. This figure has been adapted here from Hersch [146] to show not only the E field loops, but also the real current within the skin depth of the conductor, and a completed set of H field

loops. The solid lines in black in the figure are the E field loops. The solid lines in red in the figure are the real current within the skin depth of the conductor. The dashed lines in black on the conductor, and those added in blue around some of the E field loops in the figure, are the H field loops.

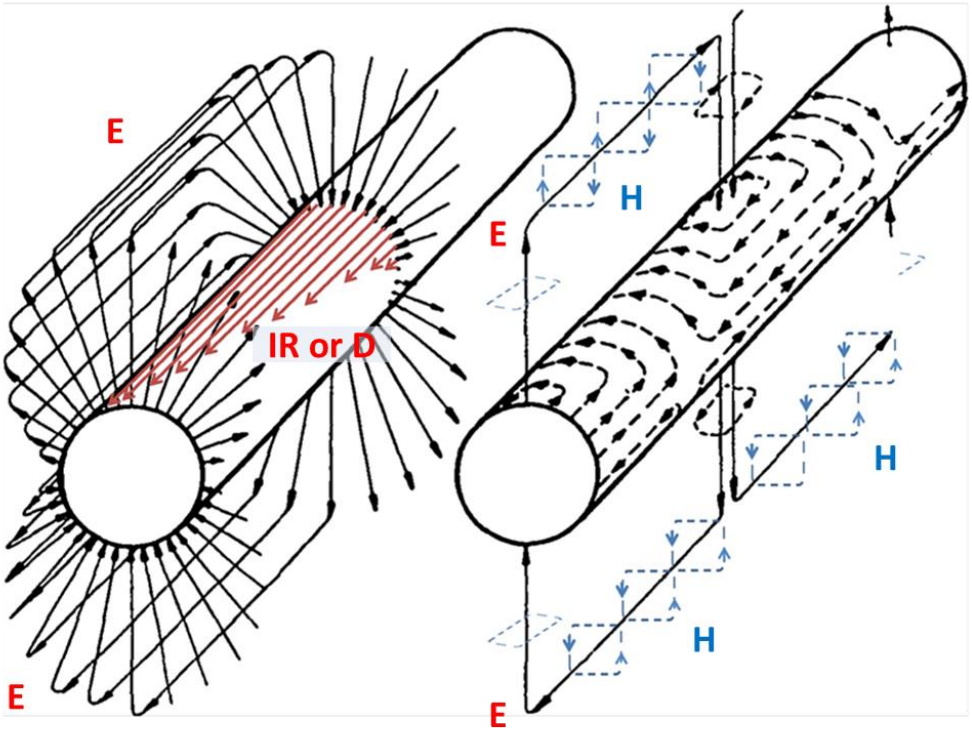

Figure 4.7 – Field pattern isoclines for the HE_{11} mode. Solid lines are E field (black), and current (red). Dashed lines are H field. Adapted from Hersch [146].

The E and H field patterns for the EH_{11} mode on a dielectric clad conductor are shown in Figure 4.8. This figure has been adapted here from Snitzer [155] to show not only the E field loops and the H field loops, but also a conductor with a dielectric cladding, and the D field loops in the dielectric cladding. The solid lines in black in the figure are the E field loops. The dashed black lines in the figure are the H field loops. The solid lines in the dielectric cladding in purple in the figure are the D field loops.

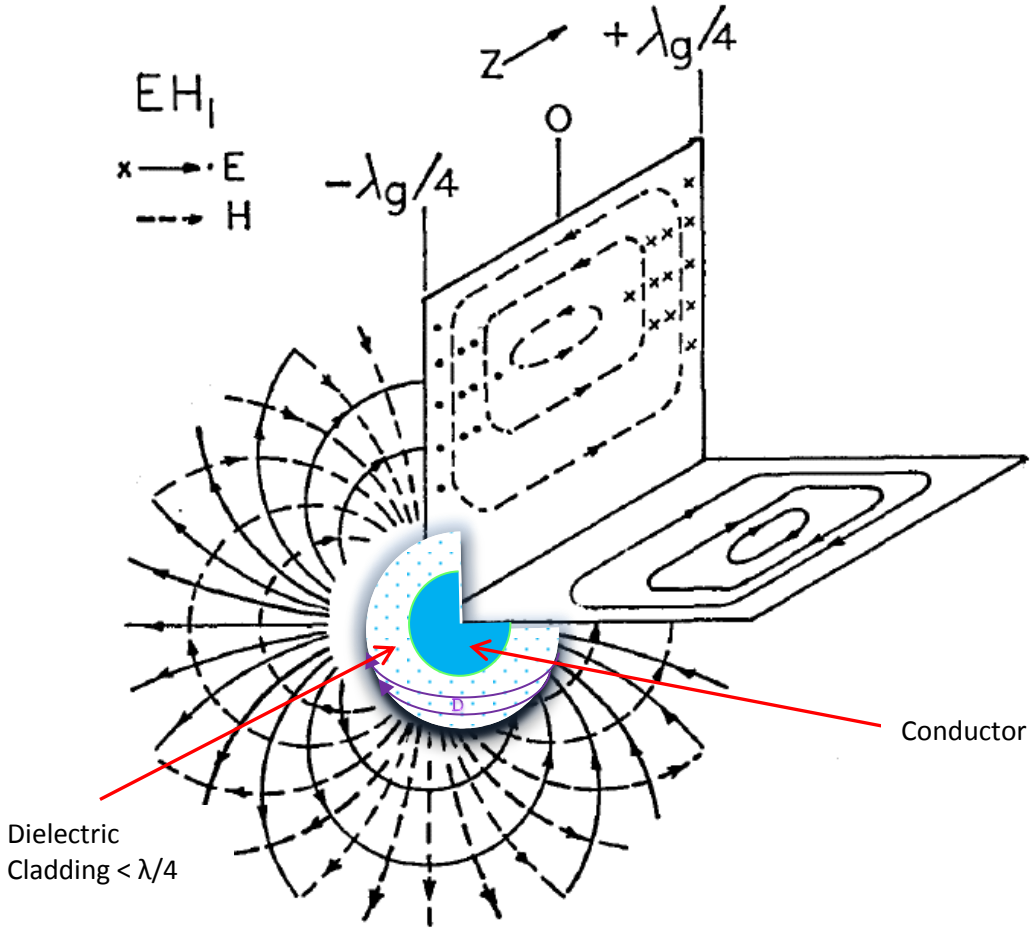

Figure 4.8 – Field pattern isoclines for the EH_{11} mode. Adapted from Snitzer [155].

4.4.1 An Alternative Interpretation

Consider the open waveguides with cylindrical symmetry:

1. A bare conductor line.
2. A dielectric waveguide (Optic Fiber).
3. A conductor with a dielectric sleeve.

In these cases, an appropriate basis set of modes is generally hybrid, this is, neither the electric field or the magnetic field is transverse to the direction of propagation, apart from the TM_{01}, which exists only on the bare conductor line or the dielectric clad conductor.

An alternative interpretation appears overdue. This one is based on the current distribution, rather than the field distribution. Consider the current on the outside of the guiding structure to be composed of two equal counter-rotating currents, as illustrated in Figure 4.9 and Figure 4.10.

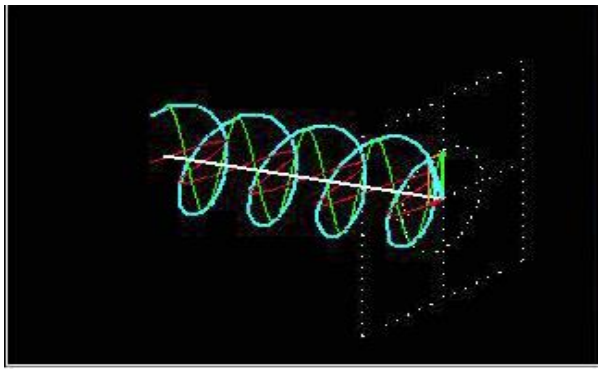

Figure 4.9 – Example of counter-rotating current on a guiding structure - propagating out of the page clockwise.

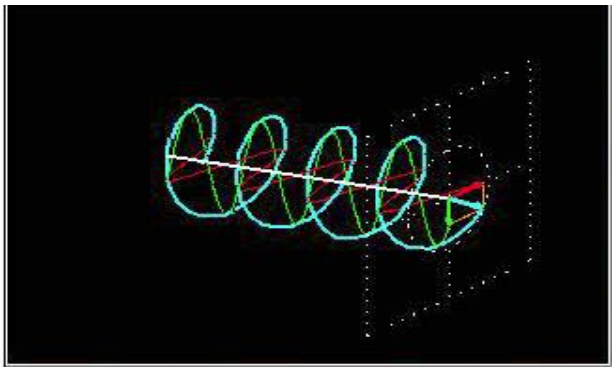

Figure 4.10 – Example of counter-rotating current on a guiding structure - propagating out of the page anti-clockwise.

For a "non-radiating" guided wave, the resultant current has a standing wave pattern in the azimuthal direction and a travelling wave pattern in the direction of propagation. A longitudinal electric field is sustained by the finite conductivity of the wire, which results in an ohmic voltage drop. This is shown in Figure 4.2 for the TM_{01} mode, and in Figure 4.7 by the red arrows for the HE_{11} mode. The electric field closes the loop around that potential drop. The magnetic field forms loops around the electric field and is shown in the Figure 4.7 below by the blue loops for the HE_{11} mode.

The two modes have 0 and 1 azimuthal standing waves, and henceforth will be designated J_0 and J_1 because that is how many axial variations of current are required. The higher order modes $(n > 1)$ are J_n and support HE_{n1} hybrid modes. However, the transverse modes constitute a basis set in that they are all orthogonal and complete [35]. Therefore, the description of the modes by the azimuthal and radial mode numbers of the transverse field is entirely justified.

The J_0 mode which supports the TM_{01} field mode has zero cutoff because there is no azimuthal dependence of the current and hence no frequency dependence.

The J_1 mode which supports the HE_{11} field mode has zero cutoff because the azimuthal dependence can be induced by interposing a perfectly conducting sheet down the middle of the waveguide. The method of images can be applied to deduce the effective image current below the conducting sheet. This process is frequency independent and does not depend on the circumference of the conductor [3].

All higher order modes have a cutoff frequency. For higher order modes, the electric field has a longitudinal component and the current loops along the conductor. Then the method of images breaks down, and the number of loops around the circumference must be relied upon. Therefore, the current is extremely tightly bunched, and the conductor circumference is the appropriate number of wavelengths for that mode:

$$n\lambda = 2\pi r, n \geq 2 \qquad (4.1)$$

where n is the azimuthal mode number, λ is the wavelength, and r is the radius. The phase velocity tends to infinity, because the equi-phase contours are almost parallel to the direction of propagation, whilst the group velocity tends to zero, because the current is almost purely azimuthal. This is analogous to the situation in hollow waveguides (and slow and fast wave structures etc.), as illustrated for example in Figure 4.3 of the field patterns of modes in closed

waveguides. Above the cutoff frequency, the current coils get further apart, so the phase velocity drops and the group velocity increases, just as for hollow waveguides.

The J_0 mode cannot be supported in a dielectric waveguide, because if it were, the electric and magnetic fields at the centre of the guide would be infinite. This is equivalent to excluding the Hankel functions from the inner region of the guide. The Hankel functions are essential in the outer region of the guide to satisfy the Sommerfeld radiation condition at infinity [142].

This suggests that Sommerfeld [141] and Hondros [144] analysed the TM_{01} mode because they believed that only transverse modes were supported by the single conductor and that was the only one which is common to both the transverse basis set and the J set (J meaning Bessel functions) of mainly hybrid modes. Their persistence in pursuing the transverse mode notion led them to conclude that all higher order transverse modes are attenuated dramatically, because their currents are driven into the conductor, where they cause dissipation [20]. They were unaware of the possibility of a different representation using hybrid modes, which were not identified explicitly until 1943 by Schelkunoff [154] and whose field patterns were first analyzed and shown by Snitzer [155].

It was Hersch [146], in the late 1950's, who concluded that the HE_{11} mode exists in the dielectric coated conductor, but deduced erroneously that the bare conductor could not support this or any higher order HE_{n1} hybrid modes, and that the dielectric sleeve was essential for the propagation of such modes. Hersch [146], derives an equation for the electrical circumference of a dielectric coating which shows that it has to be an integer multiple of wavelength as follows:

$$2\pi b = \frac{2.197(1/c)}{\sqrt{(\epsilon - 1)}}\lambda_0 \qquad (4.2)$$

where $2\pi b$ represents the circumference of the guide, c is the ratio of the radius of waveguide without dielectric to the radius of waveguide without dielectric, ϵ is the relative permittivity of a medium, and λ_0 is the free-space wavelength.

Hersch [145, 146] then concludes from examination of Equation (4.2) the following:

"Examination of," Equation (4.2), "clearly shows that the first-order surface wave cannot exist in the absence of a dielectric coating. For the case of air $(\epsilon = 1)$ *the guide would need to be of infinite circumference."*

However, Hersch's deduction is incorrect because the limit case of zero thickness dielectric cladding does not reduce to the bare conductor case as the matching of the fields at the boundaries changes the equation for a bare conductor. By setting the relative permittivity of the dielectric to unity, or shrinking the dielectric thickness to zero, Hersch incorrectly reasoned that a bare conductor, "would need to be of infinite circumference", to support the HE_{11} mode or other higher order modes. The limiting case of changing the number of interfaces from two to one, removes a boundary condition, and does not reduce to the bare conductor case as the matching of the fields at the boundaries changes dramatically when the dielectric layer thickness goes to zero.

4.5 Propagation Along an Interface

The previous section examined the propagation of the HE_{11} mode on a bare conductor. In this section the problem of the design of the interface at the conductor and propagating an electromagnetic wave along the interface with low loss will be considered.

An electromagnetic wave can propagate along an interface between two media only if the permittivity of one of the media has a nonzero imaginary part or is a negative real part [156]. In the case where the permittivity of one of the media has a nonzero imaginary part, the phase velocity of the electromagnetic wave propagating along the interface exceeds the speed

of light. These waves are called Zenneck waves for a planar geometry, Goubau waves for cylindrical geometry and radial waves for axial geometry [148], though the description in fact relates to a particular field pattern and not to an actual set of boundary conditions. In the case where the permittivity of one of the media has a negative real part, the phase velocity of the electromagnetic wave propagating along the interface is less than the speed of light. This is the Fano mode [147].

If the Fano mode can be caused to exist at the boundary of a conductor, then it follows that it is possible to propagate a wave along the interface with low loss.

4.6 Fano Mode

In the case where the permittivity of one of the media has a negative real part, the boundary condition was first described by Ugo Fano [147], who introduced it to explain it to explain anomalous scattering observed by Wood [157]. Wood went on to mentor Loomis, the instigator of the MIT Radiation Laboratory [158].

A derivation of the conditions for the existence of the Fano mode is given in [159]. That analysis is followed here.

The geometry under discussion is that of two semi-infinite media, Medium 1 and Medium 2, joined at a planar interface, see Figure 4.11. For simplicity all media shall be limited to those having a relative magnetic permeability of 1 and a dielectric constant which has no spatial dispersion. The coordinate axes are chosen so that the z axis is perpendicular to the interface with $z = 0$ corresponding to the interface. The x axis is in the direction of propagation of the surface-wave while the orthogonal axis lies in the interface plane. Medium 1 is a pure non-absorbing dielectric, $\varepsilon_1 > 0$, and Medium 2 is a surface active medium $\varepsilon_2 = \varepsilon_{r2} - i\varepsilon_{i2}$ $(\varepsilon_{i2} > 0)$.

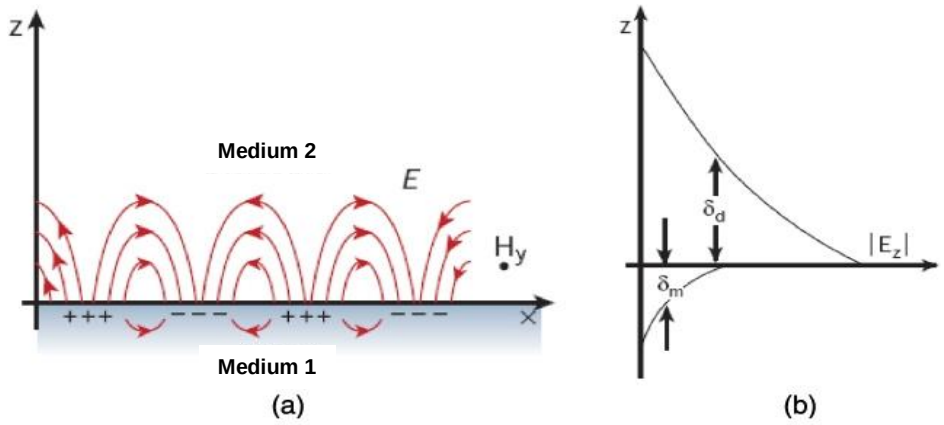

Figure 4.11 – Fano mode showing (a) electromagnetic wave and charges at the interface, and (b) the exponential decay of the electric field moving away from the interface. Adapted from [160].

The E field has to be in the direction of propagation i.e. longitudinal, otherwise the electromagnetic wave cannot propagate. So, for isotropic media, the surface electromagnetic waves are transverse magnetic and are best described by the magnetic field component which lies in the plane of the interface and in the y direction:

$$\mathbf{H} = H_0 f(z) \exp[i(\omega t - kx)] = H_y \tag{4.3}$$

where $k = k_r - ik_i$ (note the negative sign to be consistent with ε and $+i\omega t$) is the complex propagation constant parallel to the interface and $f(z)$ describes the dependence of $\mathbf{H}$ on the distance away from the interface $[f(0) = 1]$, and H_0 is a normalization constant. The electric field may be calculated from Maxwell's equations:

$$E_x = \frac{i}{\omega\varepsilon}\frac{\delta H_y}{\delta x} \tag{4.4}$$

$$E_y = \frac{-k}{\omega\varepsilon} H_y \tag{4.5}$$

and the dependence $f(z)$ for the two media is:

$$f(z) = e^{-\alpha_1 z}, z > 0, \text{Medium } 1 \tag{4.6}$$

$$f(z) = e^{-\alpha_2 z}, z < 0, \text{Medium } 2 \tag{4.7}$$

where the coefficients $\alpha_1$and α_2 are obtained from the wave equations as:

$$\alpha_1{}^2 = bk^2 - k_0{}^2\varepsilon_1 \tag{4.8}$$

and

$$\alpha_2{}^2 = bk^2 - k_0{}^2\varepsilon_2 \tag{4.9}$$

where $k_0 = \omega/c$ is the free-space wave vector at frequency ω.

Continuity of the tangential $\mathbf{E}$, E_x, at $z = 0$ leads to the dispersion relation:

$$\varepsilon_1\alpha_2 + \varepsilon_2\alpha_1 = 0 \tag{4.10}$$

This equation has to be satisfied if a surface mode is to exist. Also for a non-radiative surface mode it is clear from Equations (4.4) and (4.5) that $\mathbf{Re}(\alpha_1) > 0$ and $\mathbf{Re}(\alpha_2) > 0$.

There are then two simple situations to consider:

1. If $\varepsilon_{i2} = 0$, that is, the surface-active medium has no absorption (a physically unrealizable situation but one often assumed in the past), then $k_i = 0$. Then $\varepsilon_2 = \varepsilon_{r2}$ and $k = k_r$, so Equation (4.8) becomes an equation containing only real components. Then, for a solution to exist $\varepsilon_{r2} < 0$ and $|\varepsilon_{r2}| > \varepsilon_1$:

$$k_r = k_0\left[\frac{\varepsilon_1\varepsilon_{r2}}{\varepsilon_{r2}+\varepsilon_1}\right]^{1/2} = k_0\left[\frac{\varepsilon_1\varepsilon'_{r2}}{\varepsilon'_{r2}+\varepsilon_1}\right]^{1/2} \tag{4.11}$$

where $\varepsilon_{r2} = -\varepsilon'_{r2}$, $\varepsilon'_{r2} > 0$.

This is the Fano mode dispersion relation, which gives the decay constants α_1, and α_2 as purely real constants of the form

$$\alpha_1 = k_0\varepsilon_1\left[\frac{1}{\varepsilon'_{r2}-\varepsilon_1}\right]^{1/2} \tag{4.12}$$

$$\alpha_2 = k_0\varepsilon'_{r2}\left[\frac{1}{\varepsilon'_{r2}-\varepsilon_1}\right]^{1/2} \tag{4.13}$$

2. If $\varepsilon_{i2} \neq 0$, then ε_2, k, α_1 and α_2 are all complex, so Equation (4.8) leads to more elaborate solutions of the form:

$$k_r = k_0\left[\frac{\varepsilon_1}{(\varepsilon_{r2}+\varepsilon_1)^2+\varepsilon_{i2}^2}\right]^{1/2}\left[\frac{\varepsilon_e^2+(\varepsilon_e^4+\varepsilon_i^2\varepsilon_{i2}^2)^{1/2}}{2}\right]^{1/2} \tag{4.14}$$

$$k_i = k_0\left[\frac{\varepsilon_1}{(\varepsilon_{r2}+\varepsilon_1)^2+\varepsilon_{i2}^2}\right]^{1/2}\frac{\varepsilon_{i2}\varepsilon_1}{\left[2(\varepsilon_e^2+(\varepsilon_e^4+\varepsilon_i^2\varepsilon_{i2}^2)^{1/2})\right]^{1/2}} \tag{4.15}$$

where $A_e^2 = \varepsilon_{r2}^2 + \varepsilon_{i2}^2 + \varepsilon_1\varepsilon_{r2}$.

Also α_1 and $\alpha_2$are both complex, leading to oscillating decaying fields in both half spaces.

In the Fano case, the dielectric has negative permittivity and the propagation of electromagnetic waves then occurs without loss. By continuity of $E_{\text{tangential}}$ at the interface, there is a displacement D in opposite direction to the E field in free space. The displacement current $\varepsilon_m\frac{\delta E}{\delta t}$ where ε_m is negative closes the E field loop and permits the EM disturbance to propagate. This result is a new result and one of the key contributions of this thesis.

4.7 Artificial Dielectrics and Metamaterials

As has been mentioned previously, a dielectric material whose real part is negative is required to propagate the Fano surface wave mode. The effect occurs naturally in metals, where the "free" electrons form a plasma, and the negative dielectric occurs below the plasma frequency. Their mutual Coulomb repulsion and attraction towards the relatively fixed ions, from which they have been liberated, makes them a resonant system to incoming radiation,

typically in the UV region. For semiconductors, the resonance is typically in the infrared. A description of this naturally occurring phenomenon comes from [161] although it is treated in many other texts e.g. [3].

At optical frequencies many metals have a negative dielectric permittivity when the conduction electrons in the metals can be assumed to be reasonably free in a background of static positive ion cores, the overall system being charge neutral. It is this plasma-like behavior that is responsible for a negative dielectric permittivity at frequencies less than the plasma frequency.

4.7.1 Motion of Charged Particles in a Plasma

This section provides a description of the motion of charged particles in a plasma extracted from [161].

Consider the equation of motion for an electron in an applied time harmonic electromagnetic field with angular frequency ω_0:

$$m\ddot{\boldsymbol{r}} + m\gamma\dot{\boldsymbol{r}} = -e\boldsymbol{E}exp(-\omega_0 t) \tag{4.16}$$

where m is the mass of the electron and $m\gamma$ is a phenomenogical damping (viscous) force on the electron due to all inelastic processes. It is assumed that the wavelength of light is large compared with the distance travelled by the electron, so that it effectively sees a spatially constant field and the velocities involved are sufficiently low so that the magnetic field can be neglected. This yields a polarization per volume in the medium of:

$$\boldsymbol{P} = (\varepsilon - 1)\varepsilon_0\boldsymbol{E} = -ne\boldsymbol{r} = -\frac{ne^2/m\boldsymbol{E}}{\omega(\omega + i\gamma)} \tag{4.17}$$

$$\varepsilon = 1 - \frac{ne^2/mE}{\omega(\omega + i\gamma)} \tag{4.18}$$

where n is the number density of the conduction electrons and each electron is assumed to contribute independently to the polarization. From this is obtained the relative dielectric constant of [162]:

$$\varepsilon = 1 - \frac{\omega_p^2}{\omega(\omega + i\gamma)} \tag{4.19}$$

where $\omega_p = ne^2/\varepsilon_0 m$ is the plasma frequency. The dielectric permittivity is negative up to ω_p and the plasma shields the interior from electromagnetic radiation. Above ω_p the medium behaves as an ordinary positive dielectric. It is also responsible for the communications blackout in re-entry vehicles [163]. This is the theory of Drude and Lorentz for the dispersion characteristics of a plasma [1, 164]. Substituting the expression for the dielectric constant into Maxwell's equation, the dispersion for light in a metal is:

$$k^2c^2 + {\omega_p}^2 = \omega^2 \tag{4.20}$$

Thus, the waves below the plasma frequency correspond to the negative energy solutions, and above the plasma frequency, it appears as if the transverse modes of light had a finite rest mass of:

$$m_0 = h\,\omega_p/c^2 \tag{4.21}$$

The plasma frequency also has a physical manifestation as a collective excitation of the electron gas. This was what was studied originally. If the electron gas is displaced by a small distance in a finite metal, the excess negative (electronic) charge and the positive (background) charge that accumulate at the edges provide a restoring force proportional to the displacement and cause the entire electron gas to oscillate at frequency ω_p [165, 166]. Hence ω_p is known as the plasmon frequency. This is the dispersionless plasmon mode that occurs at:

$$\omega = \omega_p \tag{4.22}$$

As mentioned before, rendering the dielectric constant negative makes it possible for the surface to support resonances called the surface plasmons [167]. Consider the interface ($z = 0$ plane) between a metal with a dielectric constant ε_- and a positive dielectric medium (vacuum) with dielectric permittivity $\varepsilon_+(= +1)$ as shown in Figure 4.12. Now the fields for p-polarized light are:

$$\boldsymbol{E} = \boldsymbol{E}_0 exp[i(k_x x + k_y y - \omega t) - \kappa_{z+} z] \; \forall z > 0 \tag{4.23}$$

$$\boldsymbol{E} = \boldsymbol{E}_0 exp[i(k_x x + k_y y - \omega t) - \kappa_{z-} z] \; \forall z < 0 \tag{4.24}$$

where ${k_x}^2 + {k_{xy}}^2 - \kappa_{z\pm} z^2 = \varepsilon_\pm \mu \omega^2 / c^2$ are good solutions to the Maxwell equations when

$$\frac{\kappa_{z+}}{\varepsilon_+} + \frac{\kappa_{z-}}{\varepsilon_-} = 0 \tag{4.25}$$

These are collective excitations of electrons with the charges displaced parallel to the (real part of the) wave-vector. Thus a mode with longitudinal components whose fields decay exponentially into the metal and the dielectric on either side of the interface is realized. This charge density wave thus lives on the surface of the metal and is called a surface plasmon. Equation (4.24) yields the dispersion:

$$k_x = \frac{\omega}{c} \sqrt{\frac{\varepsilon_+ \varepsilon_-}{\varepsilon_+ + \varepsilon_-}} \tag{4.26}$$

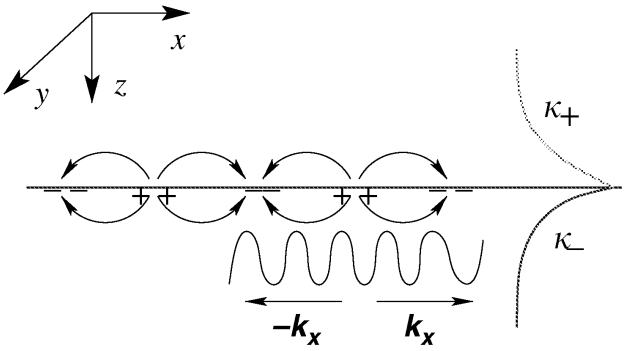

Figure 4.12 – A schematic showing the surface plasmon on an interface between a negative and a positive dielectric media and the associated charge density fluctuations. The exponential decay of the fields normal to the surface and the propagating nature along the surface are depicted schematically. From [161].

For a metal with ε_ω given by Equation (4.18) and setting $\varepsilon_+ = 1$ for vacuum, it is noted that $k_x > \omega/c$ for the surface plasmon (see Figure 4.12). Thus it will not be possible to excite the surface plasmon on a perfectly flat surface using propagating modes of light, and a coupling mechanism will have to be provided by mechanisms such as the surface roughness, a grating structure or a dielectric coupler to vacuum such as a hemisphere or a prism. Complicated surface structures can generate a variety of surface plasmon dispersions, and this has given rise to new optical phenomena such as the extraordinary transmission of light through sub-wavelength sized holes [168-170]. Next, note that for reasonably large wave-vectors the surface plasmons are nearly degenerate with a frequency of $\omega_p/\sqrt{2}$. This is the reason why the interaction of the radiation with the resonant surface plasmons is very rich and difficult to model: the radiation couples with the metal surface at all length scales. This remains true down to a nanometre or so when non-local dispersive effects kick in due to inadequate electronic screening inside the metal.

The negative dielectric constant is central to the nature of resonant interactions of structured metal surfaces with radiation. Pendry [171] provides a very insightful explanation for this. It is known that a capacitor can be formed by two parallel conducting plates with an insulating dielectric placed in between. Filling up the gap with a negative dielectric material instead

would now lead to a capacitor with negative capacitance, which is the same as being an inductor. Thus two capacitors in a circuit, one filled with a positive dielectric and the other filled with a negative dielectric material, can become resonant, see Figure 4.13. It is as if in a structured metallic structure the metal pieces form the capacitors filled by the negative dielectric material and the holes in between form the capacitors filled with the positive dielectric material. The resulting system is a very complicated circuit with many LC resonances.

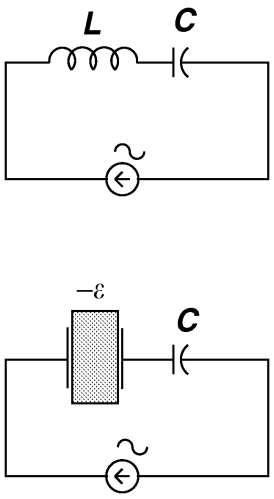

Figure 4.13 – A capacitor and an inductor form a resonant circuit that can oscillate at $\omega_0 = 1/\sqrt{LC}$. A capacitor filled with a negative dielectric has negative capacitance, acts as an inductor and can resonate with another usual capacitor. From [161].

For many metals, the plasma frequency is at ultraviolet frequencies and γ is small compared with ω_p, see [167]. Thus there are many examples of materials with a negative dielectric constant at optical frequencies. However, the dissipation in most metals is large, and difficulties arise when trying to extend this behaviour to lower frequencies where $\omega \sim \gamma$. Then it can hardly be claimed that the dielectric constant is an almost real and negative number. The dissipation dominates all phenomena and then no longer is the behaviour that of a good plasma.

It must be pointed out that negative dielectric permittivity can also be obtained in more ordinary dielectric media with bound charges, within a frequency band above a resonance frequency. Consider a medium in which the electrons are bound to positive nuclei and its response to an applied electromagnetic field. For small displacements of the electrons there is a restoring force on the electron, $-m\omega_0^2 r$. Including this term in Equation (4.15), one obtains the resonant Lorentz dielectric permittivity:

$$\varepsilon = 1 + \frac{ne^2/(\varepsilon_0 m)}{\omega_0^2 - \omega^2 - i\gamma\omega'} \tag{4.27}$$

where n is now the total density of bound electrons (here it is assumed simplistically that all the electrons are bound with the same strength). Setting $\omega_0 = 0$, immediately the Drude form for ε for a good plasma is obtained. Note now that the dielectric constant can be negative in a small frequency range above ω_0 if the resonance is sharp enough. In fact, one can make use of resonant effects such as electromagnetically induced transparency or similar effects based on atomic coherences [39, 40] to drive the dielectric constant negative over selected small frequency ranges.

In order to replicate this negative dielectric behaviour at microwave/millimeter wave frequencies, a resonance in that region has to be engineered. This has been the domain of artificial dielectrics, which have been known for more than a century [172]. Metamaterials are a special subset of these, distinguished by the fact that the real components of their permittivity and permeability are both negative somewhere in the same part of the electromagnetic spectrum.

4.7.2 Metamaterials

The special case of both being negative at the same frequency is highly prized. It has been claimed by Veselago, that in such a case, the material possesses a negative refractive index. The significance of this is that, for a positive refractive index material, refraction is towards the

normal, whereas for a negative refractive index material, refraction is away from the normal. His original paper [173] is speculative, and simply looks at "what if…". His recent paper [174] is quite different. It is dogmatic and defensive. This reflects the recent controversy over whether negative refraction (negative index) has actually been observed, and indeed, whether the theory is well-founded. Just like with the controversy over the observation and theory behind the Zenneck wave, the opponents seem to have dug themselves into their positions. There is a much more riding on negative refraction, because this is the basis for cloaks in the optical and radar sense, and perfect lenses and lots of other applications, which are heavily funded by the military.

To understand the issues involved, and to avoid misconceptions, it is instructive to study the history of artificial dielectrics.

4.8 A History of Artificial Dielectrics

The concept of an artificial dielectric is due to Prof. Sir J.C Bose [175], a pioneer of microwaves, millimeter-waves and biophysics. He may have got his idea from his advisor and mentor Lord Rayleigh from his paper on the influence of obstacles arranged in rectangular order upon the properties of a medium [176], in which Rayleigh analyses the response of a regular arrangement of conductors from a purely theoretical aspect. Bose's description and pictures of the first artificial chiral material are self-explanatory.

"In order to imitate the rotation produced by liquids like sugar solutions, I made small elements or "molecules " of twisted jute, of two varieties, one kind being twisted to the right (positive) and the other twisted to the left (negative). I now interposed a number of, say, the positive variety, end to end, between the crossed polariser and analyser; this produced a restoration of the field. The same was the case with the negative variety. I now mixed equal numbers of the two varieties, and there was now no restoration of the field, the rotation

produced by one variety being counteracted by the opposite rotation produced by the other."

From [175].

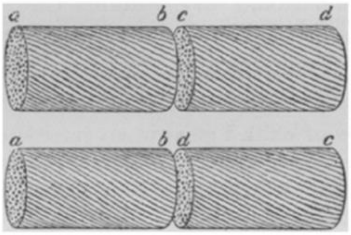

FIG. 2.—Jute elements.

Figure 4.14 – Jute elements. From [175].

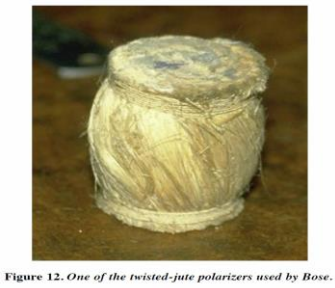

Figure 12. *One of the twisted-jute polarizers used by Bose.*

Figure 4.15 – Twisted jute polariser used by Bose. From [172].

Bose's work seems to have been overlooked, despite being communicated by Rayleigh, his advisor, mentor and lifelong friend. This applies to more than a dozen of his papers in diverse areas. It suggests that the work was "too far ahead of its time" and even Rayleigh was unsuccessful in "selling it".

It appears that the next champion of artificial dielectrics, appeared more than 20 years after Bose [177]. Karl F. Lindman was likely totally oblivious to Bose's work. All the same [177] erroneously credits Lindman with being the first:

"Karl F. Lindman has widely been referred to as being the first to demonstrate the effect of a chiral medium on electromagnetic waves, about 40 years ahead of the pack."

Regardless, Lindman's contributions to chiral media were momentous. His numerous publications were in German or Swedish, and in the few examined, there is no reference to Bose, so he may not have had access to them or maybe could not read English. Unfortunately, Lindman's contributions suffered the same fate as Bose's, and only recently [177] have they been given the credit they deserved.

The next advance took more than another 20 years, but this time, after the first two "false starts" the concept of artificial dielectrics really did take hold. The pioneer was Winston E. Kock [178]. In a seminal paper [179], Kock explored fast dielectric lenses based on parallel plate waveguides. In this momentous paper, Kock describes the concept and implementation of artificial dielectrics with refractive index less than unity. Kock credited that idea to A. P. King, G. C. Southworth, and W. P. Mason [179]:

"*The use of the increased phase velocity in a wave guide to obtain a lens or prism action was considered rather early by A. P. King, G. C. Southworth, and W. P. Mason of these Laboratories."* i.e. Bell Laboratories.

These were used as lenses to increase the directivity of operational microwave repeaters. Being at Bell Labs, such a feat was not unnoticed. However, Kock was not satisfied with such "fast lenses" and produced another revolutionary paper [180], on top of more than 200 patents [178].

In [180] he describes a variety of artificial dielectrics composed of lattices of conducting spheres, discs, wires and various variations of the above. Mostly, these are all "slow" i.e. with dielectric greater than 1. However, he shows an insight well before his time to suggest that an elemental resonance of the conducting particles used to construct the artificial dielectric could be used to control the response of the ensemble:

"It was stated earlier that the size of the elements should be small relative to a half wavelength in order for the refractive index to be independent of frequency. A qualitative idea of this criterion can be obtained by an elementary analysis of forced oscillations of dipoles. It is known that a dielectric medium which is composed of elements that resonate under the action of an alternating electric field, such as atoms having bound electrons, will exhibit a dielectric constant which varies with frequency: $\varepsilon_r = 1 + \frac{k}{f_0^2 - f^2}$ *where* f_0 *is the frequency of resonance of the element,* f *the frequency of the incident radiation and* k *a proportionality constant. Thus when* f *is small relative to* f_0, E *is practically independent of* f*."*

This above is remarkable for its time, but not unexpected, because Kock was a world authority on the theory and construction of musical instruments, being the inventor of the Baldwin Organ, had survived a Physics Ph.D. examination in Berlin, by none other than Max von Laue, and was an accomplished microwave engineer. The world saw further contributions from this brilliant mind, because he was promoted to Director of the NASA Electronics Research Centre [178].

Fortunately, the concepts that Kock introduced were taken up by Seymour Cohn [181] and John Brown of Imperial College in the early 1950's, see [163]. He, together with Prof. Willis Jackson [182] tried to explain Kock's heuristic dielectrics using transmission line theory. Jackson appears to have been influenced by M. M. Z. El-Kharadly [183], who pioneered the measurement of the properties of such dielectrics using a low voltage Schering bridge at 1 KHz. El-Kharadly appears to be active to this day, and seems to have received little credit, although his contribution was at least original and helpful. Also, G. Estrin [184] and R.W. Corkum [185] were notable contributors to the understanding of the polarizability of arrays of discs and the control of effective permeability of artificial dielectrics.

Around the same time Ronald N. Bracewell [163] became aware of the artificial dielectric concept and suggested that these could be used to model an ionospheric or re-entry plasma

of a spacecraft in the laboratory so that the effects on radio communications could be modelled.

Soon afterwards, Walter Rotman [186] combined the two concepts, graciously giving credit to all his predecessors, and formulated a coherent model of an ionospheric or re-entry plasmas using an artificial dielectric model. Rotman considered dielectric constant down to zero but not below zero.

A good literature survey of the state-of-the art in artificial dielectrics up to 1975 can be found in [187].

Artificial dielectric research progressed at a sedate pace, until John Pendry et al. published his historic paper in 1996 [188]. This paper reverses the Bracewell/Rotman logic, by using a plasma to model an artificial dielectric. This paper does not reference any of the pioneers of artificial dielectrics.

4.9 Design of a Negative Dielectric to support the HE_{11} Fano Mode

In order to design an artificial dielectric required to propagate the lossless HE_{11} Fano mode at millimetre wave frequencies, needs to be designed and fabricated. The landmark paper Pendry [188] analyses such a dielectric. However, the paper has some errors and omissions which have to be addressed in order to be useful for this design task. Aspects of this paper will now be reviewed which are pertinent to the task.

Quoting verbatim [188]:

In this Letter we show how to manufacture an artificial material in which the effective plasma frequency is depressed by up to 6 orders of magnitude. The building blocks of our new material are very thin metallic wires of the order of 1 μm in radius. These wires are to be

assembled into a periodic lattice and, although the exact structure probably does not matter, we choose a simple cubic lattice shown below in Figure 4.16.

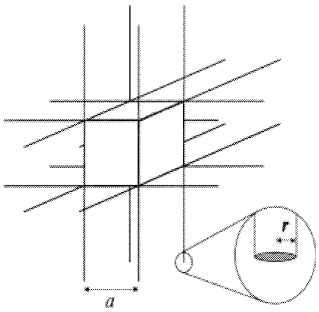

Figure 4.16 – The periodic structure is composed of infinite wires arranged in a simple cubic lattice, joined at the comers of the lattice. From [188].

We now derive the plasma frequency for collective oscillations of electrons in the wires. Consider a displacement of electrons along one of the cubic axes: The active wires will be those directed along that axis. If the density of electrons in these wires is n, the density of these active electrons in the structure as a whole is given by the fraction of space occupied by the wire,

$$n_{eff} = n\frac{\pi r^2}{a^2} \tag{4.28}$$

Before we rush to substitute this number into Equation (4.27) for the plasma frequency, we must pause to consider another effect which is at least as important: Any restoring force acting on the electrons will not only have to work against the rest mass of the electrons, but also against self-inductance of the wire structure. This effect is not present in the original calculation of the plasma frequency, but in our structure it is the dominant effect. It can be represented as a contribution to the electron mass. The important point is that the inductance of a thin wire diverges logarithmically with radius. Suppose a current I flows in the wire creating a magnetic field circling the wire,

$$H(R) = \frac{\pi r^2 nve}{2\pi R}, \tag{4.29}$$

where R is the distance from the wire centre. We have also re-expressed the current in terms of electron velocity, v, and charge density, ne. The large self-inductance of a thin wire delays the onset of current mimicking the effect of electron mass. We write the magnetic field in terms of a vector potential,

$$H(R) = \mu_0^{-1} \nabla \times \mathrm{A}(R). \tag{4.30}$$

For an isolated wire the vector potential is ill-defined until boundary conditions are specified. However, for a three-dimensional array of wires, the mutual inductance actually simplifies the problem and introduces the lattice spacing as a natural cutoff,

$$A(R) = \frac{\mu_0 \pi r^2 nve}{2\pi} \ln(a/R), \tag{4.31}$$

where a is the lattice constant.

This is the essence of Pendry's thesis. He considers the electrons in a set of wires as behaving just like in a three dimensional continuous plasma, except that there are fewer of them (reduced by the spatial occupancy factor of the wires, assuming the wires are thicker than a skin depth) and that the electrons in the wires interact by a different force field than the Coulomb type interaction in a real plasma. Likewise, the damping effects are no longer determined by a collisional frequency, but by the finite conductivity of the wires, which results in ohmic dissipation.

Pendry then assumes that the interaction is due exclusively to magnetic coupling between the wires, and treats each wire as a current element to derive the vector potential involved. Based on these assumptions Pendry inserts the reduced electron density and the interaction

force into the classical plasma resonance model, and obtains an effective plasma frequency for his wire array. This turns out to be about 6 orders of magnitude lower than the classical plasma.

Quoting verbatim [188]:

We note that, from classical mechanics, electrons in a magnetic field have an additional contribution to their momentum of eA, and therefore the momentum per unit length of the wire is

$$\pi r^2 enA(R) = \frac{\mu_0 \pi^2 r^4 e^2 n^2 v}{2\pi} \ln(a/r) = m_{eff} \pi r^2 n v, \tag{4.32}$$

where m_{eff} is the new effective mass of the electrons given by

$$m_{eff} = \frac{\mu_0 \pi r^2 e^2 n}{2\pi} \ln(a/r). \tag{4.33}$$

This new contribution is dominant for the parameters we have in mind. For instance, for aluminum wires $r = 1.0 \times 10^{-6} m$, $a = 5 \times 10^{-3} m$,

$$n = 1.806 \times 10^{29}\ m^{-3} \text{ (aluminum)} \tag{4.34}$$

gives an effective mass of

$$m_{eff} = 2.4808 \times 10^{-26}\ kg = 2.7233 \times 10^4 m_e = 14.83 m_p. \tag{4.35}$$

In other words, by confining electrons to thin wires we have enhanced their mass by 4 orders of magnitude so that they are now as heavy as nitrogen atoms.

Having both the effective density, n_{eff}*, and the effective mass,* m_{eff}*, on hand we can substitute into…*

Pendry then goes on and substitutes the effective density, n_{eff}, and the effective mass, m_{eff} into

$$\omega_p^2 = \frac{n_{eff} e^2}{\varepsilon_0 m_{eff}} \tag{4.36}$$

Neglecting the factor of $(2\pi)^2$ yields the following

$$\omega_p^2 = \frac{n_{eff} e^2}{\varepsilon_0 m_{eff}} = \frac{2\pi c_0^2}{a^2 \, ln \, (a/r)} \approx (8.2 \, GHz)^2 \tag{4.37}$$

There is a serious flaw in Pendry's theory. It concerns the interaction between the conducting wires under the assumption that this is purely magnetic. It is known from microwave theory that the electrons in a conducting wire exposed to an EM field move in response to the field. Such movement results in separation of charges, current flow and radiation. The first effect results in the excitation of a secondary magnetic field, which affects the conducting wires within its vicinity. Pendry considers this. The second effect results in the wire acting as an electrostatic dipole and thus affecting its neighbours. Pendry ignores this. The third effect produces a radiated field which also couples the wires in the lattice. Pendry ignores this also. Each of these coupling mechanisms has its own power law and is dominant for different wire separations (lattice constant). This is how the mutual coupling of patch antenna arrays has been analyzed [127]. The only difference between such antennas and Pendry's wires is the shape factor.

4.10 Analysis of a Conducting Wire

The fields generated by a conducting wire have been analyzed well before Pendry using microwave theory [189] and have included electrostatic effects and radiation. These were not considered in Pendry's analysis in the previous section.

There are two major conclusions to be drawn from the above analysis:

1. There are three different interaction mechanisms between the wires and they obey different power laws:

(a) the electrostatic dipole-dipole interaction, which dominates at short range $r \ll \frac{\lambda}{2\pi}$, varying as $\frac{1}{r^3}$,

(b) the magnetic induction interaction, which dominates around $r \approx \frac{\lambda}{2\pi}$ and varies as $\frac{1}{r^2}$, and

(c) the radiation coupling, which dominates for $r \gg \frac{\lambda}{2\pi}$ and varies as $\frac{1}{r}$.

2. The magnetic coupling dominates around $r \approx \frac{\lambda}{2\pi}$ because the electrostatic field and the radiation field are out of phase and approximately equal at that range, and therefore interfere destructively near $r \approx \frac{\lambda}{2\pi}$, leaving the magnetic coupling as the dominant interaction.
3. The analysis is valid as long as the wire length is much less than $\lambda/4$, so that inductive coupling dominates and radiation is constrained.

Pendry's choice of lattice spacing and the consequential plasma frequency puts the conditions very close to the near field range $\approx \frac{\lambda}{2\pi}$. The spacing between the conductors is 5 mm and the plasma frequency is around 8 GHz i.e. a wavelength of around 37.5 mm. Therefore each wire is near to $\frac{\lambda}{2\pi}$ from its nearest neighbour. Therefore Pendry's model is almost valid for such spacing. Pendry does not rely on the model for quantitative analysis. He leaves the simulation of a particular wire mesh geometry to Smith, his experimental collaborator and others. Of course, such simulations solve Maxwell's equations on a grid/mesh structure to arbitrary precision, so that they are often in good agreement with measurements (not surprising). However, they offer no assistance in the design of a metamaterial with prescribed properties, which is what is needed for the design here. That can only be achieved by a physical model. As demonstrated above, Pendry's model is only valid around $r \approx \frac{\lambda}{2\pi}$. In fact, it is possible to compute an approximate range of validity. A good engineering criterion is that the field being modelled is at least 10 dB greater than the residuals.

$$\text{For } r < r_c = \frac{\lambda}{2\pi},\ \left(\frac{r_c}{r}\right)^2 > \sqrt{10}\left[\left(\frac{r_c}{r}\right)^3 - \left(\frac{r_c}{r}\right)\right] \text{ i.e. } r > 0.854r_c \tag{4.38}$$

$$\text{For } r > r_c = \frac{\lambda}{2\pi},\ \left(\frac{r_c}{r}\right)^2 > \sqrt{10}\left[\left(\frac{r}{r_c}\right) - \left(\frac{r}{r_c}\right)^3\right] \text{ i.e. } r < 1.17r_c \tag{4.39}$$

Using this criterion, Pendry's model is valid in the range of ±15% of $\frac{\lambda}{2\pi}$. This is very restrictive for the design task as it is only valid over a very small range. For this task this needs to generalize as there is already other restrictions on the design of the launcher for the HE_{11} mode.

Also, Pendry does not consider the length or the thickness of the wire, which cannot be ignored in because of surface and end effects [90].

Pendry does not stop there. He concludes that the ensemble of wires behaves like an electron plasma, except that the electron density is reduced by the occupancy fraction, and the electron mass is enhanced by 1000 or more because he has assumed the magnetic interaction acts alone. However, it has just been shown that this is true only over a highly restricted density range.

Another criticism was related to the dissipation issue. Walser et al. [190], erroneously attributed the damping to physical collisions in a real plasma and concluded that the scaled down resonance Pendry had predicted would be damped out by the collisions between electrons whose frequency is independent of scaling. Walser was incorrect because the damping in the wire array is due to the finite wire conductivity and has nothing to do with the frequency of collisions. Incidentally, Rodger Walser is credited with coining the term "metamaterials".

All the same, Pendry's the paper is momentous. The model can be adjusted for $r \ll \frac{\lambda}{2\pi}$ by considering the electrostatic interaction only and for $r \gg \frac{\lambda}{2\pi}$ by considering the radiation

interaction only. This will not explored further here. Instead, the task of designing an artificial dielectric for the launcher for propagating the lossless HE_{11} Fano mode will now be pursued.

A simple simulation of an artificial dielectric launcher for the lossless HE_{11} Fano mode could be undertaken. Assume the launcher's conductor has a 2 mm diameter. In order to fulfil the requirements of an ensemble, one would need at least 1000 conducting elements within the needle cross section. This could be provided by carbon nanotubes. Therefore, it would be instructive to simulate a needle of this type: 17 rods per mm, i.e. a separation of 59 µm. A CST/HFSS simulation [114, 191] of such an ensemble should reveal the resonance frequency. It should then be possible to estimate the bandwidth of possible excitation of the Fano mode. Redesign of such an ensemble could be undertaken once the resonance frequency was known i.e. which interaction is dominant at that separation. If necessary, the design could be adjusted, based on a corrected interaction model which would apply over a much wider range than Pendry's (±15%). The next section deals with an in-depth analysis of the interaction in order to achieve this.

4.11 HE_{11} Mode and Removing Conductor Losses

Sommerfeld [141] showed that a bare cylindrical conductor of finite conductivity can support the propagation of symmetrical modes, and that the TM_{01} mode has no cut-off. Hondros [143, 144] investigated higher order modes, and determined that they are highly damped by eddy currents and do not propagate.

Hersch [145, 146] analyzed higher order modes on a dielectric-coated conductor, deducing erroneously "that the first-order surface wave cannot exist in the absence of a dielectric coating". By setting the relative permittivity of the dielectric to unity, or shrinking the dielectric thickness to zero, Hersch incorrectly reasoned that a bare conductor, "would need to be of infinite circumference", to support HE_{11} or other higher order modes.

The HE_{11} mode has two main lobes separated by nulls, i.e. is asymmetrical in the azimuthal plane. This enables the selective delivery of power to tissue in preferred directions by appropriate positioning of the two lobes, whilst avoiding others by the positioning of the nulls. Unlike the TM_{01}, the HE_{11} mode can propagate on a bare conductor as a pair of orthogonally polarized modes, enabling polarization sensing and control. However, as both modes are dominant, exciting the HE_{11} mode is a challenge. It has been shown here that the HE_{11} mode can be made to propagate on a conductor with low loss. However, loss in the conductor to support the propagation of the mode is essential, and unavoidable. The possibility of removing this requirement, by coating a bare conductor with an artificial dielectric having negative permittivity, which can support the lossless Fano mode [147], and propagating both TM_{01} and HE_{11} modes with no ohmic conductor losses is investigated later.

4.12 Simulation Results

This section presents results of a simulation performed with CST of a waveguiding structure for exciting the HE_{11} mode. For comparison, results of a simulation performed with CST of a waveguiding structure for exciting the TM_{01} mode are presented first. In this investigation, the analysis focuses on the losses due to the waveguiding structure being in contact with lossy and mismatched tissue. The finite conductivity of the waveguiding structure and conductivity of the lossy tissue below the epidermis are not considered as these are likely to be dwarfed by losses in the tissue and the mismatch at the skin and internal interfaces. They are also of minor concern as they will be minimized by the use of the Fano mode introduced in Section 4.6, a design for which is investigated in Section 4.14. Finally, measurements of the HE_{11} mode on a constructed launcher are presented confirming the azimuthal pattern of the mode.

4.12.1 Waveguiding Structure for Exciting the TM_{01} Mode – Transmission past sample

A waveguiding structure for exciting the TM_{01} mode is shown in Figure 4.17 in a back-to-back configuration. The four discs in the centre of the figure represent a double-thickness skin sample (magenta) with loss, and matching sections (blue) respectively. The structure works by launching the *TEM* mode in the coaxial section and converting this to the TM_{01} mode in the flared horn section of the structure. The TM_{01} mode then propagates on the bare conductor along to the matching section and skin sample. The dimensions of the launching structure are based on Anritsu V085 coaxial cable and on the monographs of Goubau [192, 193]. Anritsu V805 coaxial cable is the smallest flexible coaxial cable available which is rated to 65 GHz. The dimensions of the coaxial cable were used as the initial inner and outer diameters of the single conductor and coaxial guide sections of the waveguiding structure.

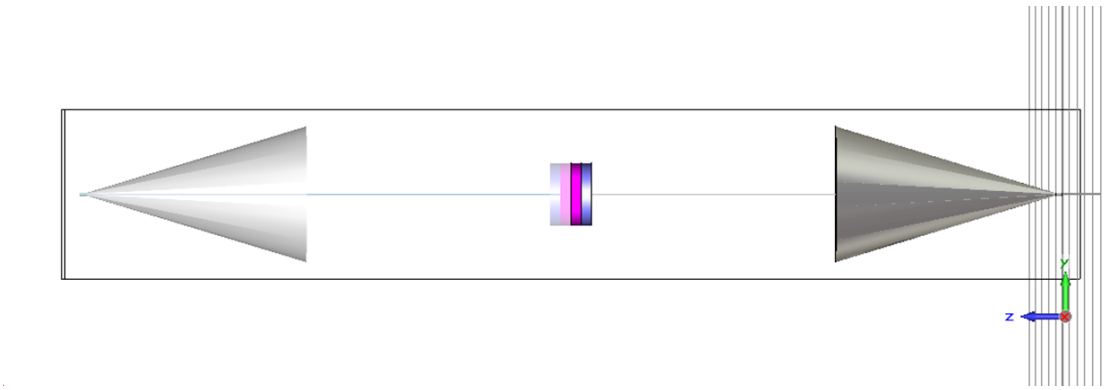

Figure 4.17 – Waveguiding structure for exciting the TM_{01} mode.

A length-wise cross-section through the waveguiding structure of Figure 4.17 is shown in Figure 4.18. This shows the characteristic longitudinal mode pattern (red/orange) of the TM_{01} mode as illustrated in Figure 4.2. Note the significant amount of transmission (yellow) past the sample.

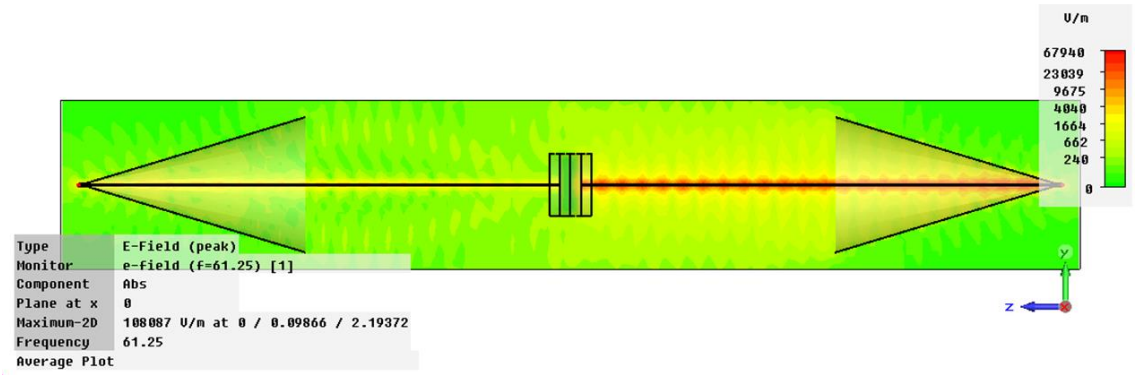

Figure 4.18 – Cross-section through the waveguiding for exciting the TM_{01} mode.

Simulated S-parameters for the waveguiding structure of Figure 4.17 are shown in Figure 4.19. At 61.25 GHz $S_{11} < -25\ dB$ and S_{21} is approximately $-18\ dB$.

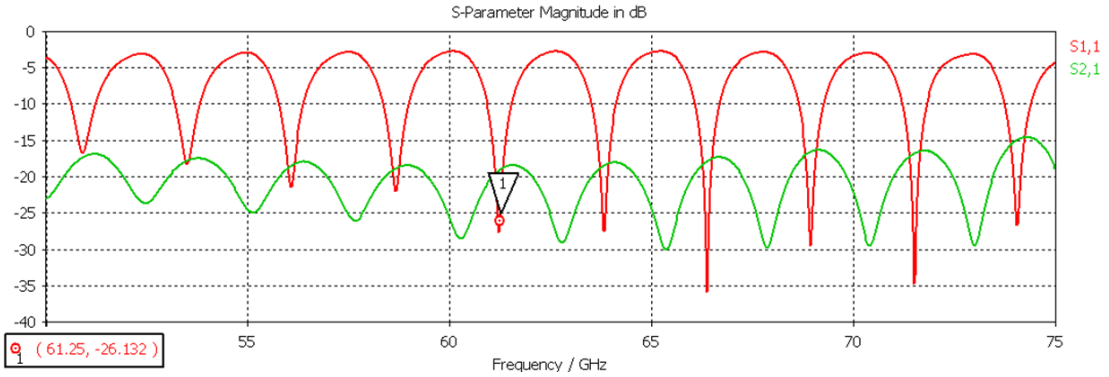

Figure 4.19 – Simulated S Parameters of the waveguiding structure for exciting the TM_{01} mode.

4.12.2 Waveguiding Structure for Exciting the TM_{01} Mode – Minimal transmission past sample

A waveguiding structure for exciting the TM_{01} mode is shown in Figure 4.20 in a back-to-back configuration. In this simulation, the diameters of the skin samples and matching sections have been increased to minimize transmission past the sample. The four discs in the centre of the figure represent a double-thickness skin sample (magenta) with loss, and a matching section (blue) respectively. The dimensions of the launching structure are based on Anritsu

V085 coaxial cable and on the monographs of Goubau [192, 193].

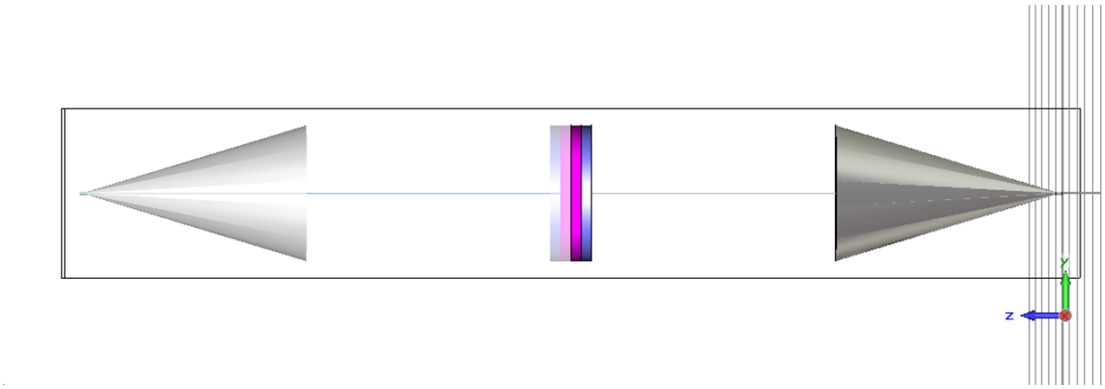

Figure 4.20 – Waveguiding structure for exciting the TM_{01} mode.

A length-wise cross-section through the waveguiding structure of Figure 4.20 is shown in Figure 4.21. This shows the characteristic longitudinal mode pattern (red/orange) of the TM_{01} mode as illustrated in Figure 4.2. Note compared with Figure 4.18, there is now a minimal amount of transmission (yellow) past the sample.

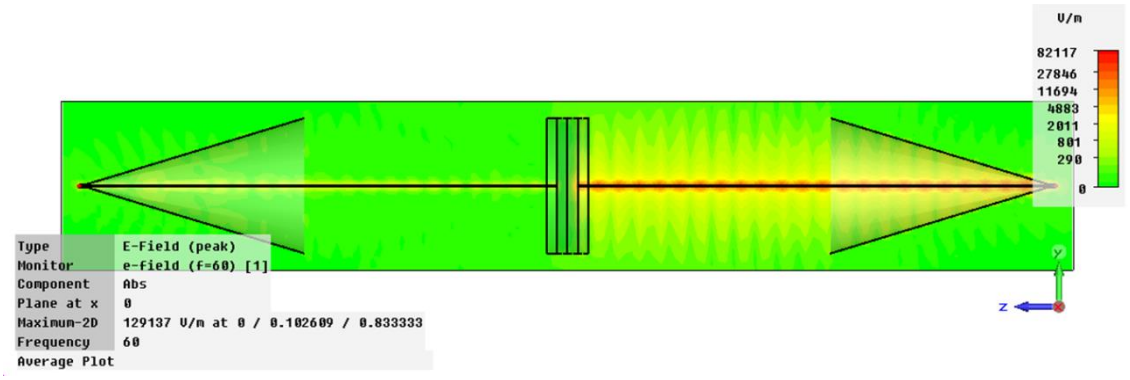

Figure 4.21 – Cross-section through the waveguiding for exciting the TM_{01} mode.

Simulated S-Parameters for the waveguiding structure of Figure 4.20 are shown in Figure 4.22. At 61.25 GHz $S_{11} < -20\ dB$ and S_{21} is approximately $-27\ dB$.

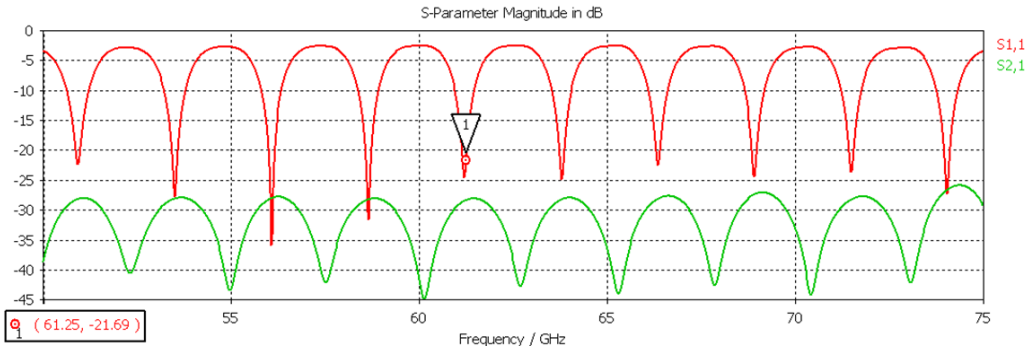

Figure 4.22 – Simulated S-Parameters of the waveguiding structure for exciting the TM_{01} mode.

4.12.3 Waveguiding Structure for Exciting the HE_{11} – Sample with no loss

A waveguiding structure for exciting the HE_{11} mode is shown in Figure 4.23 in a back-to-back configuration. The four discs in the centre of the figure represent a double-thickness skin sample (magenta) with *no* loss, and matching sections (blue) respectively. Excitation is launched as a TE_{10} mode in rectangular waveguide, e.g. WR42. It is then propagated as a HE_{11} mode via a circular dielectric transformer, a coaxial guide, and a bare conductor, diameter 1 mm.

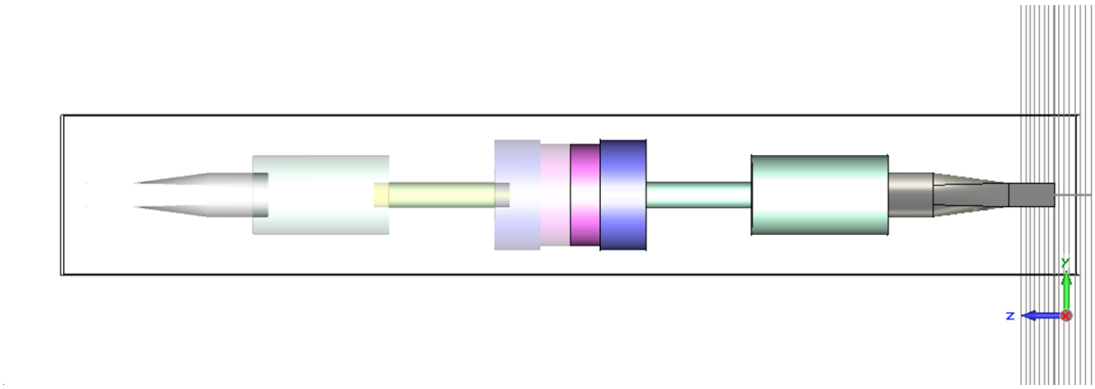

Figure 4.23 – Waveguiding structure for exciting the HE_{11} mode.

A lengthwise cross-section through the waveguiding structure of Figure 4.23 is shown in Figure 4.24. This shows the characteristic longitudinal mode pattern (red) of the HE_{11} mode as illustrated in Figure 4.7.

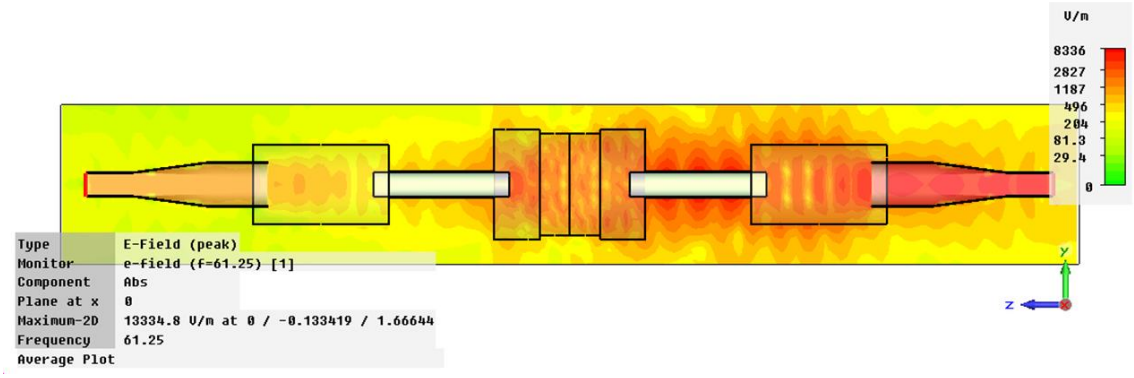

Figure 4.24 – Lengthwise cross-section through the waveguiding for exciting the HE_{11} mode.

Simulated S-Parameters for the waveguiding structure of Figure 4.23 are shown in Figure 4.25. At 61.25 GHz $S_{11} < -15\ dB$ and S_{21} is approximately $-16\ dB$. These figures are noted for comparison with the reflection coefficient and transmission loss in the next section where the skin sample has loss.

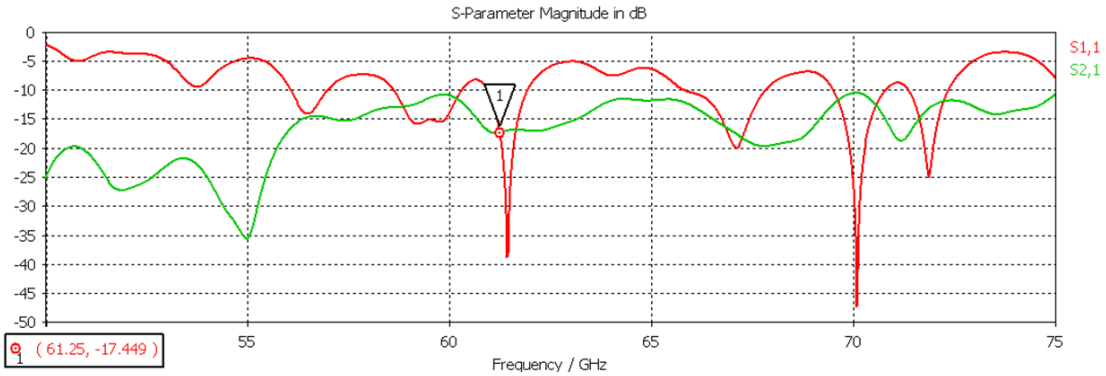

Figure 4.25 – Simulated S-Parameters of the waveguiding structure for exciting the HE_{11} mode.

4.12.4 Waveguiding Structure for Exciting the HE_{11} – Sample with loss

A waveguiding structure for exciting the HE_{11} mode is shown in Figure 4.26 in a back-to-back configuration. The four discs in the centre of the figure represent a double-thickness skin sample (magenta) with loss, and matching sections (blue) respectively. Excitation is launched as a TE_{10} mode in rectangular waveguide, e.g. WR42. It is then propagated as a HE_{11} mode via a circular dielectric transformer, a coaxial guide, and a bare conductor, diameter 1 mm.

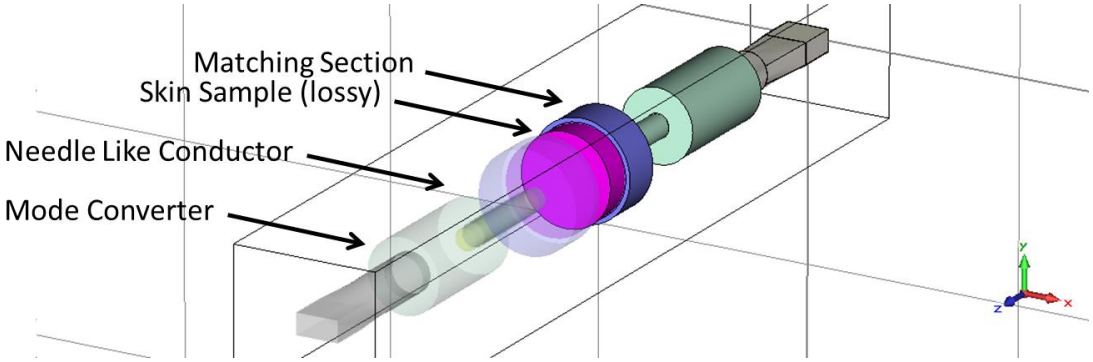

Figure 4.26 – Waveguiding structure for exciting the HE_{11} mode.

A cross-section through the waveguiding structure of Figure 4.26 is shown in Figure 4.27. This shows the characteristic mode pattern (red) of the HE_{11} mode with two main lobes diametrically opposite to each other and separated by nulls, as illustrated in Figure 4.7.

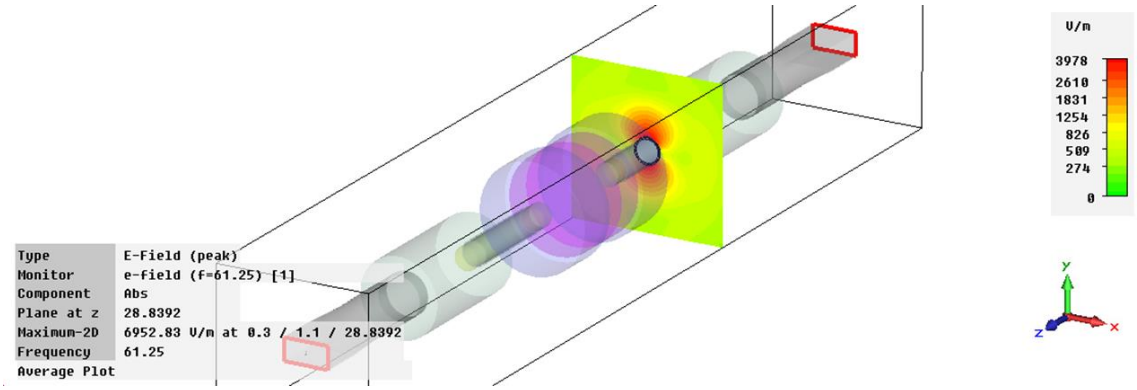

Figure 4.27 – The HE_{11} mode propagating on a bare conductor and the mode converter (two-off in back-to-back configuration) for excitation of the mode.

A lengthwise cross-section through the waveguiding structure of Figure 4.26 is shown in Figure 4.28. This shows the characteristic longitudinal mode pattern (red) of the HE_{11} mode as illustrated in Figure 4.7.

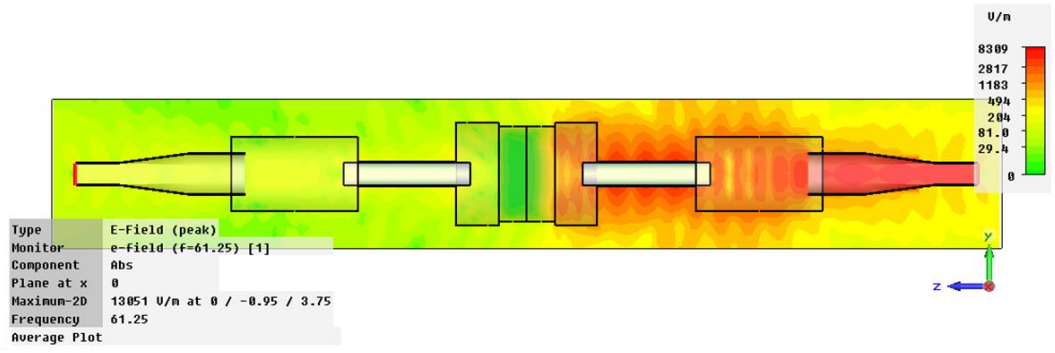

Figure 4.28 – Lengthwise cross-section through the waveguiding for exciting the HE_{11} mode.

S-Parameters for the waveguiding structure of Figure 4.26 are shown in Figure 4.29. At 61.25 GHz $S_{11} < -22\ dB$ and S_{21} is approximately $-35\ dB$.

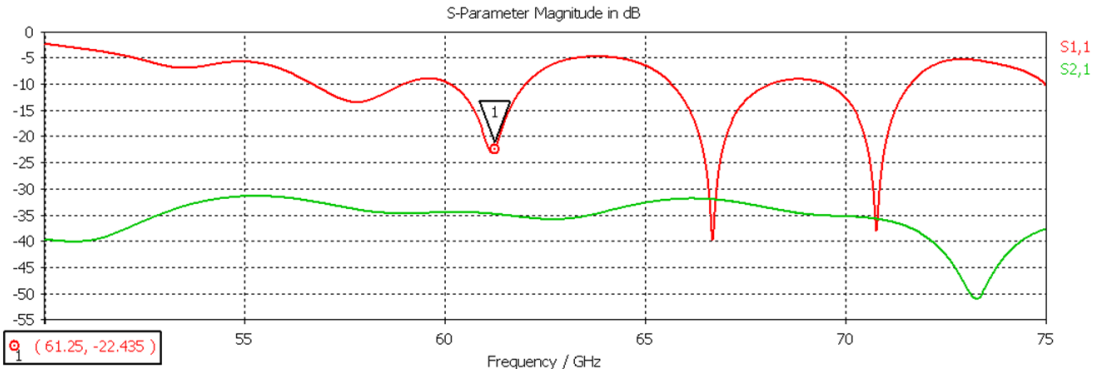

Figure 4.29 – Simulated S-Parameters of the waveguiding structure for exciting the HE_{11} mode.

4.13 Measurement of HE_{11} Mode

This section presents measurements of the HE_{11} mode on a constructed launcher, confirming the azimuthal pattern of the mode.

The setup for measuring the symmetry of the field pattern of the HE_{11} mode on a bare conductor is shown in Figure 4.30.

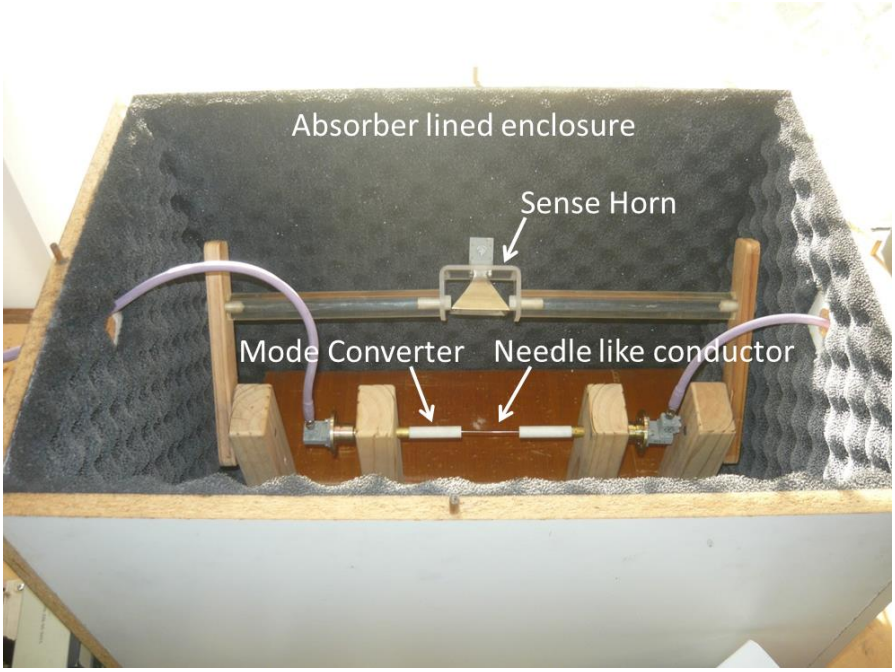

Figure 4.30 – Apparatus for measuring the properties of and determining the symmetry of a mode launched on bare conductors of different composition.

Measurements of the power received by the sense horn to measure the mode pattern as a function of angle are tabulated in Table 4.1 and plotted in Figure 4.31. Note that only the upper half plane was measured as symmetry can be invoked for the lower half plane.

Angle (degrees)	Rx Power (dB)
0	0
15	-2.5
30	-7.0
45	-9.0
60	-13.0
75	-16.5
90	-22.5

Table 4.1 – Measurements of power received by the sense horn as a function of angle.

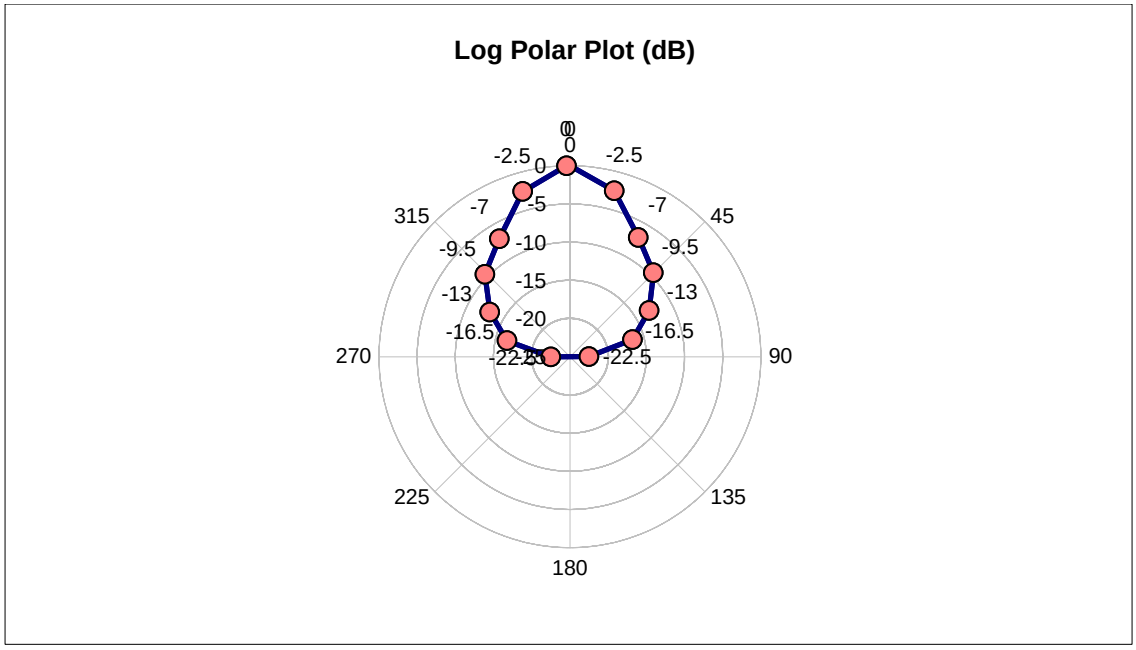

Figure 4.31 – Plot of the measurements of the HE_{11} mode pattern on a bare conductor.

The pattern has a variation from minimum to maximum of approximately 20 dB, and indicates a $\cos^2\theta$ behavior. This shows the characteristic HE_{11} mode pattern with two main lobes diametrically opposite to each other and separated by nulls, as illustrated in Figure 4.7.

4.14 Fano Mode

Having considered a large amount of foundational material, the key ideas from Sections 4.6 and 4.7 and now brought together in this section.

A lossless surface wave can be propagated by an interface if the permittivity of one of the media has a negative real part [147, 159], $\mu = 1$ for both media, and the dielectrics are assumed to have no spatial dispersion. The z axis is perpendicular to the interface with $z = 0$ corresponding to the interface. The x axis is in the direction of propagation of the surface wave while the orthogonal axis lies in the interface plane. Medium 1 is a pure non-absorbing dielectric, $\varepsilon_1 > 0$, and Medium 2 is a surface active medium $\varepsilon_2 = \varepsilon_{r2} - i\varepsilon_{i2}$ $(\varepsilon_{i2} > 0)$.

The E electric field has to be in the direction of propagation i.e. longitudinal, otherwise the electromagnetic wave cannot propagate. So, for isotropic media the surface electromagnetic

waves are transverse magnetic and are best described by the magnetic field component which lies in the plane of the interface and in the y direction:

$$\mathbf{H} = H_0 f(z) \exp[i(\omega t - kx)] = H_y \tag{4.40}$$

where $k = k_r - ik_i$ and $f(z)$ describes the dependence of $\mathbf{H}$ on the distance away from the interface $[f(0) = 1]$, and H_0 is a normalization constant.

The electric field may be calculated from Maxwell's equations:

$$E_x = \frac{i}{\omega\varepsilon}\frac{\delta H_y}{\delta x} \tag{4.41}$$

$$E_y = \frac{-k}{\omega\varepsilon} H_y \tag{4.42}$$

and the dependence f(z) for the two media is

$$f(z) = e^{-\alpha_1 z} \quad z > 0, \text{Medium 1} \tag{4.43}$$

$$f(z) = e^{-\alpha_2 z} \quad z < 0, \text{Medium 2} \tag{4.44}$$

where the coefficients α_1 and α_2 are obtained from the wave equations as

$${\alpha_1}^2 = bk^2 - {k_0}^2 \varepsilon_1 \tag{4.45}$$

$${\alpha_2}^2 = bk^2 - {k_0}^2 \varepsilon_2 \tag{4.46}$$

where $k_0 = \omega/c$ is the free-space wave vector at frequency ω. α_1 and $\alpha_2$are both complex, leading to oscillating decaying fields in both half spaces.

Continuity of the tangential electric field, E_x, at $z = 0$ leads to the dispersion relation:

$$\varepsilon_1\alpha_2 + \varepsilon_2\alpha_1 = 0 \tag{4.47}$$

This equation has to be satisfied if a surface wave mode is to exist. The propagation parameters are:

$$k_0\left[\frac{\varepsilon_1}{(\varepsilon_{r2}+\varepsilon_1)^2+\varepsilon_{i2}^2}\right]^{1/2}\left[\frac{\varepsilon_e^2+(\varepsilon_e^4+\varepsilon_i^2\varepsilon_{i2}^2)^{1/2}}{2}\right]^{1/2} \tag{4.48}$$

$$k_0\left[\frac{\varepsilon_1}{(\varepsilon_{r2}+\varepsilon_1)^2+\varepsilon_{i2}^2}\right]^{1/2}\frac{\varepsilon_{i2}\varepsilon_1}{\left[2(\varepsilon_e^2+(\varepsilon_e^4+\varepsilon_i^2\varepsilon_{i2}^2)^{1/2})\right]^{1/2}} \tag{4.49}$$

A negative dielectric can be achieved by embedding a regular lattice of various shapes in a regular dielectric. Now consider a rectangular array of thin wires as shown in Figure 4.32 below, because these have been modelled and measured, and are easy to fabricate. This has been analyzed as an electron plasma, where the electrons have a large effective mass due to the electromagnetic interaction between the wires [194]. Such a plasma exhibits a resonance, with a negative effective dielectric near resonance. Damping occurs due to resistive losses in the wires.

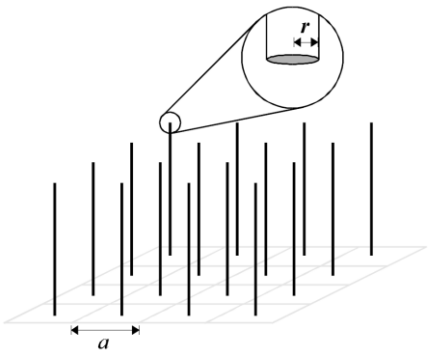

Figure 4.32 – Array of thin wires. From [194].

The analysis in [194] considers only magnetic interaction to compute the plasma frequency. However, the electromagnetic fields near a thin wire are complex:

$$E_r=\frac{|\mu|\cos\vartheta}{4\pi\varepsilon_0\varepsilon}\frac{exp(ikr)}{r}k^2\left[\frac{2}{k^2r^2}-\frac{2i}{kr}\right] \tag{4.50}$$

$$E_\vartheta=\frac{|\mu|\sin\vartheta}{4\pi\varepsilon_0\varepsilon}\frac{exp(ikr)}{r}k^2\left[\frac{1}{k^2r^2}-\frac{i}{kr}-1\right] \tag{4.51}$$

$$H = H_\varphi = \frac{|\mu|\sin\vartheta}{4\pi\varepsilon_0\varepsilon}\frac{exp(ikr)}{r}k^2\left[-\frac{i}{kr}-1\right]\sqrt{\frac{\varepsilon_0\varepsilon}{\mu_0\mu}} \tag{4.52}$$

Even the kernel of this field dependence is complex as shown in Figure 4.33 below.

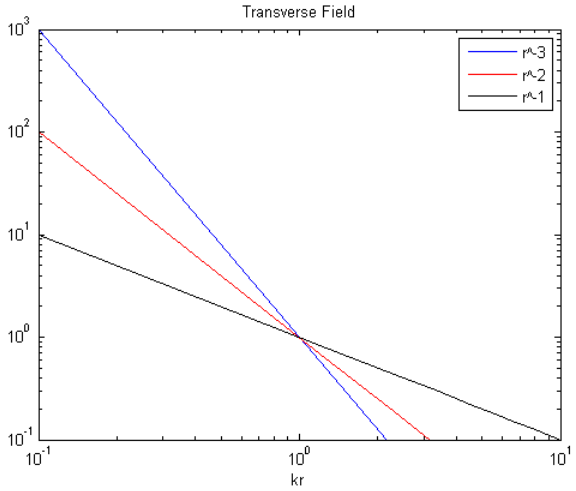

Figure 4.33 – Radial dependence of transverse field kernel.

Thus, only approximations to the interaction can be made [195]. Hence:

$$(k_p a)^2 \approx \frac{2\pi}{0.5275 + log\frac{a}{2\pi r_0}} \text{ for } r_0 \leq 0.1a \tag{4.53}$$

For a plasma resonance of 24 GHz, $a = 5$ mm, $r_0 = 0.265$ mm. Material science specialists were contacted to determine whether it would be feasible to fabricate an artificial dielectric using nanotechnology to demonstrate propagation of the Fano mode, however it could not be reasonably achieved within the timescale and resources of this research project. Future research will be to model, fabricate and test such an artificial dielectric and adapt it to something suitable as a coating for a needle near 60 GHz.

4.15 Conclusion

In this chapter a design of an acupuncture-like needle for the efficient delivery of millimeter waves through the skin has been studied. This study has been motivated by the intriguing possibilities of millimeter wave, cellular and higher level, biological interactions, that were

discussed and investigated in Section 2.5, and the potential to terminate termites, or to alter their social behavior, as reported in experiments in Section 2.7. Two facets that make this study unique are the investigation of the excitation of the HE_{11} mode on the conductor-like needle and the study of the potential for propagation of the TM_{01} mode and HE_{11} mode on the needle with low loss.

In this chapter, the problem of the existence, the excitation and the propagation with low loss of the HE_{11} mode on a conductor have been studied. Contrary to prevailing understanding, it has been shown that a bare conductor can sustain two dominant modes: the well-known symmetric TM_{01} mode, and the hitherto forgotten and overlooked asymmetrical HE_{11} mode. The HE_{11} mode has two main lobes separated by nulls, i.e. is asymmetrical in the azimuthal plane. This enables the selective delivery of power to tissue in preferred directions by appropriate positioning of the two lobes, whilst avoiding others by the positioning of the nulls. Unlike the TM_{01}, it has been shown that the HE_{11} mode can propagate on a bare conductor as a pair of orthogonally polarized modes, enabling polarization sensing and control. Nevertheless, as both modes are dominant, exciting the HE_{11} mode is a challenge. However, it has been shown that the HE_{11} mode can be made to propagate on a conductor with low loss. However, loss in the conductor to support the propagation of the mode is essential, and unavoidable.

The study has introduced an alternative interpretation of waveguide modes based on the current distribution on the guiding structure, rather than the field distribution has been introduced. It has also identified that for a dielectric with negative permittivity, there is a displacement D in the opposite direction to the E field in free space that can be used to close the E field loop and thus permits the propagation of electromagnetic waves then occurs without loss.

The study has examined the TM_{01} field mode and shown how it has zero cutoff because there is no azimuthal dependence of the current and hence no frequency dependence. It has also shown how the HE_{11} field mode has zero cutoff because the azimuthal dependence can be induced by interposing a perfectly conducting sheet down the middle of the waveguide. This study has also explained why higher order modes have a cutoff frequency.

Numerical studies have demonstrated the design of a structure to launch HE_{11} mode onto an acupuncture-like needle. Experiments at microwave frequencies have made measurements of the HE_{11} mode propagating on the conductor. In these experiments the measured nulls in the HE_{11} mode are over 20 dB.

This study investigated the possibility of removing the requirement for losses in the conductor to support either the TM_{01} mode or the HE_{11} mode, by coating a bare conductor with an artificial dielectric having negative permittivity, which can support the lossless Fano mode [147], and propagating both TM_{01} and HE_{11} modes with no ohmic conductor losses.

Contrary to that which has been known or demonstrated previously [143-146], this study has demonstrated that an acupuncture-like needle can sustain the propagation of two dominant modes: the well-known symmetric TM_{01} mode and an asymmetric HE_{11} mode, and that an artificial dielectric coating can lower or avoid losses. This phenomenon is frequency independent and does not depend on the circumference of the conductor.

This page has intentionally been left blank.

5 Conclusion

5.1 Conclusion

This chapter summarizes the investigations undertaken in this thesis and reiterates the author's original research contributions to knowledge in the field of absorption and scattering of microwaves by dielectric scatterers such as termites and ants.

The aim of the research presented in this thesis has been to study the application of radar to the detection of termites and the imaging of their activity in-situ, and to develop a design for a MIMO imaging radar for detecting and imaging termite activity.

In this thesis, it has been shown that the application of radar to the detection of termites and the imaging of their activity in-situ poses many challenges. Insects such as termites and ants are composed mainly of water, and are dielectric scatterers with large values of refractive index and absorption at microwave and millimeter wave frequencies. It has been shown that, the characteristics of absorption and scattering of a dielectric object are important in designing a radar for detection and imaging of termite activity, and that radar returns from termites are comparatively small, yet the building materials produce distortions due to losses and anisotropies and enormous backscatter returns.

The investigation present in this thesis has comprised theoretical, numerical and experimental studies, and has demonstrated the possibility of not only the detection and imaging of termite activity, but also the possibility of the provocation and control of termites using suitable millimeter and sub-millimeter waves wave emissions.

This thesis has also presented the design and experimental test results of a novel wave guiding structure consisting of an open waveguide with an artificial dielectric coating supporting the HE_{11} mode, a mode which is inherently broadband having no cut-off, and which could be used

to provide a millimeter wave stimulus directly to a termite. This guiding structure has the potential to deliver millimeter waves through the skin more efficiently than other techniques [55, 56], and has possible applications to millimeter wave therapeutic treatments including acupuncture.

Finally, this thesis has presented research on the design of an imaging MIMO radar for Unmanned Aerial Vehicles (UAVs), where target and platform velocities are very much greater than those observed in detecting and imaging termite activity. Although it has been assumed that the sequences exist and are suitable for MIMO radar, many of the proposed sequences have unsuitable properties. This thesis shows that small Kasami, Kamaletdinov construction 2 and Moreno-Tirkel Family B sequence families have properties which make them suitable candidates for the sequences for high resolution imaging MIMO radar, though the Kamaletdinov construction 2 and Moreno-Tirkel Family B sequence families are the superior of the three. These results have application to a wide range of problems in imaging radar such as through-the-wall radar, medical imaging, security screening and non-destructive testing.

5.2 Future Research

In addition to the analysis, modelling, simulation, experimentation, observations, results and conclusions presented in this thesis, further study which could be undertaken in the areas considered in this thesis may include:

- Modeling of absorption and scattering specifically of ants where it might be expected that they have higher frequency resonances as they have waists and are like two prolate spheroids touching together.
- Undertake field testing of exposing termites to microwave and millimeter waves to determine whether it is possible to eradicate termites, or to alter their social behavior by direct exposure.

- Realize a two-dimensional imaging MIMO radar, for imaging termite activity and for UAV imaging radar and undertake field measurements.
- More advanced experimental investigation of millimeter wave higher level biological interactions and of cellular biological interactions.
- Characterize through measurement, the attenuation and losses, small as they may be, of the HE_{11} mode on a (bare) conductor.
- Develop the alternative interpretation of waveguide modes based on the current distribution on the guiding structure, rather than the field distribution.
- Scale the acupuncture-like needle for the efficient delivery of millimeter waves through the skin to the millimeter wave band between 60 and 90 GHz, which are considered therapeutically important.
- Demonstrate the potential for propagation of both the TM_{01} mode and the HE_{11} mode on the needle with low loss.
- Fabricate and characterize an artificial dielectric and adapt it as a coating for a needle in the millimeter wave band between 60 and 90 GHz.
- Trial under laboratory and clinical conditions the efficacy of a conductor-like needle to efficiently deliver millimeter waves through the skin.

This page has intentionally been left blank.

Appendix A Microwave Scattering and Insect Morphology

A.1 Introduction

A thorough understanding of insect morphology and its effects upon microwave scattering is required if in order to detect termites successfully. The objectives of this appendix are to develop the theory of insect movement detection using near-field techniques. This is important because it provides the underlying understanding of the mechanisms of detecting termites using near field techniques and the theory on which a termite detector could successfully be developed.

A transmitter antenna located at coordinates $(-r_T, -\theta_T, -\phi_T)$, as shown in Figure A.5.1 and Figure A.5.2 below, is excited by an equivalent current $I = I_T \cos(\omega t)$, which induces an equivalent voltage $V = V_T \cos(\omega t)$, where the impedance of free space, $Z_o = 377\Omega$. An alternative description can be provided by $\left(E_\theta, E_\varphi, H_\theta, H_\varphi\right)$. The transmitter has a spatial magnitude distribution pattern, $\Psi_T(r_T, \theta_T, \phi_T)$ and phase distribution pattern, $\Phi_T(r_T, \theta_T, \phi_T)$.

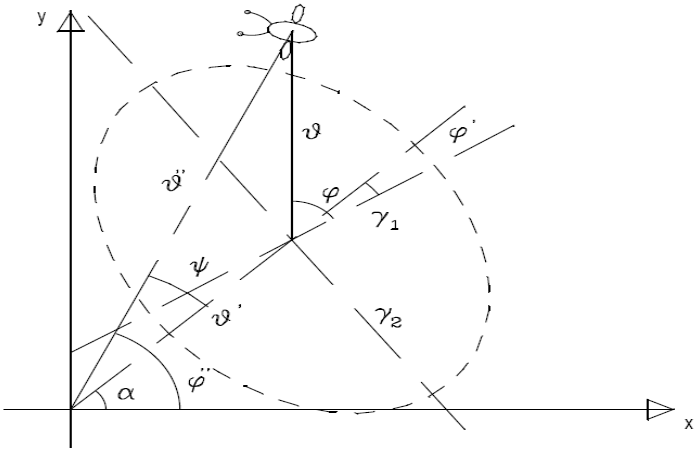

Figure 2.2: Target position relative to the beam axes and fixed system axes. Note that the radial displacements $(\theta, \theta', \theta'')$ are expressed as angles by dividing by the target range.

Figure A.5.1 – Target position relative to the beam axis and the fixed system axis. From [196].

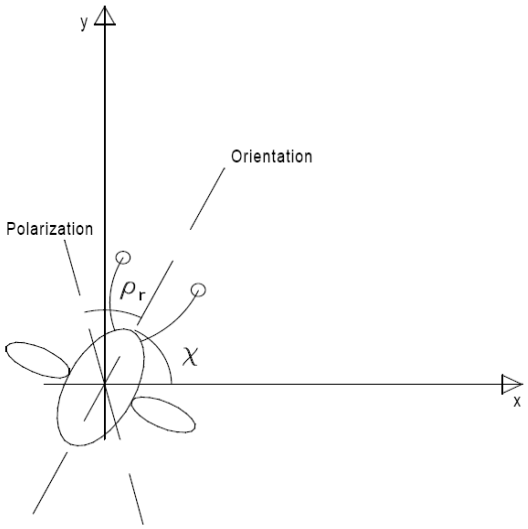

Figure 2.3: Target relative polarization ρ_r and the absolute orientation χ. The absolute polarization is $\rho = \rho_r + \chi$.

Figure A.5.2 – Target relative polarization. From [196].

Scattering by moving targets requires knowledge of the spatial magnitude distribution pattern and the phase distribution pattern and their local gradients in order to differentiate termites and insects from stationary background clutter by target Doppler and amplitude fluctuations

as discussed in Section 3.1. In the far field, an equi-amplitude contour is described by, $\Psi_T = \frac{1}{r_T}$, so $\underline{\nabla}\,\Psi_T = -\frac{\widehat{r_T}}{r^2}$, and in the near field an equi-amplitude contour is a function of $\frac{1}{r_T}, \frac{1}{r_T^2}$ and $\frac{1}{r_T^3}$. Likewise, in the far field an equi-phase contour is described by, $\Phi_T = \frac{r_T}{c}$, so $\underline{\nabla}\,\Phi_T = \frac{\widehat{r_T}}{\mathrm{c}}$, and in the near field an equi-phase contour is a function of $\frac{1}{r_T}, \frac{1}{r_T^2}$ and $\frac{1}{r_T^3}$.

Consider a target centred at the origin, occupying a volume $\Delta\,\mathrm{V}$, with scattering cross-section σ, moving with a velocity $v(r, \theta, \phi)$. The target is small, that is small compared with the variations in the magnitude and phase profiles of the transmitter antenna and a receiver antenna, so that the magnitude and phase of the transmitter signal and a receiver signal can be considered as constant over the target volume. The scattered energy is determined by the product of the scattering cross-section of the target, σ, and the incident field at the target. If the target is large, it can be represented as an ensemble of small targets.

The scattered energy is directed in all directions. However, the only direction of interest is that towards the receiver antenna, located at (r_R, θ_R, ϕ_R) with respect to the target. This ignores the possibility of multipath propagation (multiple scattering). The scattering cross-section is therefore a function of the bistatic angle, $\zeta_B = (\theta_T - \theta_R, \phi_T - \phi_R)$. For non-spherical targets, it may also be a function of the incidence angle, variously called aspect angle, or orientation angle, $\xi_I = (\theta_I - \theta_P,\ \phi_I - \phi_P)$, with respect to the orientation of the target's principal axes, $\chi_P(\theta_P, \phi_P)$, and the polarization vector, $\chi_E = (\theta_E - \theta_P, \phi_E - \phi_P)$, also considered with respect to the orientation of the target's principal axes. The above analysis is true for all targets regardless of their symmetry.

A.1.1 Targets with Symmetry

However, most insects approach cylindrical symmetry, so in such cases, the angles can be reduced to $\xi_I = (\theta_I - \theta_P)$, and $\chi_E = (\theta_E - \theta_P)$, as analysed by Huynen [197]. Clearly, insects

are really not quite symmetrical in a rotational sense. Insects generally exhibit bilateral symmetry [198], i.e. they are approximately mirror-symmetric about the plane defined by their head-tail and dorsal-ventral axes. Then again, "an organism's bilateral symmetry is not perfect" [199]. Therefore, the following analysis remains general, and the Huynen reduction of angular complexity [197], that the polarimetric matrix can be uniquely determined by measuring a target's response for six polarisations and inverted, can be introduced subsequently as a simplification. This simplification will be applied to the specific case of insects with bilateral symmetry in the following section.

Consider a principal axis oriented at some spherical angle, $\chi_P(\theta_P, \phi_P)$, with respect to the polarization vector of the incident electric field. Linear polarization is assumed, although this could be generalized to any polarization. Many targets (prolate and oblate spheroids, cylinders, cones, ovoids, ogives etc. [2]) have two orthogonal principal axes, and the scattering cross-section for all polarizations is known. For targets composed of a combination of standard shapes, e.g. insects, the scattering is complicated. For example, an ant can be described as three conjoined prolate spheroids, with legs and antennae. In this case, multiple scattering reflections (i.e. multipath propagation) cannot be ignored, and therefore scattering from such complicated targets is beyond the scope of this analysis.

A.1.2 Scattering Cross-section

The following analysis is from Dean and Drake [200]. The simplified geometry and underlying assumptions about aspect angle and polarization dependence of backscattered radar cross-section (RCS) are taken from Wolf et al. [201].

The following is extracted from Wolf et al. [201], with geometry shown in Figure A.5.3 below.

Aspect Angle Effects

Aspect angle refers to target alignment with respect to the radar beam as illustrated in Figure A.5.3. *Ruck et al. [2], give the Rayleigh region RCS of an ellipsoid for varying aspect angles. For our* (ventral i.e. insects viewed from below) *aspect angles, Ruck's equation can be simplified to:*

$$\mathrm{RCS} = K_1(1 + K_2 \cos^2 \alpha)^2 \qquad \text{(A.1)}$$

where α is aspect angle, while $K_1$and K_2depend on the dimensions of the ellipsoid and its composition. Additionally, K_1depends on the observing wavelength and K_2depends on polarization.

Polarization Effects

Huynen [197] derived and expression for the RCS of any target versus polarization angle for a fixed aspect angle. Aldhous [202] rearranged Huynen's equations for a target with a plane of mirror symmetry that includes the observing line of sight. The rearranged equation is:

$$\mathrm{RCS} = a_0 + a_1 \cos 2(\phi - \theta_1) + a_2 \cos 4(\phi - \theta_2) \qquad \text{(A.2)}$$

where the constraints a_1, a_2, θ_1 and $\theta_2$describe the shape of the curve shown in figure 3 of [201]. Constant a_0 is the average RCS as polarization angle changes from 0° to 180°. The polarization angle ϕ that produces the maximum RCS indicates to which direction (to an uncertainty of $\pm$90° or 180°) the long axis of the insect's body.

Define the polarization modulation as:

$$\mathrm{Mod} = (\mathrm{RCS}_{max} - a_0)/a_0 \qquad \text{(A.3)}$$

This RCS parameter is related to target shape. Maximum and average RCS values are obtained from Equation (A.2). Spherical targets have zero modulation.

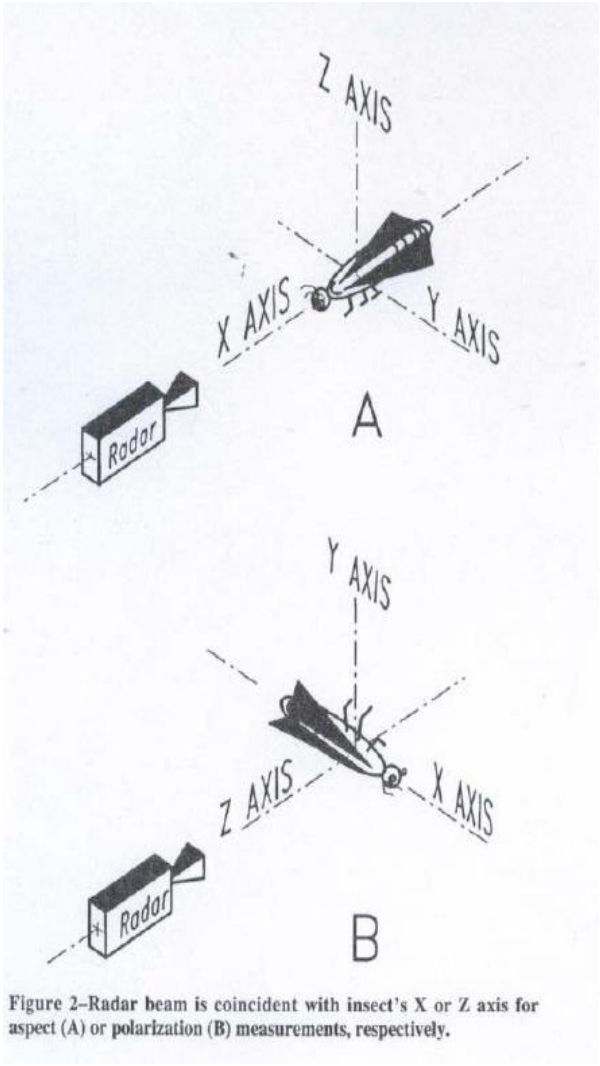

Figure 2–Radar beam is coincident with insect's X or Z axis for aspect (A) or polarization (B) measurements, respectively.

Figure A.5.3 – Geometry for the measurement of aspect angle and polarization effects. Extract from Wolf et al. [201].

The underlying assumption is that σ is invariant under polarization or aspect angle changes of 180^{o} (since this is equivalent to a phase shift of 180^{o}). Therefore σ is a sum of even harmonics of the polarization or aspect angles only. The components $\cos 2\theta$ and $\cos 4\theta$, with θ aligned with one of the symmetry axes, appear to be sufficient to provide a good fit with observed data. However, aspect angle harmonics are all even, since there is a head-tail asymmetry, and a fit with $\cos \theta$ should be possible.

The following is extracted from Dean and Drake [200].

For a general treatment, see Huynen [197] equation (20), or a more specific treatment, see Aldhous [202], of electromagnetic backscattering employing the scattering matrix $\boldsymbol{S}$*, it can be shown for the co-polar-linear configuration, the instantaneous received power* P *at the antenna will vary with polarization angle* ϕ *as*

$$P(\phi) = P_0(A_1 + A_2 \cos 2(\phi - \beta) + A_3 \cos 4(\phi - \beta) + A_4 \sin 4(\phi - \beta))$$

(A.4)

where, A_1*,* A_2*,* A_3*, and* A_4 *are properties of the target (and of its aspect to the beam),* β *defines a target-orientation direction, and* P_0 *is the power that would be received from a target of unit size at the same position.*

$$p(\phi) = 1 + \alpha_2 \cos 2(\phi - \beta) \pm \alpha_4 \cos 4(\phi - \beta) \quad \text{(A.5)}$$

Dean and Drake [200], analyze physical and mathematical constraints on α_2 and α_4 to obtain the following polarization patterns, see Figure A.5.4 below. Observational data for the ventral aspect of airborne insects demonstrates a good fit for this model, see Figure A.5.5 below.

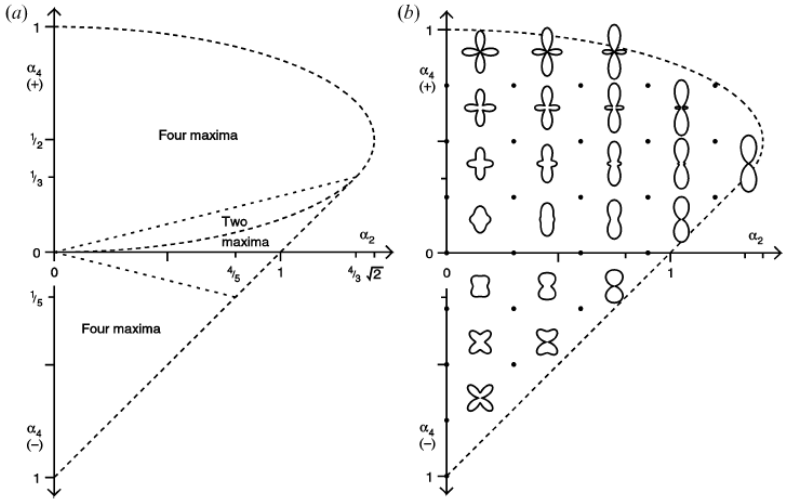

Figure 1. (*a*) The boundary of the region of the α_2–α_4 plane in which the symmetric CLPP (equation (5)) remains +ve at all polarization angles ϕ. The upper half shows the boundary for when the sign of the α_4 term in equation (5) is +ve, and the lower half for when it is –ve. Lines subdividing the region according to whether the pattern has two or four maxima are also shown, along with the lower constraint boundary arising from equation (13) and the values of α_2 and α_4 for the various intersection and extremum points. (*b*) Symmetric CLPP forms (equation (5)) for a range of α_2 and α_4 values, each shown at its corresponding location in the α_2–α_4 plane and with β aligned to the vertical (α_4) axis. The small circles indicate the set of 26 (α_2, α_4) pairs used in the simulation analysis.

Figure A.5.4 – Possible observable polarizations (i.e constrained) of airborne insects, ventral aspect. From [200].

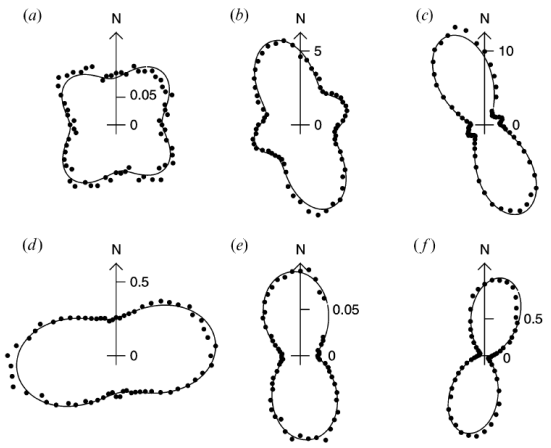

Figure 2. Examples of CLPPs retrieved from good-quality echoes. Radial units are cm^2. Target heights and parameter values are given in table 1. Observations made at Bourke on 15 November 1999 between 22.00 and 22.45 h AEST.

Figure A.5.5 – Observed polarizations of airborne insects, ventral aspect. From [200].

Variation with Target Movement

Additionally, the scattering cross-section of some targets may vary with time, e.g. if the target changes its shape during its movement. Henceforth, the coordinates are assumed to be

referenced from the transmitter for subscript T. The scattered signal consists of a static scatter, I_S^0, with Ψ_T and Φ_T as defined previously is:

$$I_S^0 = \sigma I_T[\Psi_T(r_T, \theta_T, \phi_T)] \cos(\omega t - \Phi_T(r_T, \theta_T, \phi_T)) \tag{A.6}$$

and a time varying scatter, $\mathrm{d}I_S$:

$$\begin{aligned} \mathrm{d}I_S = \big\{ & \Delta\sigma I_T[\Psi_T(r_T, \theta_T, \phi_T)] \cos\big(\omega t - \Phi_T(r_T, \theta_T, \phi_T)\big) \\ & + \sigma I_T\big[\underline{\nabla}\Psi_T(r_T, \theta_T, \phi_T) \cdot \underline{v}\big] \cos\big(\omega t - \Phi_T(r_T, \theta_T, \phi_T)\big) \\ & - \sigma I_T[\Psi_T(r_T, \theta_T, \phi_T)] \sin\big(\omega t + (\underline{\nabla}\Phi_T(r_T, \theta_T, \phi_T) \cdot \underline{v})\big)\big\} dt \end{aligned} \tag{A.7}$$

where, with ξ_I, ζ_B and χ_E as defined previously (see Section A.1.1),

$$\Delta\sigma = \left[\frac{\partial\sigma(\xi_I, \zeta_B, \chi_E, t)}{\partial\xi_I}\frac{\partial\xi_I}{\partial t} + \frac{\partial\sigma(\xi_I, \zeta_B, \chi_E, t)}{\partial\zeta_B}\frac{\partial\zeta_B}{\partial t} + \frac{\partial\sigma(\xi_I, \zeta_B, \chi_E, t)}{\partial\chi_E}\frac{\partial\chi_E}{\partial t} + \frac{\partial\sigma(\xi_I, \zeta_B, \chi_E, t)}{\partial t}\right] \tag{A.8}$$

The first term in the time-varying scatter from insects is due to:

1. Fluctuations in the incidence angle due to linear insect movement, and rotational insect movements: yaw, pitch, roll.
2. Fluctuations in the bistatic angle due to linear insect movement.
3. Fluctuations in the principal axes orientation due to insect rotations, affecting polarization.
4. Fluctuations in insect scattering cross-section due to movement of its body parts.

Simplification for a Spherical Droplet

There is one notable example, where this scattering is simple - that of a falling water droplet. Its shape is approximately spherical, and the scattering cross-section is a function of the

bistatic angle only. It is also a model for the scattering from insects, as shown by Riley [203], who has found good correlation in general for this model.

Complication for Insects

The scattering cross-section of insects follows that of water drops of comparable size, as a function of incident wavelength (Rayleigh, Mie and optical region). However, there are significant individual departures, which may be due to the fact that a lot of data is obtained from far field scattering from moving insect swarms, and deviations may be due to the factors summarised in the equation above. Also, the scattering depends on the dielectric constant and loss factor of the insect. This has been studied extensively by Nelson [204], who found the dielectric factor to be between approximately 20 and 45 and for the loss factor to between approximately 10 and 30 respectively, for rice weevils, as shown in Figure A.5.6 and Figure A.5.7 below. Note the temperature dependence.

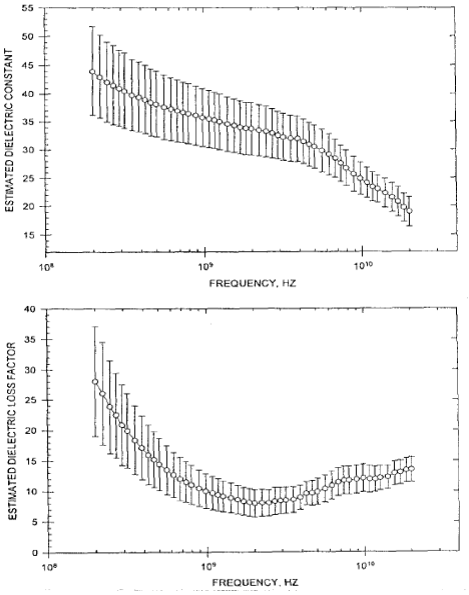

Fig. 5. Mean values of adult rice weevil permittivities at 25 °C estimated by computation with (2) from measured permittivities of bulk adult rice weevil samples and bulk densities corrected with (1). Error bars represent ±one standard deviation over eight measurement sequences.

Figure A.5.6 – Mean values of rice weevil permittivity at 25°C. From [204].

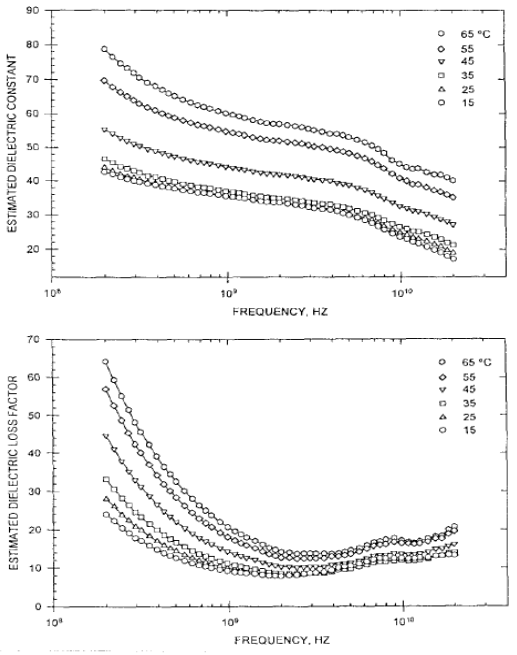

Fig. 6. Mean values of estimated permittivities of adult rice weevils at indicated temperatures.

Figure A.5.7 – Mean values of rice weevil permittivity at temperatures indicated. From [204].

The radar configuration can determine which of the above mechanisms are important. A desirable feature of the radar is that it should be sensitive to any parameter associated with insect movement. Clearly, the incidence angle will vary with insects traversing large distances on the inner surface of a wall. Such changes of incidence can produce changes in cross-section and therefore changes in the received signal magnitude (desirable). However, a radar has no control over that angle, unless it is free to move, and this is impractical.

The bistatic angle is a different entity. It is governed by the insect movement, but also, by the displacement between the transmitter and receiver. Every object, even a sphere, exhibits cross-section fluctuations with bistatic angle [2]. However, these features occur for high bistatic angles, around 60 ^{o} to 120^{o}. This requires very large separation of transmitter and receiver, and possibly movement thereof, so it is also impractical. The movement is mentioned because the insect motion causes only one component of the bistatic angle to change, without any effect in the orthogonal direction. Therefore, any cross-section fluctuations depend on the direction of insect motion. This can lead to missed detections.

Therefore, the radar may as well be monostatic (bistatic angle, $\zeta_B = (\theta_T - \theta_R, \phi_T - \phi_R)$ =180^o. For such a radar, the cross-section variation is described by:

$$\Delta\sigma = \left[\frac{\partial\sigma(\xi_I, \chi_E, t)}{\partial\xi_I}\frac{\partial\xi_I}{\partial t} + \frac{\partial\sigma(\xi_I, \chi_E, t)}{\partial\chi_E}\frac{\partial\chi_E}{\partial t} + \frac{\partial\sigma(\xi_I, \chi_E, t)}{\partial t}\right] \quad \text{(A.9)}$$

In a practical application, the presence of a varying bistatic angle may be a complication, but a good one, in that any peaks and dips in the RCS as a function of the bistatic angle may translate into additional modulation. Such modulation may be complicated and difficult to analyze, but it can provide more signal. For an insect travelling on a flat surface at range, R from the radar, the incidence angle changes due to any motion. If the insect moves in a curve, or exhibits yaw, then the second term can also change. At its most sensitive, this change can be 0.2 dB per degree, see Riley [203], Figure 2. Therefore, a 15^o change of orientation can be significant.

In summary, signal variations can occur due to insect motion, because the first two terms in Equation (A.9) depend implicitly on insect velocity (magnitude and direction). Control over the incidence (aspect) angle is difficult (maybe impossible), whilst polarization control is possible. Rotating linear polarization offers the following advantages:

1. SNR improvement at the aligned direction i.e. peak scattering cross-section for that aspect angle (up to 10dB improvement).
2. Information about insect orientation. Important for tracking and insect movement analysis[2].
3. Polarization modulation allows for observation frequency to be moved to something useful like 100Hz or so. This avoids 1/f noise components from the receiver and the radar amplitude modulation noise. SNR improvement up to 10dB.

[2] The main objective is to track the termites back to the nest. Termites usually move straight ahead, so knowing their orientation can help in deducing the direction of their local trail and eventually the nest.

4. Coherent detection of modulation offers another 3-6 dB SNR improvement.
5. Filtering (digital signal processing) at 100Hz is much easier i.e. bandpass filters, etc. become straightforward.

If the polarization is rotated at a constant rate, ω, then Dean and Drake [200], suggest that target cross-section variations should induce amplitude modulation at 2ω and 4ω. The relative magnitudes at these two frequencies indicate the shape of the target, as shown in [200]. Of course, some of these results will have to be modified, since Termatrac® can encounter termites at various aspect angles, whereas entomological radar in [200] is restricted to the ventral aspect. These modulations may also be superimposed on material induced modulation.

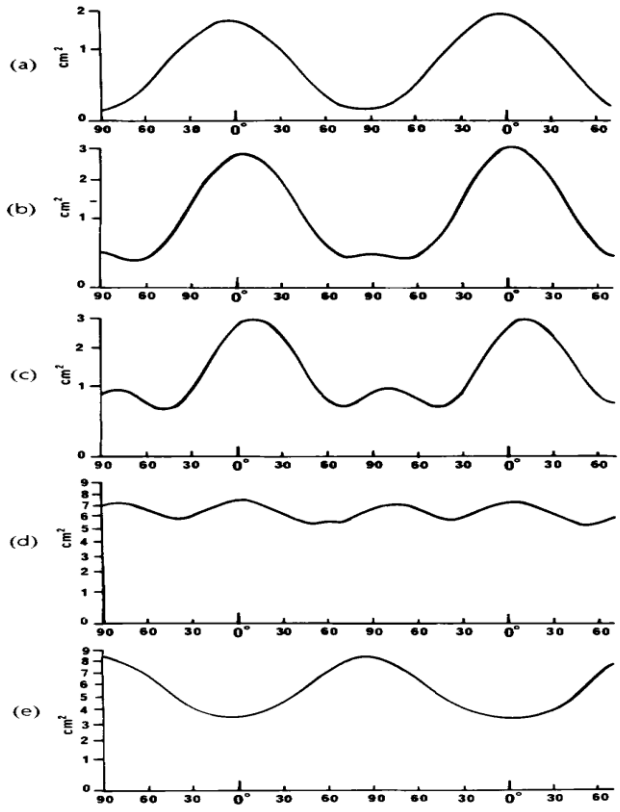

Fig. 2. Variation of radar cross section as a function of angle between body axis and *E*-vector. The progression from (a) to (d) shows the effect of increasing insect size on the development of subsidiary maxima when the *E*-vector is at 90° to the body axis. (a) *Spodoptera littoralis*, 95 mg. (b) *Spodoptera littoralis*, 220 mg. (c) *Melanoplus sanguinipes*, 320 mg. (d) *Schistocerca gregaria*, 2590 mg. (e) *Locusta migratoria*, 3120 mg. All insects were alive but anaesthetized.

Figure A.5.8 – Variation of radar cross section as a function of angle between body axis and E vector. From [200].

It should be noted that the above changes result in signal fluctuations independently of the transmitter and receiver field profiles and occur in the near or far field of either. In general, radar cross-section fluctuations are described by log-normal processes or the Swerling model, see Figure A.5.9 below.

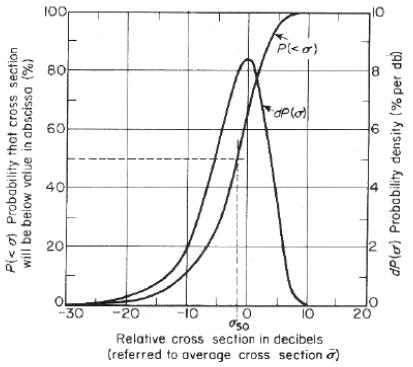

Figure 10.16: Log plot of the Rayleigh distribution

Figure A.5.9 – Log plot of the Rayleigh distribution. From [205].

The second term in Equation (A.7) is amplitude modulation due to the insect traversing equi-amplitude contours, whilst the third term is phase modulation due to the insect traversing equi-phase contours (Doppler). It is assumed that the observation interval dt is small, so that all the terms in Equation (A.7) are small compared to the static scatter in Equation (A.6) so that cross-products are negligible.

The signal scattered from the termite travels back to the receiver antenna. The receiver has its own equi-amplitude and equi-phase contours. Henceforth, the coordinates are assumed to be referenced from the transmitter for subscript T and from the receiver for subscript R. The static received signal at the receiver antenna, I_R^0, with Ψ_T and Φ_T as defined previously is:

$$I_R^0 = \sigma I_T[\Psi_T(r,\theta,\phi)]\,[\Psi_R(r,\theta,\phi)]\cos\big(\omega t - \Phi_T(r,\theta,\phi) - \Phi_R(r,\theta,\phi)\big)$$

(A.10)

and the dynamic receiver signal, $\mathrm{d}I_R$ is:

$$\begin{aligned}\mathrm{d}I_R = \Big\{&\Delta\sigma I_T[\Psi_T(r,\theta,\phi)]\,[\Psi_R(r,\theta,\phi)]\cos\big(\omega t - \Phi_T(r,\theta,\phi) - \Phi_R(r,\theta,\phi)\big)\\ &+ \sigma I_T[\Psi_R(r,\theta,\phi)]\big[\underline{\nabla}\Psi_T(r,\theta,\phi)\cdot\underline{v}\big]\cos\big(\omega t - \Phi_T(r,\theta,\phi) - \Phi_R(r,\theta,\phi)\big)\\ &- \sigma I_T[\Psi_T(r,\theta,\phi)][\Psi_R(r,\theta,\phi)]\sin\Big(\omega t + (\underline{\nabla}\Phi_T(r,\theta,\phi)\cdot\underline{v}) - \Phi_R(r,\theta,\phi)\Big)\\ &+ \sigma I_T[\Psi_T(r,\theta,\phi)]\big[\underline{\nabla}\Psi_R(r,\theta,\phi)\cdot\underline{v}\big]\cos\big(\omega t - \Phi_T(r,\theta,\phi) - \Phi_R(r,\theta,\phi)\big)\\ &- \sigma I_T[\Psi_T(r,\theta,\phi)][\Psi_R(r,\theta,\phi)]\sin\Big(\omega t + (\underline{\nabla}\Phi_R(r,\theta,\phi)\cdot\underline{v})\\ &- \Phi_T(r,\theta,\phi)\Big)\Big\}\,dt\end{aligned}$$

(A.11)

Higher order (non-linear) terms are neglected and isotropic scattering is assumed. If circular polarization is involved, then an extra phase term needs to be included. This is analyzed in Section A.3.

The receiver mixer down-converts the signal to DC by removing the carrier $\cos\omega t$ and therefore the static scattering term, leaving the dynamic signal:

$$\begin{aligned}dI_R = \Big\{&\Delta\sigma I_T[\Psi_T(r,\theta,\phi)]\,[\Psi_R(r,\theta,\phi)]\cos\big(\Phi_T(r,\theta,\phi) + \Phi_R(r,\theta,\phi)\big)\\ &+ \sigma I_T[\Psi_R(r,\theta,\phi)]\big[\underline{\nabla}\Psi_T(r,\theta,\phi)\cdot\underline{v}\big]\cos\big(\Phi_T(r,\theta,\phi) + \Phi_R(r,\theta,\phi)\big)\\ &- \sigma I_T[\Psi_T(r,\theta,\phi)][\Psi_R(r,\theta,\phi)]\sin\Big(\big(\underline{\nabla}\Phi_T(r,\theta,\phi)\cdot\underline{v}\big) - \Phi_R(r,\theta,\phi)\Big)\\ &+ \sigma I_T[\Psi_T(r,\theta,\phi)]\big[\underline{\nabla}\Psi_R(r,\theta,\phi)\cdot\underline{v}\big]\cos\big(\Phi_T(r,\theta,\phi) + \Phi_R(r,\theta,\phi)\big)\\ &- \sigma I_T[\Psi_T(r,\theta,\phi)][\Psi_R(r,\theta,\phi)]\sin\Big(\big(\underline{\nabla}\Phi_R(r,\theta,\phi)\cdot\underline{v}\big) - \Phi_T(r,\theta,\phi)\Big)\Big\}\,dt\end{aligned}$$

(A.12)

In the far field, $\Psi_R = \Psi_T$, so

$$dI_R = \Big\{\Delta\sigma I_T[\Psi_T(r,\theta,\phi)]^2 \cos\big(2\Phi_T(r,\theta,\phi)\big) + 2\sigma I_T[\Psi_T(r,\theta,\phi)]\big[\underline{\nabla}\Psi_T(r,\theta,\phi)\cdot\underline{v}\big]\cos\big(2\Phi_T(r,\theta,\phi)\big) - 2\sigma I_T[\Psi_T(r,\theta,\phi)]^2 \sin\Big((\underline{\nabla}\Phi_T(r,\theta,\phi)\cdot\underline{v}) - \Phi_R(r,\theta,\phi)\Big)\Big\}dt$$

(A.13)

Substituting for the far field approximations:

$$dI_R = \frac{I_T}{r^2}\left\{\Delta\sigma\cos\left(\frac{2r}{c}\right) + 2\sigma\big(\hat{r}\cdot\underline{v}\big)\cos\left(\frac{2r}{c}\right) - 2\sigma\sin\left(\frac{\big(\hat{r}\cdot\underline{v}\big)}{r^2} - \frac{r}{c}\right)\right\}dt$$

(A.14)

This seems to have all the required characteristics, apart from some multiplying constants. Clearly, the receiver power varies as I_R^2 i.e. $\alpha\,\frac{1}{r^4}$.

The above summarizes the received signal from one termite. The signals from a collection of termites are just summations of the above signals.

Note, that the receiver Ψ'_R and Φ'_R can be controlled by post-processing beamforming, using DSP software based techniques. This is the most flexible method.

Beamforming is based on combining received signals from an array of sensors. Our termite detector has independent transmitters. Hence, the scattered signals must take into account the location of each transmitter. The receiver antennas of the termite detector are displaced from the transmit antennas. Taking into account all of these geometrical factors, the signals received by the array of receivers are processed, as if the receiver was a large array, with its own Ψ'_R and Φ'_R. The aim of traditional beamforming is to place a maximum in Ψ_R at a point in space where the desired source is located and place nulls in Ψ_R at locations where there are sources of interference. The beamforming algorithm does this automatically, by maximising

cross-correlation coefficients in the beam direction and minimizing (RMS) interference (and noise) from all other directions [123].

Now, consider the effects of beamforming on the signal in Equation (A.13). Assume that the transmitter is isotropic and consider a receiver beam focused on the scattering termite. The local receiver response is flat around the maximum, so $\Psi_R \approx 0$ near the focus.

$$\begin{aligned} dI_R = \Big\{ & \Delta\sigma I_T[\Psi_T(r,\theta,\phi)]\,[\Psi_R(r,\theta,\phi)]\cos\big(\Phi_T(r,\theta,\phi) + \Phi_R(r,\theta,\phi)\big) \\ & + \sigma I_T[\Psi_R(r,\theta,\phi)]\big[\underline{\nabla}\Psi_T(r,\theta,\phi)\cdot\underline{v}\big]\cos\big(\Phi_T(r,\theta,\phi) + \Phi_R(r,\theta,\phi)\big) \\ & - \sigma I_T[\Psi_T(r,\theta,\phi)][\Psi_R(r,\theta,\phi)]\sin\Big(\big(\underline{\nabla}\Phi_T(r,\theta,\phi)\cdot\underline{v}\big) - \Phi_R(r,\theta,\phi)\Big) \\ & - \sigma I_T[\Psi_T(r,\theta,\phi)][\Psi_R(r,\theta,\phi)]\sin\big(-\Phi_T(r,\theta,\phi)\big)\Big\}\,dt \end{aligned}$$

(A.15)

One of the five terms vanishes and the other four are maximised. There may be a clear overall maximum, so a search for the maxima will succeed in finding it.

Now consider the effect of placing a sharp null at the same point i.e. $\Psi_R \approx 0$ but $\underline{\nabla}\Psi_R \neq 0$. Then

$$dI_R = \big\{\sigma I_T[\Psi_T(r,\theta,\phi)]\big[\underline{\nabla}\Psi_R(r,\theta,\phi)\cdot\underline{v}\big]\cos\big(\Phi_T(r,\theta,\phi) + \Phi_R(r,\theta,\phi)\big)\big\}dt$$

(A.16)

This may be an unambiguous global minimum, so a minima algorithm can find it. However, if a broad null is placed at the same spot, then $dI_R = 0$. Perhaps this offers a better strategy: constrain the algorithm to produce broad nulls around the interference sources.

The issues of beamforming and finding maxima or placing a null to form an unambiguous minima will not likely pose problems in the detection and tracking of termites. However, a more serious problem may arise because of the assumption of short observation period dt,

assumed in all the calculations. This assumes that the detection of signals, calculation of DFT's and cross-correlation matrices, the multiplication of those matrices to form beams and the detection of RMS values and comparison with constraints (and therefore beam and null formation) can be performed in a short time. This may not be the case. The low SNR requires longer averaging times for detection, but insects may move during the longer averaging period and hence reduce the effects of averaging. Although sampling of the receiver signals can be performed at high rates and so can the DFT etc., the high-passed signal variations are small and hence corrupted by noise.

In any case, this analysis suggests that the ADC should be sampled at a high rate, say 4K times per second and some signal enhancement techniques used. Using a 256 sample DFT, and assuming pipelined processing, this would enable beam updates at 16 times per second. Assuming insects move at speeds less than 16 mm/s, this may just meet the criteria. An alternative approach would be to use overlapping DFT frames, but this may require significant computational overhead. The bottom line impact on the ADC is that speed is needed.

A.1.3 Conclusion

It is clear that receiver based beamforming (software based) will be a major enhancement for Termatrac®, providing information about individual insects, insect count, motional tracking etc. By generating receiver amplitude/phase gradients at insect locations, and nulls or flat profiles at unwanted locations, better SNR and information about the insects will be available. Originally it was planned to enhance this by hardware based field distribution control at the transmitter. However, this analysis suggests that a better strategy is to provide polarization control, since this has better impact on the SNR, and provides more information about insect orientation and hence likely bearing.

Whilst it may appear that the beamforming is a known art, the complicating circumstances here include: merging of DOA with beamforming (unlike in the communications application, here beamforming has to be approached without prior knowledge, in a dynamic environment, because of unknown termite motion), near field effects, material induced effects, and a complex, multi-target environment.

A.2 Termite Cross-Section Fluctuations

Although Riley [81] notes that the radar cross-section of an insect may be approximately represented by that of a spherical water droplet of the same mass, a better approximation is a prolate spheroid. Examples of West Indian drywood termites are shown in Figure A.5.10, Figure A.5.11 and Figure A.5.12 below.

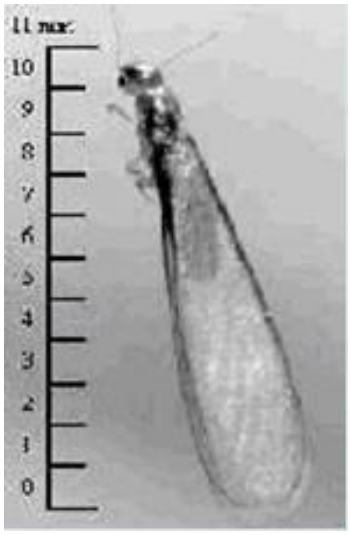

Figure A.5.10 – West Indian drywood termite - Reproductive (Alate). From [206].

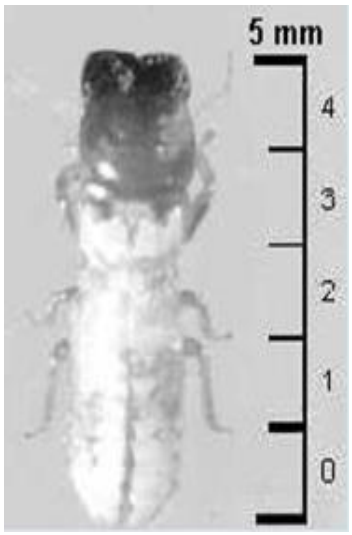

Figure A.5.11 – West Indian drywood termite - Soldier. From [206].

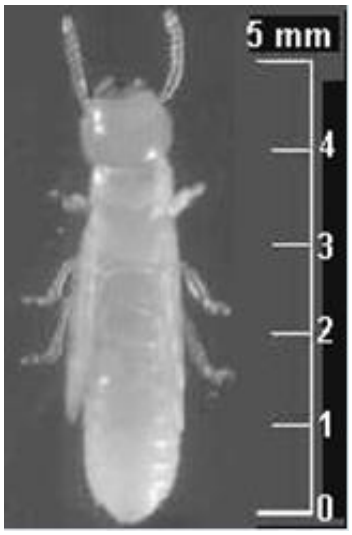

Figure A.5.12 – West Indian drywood termite - Nymph. From [206].

The soldier and nymph approximate prolate spheroids with axial ratio of between approximately 2.5:1 and 3:1. Cross-section fluctuations can be attributed to relative movement of body parts and body rotations. The former are difficult to model. The latter can be broken down into roll, pitch and yaw. Since roll involves rotation of a circular object, it should cause no significant effects. The same symmetry ensures that the effects of yaw and pitch are equivalent. Hence, the only degrees of freedom are angle of incidence, electric field polarization, and axis of yaw/pitch. Clearly, in the optical scattering region, the asymmetry of

the termite results in a small cross-section end-on and a larger one at broadside. In the Mie (resonance) scattering region, the situation is further complicated by the asymmetry of the termite at broadside. The analysis below assumes that termites are composed of a uniform dielectric, with a loss tangent similar to other insects [204]. Legs, wings and antennae are not considered [202]. Clearly these are significantly restrictive assumptions.

A.2.1 Incidence in the Plane of the Two Principal Axes

In this case of incidence in the plane of the two principal axes of the insect, see Figure A.5.3, the scattering cross section in the optical region for end-on exposure is significantly different from that for side-on exposure (about 1/10). In the Mie (resonance) region, it exhibits peaks, see Figure A.5.13 (a) below.

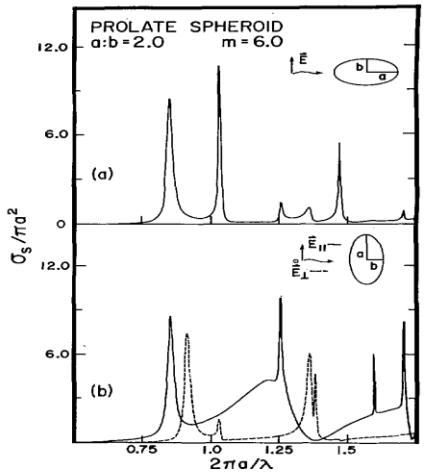

Fig. 5. Calculated spectra for 2:1 prolate spheroid in the two symmetrical orientations.

Figure A.5.13 – Spectra for prolate spheroid. From [207].

These are due to nulls in the wave expansion (in the Bessel and Hankel functions). Physically, these can be explained as excitation of resonant surface wave modes, which creep around the object and decay exponentially from it (Zenneck waves). A termite oriented at an angle ψ in that plane, see Figure A.5.3, will result in a cross-section proportional to $cos^2\psi$ or $cos^4\psi$, see Equation (A.4). If the insect changes its attitude ψ with time, this results in significant $\frac{\partial\sigma(t)}{\partial t}$.

For a given insect size and operating frequency, the scattering cross-section varies between the solid and dashed curve, see Figure A.5.14, according to insect long axis orientation with respect to the electric field. The effect is greatest around 45°, where the gradient is greatest, and the gradient is zero for incidence aligned with one of the principal axes. This happens when a termite meanders on a horizontal surface and is side-on. If it is end on, then it must be moving towards or away from the transceiver and hence will be detected by Doppler (phase changes). This effect is borne out by the theoretical results shown in Figure A.5.14.

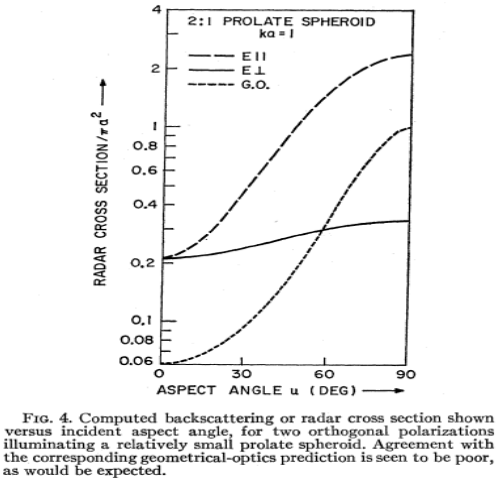

FIG. 4. Computed backscattering or radar cross section shown versus incident aspect angle, for two orthogonal polarizations illuminating a relatively small prolate spheroid. Agreement with the corresponding geometrical-optics prediction is seen to be poor, as would be expected.

Figure A.5.14 – Computed backscatter versus aspect angle for two orthogonal polarizations illuminating a relatively small prolate spheroid. From [208].

It should be noted that for smaller insects, $ka \gg 1$, this smooth transition between two scattering cross-sections is complicated by more wiggles, as shown below in Figure A.5.15 and Figure A.5.16 below. These secondary wiggles are due to higher order surface wave modes being excited. The gradients in scattering cross-section at certain azimuth and elevation angles become very high, as evidenced by Nye's measurements of contours in Figure 3.3 and Figure 3.4 (see Chapter 3, Section 3.1) and can be responsible for significant temporal scattering variations as the insect meanders around.

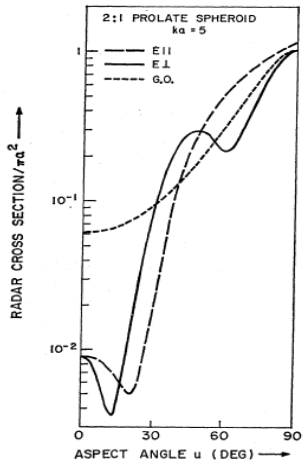

FIG. 5. Computed radar cross section, and the corresponding geometrical-optics limit, are shown as a function of direction of incidence for a prolate spheroid well above the Rayleigh region.

Figure A.5.15 – Computed backscatter versus aspect angle, and the corresponding geometrical optics limit for a prolate spheroid well above the Rayleigh region. From [208].

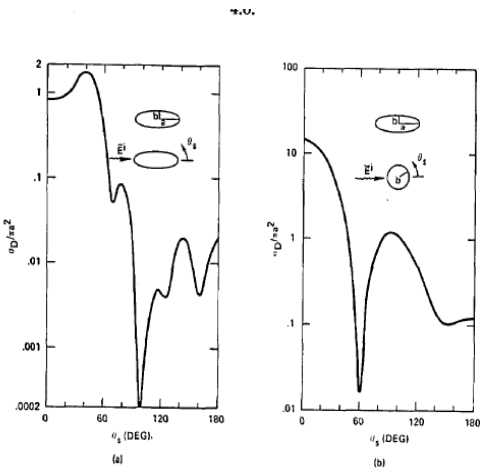

Fig. 10. 3:1 prolate spheroid scattering, vertical polarization, $ka = 7.114$, $\epsilon_r = 5.0$: (a) azimuthal plane; (b) equatorial plane.

Figure A.5.16 –3:1 prolate spheroid scattering, vertical polarization: (a) azimuthal plane; (b) equatorial plane. From [209].

A.2.2 Incidence Along a Short Axis

The case of incidence along the short axis of the insect, see Figure A.5.3, is a more common occurrence, as termites meander on the wall surface. Here, the physical cross-section section

does not vary with the attitude of the termite. However, the polarization of the incident wave has significant effects. This has been both modelled, see Figure A.5.13 (b) above, and measured, see Figure A.5.17 below, for prolate spheroids.

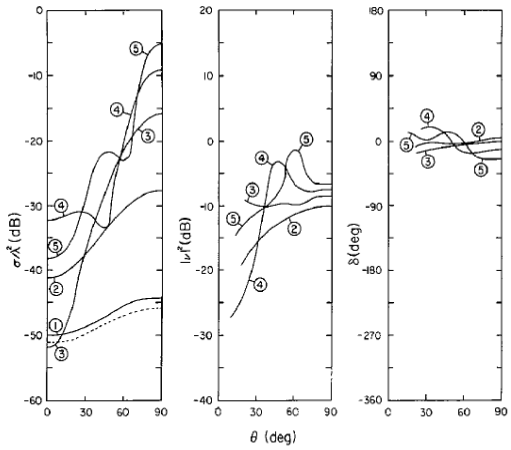

SAMPLE NUMBER	①	②	③	④	⑤
ka	0.152	0.305	0.459	0.609	0.759
c/a	4.90	4.96	4.99	5.00	5.01
Re(*e*)	3.30	3.20	3.20	3.14	3.14

Fig. 2. Scattering coefficients of prolate spheroids as a function of aspect angle. Stevenson [2] calculations shown by dashed curve.

Figure A.5.17 – Scattering coefficients of prolate spheroids as a function of aspect angle. From [210].

A.2.3 Comparative Insect and Termite Polarization

Dean and Drake [200] have measured the scattering cross-section of various insects at 9.4GHz, as a function of polarization, see Figure A.5.8 above. Their experiments cover a large variation in $ka = \frac{2\pi a}{\lambda}$ (up to 3.8). Nevertheless, they show that the cross-section can vary by up to 10:1 depending on polarization, with peaks at one or both of the principal axes. By contrast, soldier or nymph termites exhibit much smaller $ka = \frac{2\pi a}{\lambda} \approx 1.2$ at 24.125GHz. So fluctuations due to changes in polarization will be smaller for termites. For aerial sensing of insects the effects are greater, power levels are higher, clutter is generally not an issue as sensing is against the sky. Hence nutuating beam steering is entirely feasible. However, for termites,

since the effect is weaker, losses in polarization sensing cannot be tolerated to a similar degree and this drives designers to consider circular or dual polarizations sensing schemas.

In summary, it appears that the relationship between the frequency (wavelength), direction of incidence and polarization of the transmitter beam and the orientation (principal axes) of the termite is responsible for cross section variations as high as 20 dB. This is at least as significant as the antenna amplitude or phase gradients in the transmit and receive beam. It is possible that the signals are due mainly to the cross-section fluctuations, and that the field gradients produce beneficial, but incidental modulation. Consider for example the plot in Figure A.5.14 above. Both polarizations result in a small and equal cross-section for end on incidence (0.2 of the optical cross-section). When the insect turns broad-side the polarization along the short axis sees an only marginally larger cross-section (about 0.25 of the optical) whilst the polarization along the long axis sees a cross section of 2.5 times the optical: i.e. a 10:1 ratio. Therefore, a termite at broadside will produce large signals as it moves through field/phase gradients. A termite at 45^{o} will produce large $\frac{\partial\sigma(t)}{\partial t}$ and termites closer to end-on orientation will probably be below the noise threshold. Fortunately, termites are probably mainly observed at broadside, so the polarization issue is more significant. Termites observed end-on are likely to be moving towards or away from the radar and hence will produce significant Doppler. The only other reason to see a change in that angle is if they rear up. This is not likely to be a frequent occurrence.

Variation of frequency (i.e. a frequency sweep) could be a good method of discrimination between targets and stationary clutter, but it would need to be a wideband type sweep, covering say a full octave. This is prohibited by regulatory authorities and requires broadband microwave circuits and antennas and is therefore out of contention. Variation of the incidence angle is not feasible, so only the polarization can be altered. Ideally, the transmitter and receiver should be rotated for maximum signal. This was done in one instance, many

years ago, and a 10 dB variation was noticed. It was then attributed to anisotropic absorption through the tile material. However, based on the above analysis, it could also be due to cross-sectional variations. Rotation of components is impractical in a field instrument, so the next best solution was to opt for circular polarization. This was achieved by the construction of a polarization convertor. The original motivation was to provide a guaranteed 6 dB excess attenuation for penetration through materials with anisotropic attenuation. It may well be that the more likely benefit is providing the matching in polarization with the long axis of the termites.

A.3 Circular Polarization

The polarization effects are modified when the incident wave is circularly polarized. Consider a circularly polarized wave represented by $E(e^{j\omega t}\hat{\imath} + e^{j\omega t+\pi/2}\hat{\jmath})$, see Figure A.5.3 with $\hat{\imath}$ aligned to the x axis and $\hat{\jmath}$ aligned with the y axis. Because of different scattering cross-sections for the i and j directions (depending on the orientation angles of the insect in the azimuthal and equatorial planes), typically, the scattered wave is elliptically polarized $E(ae^{j\omega t}\hat{\imath} + be^{j\omega t+\pi/2}\hat{\jmath})$, where a and b depend on the scattering from both directions. In many cases, the disparity between a and b is so great that an almost linear polarization is scattered, with orientation given by some angle ϕ to the i vector in the ij plane. In the case of interest here, the circular polarization was produced by a polarization converter. Now, this scattered linearly polarized wave enters the convertor on its way back to the receiver. Consider i to be aligned with the fast axis [1] of the convertor. Then a component $E\cos\varphi$ of the scattered electric vector will be travelling along the fast axis and $E\sin\varphi$ will travel along the slow axis. The wave emerging from the polarization converter will be circularly polarized with $E(\cos\varphi\, e^{j\omega t}\hat{\imath} + \sin\varphi\, e^{j\omega t+\pi/2}\hat{\jmath})$. However, the receiver is only sensitive to vertical polarization (at 45°, bisecting i and j). There are three points to note:

1. The field is attenuated by 3 dB in passage to the receiver. The same process occurred in the scattering. The depolarization (change from circular to plane) resulted in a 3 dB loss. Therefore the overall loss is 6 dB.
2. The scattered field rejected by the receiver may be absorbed or reflected back, causing potential ghosts.
3. If the insect changes its attitude, it affects φ and hence the received signal is phase modulated, independent of the insect crossing phase contour lines.

A.3.1 Termite Sensing Through Building Materials

In practice, termites are sensed through obscuring building materials, such as walls, floors etc. Some of these materials have anisotropic absorption. Studies of these materials have included timber [211, 212], tiles [213], and composite structures such as walls, floors and ceilings [214, 215], and [216]. Timber exhibits this because of the grain orientation. Some tiles exhibit up to 5 dB difference in absorption along orthogonal axes. This (worst case) translates to a 10 dB disparity on round trip passage.

The long axis of a termite can make an arbitrary angle with respect to the preferred direction for transmission through the obscuring material. The scattering cross-section is a function of polarization for a fixed aspect. Suppose the ratio of scattering cross-section for polarization along the principal axes is γ. Then circular polarization is not bad at providing throughput (6 dB loss with respect to the rotating linear) but gives no information about the orientation of the insects.

Suppose however that the round trip attenuation disparity in attenuation through the obscuring material is 2β. Then, if $\gamma \gg 2\beta$, the scattered signal at the receiver is strongest for polarization determined by the termite(s). Then, if $\gamma \ll 2\beta$, the scattered signal at the receiver is strongest for polarization determined by the easy axis of the absorbing material.

Then, if γ and 2β are comparable, the scattered signal at the receiver varies in a complicated manner.

It is important to determine the values of γ and β.

Rotating a linear polarization to find a maximum has two benefits:

1. It maximizes SNR and hence all the terms in the GUT equations.
2. In cases where the anisotropy of the obscuring medium is negligible, it establishes direction of motion. Termites move predominantly in the direction of their long axis. For multiple termites moving in different directions, there may be multiple signal peaks.

Clearly, therefore, the preferred polarization is rotating linear. Mechanical rotation is the easiest solution, but is impractical. Electronic sweeping is preferred. However, there is a drawback in that the sweep speed must be slow, to accommodate signal processing. Termites move slowly, with typical signal bandwidth of 1-10 Hz. Hence a scan would have to take 100 seconds to allow enough time to dwell in each azimuth/elevation direction to acquire an image.

Polarimetric Modulation Depth

As the polarization is swept around a complete revolution, the amplitude of the backscattered signal undergoes modulation. The following signatures were obtained by Dean and Drake [200] from individual locusts at 9.6GHz, see Figure A.5.18 below.

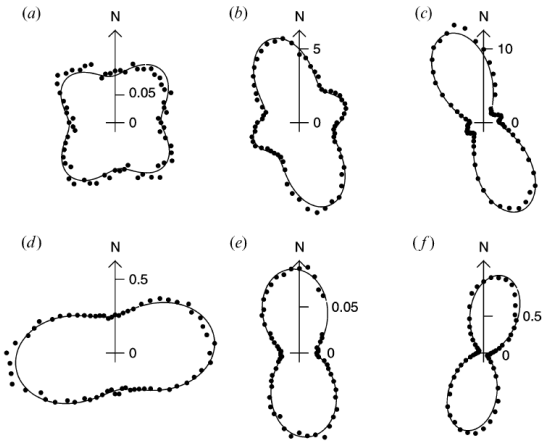

Figure 2. Examples of CLPPs retrieved from good-quality echoes. Radial units are cm^2. Target heights and parameter values are given in table 1. Observations made at Bourke on 15 November 1999 between 22.00 and 22.45 h AEST.

Figure A.5.18 – Observed polarizations of airborne insects, ventral aspect. From [200].

The max/min ratio ranges from 2:1 to 16:1. This is expected to be similar for termites, which have similar symmetry and scale, when observed at 24 GHz. For a ratio, $= \frac{\sigma_{min}}{\sigma_{max}}$, this results in a Polarization Modulation of $10log(1-R)dB$ below the absolute maximum scattering for σ_{max}.

This amplitude modulation appears predominantly at 2nd and 4th harmonic of the modulation frequency and exists regardless of insect motion. For an insect obscured by a material with anisotropic properties, this modulation can be distorted. Also, reflections from the faces of the intervening material may contribute modulated clutter. Such clutter can be sampled from a reference area of a wall/floor and used for subtraction purposes. The polarimetric signature of this clutter may also be used for diagnostic purposes. It may contain information about anisotropic inclusions, such as studs, noggins, electrical wiring, plumbing or other, obscured material objects hidden behind a wall/floor.

A.4 Far Field Scattering From Insects

The following scattering data from Riley, Figure A.5.19, shows raw (un-normalised) scattering cross-section from various insects at a wavelength of 32 mm (10 GHz) overlaid on the classical scattering from water droplets of equivalent mass. It is clear that insects scatter like drops of water of equivalent mass.

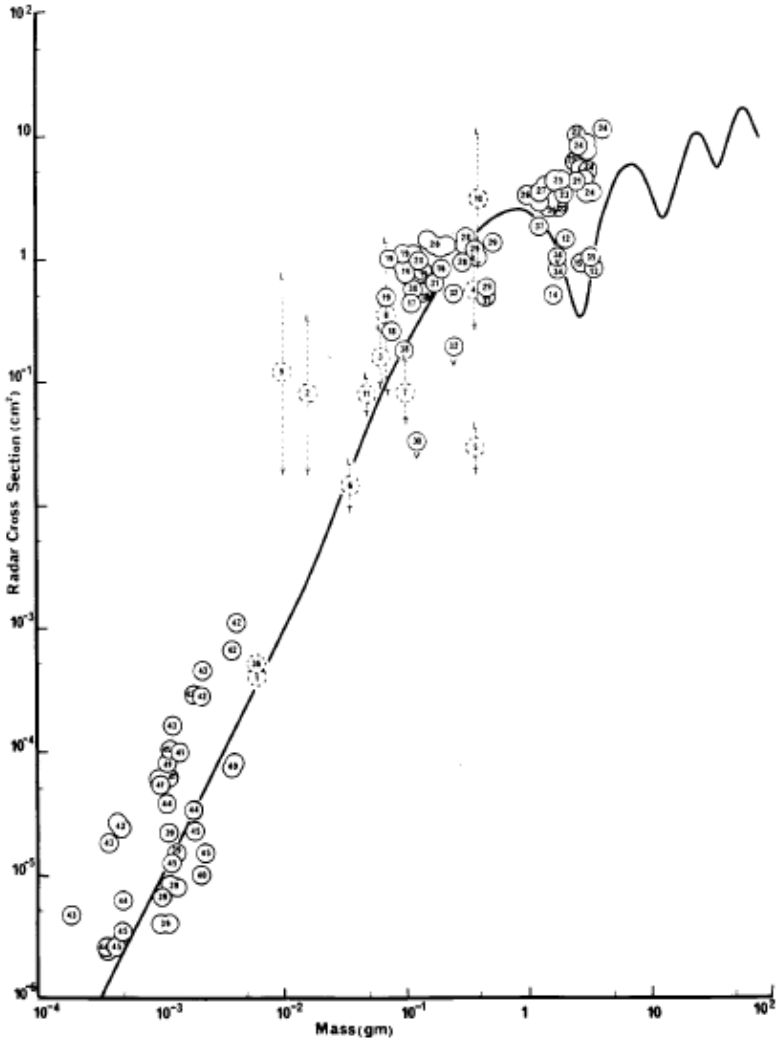

Fig. 4. Insect radar cross sections as a function of their mass. With the exception of point 1 (which was scaled from $\lambda = 1.9$ cm) all the results are for $\lambda = 3.2$ cm. Linear polarization was used in all cases. The insect mass for some measurements was not given by the author and so has been estimated from body dimensions—their positions on the graph are thus of lower significance than those of other points, and they are correspondingly plotted with dotted lines. The curve for water spheres is from the data of Herman *et al.* [11]. A key to data points is given in Table 1.

Figure A.5.19 – Insect backscatter as a function of their mass. From [81].

The normalized scattering cross-section of water drops [122], is shown in Figure A.5.20 below.

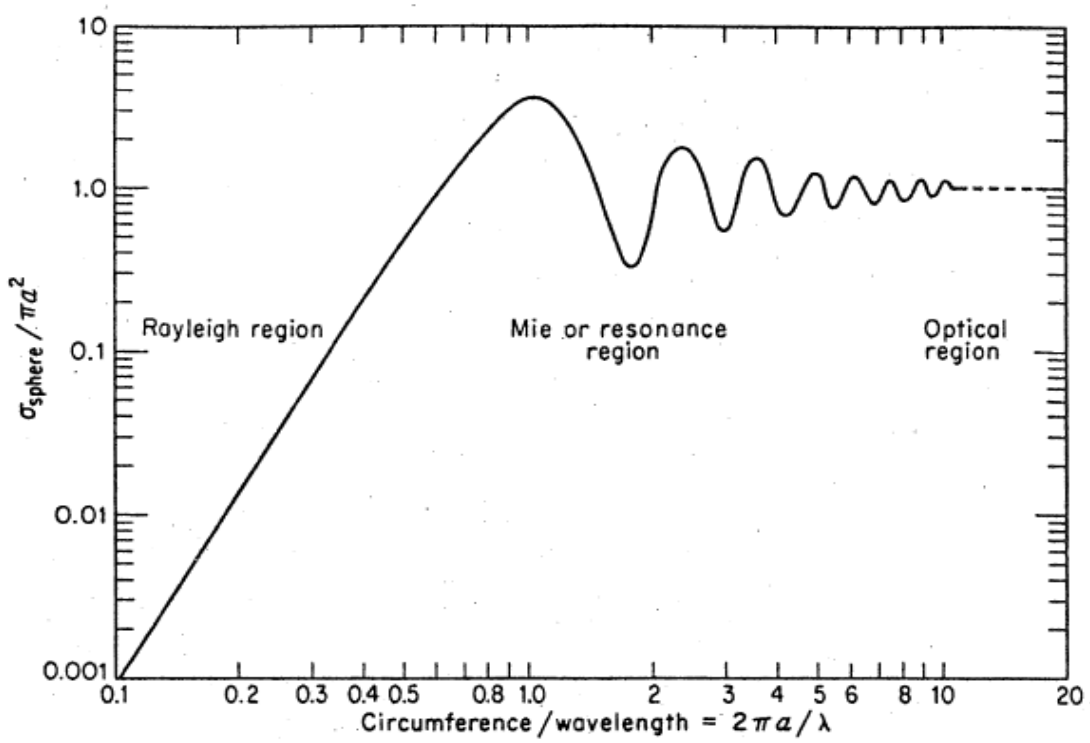

Figure A.5.20 – Rayleigh, Mie and Optical scattering regions. From [122].

Three obvious regions can be seen:

1. Optical region, where the scattering cross-section and the physical cross-section are identical $\lambda < 2\pi a/10$.
2. Rayleigh region where the scattering cross-section is smaller than the physical cross-section and varies as λ^{-4}. This region applies to $\lambda > 1.4\pi a$.
3. Resonant or Mie scattering, where the scattering cross-section oscillates between 3 times and $1/3$ of the physical cross-section for the 1st resonance and decays exponentially for subsequent resonances. $1.4\pi a > \lambda > 2\pi a/10$.

24.125 GHz corresponds to the first Mie resonance for water drops of mass $m = 32.5\, mg$. Drops below that size scatter with a cross-section $\sigma = km^2$ i.e. a 3 mg drop scatters only 1% as much as a 30 mg one.

Drops above that size scatter irregularly, but with a trend of $\sigma = km^{2/3}$ until at about 32.5 g, where the trend becomes smooth (optical region). This is 1000 times the Mie resonant mass (i.e. 10 times the radius).

A Mie resonance of 9.0 GHz corresponds to a mass of 625 mg, which is in agreement with Riley's curve, taking into account that his interpretation is "un-normalised" cross-section.

The first Mie resonance occurs at 42 GHz for a 3mg termite. Since termites between 3 mg and 30 mg are to be accommodated, 24 GHz is a good compromise.

The above refers to static scattering from the whole insect. A stationary insect contributes the equivalent amount of static clutter, noting that termites that are alive move continuously. In order to be detected by a scattered signal, the insect must move its body parts or must cross equi-phase contours (Doppler) or equi-amplitude contours. The latter effect is negligible in the far field, because the equal amplitude contours are smooth and spherical and the amplitude varies as $\frac{1}{r}$ (power varies as $\frac{1}{r^2}$). At 24 GHz, an insect moving 10mm in the range direction at a range of 1m changes the amplitude of its scattered radiation by 1%. However, the phase of that reflection goes through almost two complete sine wave cycles, and this phenomenon affects 100% of the scatter (Doppler). An insect moving 10 mm in the cross-range direction i.e. perpendicular (much more common) at 1 m range results in a range change of 0.05 mm (negligible effect on amplitude). Such movements occur on the inside of a wall or floor. This produces a round trip phase change of three degrees. This is still a weak effect. Such changes are difficult or impossible to measure when the SNR is between 10 and 20 dB, which is typical.

A.5 Near Field Effects

The assumptions in the above arguments are that the transceiver antenna is a point source/receiver and that the equal amplitude and equal phase contours are spherical.

However detection at short range implies operation in the near field of the antenna and for an array the near field extends even further into space.

A.5.1 Pyramidal Horn

In general, the near field phase and amplitude contours of antennas or arrays have not been studied, expect for a pyramidal horn [102].

Consider then a pyramidal horn operating at 24.125 GHz, with an aperture of 60×40 mm. Then, the assumption that the transceiver antenna is a point source/receiver and that the equal amplitude and equal phase contours are spherical begins to break down at ranges less than about 200 mm.

Near field profiles for a pyramidal horn have been studied by [102]. Amplitude and phase variations occur in a few millimeters of travel in Figure 3.3 and Figure 3.4 (see Chapter 3, Section 3.1). From the spacing of the equi-phase and amplitude contours, and assuming a termite travelling between 6 mm/s and 20 mm/s (2 body lengths per second), such an insect will display significant AM between 0.2 Hz and 1 Hz, with some harmonics due to uneven spacing of the contours.

An approximate received signal power can be calculated as follows:

Assuming transmit power is 5 mW, and uniform distribution over the horn face, power density is 2.1 μW/mm^2. Actually, the distribution is uniform in the E plane and follows a cosine pattern in the H plane for TE_{10} distribution, but this effect should be small. Therefore, the incident power on a 10 mm^2 insect is 21 μW. This is a 24 mg type insect and has approximately the same scattering cross section as its physical dimensions. The receive antenna subtends about 1/3 of a full sphere (scattering can occur in all directions). Hence about 7 μW is scattered from the insect. Assuming wobbles of the order of 25% consistent

with the amplitude modulation, this should contribute about 2 µW of modulation around 1 Hz. Assuming a conversion loss of 13 dB for a single ended, somewhat starved mixer, this should result in about 100 nW wobble at the IF of 1 Hz. This is about 2mV RMS in a 50Ω system. Since the return phase is random, a single mixer output is reduced by 3 dB on average compared to an IQ mixer, resulting in a best signal of about 1.4 mV RMS.

Of course, this corresponds to the insect traversing the contours of the antenna pattern. Other paths may not be so obliging and signals up to 100 times less can be expected (down to 14 µV RMS).

Also, termites down to 3 mg mass could then result in a scattering cross section approximately 10 times smaller, an intercept cross-section about four times smaller, and therefore a signal of 200 µV RMS at best and about 2 µV at worst.

A.5.2 Original Experimental Measurements

Original measurements circa 1994 were performed at 9.5 GHz, using a horn with an aperture of 75×75 mm.

Under these conditions, a 24 mg insect should display a scattering cross section 0.024 times that at 24.125 GHz (Rayleigh region). Assuming the same power output, the power density is about 0.4 times that for 24 GHz. The only boresight near-field null is 6 mm from the front face with a 3 dB point about 36 mm from the front face. The 3 dB points are about 27 mm either side of boresight. This is almost double the case for 24 GHz. Hence, the cross-range movements will occur at approximately one half the frequency. Since this low IF is in the 1/f noise region of the mixer or the opamp, the noise level is doubled. Hence, the effective SNR is about 0.5×0.4×0.024 compared with 24 GHz or 23 dB less. The lower IF compared to the case for 24 GHz results in longer observation time as well. Therefore, it is hardly surprising that these first tests at X-Band were disappointing and were thus abandoned [78].

Bibliography

[1] M. Born and E. Wolf, *Principles of Optics : Electromagnetic Theory of Propagation, Interference and Diffraction of Light*. New York: Macmillan, 1964.

[2] G. T. Ruck, D. E. Barrick, W. D. Stuart, and C. K. Krichbaum, *Radar Cross Section Handbook*. New York: Plenum Press, 1970.

[3] S. Ramo, J. R. Whinnery, and T. Van Duzer, *Fields and Waves in Communication Electronics*. New York: Wiley, 1984.

[4] A. R. Von Hippel, *Dielectrics and Waves*. Cambridge, Mass: M.I.T. Press, 1954.

[5] L. D. Landau, E. M. Lifshitz, and L. P. Pitaevskii, *Electrodynamics of Continuous Media translated from Russian by J.B. Sykes, J.S. Bell and M.J. Kearsley*. Oxford, New York: Pergamon Press, 1984.

[6] T. Rother, *Electromagnetic Wave Scattering on Nonspherical Particles : Basic Methodology and Simulations*. Berlin, Heidelberg: Springer, 2009.

[7] A. Mugnai and W. J. Wiscombe, "Scattering from Nonspherical Chebyshev Particles. I: Cross-Sections, Single-Scattering Albedo, Asymmetry Factor, and Backscattered Fraction," *Applied Optics,* vol. 25, pp. 1235-1244, 1986.

[8] G. Mie, "Beiträge zur Optik trüber Medien, speziell kolloidaler Metallösungen," *Annalen der Physik,* vol. 330, pp. 377-445, 1908.

[9] J. Creffield. (2005). *Call for the Immediate Declaration of All Municipalities (Metropolitan Melbourne & Regional Victoria) as Regions Where Homes, Buildings and Structures are Subject to Termite Infestation*. Available: www.csiro.au

[10] CSIRO. (2005, 2011). *Termites And Wood Protection*. Available: www.csiro.au

[11] R. J. Saykally, "Terahertz Spectroscopy of Water Clusters," presented at the 39th International Conference on Infrared, Millimeter, and Terahertz Waves, Tucson, AZ, U.S.A., 2014.

[12] T. Meissner and F. J. Wentz, "The Complex Dielectric Constant of Pure and Sea Water from Microwave Satellite Observations," *IEEE Transactions on Geoscience and Remote Sensing,* vol. 42, pp. 1836-1849, 2004.

[13] S. Mashimo, S. Kuwabara, S. Yagihara, and K. Higasi, "Dielectric-Relaxation Time and Structure of Bound Water in Biological Materials," *Journal of Physical Chemistry,* vol. 91, pp. 6337-6338, 1987.

[14] N. Nandi, K. Bhattacharyya, and B. Bagchi, "Dielectric Relaxation and Solvation Dynamics of Water in Complex Chemical and Biological Systems," *Chemical Reviews,* vol. 100, pp. 2013-2045, 2000.

[15] G. N. Watson, "The Diffraction of Electric Waves by the Earth," *Proceedings of the Royal Society of London,* vol. 95, pp. 83-99, 1918.

[16] P. C. Waterman, "Matrix Formulation of Electromagnetic Scattering," *Proceedings of the Institute of Electrical and Electronics Engineers,* vol. 53, pp. 805-812, 1965.

[17] J. Wauer, K. Schmidt, T. Rother, T. Ernst, and M. Hess, "Two Software Tools for Plane-Wave Scattering on Nonspherical Particles in the German Aerospace Centre's Virtual Laboratory," *Applied Optics,* vol. 43, pp. 6371-6379, 2004.

[18] H. Inada and M. A. Plonus, "The Geometric Optics Contribution to the Scattering from a Large Dense Dielectric Sphere," *IEEE Transactions on Antennas and Propagation,* vol. 18, pp. 89-99, 1970.

[19] H. Inada and M. A. Plonus, "The Diffracted Field Contribution to the Scattering from a Large Dense Dielectric Sphere," *IEEE Transactions on Antennas and Propagation,* vol. 18, pp. 649-660, 1970.

[20] J. A. Stratton, *Electromagnetic Theory*. New York: McGraw-Hill, 1941.
[21] R. D. Richtmyer, "Dielectric Resonators," *Journal of Applied Physics,* vol. 10, pp. 391-398, 1939.
[22] H. Bremmer, *Terrestrial Radio Waves: Theory of Propagation*. New York: Elsevier Publising Company, 1949.
[23] V. Fock, "Diffraction of Radio Waves Around the Earth's Surface," *Zhurnal Eksperimentalnoi I Teoreticheskoi Fiziki,* vol. 15, pp. 479-496, 1945.
[24] E. C. J. von Lommel, *Studien über die Bessel'schen Functionen*. Leipzig: B. G. Teubner, 1990.
[25] G. N. Watson, *A Treatise on the Theory of Bessel Functions*. Cambridge: Cambridge University Press, 1922.
[26] A. Gray, G. B. Mathews, and T. M. MacRobert, *A Treatise on Bessel Functions and Their Applications to Physics*. London: Macmillan & Co., 1895.
[27] L. C. P. Van Hove, "Topics on Regge-Pole Theory of High-Energy Scattering," ed. Geneva: CERN, 1968, p. 81.
[28] J. W. Nicholson, "A Type of Asymptotic Summation," *The Messenger of Mathematics,* vol. 37, pp. 84-90, 1907.
[29] M. H. Poincaré, "Sur la Diffraction des Ondes Hertziennes," *Rendiconti del Circolo Matematico di Palermo,* vol. 29, pp. 169-259, 1910.
[30] A. Sommerfeld, *Partial Differential Equations in Physics : Lectures on Theoretical Physics Volume VI*. New York: Academic Press, 1964.
[31] H. M. Nussenzveig, *Diffraction Effects in Semiclassical Scattering*. Cambridge: Cambridge University Press, 1992.
[32] P. Y. Ufimtsev, *Metod Krayevykh Voln v Fizicheskoy Teorli Difraktsli (Method of Edge Waves in the Physical Theory of Diffraction)*: Izd-Vn Snvptskoye Radio 1962.
[33] E. Hecht, *Optics*. San Francisco, Sydney: Addison-Wesley, 2002.
[34] V. V. Shevchenko, *Continuous Transitions in Open Waveguides*. Boulder: Golem Press, 1971.
[35] S. F. Mahmoud, *Electromagnetic Waveguide: Theory and Applications*. London: Institution of Engineering and Technology, 2006.
[36] H. M. Macdonald, "The Bending of Electric Waves Round a Conducting Obstacle," *Proceedings of the Royal Society of London,* vol. 71, pp. 251-258, 1902.
[37] H. M. Macdonald, "The Bending of Electric Waves Round a Conducting Obstacle: Amended Result," *Proceedings of the Royal Society of London,* vol. 72, pp. 59-68, 1903.
[38] H. M. Macdonald, "The Diffraction of Electric Waves Round a Perfectly Reflecting Obstacle," *Philosophical Transactions of the Royal Society of London. Series A, Containing Papers of a Mathematical or Physical Character,* vol. 210, pp. 113-144, 1911.
[39] H. W. March, "Über die Ausbreitung der Wellen der drahtlosen Telegraphie auf der Erdkugel," *Annalen der Physik,* vol. 342, pp. 29-50, 1912.
[40] A. E. H. Love, "The Transmission of Electric Waves over the Surface of the Earth," *Philosophical Transactions of the Royal Society of London. Series A, Containing Papers of a Mathematical or Physical Character,* vol. 215, pp. 105-131, 1915.
[41] B. van der Pol, "On the Energy Transmission in Wireless Telegraphy," *Yearbook of Wireless Telegraphy and Telephony,* 1918.
[42] H. C. van de Hulst, *Light Scattering by Small Particles*. New York: Wiley, 1957.
[43] "LightTools," ed: Synopsys.
[44] W. Magnus and L. Kotin, "The Zeros of the Hankel Function as a Function of Its Order," *Numerische Mathematik,* vol. 2, pp. 228-244, 1960.
[45] E. C. Titchmarsh, *The Theory of Functions*. London: Oxford University Press, 1939.

[46] J. Lekner, *Theory of Reflection of Electromagnetic and Particle Waves*. Dordrecht, Boston, Lancaster: Nijhoff, Kluwer, 1987.
[47] D. Jiao and J. M. Jin, "Asymptotic Waveform Evaluation for Scattering by a Dispersive Dielectric Object," *Microwave and Optical Technology Letters,* vol. 24, pp. 232-234, 2000.
[48] J. Rheinstein, "Backscatter from Spheres - A Short Pulse View," *IEEE Transactions on Antennas and Propagation,* vol. 16, pp. 89-97, 1968.
[49] H. Inada, "Backscattered Short Pulse Response of Surface-Waves from Dielectric Spheres," *Applied Optics,* vol. 13, pp. 1928-1933, 1974.
[50] J. R. Mautz and R. F. Harrington, "Electromagnetic Scattering from a Homogeneous Material Body of Revolution," *AEÜ - International Journal of Electronics and Communications,* vol. 33, pp. 71-80, 1979.
[51] T. K. Wu and L. L. Tsai, "Scattering from Arbitrarily-Shaped Lossy Dielectric Bodies of Revolution," *Radio Science,* vol. 12, pp. 709-718, 1977.
[52] H. Ikuno, T. Ohmori, and M. Nishimoto, "Extended Ray Theory for Analyzing Electromagnetic Scattering Process on Two-Dimensional Smooth Objects," *Electronics and Communications in Japan (Part II: Electronics),* vol. 76, pp. 14-27, 1993.
[53] P. W. Barber, "Resonance Electromagnetic Absorption by Nonspherical Dielectric Objects," *IEEE Transactions on Microwave Theory and Techniques,* vol. 25, pp. 373-381, 1977.
[54] M. L. Shough, "Radar Detection of Spherical Targets," *NARCAP Report,* 2009.
[55] M. Zhadobov, N. Chahat, R. Sauleau, C. Le Quement, and Y. Le Drean, "Millimeter-wave Interactions with the Human Body: State of Knowledge and Recent Advances," *International Journal of Microwave and Wireless Technologies,* vol. 3, pp. 237-247, 2011.
[56] M. Sluijter and G. Racz, "Technical Aspects of Radiofrequency," *Pain Practice : The Official Journal of World Institute of Pain,* vol. 2, pp. 195-200, 2002.
[57] H. Fröhlich, "Coherent Electric Vibrations in Biological Systems and the Cancer Problem," *IEEE Transactions on Microwave Theory and Techniques,* vol. 26, pp. 613-617, 1978.
[58] G. J. Hyland, "From Theoretical Physics to Biology: The Forward Path of Theory with Herbert Fröhlich," in *Energy Transfer Dynamics: Studies and Essays in Honour of Herbert Fröhlich on His Eightieth Birthday*, T. W. Barrett and H. A. Pohl, Eds. Berlin Heidelberg New York: Springer Verlag, 1987, pp. 146-163.
[59] I. P. Herman, "Peak Temperatures from Raman Stokes/anti-Stokes Ratios During Laser Heating by a Gaussian Beam," *Journal of Applied Physics,* vol. 109, 2011.
[60] S. J. Webb, M. E. Stoneham, and H. Fröhlich, "Evidence for Nonthermal Excitation of Energy Levels in Active Biological Systems," *Physics Letters A,* vol. 63, pp. 407-408, 1977.
[61] W. Grundler, F. Keilmann, and H. Fröhlich, "Resonant Growth-Rate Response of Yeast Cells Irradiated by Weak Microwaves," *Physics Letters A,* vol. 62, pp. 463-466, 1977.
[62] O. Katz, J. M. Levitt, E. Grinvald, and Y. Silberberg, "Single-Beam Coherent Raman Spectroscopy and Microscopy via Spectral Notch Shaping," *Optics Express,* vol. 18, pp. 22693-22701, 2010.
[63] A. S. Davydov, "Solitons and Energy Transfer Along Protein Molecules," *Journal of Theoretical Biology,* vol. 66, pp. 379-387, 1977.
[64] V. R. Makar, M. K. Logani, A. Bhanushali, M. Kataoka, and M. C. Ziskin, "Effect of Millimeter Waves on Natural Killer Cell Activation," *Bioelectromagnetics,* vol. 26, pp. 10-19, 2005.
[65] (23 Nov 2012). *Rife Generators*. Available: http://www.electroherbalism.com/Bioelectronics/RifeBare/index.htm

[66] I. Y. Belyaev, V. S. Shcheglov, Y. D. Alipov, and V. A. Polunin, "Resonance Effect of Millimeter Waves in the Power Range from 10(-19) to 3x10(-3) W/cm(2) on Escherichia Coli Cells at Different Concentrations," *Bioelectromagnetics,* vol. 17, pp. 312-321, 1996.

[67] J. M. Osepchuk and R. C. Petersen, "Resonance Effect of Millimeter Waves in the Power Range from 10(-19) to 3x10(-3) W/cm(2) on Escherichia Coli Cells at Different Concentrations - Comment," *Bioelectromagnetics,* vol. 18, pp. 527-528, 1997.

[68] I. Y. Belyaev, V. S. Shcheglov, Y. D. Alipov, and V. L. Ushakov, "Resonance Effect of Millimeter Waves in the Power Range from 10(-19) to 3x10(-3) W/cm(2) on Escherichia Coli Cells at Different Concentrations - Reply," *Bioelectromagnetics,* vol. 18, pp. 529-530, 1997.

[69] N. K. Agafonova, N. E. Krassova, and E. E. Fesenko, "Rapid changes in phosphoinositide metabolism in antennae of insects exposed to low-intensity millimeter microwaves," *Biophysics,* vol. 43, 1998.

[70] P. S. Callahan, "Insect Antennae with Special Reference to the Mechanism of Scent Detection and the Evolution of the Sensilla," *International Journal of Insect Morphology and Embryology,* vol. 4, pp. 381-430, 1975.

[71] P. S. Callahan, "Dielectric Wave-Guide Modeling at 3.0 cm of the Antenna Sensilla of the Lovebug, Plecia-Neartica Hardy," *Applied Optics,* vol. 24, pp. 1094-1097, 1985.

[72] J. Gavan and J. S. Ishay, "Hypothesis of Natural Radar Tracking and Communication Direction Finding Systems Affecting Hornets Flight," *Progress In Electromagnetics Research,* vol. 34, pp. 299-312, 2001.

[73] J. Gavan, "Hypothesis of Hornets Biological THF Radar for Detection Tracking and Communication DF," presented at the 4th Asia-Pacific Conference on Environmental Electromagnetics, pp. 534-538, 2006.

[74] R. Wehner, "Polarization Vision - A Uniform Sensory Capacity?," *Journal of Experimental Biology,* vol. 204, pp. 2589-2596, 2001.

[75] T. A. Evans, J. C. S. Lai, E. Toledano, L. McDowall, S. Rakotonarivo, and M. Lenz, "Termites Assess Wood Size by Using Vibration Signals," *Proceedings of the National Academy of Sciences of the United States of America,* vol. 102, pp. 3732-3737, 2005.

[76] G. Becker, "Communication Between Termites by Biofields," *Biological Cybernetics,* vol. 26, pp. 41-44, 1977.

[77] D. M. S. Esquivel, E. Wajnberg, G. R. Cernicchiaro, and O. C. Alves, "Comparative Magnetic Measurements of Migratory Ant and Its Only Termite Prey," *Journal of Magnetism and Magnetic Materials,* vol. 278, pp. 117-121, 2004.

[78] A. Z. Tirkel, "Private Communication," ed, 2011.

[79] Y. Fujii, Y. Fujiwara, Y. Yanase, S. Okumura, K. Narahara, T. Ngatsuma*, et al.*, "Nondestructive Detection of Termites Using a Millimeter-Wave Imaging Technique," *Forest Products Journal,* vol. 57, pp. 75-79, 2007.

[80] A. Z. Tirkel, J. C. S. Lai, T. A. Evans, and G. A. Rankin, "Heating and Provocation of Termites Using Millimeter Waves," presented at the Progress in Electromagnetics Research Symposium, Marrakesh, Morocco, pp. 1586-1589, 2011.

[81] J. R. Riley, "A Millimetric Radar to Study the Flight of Small Insects," *Electronics & Communication Engineering Journal,* vol. 4, pp. 43-48, 1992.

[82] C. E. Cooper and P. C. Withers, "Termite Digestibility and Water and Energy Contents Determine the Water Economy Index of Numbats (Myrmecobius Fasciatus) and Other Myrmecophages," *Physiological and Biochemical Zoology,* vol. 77, pp. 641-650, 2004.

[83] E. Pickwell, B. E. Cole, A. J. Fitzgerald, V. P. Wallace, and M. Pepper, "Simulation of Terahertz Pulse Propagation in Biological Systems," *Applied Physics Letters,* vol. 84, pp. 2190-2192, 2004.

[84] S. Mashimo, S. Kuwabara, S. Yagihara, and K. Higasi, "Dielectric relaxation time and structure of bound water in biological materials," *The Journal of Physical Chemistry,* vol. 91, pp. 6337-6338, 1987.
[85] C. G. A. Lima, R. S. de Oliveira, S. D. Figueiro, C. F. Wehmann, J. C. Goes, and A. S. B. Sombra, "DC Conductivity and Dielectric Permittivity of Collagen-Chitosan Films," *Materials Chemistry and Physics,* vol. 99, pp. 284-288, 2006.
[86] P. S. Callahan, "A High Frequency Dielectric Waveguide on Antennae of Night-Flying Months (Saturnidae)," *Applied Optics,* vol. 7, pp. 1425-1430, 1968.
[87] (27 Feb 2012). *Luxpop*. Available: http://www.luxpop.com/
[88] M. Chaplin. (27 Feb 2012). *Water and Microwaves*. Available: http://www.lsbu.ac.uk/water/microwave.html
[89] O. P. Gandhi, "Frequency and Orientation Effects on Whole Animal Absorption of Electromagnetic Waves," *IEEE Transactions on Biomedical Engineering,* vol. 22, pp. 536-542, 1975.
[90] E. C. Jordan and K. G. Balmain, *Electromagnetic Waves and Radiating Systems*. Englewood Cliffs: Prentice-Hall, 1968.
[91] L. D. Landau and E. M. Lifshitz, *Electrodynamics of Continuous Media*. Oxford, New York: Pergamon Press, 1960.
[92] T. A. Milligan, *Modern Antenna Design*, 2nd ed. Hoboken: Wiley, 2005.
[93] P. W. Barber and S. C. Hill, *Light Scattering by Particles : Computational Methods*. Singapore, Teaneck: World Scientific, 1990.
[94] B. J. Cabrera and M. K. Rust, "Behavioral Responses to Light and Thermal Gradients by the Western Drywood Termite (Isoptera: Kalotermitidae)," *Environmental Entomology,* vol. 25, pp. 436-445, 1996.
[95] N. W. D. Le Marshall, G. A. Rankin, and A. Z. Tirkel, "Hybrid Array for the Detection and Imaging of Termites," presented at the IEEE Radio and Wireless Symposium, Orlando, FL, U.S.A., pp. 288-291, 2010.
[96] A. Z. Tirkel, J. C. S. Lai, T. A. Evans, and G. A. Rankin, "Effects of Millimeter Wave Exposure on Termite Behavior," presented at the Progress in Electromagnetics Research Symposium, Marrakesh, Morocco, pp. 171-175, 2011.
[97] A. Z. Tirkel, G. J. Sanderson, and R. J. Davies, "Termite Detection System," US 6313643, WO 9709611, JP 11512178T, 2001.
[98] N. W. D. Le Marshall, G. A. Rankin, and A. Z. Tirkel, "High Resolution, Wide Coverage Termite Imager," presented at the Progress in Electromagnetics Research Symposium, Xi'an, China, pp. 663-667, 2010.
[99] G. A. Rankin, A. Z. Tirkel, L. Q. Bui, and N. W. D. Le Marshall, "Radar Imaging: Conventional and MIMO," presented at the International Conference on Communications and Electronics, Hue, Vietnam, pp. 171-176, 2012.
[100] O. Moreno and A. Tirkel, "New Optimal Low Correlation Sequences for Wireless Communications," presented at the 7th International Conference on Sequences and Their Applications - SETA 2012, Waterloo, Canada, pp. 212-23, 2012.
[101] B. D. Steinberg and H. M. Subbaram, *Microwave Imaging Techniques*. New York: Wiley, 1991.
[102] J. F. Nye and W. L. Liang, "Theory and Measurement of the Field of a Pyramidal Horn," *IEEE Transactions on Antennas and Propagation,* vol. 44, pp. 1488-1498, 1996.
[103] (August 2013). *Helicopter Survivability Enhanced with MFRF Contract*. Available: http://www.baesystems.com/article/BAES_045529/helicopter-survivability-enhanced-with-mfrf-contract
[104] N. W. D. Le Marshall and A. Z. Tirkel, "MIMO Radar Array for Termite Detection and Imaging," *Progress In Electromagnetics Research B,* vol. 28, pp. 75-94, 2011.

[105] B. Shannon, M. Abushaaban, H. Ashoka, and D. Longstaff, "A Low Visibility Landing Aid Based on a Multi Beam Radar Altimeter," presented at the 7th EMRS DTC Technical Conference - Edinburgh, 2010.
[106] Y. Huang, P. V. Brennan, D. Patrick, I. Weller, P. Roberts, and K. Hughes, "FMCW Based MIMO Imaging Radar for Maritime Navigation," *Progress in Electromagnetics Research,* vol. 115, pp. 327-342, 2011.
[107] J. Ortiz-Ubarri, O. Moreno, A. Z. Tirkel, R. Arce-Nazario, and S. W. Golomb, "Algebraic Symmetries of Generic (m+1)-Dimensional Periodic Costas Arrays," *IEEE Transactions on Information Theory,* vol. 59, pp. 1076-1081, 2013.
[108] E. E. Fenimore and T. M. Cannon, "Coded Aperture Imaging with Uniformly Redundant Arrays," *Applied Optics,* vol. 17, pp. 337-347, 1978.
[109] R. A. Haubrich, "Array Design," *Bulletin of the Seismological Society of America,* vol. 58, pp. 977-991, 1968.
[110] A. Leukhin, O. Moreno, and A. Tirkel, "Secure CDMA and Frequency Hop Sequences," in *Wireless Communication Systems (ISWCS 2013), Proceedings of the Tenth International Symposium on*, 2013, pp. 1-5.
[111] S. T. Blake, O. Moreno, and A. Z. Tirkel, "Families of 3D Arrays for Video Watermarking," presented at the 8th International Conference on Sequences and Their Applications - SETA 2014, Melbourne, Australia, pp. 134-45.
[112] O. Moreno, A. Z. Tirkel, U. Parampalli, and R. G. van Schyndel, "New Families of Arrays in Two Dimensions for Watermarking Applications," *Electronics Letters,* vol. 46, pp. 1500-1501, 2010.
[113] K. J. Horadam, *Hadamard Matrices and Their Applications*. Princeton: Princeton University Press, 2011.
[114] "CST," ed. Darmstadt, Germany: CST GmbH.
[115] B. H. Sasser, "A Highly Thinned Array Using The Image Element," *1980 International Symposium Digest. Antennas and Propagation,* pp. 150-3, 1980.
[116] L. Yanfei, R. Mittra, L. Guizhen, and K. Yoo, "Realization of High Directivity Enhancement by Using an Array of Microstrip Patch Antennas (MPAs) Covered by a Dielectric Superstrate," presented at the Loughborough Antennas & Propagation Conference, pp. 493-495, 2009.
[117] Y. B. Hua, "Estimating Two-Dimensional Frequencies by Matrix Enhancement and Matrix Pencil," *IEEE Transactions on Signal Processing,* vol. 40, pp. 2267-2280, 1992.
[118] S. Burintramart and T. K. Sarkar, "Target Localization in Three Dimensions," in *Advances in Direction-of-Arrival Estimation*, S. Chandran, Ed. Norwood: Artech House, 2006, pp. 87-101.
[119] O. G. Vendik and M. D. Parnes, *Antennas with Electrical Scanning*. Moscow: Science Press, 2002.
[120] S. Mestdagh, W. De Raedt, and G. A. E. Vandenbosch, "CPW-Fed Stacked Microstrip Antennas," *IEEE Transactions on Antennas and Propagation,* vol. 52, pp. 74-83, 2004.
[121] Y. Murakami, W. Chujo, and M. Fujise, "Mutual Coupling Between Two Ports of Dual Slot-Coupled Circular Patch Antennas," presented at the Antennas and Propagation Society International Symposium, pp. 1469-1472, 1993.
[122] M. I. Skolnik, *Introduction to Radar Systems*. Boston: McGraw Hill, 2001.
[123] H. L. Van Trees, *Detection, Estimation, and Modulation Theory*. New York: Wiley, 1968.
[124] B. Friedlander and A. J. Weiss, "Direction Finding in the Prescence of Mutual Coupling," *IEEE Transactions on Antennas and Propagation,* vol. 39, pp. 273-284, 1991.
[125] A. K. Bhattacharyya, *Active Phased Array Antenna : Floquet Analysis, Synthesis, BFNs, and Active Array Systems*: Wiley-Interscience, 2006.
[126] T. Sarkar, *Smart Antennas*. New York: IEEE Press Wiley-Interscience, 2003.

[127] Y. X. Sun, Y. L. Chow, and D. G. Fang, "A Mutual Impedance Formula Between Patch Antennas Based on Synthetic Asymptote and Variable Separation," *Microwave and Optical Technology Letters,* vol. 36, pp. 48-53, 2003.
[128] J. F. Zurcher and F. E. Gardiol, *Broadband Patch Antennas*. Dedham: Artech House, 1995.
[129] M. C. Bailey, "Closed-Form Evaluation of Mutual Coupling in a Planar Array of Circular Apertures," *NASA Technical Paper 3552,* 1996.
[130] M. D. Deshpande and M. C. Bailey, "Analysis of Finite Phased-Arrays of Circular Microstrip Patches," *IEEE Transactions on Antennas and Propagation,* vol. 37, pp. 1355-1360, 1989.
[131] D. E. J. Humphrey and V. F. Fusco, "A Mutual Coupling Model for Microstrip Patch Antenna Pairs with Arbitrary Orientation," *Microwave and Optical Technology Letters,* vol. 18, pp. 230-233, 1998.
[132] E. H. Fooks and R. A. Zakarevicius, *Microwave Engineering Using Microstrip Circuits*. New York, Sydney: Prentice Hall, 1990.
[133] C. Wood, "Analysis of Microstrip Circular Patch Antennas," *IEE Proceedings-H Microwaves Antennas and Propagation,* vol. 128, pp. 69-76, 1981.
[134] F. Yang, *Electromagnetic Band Gap Structures in Antenna Engineering*. Cambridge: Cambridge University Press, 2008.
[135] T. S. Laverghetta, *Microwave Materials and Fabrication Techniques*, 3rd ed. Boston, Mass. ; London: Artech House, 2000.
[136] L. H. Weng, Y. C. Guo, X. W. Shi, and X. Q. Chen, "An Overview on Defected Ground Structure," *Progress In Electromagnetics Research B,* vol. 7, pp. 173-89, 2008.
[137] "Federal Communications Commission Office of Engineering and Technology, FCC Online Table of Frequency Allocations, 47 C.F.R. § 2.106. Revised on July 25, 2014."
[138] "The European Table of Frequency Allocations and Applications in the Frequency Range 8.3 kHz to 3000 GHz (ECA Table). Approved May 2014."
[139] "Federal Communications Commission Office of Engineering and Technology, Millimeter Wave Propagation: Spectrum Management Implications, Bulletin Number 70, July, 1997."
[140] H. Hassanieh, F. Adid, D. Katabi, P. Indyk, and Acm, "Faster GPS via the Sparse Fourier Transform," *Mobicom 12: Proceedings of the 18th Annual International Conference on Mobile Computing and Networking,* pp. 353-364, 2012.
[141] A. Sommerfeld, "Ueber die Fortpflanzung Elektrodynamischer Wellen Längs Eines Drahtes," *Annalen der Physik,* vol. 303, pp. 233-290, 1899.
[142] A. Sommerfeld, *Electrodynamics : Lectures on Theoretical Physics Volume III*. New York: Academic Press, 1964.
[143] D. Hondros, "Über Elektromagnetische Drahtwellen," Doktorwürde der Hohen Philosophischen, Universität zu München, 1909.
[144] D. Hondros, "Über Elektromagnetische Drahtwellen," *Annalen der Physik,* vol. 335, pp. 905-950, 1909.
[145] W. Hersch, "Investigation into the Radiation Pattern of Surface Wave Aerials at 150 Mc/s and at 9000 Mc/s," Doctor of Philosophy, Univesity of London, 1958.
[146] W. Hersch, "The Surface-Wave Aerial," *Proceedings of the Institution of Electrical Engineers - Part C,* vol. 107, pp. 202-212, 1960.
[147] U. Fano, "The Theory of Anomalous Diffraction Gratings and of Quasi-Stationary Waves on Metallic Surfaces (Sommerfeld's Waves)," *Journal of the Optical Society of America,* vol. 31, pp. 213-222, 1941.
[148] H. M. Barlow and J. Brown, *Radio Surface Waves*. Oxford: Clarendon Press, 1962.

[149] H. M. Barlow, A. L. Cullen, G. G. Macfarlane, B. I. Stuart, J. G. Linhart, R. B. Dyott*, et al.*, "Surface Waves," *Proceedings of the Institution of Electrical Engineers,* vol. 100, pp. 329-347, 1953.
[150] F. Harms, "Elektromagnetische Wellen an einem Draht mit isolierender zylindrischer Hülle," *Annalen der Physik,* vol. 328, pp. 44-60, 1907.
[151] E. V. D. Glazier and H. R. L. Lamont, *The Services' Textbook of Radio, VOLUME 5 : TRANSMISSION AND PROPAGATION*: Her Majesty's Stationary Office, 1958.
[152] F. E. Terman and R. A. Helliwell, *Electronic and Radio Engineering*. New York: McGraw-Hill & Co., 1955.
[153] Y. Hargsoon, K. D. Song, L. Uhn, and S. H. Choi, "Microwave Thermal Radiation Effects on Skin Tissues," *Proceedings of the SPIE - The International Society for Optical Engineering,* vol. 8548, p. 85482R (12 pp.), 2012.
[154] S. A. Schelkunoff, *Electromagnetic Waves*. New York: Van Nostrand, 1943.
[155] E. Snitzer, "Cylindrical Dielectric Waveguide Modes," *Journal of the Optical Society of America,* vol. 51, pp. 491-498, 1961.
[156] V. N. Datsko and A. A. Kopylov, "On Surface Electromagnetic Waves," *Physics-Uspekhi,* vol. 51, pp. 101-102, 2008.
[157] R. W. Wood, "On a Remarkable Case of Uneven Distribution of Light in a Diffraction Grating Spectrum," *Philosophical Magazine,* vol. 4, pp. 396-402, 1902.
[158] J. Conant, *Tuxedo Park : A Wall Street Tycoon and the Secret Palace of Science that Changed the Course of World War II*. New York: Simon & Schuster, 2003.
[159] Y. Fuzi, J. R. Sambles, and G. W. Bradberry, "Long-Range Surface Modes Supported by Thin Films," *Physical Review B,* vol. 44, pp. 5855-72, 1991.
[160] J. Zhang, L. Zhang, and W. Xu, "Surface Plasmon Polaritons: Physics and Applications," *Journal of Physics D-Applied Physics,* vol. 45, p. 113001, 2012.
[161] S. A. Ramakrishna, "Physics of Negative Refractive Index Materials," *Reports on Progress in Physics,* vol. 68, pp. 449-521, 2005.
[162] N. W. Ashcroft and N. D. Mermin, *Solid State Physics*. New York: Holt, Rinehart and Winston, 1976.
[163] R. N. Bracewell, "Analogues of an Ionized Medium, Applications to the Ionosphere," *Wireless Engineer,* vol. 31, pp. 320-326, 1954.
[164] J. D. Jackson, *Classical Electrodynamics*. New York: Wiley, 1962.
[165] D. Pines and D. Bohm, "A Collective Description of Electron Interactions: II. Collective vs Individual Particle Aspects of the Interactions," *Physical Review,* vol. 85, pp. 338-353, 1952.
[166] D. Bohm and D. Pines, "A Collective Description of Electron Interactions: III. Coulomb Interactions in a Degenerate Electron Gas," *Physical Review,* vol. 92, pp. 609-625, 1953.
[167] H. Raether, *Excitation of plasmons and interband transitions by electrons / Heinz Raether*. Berlin ; New York: Berlin ; New York : Springer-Verlag, 1980.
[168] T. W. Ebbesen, H. J. Lezec, H. F. Ghaemi, T. Thio, and P. A. Wolff, "Extraordinary Optical Transmission through Sub-wavelength Hole Arrays," *Nature,* vol. 391, pp. 667-669, 1998.
[169] L. Martin-Moreno, F. J. Garcia-Vidal, H. J. Lezec, K. M. Pellerin, T. Thio, J. B. Pendry*, et al.*, "Theory of Extraordinary Optical Transmission through Subwavelength Hole Arrays," *Physical Review Letters,* vol. 86, pp. 1114-1117, 2001.
[170] L. Martin-Moreno, F. J. Garcia-Vidal, H. J. Lezec, A. Degiron, and T. W. Ebbesen, "Theory of Highly Directional Emission from a Single Subwavelength Aperture Surrounded by Surface Corrugations," *Physical Review Letters,* vol. 90, 2003.

[171] J. B. Pendry, "Intense Focusing of Light Using Metals," in *Proceedings of the NATO Advanced Study Institute on Photonic Crystals and Light Localization in the 21st Century*. vol. 563, C. M. Soukoulis, Ed. Netherlands: Springer, 2001, pp. 329-349.
[172] D. T. Emerson, "The Work of Jagadis Chandra Bose: 100 Years of Millimeter-Wave Research," *IEEE Transactions on Microwave Theory and Techniques,* vol. 45, pp. 2267-2273, 1997.
[173] V. G. Veselago, "Electrodynamics of Substances with Simultaneously Negative Values of Sigma and Mu," *Soviet Physics Uspekhi,* vol. 10, pp. 509-599, 1968.
[174] V. Veselago, L. Braginsky, V. Shkover, and C. Hafner, "Negative Refractive Index Materials," *Journal of Computational and Theoretical Nanoscience,* vol. 3, pp. 189-218, 2006.
[175] J. C. Bose, "On the Rotation of Plane of Polarisation of Electric Waves by a Twisted Structure," *Proceedings of the Royal Society of London,* vol. 63, pp. 146-152, 1898. Communicated by Lord Rayleigh.
[176] L. Rayleigh, "On the Influence of Obstacles Arranged in Rectangular Order Upon the Properties of a Medium," *Philosophical Magazine Series 5,* vol. 34, pp. 481-502, 1892.
[177] I. V. Lindell, A. H. Sihvola, and J. Kurkijarvi, "Karl F. Lindman: The Last Hertzian, and a Harbinger of Electromagnetic Chirality," *IEEE Antennas and Propagation Magazine,* vol. 34, pp. 24-30, 1992.
[178] W. E. Kock, *The Creative Engineer : The Art of Inventing*. New York: Plenum Press, 1978.
[179] W. E. Kock, "Metal-Lens Antennas," *Proceedings of the Institute of Radio Engineers,* vol. 34, pp. 828-836, 1946.
[180] W. E. Kock, "Metallic Delay Lenses," *Bell System Technical Journal,* vol. 27, pp. 58-82, 1948.
[181] S. B. Cohn, "Analysis of the Metal-Strip Delay Structure for Microwave Lenses," *Journal of Applied Physics,* vol. 20, pp. 257-262, 1949.
[182] J. Brown and W. Jackson, "The Properties of Artificial Dielectrics at Centimetre Wavelengths," *Proceedings of the Institution of Electrical Engineers,* vol. 102, pp. 11-16, 1955.
[183] M. M. Z. Kharadly and W. Jackson, "The Properties of Artificial Dielectrics Comprising Arrays of Conducting Elements," *Proceedings of the Institution of Electrical Engineers,* vol. 100, pp. 199-212, 1953.
[184] G. Estrin, "The Effects of Anisotropy in a 3-Dimensional Array of Conducting Disks," *Proceedings of the Institute of Radio Engineers,* vol. 39, pp. 821-826, 1951.
[185] R. W. Corkum, "Isotropic Artificial Dielectric," *Proceedings of the Institute of Radio Engineers,* vol. 40, pp. 574-587, 1952.
[186] W. Rotman, "Plasma Simulation by Artificial Dielectrics and Parallel-Plate Media," *Institute of Radio Engineers Transactions on Antennas and Propagation,* vol. 10, pp. 82-95, 1962.
[187] L. L. Tsai, "Phase-Delay-Type Artificial Dielectrics," *Technical Note 1975-4, Massachsetts Institute of Technology, Lincoln Laboratory,* 1975.
[188] J. B. Pendry, A. J. Holden, W. J. Stewart, and I. Youngs, "Extremely Low Frequency Plasmons in Metallic Mesostructures," *Physical Review Letters,* vol. 76, pp. 4773-4776, 1996.
[189] (20 Aug 2013). *Short Current Element*. Available: http://www.hirf-se.eu/portal/?q=node/108
[190] R. M. Walser, A. P. Valanju, and P. M. Valanju, "Comment on Extremely Low Frequency Plasmons in Metallic Mesostructures," *Physical Review Letters,* vol. 87, 2001.
[191] "ANSYS HFSS," ed. Canonsburg, PA, USA: ANSYS Inc.

[192] G. Goubau, "Surface Waves and Their Application to Transmission Lines," *Journal of Applied Physics,* vol. 21, pp. 1119-1128, 1950.
[193] G. Goubau, "Single-Conductor Surface-Wave Transmission Lines," *Proceedings of the Institute of Radio Engineers,* vol. 39, pp. 619-624, 1951.
[194] J. B. Pendry, A. J. Holden, D. J. Robbins, and W. J. Stewart, "Low Frequency Plasmons in Thin-Wire Structures," *Journal of Physics-Condensed Matter,* vol. 10, pp. 4785-4809, 1998.
[195] S. I. Maslovski and M. G. Silveirinha, "Nonlocal Permittivity from a Quasistatic Model for a Class of Wire Media," *Physical Review B,* vol. 80, 2009.
[196] S. E. Hobbs, K. Allsopp, and W. Wolf, "Signal Analysis for an Entomological Radar with a Vertical Nutating Beam," *College of Aeronautics Report 9919 ISBN 1 86194 0483* 2000.
[197] J. R. Huynen, "Measurement of Target Scattering Matrix," *Proceedings of the Institute of Electrical and Electronics Engineers,* vol. 53, pp. 936-946, 1965.
[198] J. F. Lawrence, E. S. Nielsen, I. M. Mackerras, I. D. Naumann, and P. B. Carne, "Skeletal Anatomy and Key to Orders," *The Insects of Australia,* pp. 3-32, 1991.
[199] D. F. Ward, F. Thomas, and R. Poulin, "Fluctuating Asymmetry and Parasitism in Six New Zealand Insects," *Acta Oecologica, International Journal of Ecology,* vol. 19, pp. 409-412, 1998.
[200] T. J. Dean and V. A. Drake, "Monitoring Insect Migration with Radar: The Ventral-Aspect Polarization Pattern and Its Potential for Target Identification," *International Journal of Remote Sensing,* vol. 26, pp. 3957-3974, 2005.
[201] W. W. Wolf, C. R. Vaughn, R. Harris, and G. M. Loper, "Insect Radar Cross-Sections for Aerial Density-Measurements and Target Classification," *Transactions of the American Society of Agricultural Engineers,* vol. 36, pp. 949-954, 1993.
[202] A. C. Aldhous, "An Investigation of the Polarisation Dependence of Insect Radar Cross Sections at Constant Aspect," Ecological Physics Research Group, Cranfield Institute of Technology, PhD, 1989.
[203] J. R. Riley, "Radar Cross-Section of Insects," *Proceedings of the IEEE,* vol. 73, pp. 228-232, 1985.
[204] S. O. Nelson, P. G. Bartley, and K. C. Lawrence, "Measuring RF and Microwave Permittivities of Stored-Grain Insects," *Joint Conference - 1996: IEEE Instrumentation and Measurement Technology Conference & Imeko Technical Committee 7, Conference Proceedings, Vols I and II: Quality Measurements: The Indispensable Bridge between Theory and Reality (No Measurements? No Science!),* pp. 1108-1113, 1996.
[205] D. K. Barton, *Radar System Analysis*. Dedham: Artech House, 1976.
[206] B. C. Peters and J. F. Kennedy, *Drywood Termites in Queensland*. Indooroopilly: Queensland Forestry Research Institute, Department of Primary Industries Forestry, 1998.
[207] P. Barber, J. Owen, and R. Chang, "Resonant Scattering for Characterization of Axisymmetric Dielectric Objects," *IEEE Transactions on Antennas and Propagation,* vol. 30, pp. 168-172, 1982.
[208] P. C. Waterman, "Symmetry, Unitarity, and Geometry in Electromagnetic Scattering," *Physical Review D,* vol. 3, pp. 825-839, 1971.
[209] P. Barber and C. Yeh, "Scattering of Electromagnetic Waves by Arbitrarily Shaped Dielectric Bodies," *Applied Optics,* vol. 14, pp. 2864-2872, 1975.
[210] L. Allan and G. McCormick, "Measurements of the Backscatter Matrix of Dielectric Bodies," *IEEE Transactions on Antennas and Propagation,* vol. 28, pp. 166-169, 1980.
[211] E. Peyskens, M. Pourcq, M. Stevens, and J. Schalck, "Dielectric Properties of Softwood Species at Microwave Frequencies," *Journal of the International Academy of Wood Science,* vol. 18, pp. 267-280, 1984.

[212] H. Sahin and N. Ay, "Dielectric Properties of Hardwood Species at Microwave Frequencies," *Journal of Wood Science,* vol. 50, pp. 375-380, 2004.

[213] V. Matveev and V. Budov, "Dielectric Parameters of Some Refractory Materials at Ultrahigh Frequencies," *Glass Ceram,* vol. 29, pp. 430-433, 1972.

[214] K. Sato, H. Kozima, H. Masuzawa, T. Manabe, T. Ihara, Y. Kasashima*, et al.*, "Measurements of Reflection Characteristics and Refractive Indices of Interior Construction Materials in Millimeter-Wave Bands," *1995 IEEE 45th Vehicular Technology Conference - Countdown to the Wireless Twenty-First Century, Vols 1-2,* pp. 449-453, 1995.

[215] K. Sato, T. Manabe, T. Ihara, H. Saito, S. Ito, T. Tanaka*, et al.*, "Measurements of Reflection and Transmission Characteristics of Interior Structures of Office Building in the 60-GHz Band," *IEEE Transactions on Antennas and Propagation,* vol. 45, pp. 1783-1792, 1997.

[216] R. Piesiewicz, C. Jansen, S. Wietzke, D. Mittleman, M. Koch, and T. Kuerner, "Properties of Building and Plastic Materials in the THz Range," *International Journal of Infrared and Millimeter Waves,* vol. 28, pp. 363-371, 2007.